

Exploitation of the synergetic effect of Mo and Nb on high strength quenched and tempered boron steels

Dissertation

submitted for the Degree of Doctor of
Philosophy at University of Navarra by

Irati Zurutuza Renom

under the supervision of

Pello Uranga Zuaznabar and

Nerea Isasti Gordobil

Donostia-San Sebastián, May 2022



tecnun
Universidad
de Navarra

NAFARROAKO UNIBERTSITATEA
INGENIARIEN GOI MAILAKO ESKOLA
UNIVERSIDAD DE NAVARRA
ESCUELA SUPERIOR DE INGENIEROS



Universidad
de Navarra

**Exploitation of the synergetic effect of Mo and
Nb on high strength quenched and tempered
boron steels**

Thesis

Submitted for the Degree of Doctor
of Philosophy at University of Navarra by

Irati Zurutuza Renom

Under the supervision of
Pello Uranga Zuaznabar
Nerea Isasti Gordobil

Donostia-San Sebastián, May 2022

*Ama, Aita, Amona, Aitona eta Mikele-ri
bihotz-bihotzez*

Esker onak

Lehenik eta behin, CEIT eta Nafarroako Unibertsitateari eman nahi dizkiet eskerrak, bertan tesia burutzeko aukera emateagatik. Bestetik, nire tesiko zuzendaria izan den Pello Urangari eskertu nahi diot urte hauetan zehar eskaini didan ezagutza zabala eta gertutasuna. Aldi berean, Nerea Isastiri eskerrak eman nahi dizkiot egunerokotasunean transmititu didan babesa eta jakintsunagatik, baina batez ere behar izan dudan guztian lagundu didalako. Mila esker biei, zorte handia izan dut zuek bezalako zuzendariekin topo egitean.

Eskerrik beroenak tratamenduen taldea osatzen duzuen kide bakoitzari. Beti irrifar batekin lagundu didazuelako. Mila esker bereziki zuri Jon, zurekin lan egitea horren erraza bilakatzeagatik eta erakutsi didazun guztiagatik. Eskerrik asko Itziar eta Iñigori ere, nire zalantza guztiak argitzeagatik. Horiez gain, mila esker laborategietan giro ona eta momentu entretenigarriak eskaini dizkidazuen lankide orori, baita ordenagailuko arazoak konpondu dizkidazuenei ere jaja.

Eskerrik asko bidean egindako lagunei, egon zirenei eta daudenei, zuek izan zarete guzti honen esentzia. Eskerrik asko despatxuan, kafean, bazkaltzen zein lanetik kanpo egindako planetan bizitako une bakoitzarengatik. Eskerrik asko egun tristean poztu eta astegunak dibertigarriak bilakatu dituzuelako. Zuen zatitxo bat nerekin etorriko da betirako.

Bestetik, eskerrik asko beti hor daudenei, inoiz huts egiten ez didan kuadrillari, egiten dudana egiten dudala, hoberena naizela uste izateagatik. Mila esker anoetako entrenatzaile zein lagunei, batez ere Valentin eta Rockyteam-ari, arratsaldero eta pistetatik kanpo partekatutako entrenamendu zein momentuengatik. Eskerrik asko Martin, askotan nire buruak baino gehiago nigan sinisteagatik eta erori naizen bakoitzean jaikitzen laguntzeagatik. Eskerrik asko beti alboan egon eta nire ametsen bila bultzatzeagatik.

Azkenik, eskerrik asko nire familiari, Ama, Aita, Amona, Aitona eta Mikeleri. Zuei esker bilakatu naiz egun naizen pertsona eta zuengatik lortu ditut proposatu ditudan helburu guztiak. Mila esker edozer lortzeko gai naizela uste izateagatik eta hartzen dudan erabaki oro babesteagatik. Eskerrik asko atletismoa ikasketa zein lanarekin uztartzea errazagoa bilakatzeagatik eta beti nire aukeren ginetik amesteagatik.

Eskerrik asko bide honen zati izan zareten guztiei!!

Laburpena

Egun, industrian, hainbat aplikazio estrukturalen eskakizunak asetzeko eta altzairuen erresistentzia propietateak hobetzeko asmoarekin, xafla lodiak tenplatu eta irautzen (Q&T) ari dira. Erresistentzia altuko altzairu hauek fabrikatzeko, berotako ijezketa ondorengo hozketa azkarra aplikatzen da. Estrategia honek, tenplaketa eta iraketa konbentzionalarekin alderatuta, ekoizpen eta ekonomiaren aldetik abantailak eskaintzen ditu. Hori dela eta, ikerketa honetan, berotako ijezketa ondorengo hozketa azkarrak duen erabilgarritasuna ebaluatuko da. Horrez gain, boroaren gehikuntza ohikoa da altzairuen erresistentzia eta tenplagarritasuna hobetu eta egitura baintiko/martensitikoaren sorrera bultzatzeko. Kasu batzuetan, boroa gehitzea ez da nahikoa egitura guttiz martensitikoak lortzeko eta beraz, Nb eta Mo-ren gehikuntza nahitaezkoa bilakatzen da boroaren eraginkortasuna areagotzeko.

Tesi hau, Molibdenoaren Nazioarteko Elkartearen (IMOA), Dillinger eta Ceit-en arteko kolaborazio baten emaitza da. Ikerketa honetan, Nb, Mo eta NbMo gehikuntzaren eragina aztertu da boro altzairuetan, mikroegitura eta propietate mekanikoen ikuspuntutik. Lan honetan zehar lortutako emaitzak, merkatuko eskakizun zorrotzak betetzen dituzten altzairu-gradu berriak garatzeko erabilgarriak izan dira. Proiektu honetan egindako ikerketa eta laborategiko entseguetan oinarrituta, Dillinger altzairutegiak, saiakuntza industrial batzuk burutu ditu, emaitza arrakastatsuak lortuz.

Konposizio kimikoaren inpaktua, aplikatutako estrategiak berotako ijezketan duen portaera, fase-transformazioaren eragina eta propietate mekanikoak aztertzeko helburuarekin, analisi ezberdinak burutu dira, berotako plantxoien ijezketa eta Q&T prozesuak simulatzeko asmoarekin. Horretarako, laborategiko saiakuntza ezberdinak erabili dira, hala nola, bihurtura, dilatometria eta konpresio laua. Proiektu hau, hiru atal nagusitan banatzen da eta atal bakoitza prozesu industrialaren urrats ezberdinekin lotuta dago.

Lehenengo atalean, aztertutako altzairuek berotako ijezketan zehar duten portaera aztertu da eta, horretarako, deformazio-iraganaldi anitzezko eta deformazio-iraganaldi bikoitzeko bihurtura saiakuntzak diseinatu dira. Lehenik, deformazio-iraganaldi anitzezko bihurtura probak egin dira tenperatura kritikoak definitzeko, hala nola, ez-birkristaltze tenperatura (T_{nr}). Horrez gain, deformazio-iraganaldi bikoitzeko bihurtura saiakuntzak egin dira, biguntze-zinetika aztertzeko eta birkristaltze-zinetikak inguruan dauden planteamendu ezberdinak balioztatzeko.

Ildo honetan, berotako ijezketa prozesua simulatu da bihurtura saiakuntzen bidez, birkristaltze dinamikoaren fenomenoak sakonago aztertzeko helburuarekin.

Bigarren atalean, fase-transformazioak aztertu dira. Ijezketa ondorengo tenplaketa azkarra (DQ) eta tenplaketa konbentzionala (CQ) prozesatzeko bideak simulatu dira dilatometria saiakuntzen bidez. Entsegu honetan lortutako kurbetatik abiatuta, hozte jarraiko transformazio (CCT) diagramak eraiki dira.

Hirugarren atalean, mikroegituraren eta lortutako propietate mekanikoen arteko erlazioa aztertu da. Horretarako, konpresio lauko saiakuntzak burutu dira, bi ziklo termomekanikoetan oinarrituz, tenplaketa (Q) eta tenplaketa eta iraketa (Q&T). Lortutako laginetatik, trakzio eta Charpy laginak mekanizatu dira, erresistentzia eta zailtasun propietateak aztertzeko. Erresistentzia propietateei dagokienez, gogortze-mekanismo ezberdinen kontribuzioaren eragina kuantifikatu da elastikotasun-mugan (soluzio solidoa, ale-tamaina, dislokazio-dentsitatea, karbonoa soluzio solidoan eta hauspeatze fina). Era berean, mikroegitura-parametro ezberdinek (ale-tamaina, soluzio solidoa, dislokazio-dentsitatea, karburoen presentzia, karbonoa soluzio solidoan, hauspeatze fina eta mikroegituraren heterogeneotasuna) zailtasun propietateetan duten eragina ebaluatu da. Gainera, inpaktu trantsizio-tenperatura aurreikusteko ekuazio bat (ITT%50) proposatu da, iraututako mikroegitura martensitikoetzat baliagarria dena.

Mikroegituraren karakterizazioari dagokionez, atal bakoitzean lortutako mikroegiturak karakterizazio-teknika aurreratuak erabiliz aztertu dira, mikroskopia optikoa, eremu-igorpen bidezko ekorketazko mikroskopia elektronikoa (FEG-SEM) eta transmisiozko mikroskopia elektronikoa (TEM) bidez esaterako. Mikroegituren karakterizazioa, Atzera Barreiatutako Elektroien Difrakzio (EBSD) teknikaren bidez osatu da, unitate-kristalografikoen tamainak eta dislokazio dentsitateak kuantifikatzeko.

Summary

In response to the demanding strength and impact resistance market requirements, plates and pipes are usually quenched and tempered (Q&T) for several applications. Regarding the production of these high strength steels, the direct quenching process offers operational and economic advantages compared to the conventional quenching route. In this study, the applicability of the direct quenching strategy is evaluated. Moreover, the addition of boron as an alloying element is a common practice in high strength steels to ensure hardenability and promote bainitic and martensitic microstructures. In some cases, the addition of boron is not enough to ensure full martensite formation, and thus, the addition of Nb and Mo can increase the efficiency of boron.

This thesis, is in the frame of an industrial project developed thanks to the collaboration of the International Molybdenum Association (IMOA), Dillinger and Ceit. This thesis is focused on the study of the addition of Nb, Mo and NbMo in boron high strength steels in terms of microstructure and mechanical properties. The results extracted during this project were useful for the development of new steel grades that fulfil the most demanding market requirements. Successful results were achieved from the industrial trials performed at Dillinger.

With the purpose of analysing the impact of chemical composition, the applied strategy on hot working behaviour, phase transformation and mechanical properties, several thermomechanical treatments were completed. By means of different laboratory tests, such as torsion, dilatometry and plane strain compression tests, plate hot rolling and Q&T process were simulated. This project is divided in three main tasks and each of the task is in line with the different steps involved in a real industrial process.

The first task is focused on the hot working behaviour of the studied steels and multipass and double-pass torsion tests were done. Multipass torsion tests were performed in order to define the critical temperatures such as the non-recrystallization temperature (T_{nr}). Additionally, double-pass torsion tests were carried out to analyse the softening kinetics and to validate different approaches available regarding recrystallization kinetics. Furthermore, plate hot rolling simulations were performed in torsion, with the purpose of analysing dynamic recrystallization behaviour in more depth.

The second task is focused on the phase transformation analysis. Direct quenching (DQ) and conventional quenching (CQ) processing routes were simulated by

dilatometry tests and from the dilatometry curves, Continuous Cooling Transformation (CCT) diagrams were built.

In the third task, the relationship between microstructure and the resulting mechanical properties were analysed. To that end, plane strain compression tests were performed for simulating quenching (Q), as well as quenching and subsequent tempering (Q&T). From the obtained samples, tensile and Charpy specimens were machined to analyse the tensile and toughness properties. Regarding tensile properties, the contribution of different strengthening mechanism to yield strength (solid solution, grain size, dislocation density, carbon in solid solution and fine precipitation) were quantified. Likewise, the impact of different microstructural parameters (grain size, solid solution, dislocation density, presence of carbides, carbon in solid solution, fine precipitation and microstructural heterogeneity) on toughness were evaluated. Furthermore, an existing equation able to predict the impact transition temperature (ITT50%) for ferrite-pearlite and bainitic microstructures was extended to tempered martensitic microstructures.

Regarding microstructural characterization, the obtained microstructures in each task were characterized using advanced characterization techniques, such as optical microscopy, field emission gun scanning electron microscopy (FEG-SEM) and transmission electron microscopy (TEM). The microstructural characterization was completed by the electron backscattered diffraction (EBSD) technique, in order to quantify the crystallographic unit sizes and dislocation densities.

Thesis

This PhD dissertation is presented in a paper-based format. The papers published by the author are listed below. Impact factor (IF) and quartile (Q) are included.

Appended papers

Paper I

I. Zurutuza, N. Isasti, E. Detemple, V. Schwinn, H. Mohrbacher, and P. Uranga, 2022, Effect of Nb and Mo on austenite microstructural evolution during hot deformation in Boron high strength steels, *Metallurgical and Materials Transactions A*, Vol. 53, pp. 1529-1539. DOI: 10.1007/S11661-022-06618-0

IF (2020) 2.556. Q1 (20/80) in Metallurgy & Metallurgical Engineering.

Paper II

I. Zurutuza, N. Isasti, E. Detemple, V. Schwinn, H. Mohrbacher, and P. Uranga, 2022, Effect of Dynamic Recrystallization on Microstructural Evolution in B Steels Microalloyed with Nb and/or Mo, *Materials*, Vol. 15, no. 4, 1424. DOI: 10.3390/ma15041424

IF (2020) 3.623. Q1 (17/80) in Metallurgy & Metallurgical Engineering.

Paper III

I. Zurutuza, N. Isasti, E. Detemple, V. Schwinn, H. Mohrbacher, and P. Uranga, 2021, Effect of Quenching Strategy and Nb-Mo Additions on Phase Transformations and Quenchability of High-Strength Boron Steels, *JOM*, Vol. 73, no. 11, pp. 3158–3168. DOI: 10.1007/s11837-021-04773-0

IF (2020): 2.471. Q2 (21/80) in Metallurgy & Metallurgical Engineering.

Paper IV

I. Zurutuza, N. Isasti, E. Detemple, V. Schwinn, H. Mohrbacher, and P. Uranga, 2021, Effect of Nb and Mo additions in the microstructure/tensile property relationship in high strength quenched and quenched and tempered boron steels, *Metals*, Vol. 11, no. 1, 29. DOI: 10.3390/met11010029

IF (2020): 2.351. Q2 (24/80) in Metallurgy & Metallurgical Engineering.

Paper V

I. Zurutuza, N. Isasti, E. Detemple, V. Schwinn, H. Mohrbacher, and P. Uranga, 2021, Toughness property control by Nb and Mo additions in high-strength quenched and tempered boron steels, *Metals*, Vol. 11, no. 1, 95. DOI: 10.3390/met11010095

IF (2020): 2.351. Q2 (24/80) in Metallurgy & Metallurgical Engineering.

In addition to the papers published in journals, several contributions to conferences were submitted.

Contribution to conferences

I. Zurutuza, N. Isasti, E. Detemple, V. Schwinn, H. Mohrbacher, and P. Uranga, Effect of Thermomechanical Strategy and Mo-Nb-B Alloying Additions on High Strength Medium Carbon Q/Q&T Steels, in *Materials Science and Technology (MS&T19)*, 2019, Portland, OR, USA, pp. 1401–1408.

I. Zurutuza, N. Isasti, E. Detemple, V. Schwinn, H. Mohrbacher, and P. Uranga, Relationship between microstructure and tensile properties on high strength medium carbon Mo-Nb microalloyed Q/Q&T steels, in *Materials Science and Technology (MS&T20)*, 2020, Virtual.

I. Zurutuza, N. Isasti, E. Detemple, V. Schwinn, H. Mohrbacher, and P. Uranga, Microstructure and toughness correlation in high strength Q/Q&T Boron steels microalloyed with Nb and Mo, in *Materials Science and Technology (MS&T21)*, 2021, Virtual.

I. Zurutuza, N. Isasti and P. Uranga, Nb eta Mo gehikuntzaren eragina mikroegitura/propietate mekanikoetan karbono ertaineko Q/Q&T boro altzairuetan, in *Materialen Zientzia eta Teknologia (MZT2021)*, 2021, Bilbo, pp. 187-192.

International Award

The international 2021 Gilbert R. Speich Award (AIST) was received to the best contribution to Physical Metallurgy for the presentation entitled “Relationship between microstructure and tensile properties on high strength medium carbon Mo-Nb microalloyed Q/Q&T steels”, presented at the MS&T’20 Conference.

Index

1. Introduction	1
2. Literature review	3
2.1. High strength Quenched and Quenched and Tempered steels	3
2.1.1. Application of high strength Q/Q&T steels	5
2.1.2. Microalloyed steels	5
2.1.2.1. Effect of microalloying elements	5
2.1.2.2. Influence of microalloying elements	7
2.1.2.3. Effect of boron on hardenability	8
2.1.2.4. Influence of Nb and Mo microalloying on boron steels	9
2.2. Hot rolling processes	10
2.2.1. Types of controlled rolling	11
2.2.1.1. Recrystallization controlled rolling	11
2.2.1.2. Conventional controlled rolling	12
2.2.2. Direct Quenching/Quenching and Tempering (Q&T)	13
2.2.2.1. Direct Quenching (DQ)	13
2.2.2.2. Quenching and Tempering (Q&T)	13
2.3. Metallurgical mechanisms during hot rolling	14
2.3.1. Softening processes	14
2.3.1.1. Recovery	15
2.3.1.2. Recrystallization	15
2.3.1.3. Recrystallized grain size	18
2.3.2. Delay in softening kinetics	19
2.3.2.1. Solute drag effect	19
2.3.2.2. Precipitate pinning	20
2.3.3. Precipitation	20
2.3.3.1. Types of precipitation	22
2.3.4. Phase transformation	23
2.3.4.1. CCT diagrams	23
2.3.4.2. Transformation products	24
2.3.4.3. Phase transformation during DQ process	27

2.4. Relationship between microstructure and mechanical properties.....	31
2.4.1. Tensile properties	31
2.4.1.1. Strengthening mechanisms	31
2.4.2. Toughness properties.....	36
2.4.2.1. Contributions to toughness	37
2.4.3. Relationship between microstructure and tensile/toughness properties in high strength Q/Q&T steels.....	38
3. Summary of appended papers	41
4. Appended papers	45
5. Discussion	129
6. Conclusions and future work.....	147
References.....	151

1. Introduction

In the steel industry, there is a significant and increasing demand for improving the mechanical properties of the steels for a large variety of applications. For the production of high strength steels, advanced thermomechanical hot rolling schedules followed by direct quenching are being developed in order to avoid reheating and quenching treatment after hot rolling to eliminate an energy and cost consuming step.

In order to satisfy the demanding market requirements and achieve a good balance between strength and toughness, the addition of microalloying elements is commonly accepted in industry. The use of boron as an alloying element is a widely known practice in high strength quenched and tempered (Q&T) steels, due its ability for enhancing hardenability and ensuring the formation of bainitic/martensitic microstructures. These steels are considered the material of choice for many advanced applications where yield strength above 500 MPa is required to reduce component weigh. Moreover, significant synergetic effect on hardenability can be reached through the combination of Nb and Mo in boron steels, achieving yield strength values in the range of 800-1000 MPa. The effect of the addition of these microalloying elements individually has been intensively studied for microstructures composed of ferrite and/or bainite. Nevertheless, the effect of B-Nb-Mo combinations on martensitic microstructures has been less explored and requires more study and comprehension.

Furthermore, besides selecting an optimum alloy concept, an appropriate design of the thermomechanical process becomes crucial for achieving pancaked austenite that promotes the formation of refined microstructures and improves the resulting mechanical properties. The effect of different hot rolling and heat treatment strategies have been explored with the aim of developing more efficient processing routes that promotes important weight-reductions.

The main objective of this project is to study the synergetic effect of Nb, Mo and B on high strength Q/Q&T steels. For that purpose, the combined effect of Nb, Mo and B on hot working behaviour, phase transformations and tensile/toughness properties will be deeply investigated. Furthermore, the effect of different hot rolling and heat treatment strategies will be explored, with the aim of developing more efficient

processing routes that promote important weight-reductions. In order to further the understanding concerning advanced processing strategies and achieve higher strength Q/Q&T steels, the influence of austenite pre-conditioning on the martensitic microstructures obtained after CQ and DQ treatments will be evaluated.

The specific objectives of this thesis are the following:

- To evaluate the impact of adding microalloying elements (Nb, Mo and Nb-Mo) and process parameters on hot working behaviour and austenite conditioning. To validate the available equations regarding recrystallization kinetics for the current steel grades.
- To determine the effect that alloying elements such as Mo, Nb and Nb-Mo have on phase transformation (for martensitic microstructures). Additionally the effect of austenite conditioning (recrystallized or deformed austenite) will be evaluated. To select the optimum alloy concept and process strategy to obtain fully martensitic microstructure.
- To achieve an exhaustive characterization of resulting microstructures obtained in thermomechanically treated samples using different microscopy techniques such as SEM, FEGSEM, EBSD/OIM and TEM. The main objective will be the determination of the low/high angle crystallographic units in martensitic microstructures to evaluate the contribution of grain size, precipitation and dislocation density to mechanical properties.
- The relationship between the obtained microstructures and the resulting mechanical properties will be analysed by means of tensile and Charpy tests. The contribution of different strengthening mechanisms to final strength and toughness will be evaluated for martensitic microstructures by means of mechanical test data, microstructural characterization and precipitation analysis.

2. Literature review

2.1. High strength Quenched and Tempered steels

The use of high strength steels is widely accepted in industry since they provide several benefits compared to the traditional lower strength steel grades. In order to decrease the environmental impact concerning the increase of greenhouse gases, high strength steels offer great possibilities, especially in the transportation and energy sectors. For instance, the use of high strength steels allows lightweight constructions of vehicles leading to lower fuel consumption and higher load capacity. Regarding the production of high strength steels in the steel industry, the process of direct quenching can lead to the desirable combination of strength and toughness, combined with relatively low energy consumption, compared to the traditional reheating and quenching process [1].

Moreover, the use of boron as an alloying element is a common practice in high strength Q/Q&T steels to increase the strength, ensure hardenability and promote bainitic/martensitic microstructures. This alloy concept has been used in many advanced applications where yield strength above 500 MPa is required to reduce component weight [2, 3]. The addition of microalloying elements, such as Nb and/or Mo in these steels is well established as a mean to increase the yield strength values between 800-1000 MPa [4].

Molybdenum is an important alloying element in ultrahigh strength steels when the required yield strength exceeds about 500 MPa (Figure 2.1, [5]). As shown in Figure 2.1, the addition of Mo improves yield strength and consequently, lower plate thickness is needed to fulfil the requirements. The formation of low-temperature transformation products such as bainite and martensite could be achieved through the addition of Mo [6]. Furthermore, the combined addition of Nb and B to a Ti-protected steel increases the tensile strength [7].

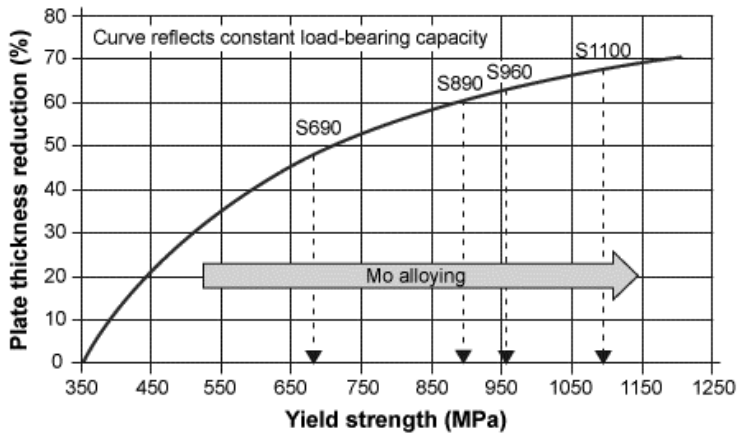


Figure 2.1. Thickness (and weight) reduction caused by yield strength improvement [5].

Therefore, the main objective of these high strength steels is to achieve the desired final microstructure combined with suitable mechanical properties. To that end, an appropriate design of the thermomechanical process becomes crucial. Quenching (Q) and quenching and tempering (Q&T) treatments are well established in industry to produce high strength steels. The benefits of thermomechanical treatments are well known to obtain an optimum pancaked austenitic structure resulting in refined final grain size [8]. Through conventional controlled rolling and accelerated cooling, it is possible to obtain fine-grained microstructure with excellent combination of strength and toughness properties.

Quenched (Q) and quenched and tempered (Q&T) steels are usually produced by conventional quenching (CQ) routes, in which the hot rolled plate is reheated to austenite in a separate process. Direct quenching is an efficient process to make tough high-strength and cost effective steels for demanding applications [9]. In the DQ process, the conditioned austenitic microstructure is subjected to high cooling rate immediately after hot rolling promoting the transformation of martensite. Moreover, the DQ route has economic and operational advantages over the CQ route, as allows producing higher volumes of ultrahigh strength steels [10]. Additionally, the tempering treatment is required to soften the martensitic microstructure, promoting an improvement of toughness and ductility [11–13].

2.1.1. Application of high strength Q/Q&T steels

In response to the demanding strength and impact resistance market requirements, plates and pipes are usually quenched and tempered for a large variety of applications, such as crane booms, support structures, mechanical equipment, machinery, wear plate, pressure vessels, storage tanks, wear resistance steel plates for dumpers and offshore rig-legs. The chemical compositions of the steel grades are adapted to obtain the required mechanical properties for each specific application. Some examples of different applications are plotted in Figure 2.2.



Figure 2.2. Examples of applications of High Strength Q/Q&T steels (a) Wear resistance steel plates used in dumpers (b) Heavy weigh cranes and (c) Offshore rig-legs.

2.1.2. Microalloyed steels

The addition of microalloying elements is extensively employed in the development of advanced steels. Small additions of microalloying elements such as Nb, Mo or Ti can introduce significant changes in the evolution of the microstructure during steel processing and in the final mechanical properties.

2.1.2.1. Effect of microalloying elements

The main phenomenon that take place after the addition of microalloying elements and during hot rolling process are summarized below.

Grain refinement

The addition of microalloying elements such as Nb, provides the control of austenite grain size during hot rolling, leading to a finer grain size after phase transformation and an improvement on strength and toughness. The refinement of the grain size depends on the composition and process parameters employed in the hot rolling. The reduction of the transformed grain size is obtained by increasing the surface area per unit volume of the austenite prior to transformation (S_v) [14, 15]. Furthermore, controlled hot rolling is widely used in order to obtain the refinement of the final microstructure. Austenite conditioning could be achieved through fine recrystallized austenite grains or by the formation of deformed austenite. The aim of both strategies is to achieve a fine microstructure and suitable combination of strength and toughness. The addition of Ti and Nb to steels is a common practice when microstructural refinement is required. While Ti addition controls the grain growth of the recrystallized microstructure, Nb promotes the accumulation of deformation in the prior austenite [16].

Delay of recrystallization kinetics

The application of deformation at high temperatures promotes the activation of softening mechanisms (recrystallization and recovery) in the microstructure, based on the reorganization and elimination of the crystalline lattice defects through the movement of grain boundaries. The addition of some specific microalloying elements can produce a delay in recrystallization kinetics due to the presence of these elements in solid solution. The Nb and Mo are two most effective elements retarding recrystallization kinetics due to solute drag, being Nb the most effective microalloying element for delaying recrystallization via solid solution [17, 18] and in precipitate form [19, 20]. The delay in recrystallization could also be related to the formation of carbides, nitrides or carbonitrides during hot rolling. This precipitation, known as *strain induced precipitation*, can completely inhibit the recrystallization process.

Precipitation hardening

The precipitation of fine and homogeneously distributed carbides could also promote an important strengthening effect [21]. Moreover, in microalloyed steels, a suitable thermomechanical treatment is required in order to promote the formation of fine precipitates during or after transformation. The most effective hardening effect is achieved when the size of the precipitates decreases and the volume fraction of the precipitates increases. V and Ti are the most effective microalloying element in terms of precipitation hardening. When V and Ti are added, fine precipitates are formed

during continuous cooling or coiling, promoting strengthening. Also, the formation of NbC and MoC precipitates are also considered to provide a strong hardening effect [22, 23].

Phase transformation

The addition of microalloying elements can affect phase transformation and the resulting microstructure. The addition of Nb or Mo can retard phase transformation leading to a decrease of transformation start temperatures and promoting the formation of non-polygonal microstructures [6, 24]. A finer grained transformation product is produced in this way, increasing the strengthening due to grain size refinement [4].

2.1.2.2. Influence of microalloying elements

The characteristics of the microalloying elements studied in this work are described in the following lines.

Niobium (Nb)

The use of niobium as microalloying element is a common practice in conventional controlled rolling, due to Nb effect in solid solution and through the precipitation of Nb (C,N). The addition of niobium is well known because of its ability to delay static recrystallization. Nb addition retards static recrystallization of hot rolled austenite by the accumulation of deformation in the austenite prior to transformation, resulting in grain size refinement with improved mechanical properties [25, 26]. This could be attributed to the formation of strain induced precipitates or Nb in solid solution. The formation of fine Nb carbides during cooling, can also increase the hardening effect.

Molybdenum (Mo)

Molybdenum is usually added to steels to increase strength due to its effect to promote low temperature transformation products such as bainite and martensite after hot rolling [4, 27]. The presence of Mo in solid solution reduces carbon diffusivity in the transformation interface, delaying the initial transformation temperatures and obtaining complex phases to provide greater strength to the steel. In addition, Mo in solid solution can also retard static recrystallization kinetics leading to the formation of finer microstructures [28].

NbMo microalloyed steels

The combined addition of Nb and Mo is widely used when producing advanced high strength low alloy (HSLA) steels. The addition of Mo to Nb microalloyed steels is known to have synergetic influences providing more benefits than Nb and Mo alone, due to the effect of both elements in phase transformation, microstructural refinement and precipitation hardening [29, 30]. This combined addition presents higher non-recrystallization temperatures (T_{nr}) than Nb microalloyed steels, due to the synergy effect of both elements retarding static recrystallization [26, 28]. Nb-Mo addition ensures accumulation of deformation in the austenite prior to transformation and therefore, a refined final microstructure is obtained [31]. Moreover, the synergy effect of Nb and Mo on the delay of phase transformation is also reported in the literature [32, 33]. The addition of Mo to Nb microalloyed steel increases precipitation hardening by two different mechanisms; Molybdenum increases the solubility of Nb in austenite, providing a higher amount of solute niobium available for precipitation and increasing the precipitation hardening effect [34]. In addition, Mo also delays Nb precipitation in austenite, due to the reduction of the diffusivity of C and N, promoting a finer-sized and a copious Nb (C,N) precipitate formation during or after phase transformation, resulting in more pronounced precipitation hardening [30, 35, 36].

2.1.2.3. Effect of boron on hardenability

Boron is an efficient microalloying element, commonly used in high strength quenched and quenched and tempered steels, in substitution of more expensive elements. The use of boron as an alloying element is a widely known practice in high strength steels to increase the strength due its ability for delaying phase transformation, enhancing hardenability and ensuring the formation of bainitic/martensitic microstructures [2, 10]. The segregation of boron in austenite grain boundaries ensures hardenability and delays the formation of softer phases such as pearlite and ferrite. Nevertheless, to guarantee its effectiveness it is essential to maintain B in solid solution [37]. However, B can interact with N and/or C to form nitrides and carbides at high temperatures, limiting its effect on hardenability. In order to avoid the formation of BN and $Fe_{23}(C,B)_6$ precipitates, it is a common practice to add titanium microalloying to protect the loss of solute boron as BN and $Fe_{23}(C,B)_6$, forming more stable TiN precipitates at high temperatures [38]. Simultaneously, Al also is considered a strong nitride-forming element and is usually used to protect boron [39]. Consequently, the segregation of B atoms to the austenite grain boundaries is favoured delaying the nucleation of ferrite and promoting a strong effect on hardenability. In order to ensure good mechanical properties, it is

vital to avoid soft phases and to ensure fully martensitic and homogeneous microstructures [31, 40].

2.1.2.4. Influence of Nb and Mo microalloying on boron steels

In order to verify the effect of boron on hardenability, the segregation and precipitation of B needs to be controlled. Combined alloying of Nb and B as well as Mo and B can also improve hardenability in boron steels [3, 31, 41]. Boron segregation at the austenite grain boundaries is ensured by the formation of Nb or Mo carbides, reducing carbon content and suppressing the formation of $\text{Fe}_{23}(\text{C},\text{B})_6$ boron carbides [26, 29]. These precipitates have some detrimental effects on hardenability, acting as a preferential nucleation sites for the austenite to ferrite transformation. In Figure 2.3, the mechanisms for suppression of $\text{Fe}_{23}(\text{C},\text{B})_6$ is schematically shown for both Nb-B and Mo-B additions [7]. When B is added alone (Figure 2.3a) B and C segregates in the grain boundary and $\text{Fe}_{23}(\text{C},\text{B})_6$ are partially formed. Depending on the alloy concept (Nb-B or Mo-B) the mechanisms involving the suppression of boron carbides are different. The addition of Mo improves the effectiveness of B due to the intragranular Mo-C cluster formation that reduces the carbon diffusion into the austenite grain boundary (Figure 2.3c). Niobium microalloying was found to avoid $\text{Fe}_{23}(\text{C},\text{B})_6$ precipitation, related to Nb-C clusters and Nb carbonitride precipitation reducing solute carbon in the austenite grain boundary, see Figure 2.3b. Furthermore, reference [7] claims that the addition of Nb to a B steel promotes the formation of more abundant C precipitates and C clusters than in Mo-B steel, obtaining an increase on hardenability. Moreover, when Nb is added to a boron steel, B can also act as a recrystallization delaying element when is in solid solution. Nevertheless, molybdenum can act as a hardenability element by itself, enhancing the B effect. Compared to Nb-B steel where only B acts as hardenability agent, Mo-B steel shows lower transformation temperatures as well as higher hardness at any cooling rate [42].

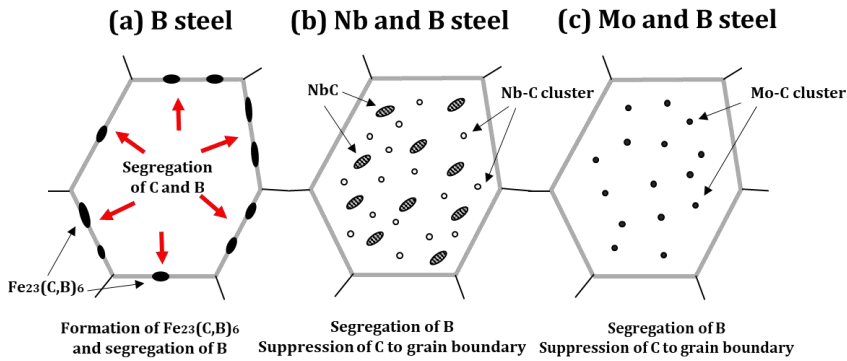


Figure 2.3. Schematic diagram showing different mechanisms for suppression of formation of Fe₂₃(C,B)₆ due to combined addition of Nb and B or Mo and B [7].

2.2. Hot rolling processes

In industry, the steel products can be obtained by means of continuous casting and in most cases the required characteristics both geometrical as well as mechanical are not good enough for a commercial use, so a subsequent hot working process becomes crucial. Hot rolling is extensively used in a wide range of materials. Hot rolling can be described as an industrial route that includes hot deformation schedules able to achieve a suitable austenite microstructure that will be transformed, during successive cooling, into a microstructure that meets the mechanical property requirements. For that purpose, an adequate understanding, evaluation and control of the microstructural changes that occur at each step of a rolling schedule is needed [43].

In Figure 2.4 hot rolling process is shown schematically. During this process, deformation is applied in a series of passes separated by different periods of time. After continuous casting and subsequent cooling, in the first step the slab is reheated in the reheating furnace in order to increase the material workability and dissolve the microalloying elements. After that, roughing is applied to the steel, consisting on the highest thickness reduction of the entire process by means of plastic deformation in successive rolling passes, with the aim of obtaining the desired thickness of the product. In addition, in this step the deformation passes are applied at high temperatures with the purpose of ensuring the recrystallization of the material between passes and to obtain an equiaxed, homogeneous and fine austenitic microstructure. In the finishing step, the steel is subjected to smaller deformation passes at lower temperatures. Rolling at low temperatures in Nb microalloyed steels

promotes the formation of strain induced precipitates and the subsequent grain size pancaking of austenite grains and control of the final microstructure. To conclude, the steel is cooled down following different cooling strategies depending on the required mechanical properties [44].

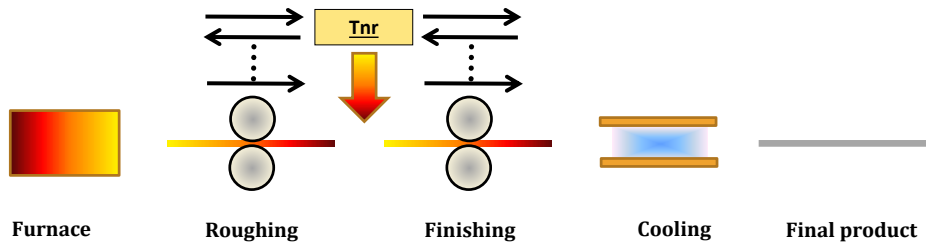


Figure 2.4. Schematics of a hot rolling process [45].

The most relevant process parameters involved in defining the evolution of the microstructure from pass to pass are strain, strain rate and temperature in each pass and the interpass time. In addition, the chemistry of the steel and the characteristics of the microstructure at the entry of the rolling pass also can affect the evolution of the microstructure [46].

2.2.1. Types of controlled rolling

The main objective of thermomechanical treatments is to achieve a final refined microstructure, being this the only microstructural parameter that simultaneously improves the strength and toughness properties of the steels. In order to obtain a refined microstructure, an adequate alloy design and deformation conditions needs to be defined. Recrystallization Controlled Rolling and Conventional Controlled Rolling are the most used hot rolling strategies in industry, as shown in Figure 2.5 [44]. In both thermomechanical treatments, a suitable control of austenite conditioning becomes crucial as means to achieve a refined microstructure with improved mechanical properties [47, 48]. The aim of thermomechanical treatments is to increase the effective austenite boundary area per unit volume (S_v), and thus, promote the formation of nucleation sites for phase transformation [6].

2.2.1.1. Recrystallization controlled rolling

Recrystallization controlled rolling is based on the application of rolling passes above the non-recrystallization temperature (T_{nr}) preventing austenite grain growth during reheating, rolling and after rolling (see Figure 2.5, [44]). The main objective of this process is to obtain a refined austenite grain size prior to transformation. This

austenite control is obtained with Ti microalloying that provides the presence of fine dispersed TiN particles able to exert pinning effect on the grain boundaries and consequently avoiding austenite grain growth [49]. As a result, the specific grain boundary area, S_v , is increased by reducing the austenite grain size to an equiaxed microstructure.

2.2.1.2. Conventional controlled rolling

The objective in conventional controlled rolling is to obtain a pancaked austenite with accumulated strain before transformation. To that end, several deformation passes are applied at temperatures below the non-recrystallization temperature (T_{nr}) (see Figure 2.5, [44]). The obtained microstructure is characterized by a high density of nucleation sites that, during transformation, results in a finer final microstructure [43]. Nb microalloying is widely used in this rolling strategy. The precipitation of Nb during hot rolling delays or inhibits static recrystallization and promotes the accumulation of deformation in the austenite prior to transformation.

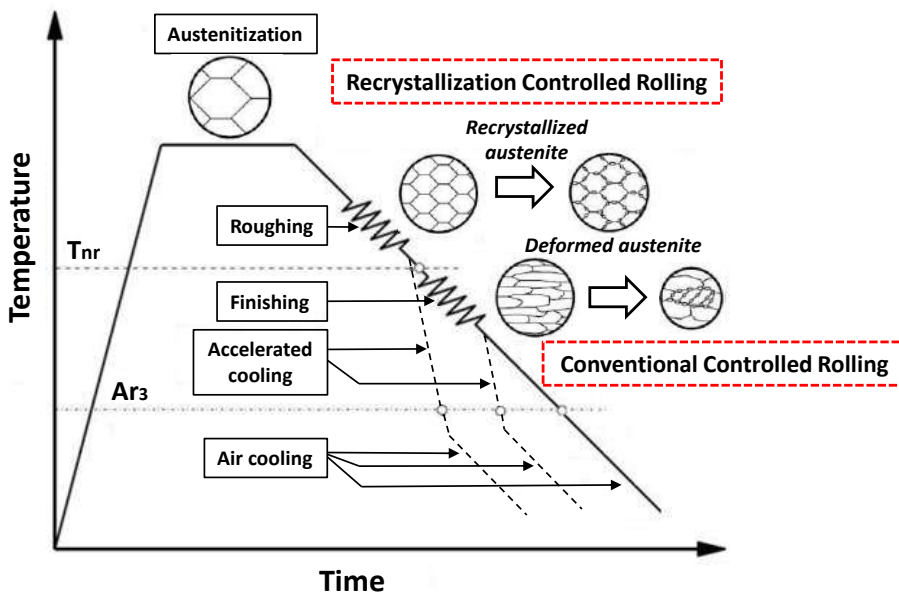


Figure 2.5. Scheme of different rolling strategies [44].

2.2.2. Direct Quenching/Quenching and Tempering (Q&T)

In the present study, two different thermomechanical routes are studied, quenching (Q) and quenching and tempering (Q&T). In the following lines, a brief description of each thermomechanical treatment is detailed.

2.2.2.1. Direct Quenching (DQ)

The direct quenching (DQ) strategy is based on the application of fast cooling to the conditioned austenitic microstructure immediately after hot rolling process, promoting the formation of martensite. The DQ route is economically attractive as it can remarkably reduce the procedural steps to make lighter and more energy-efficient structures with high strength steels [50–52]. This is an efficient process used to improve the strength and toughness of steels by pancaking the austenite below the recrystallization stop temperature (RST) prior to quenching [53]. Depending on the rolling conditions and the alloy concept, there may be a risk of forming undesirable soft phases, such as ferrite and bainite. To that end, thermomechanical processing must be carefully designed in order to obtain an optimum pancaked austenitic structure resulting in refined final grain size. For ensuring full transformation into martensite, hardenability increasing microalloying elements have to be used. The use of boron in conjunction with microalloying elements (Nb, Mo or Nb-Mo) is a common practice for increasing hardenability [30].

2.2.2.2. Quenching and Tempering (Q&T)

Tempering consists on a reheating process usually applied to steels after quenching. The tempering treatment softens the martensitic microstructure thereby promoting an improvement of toughness and ductility [11].

As mentioned before, the aim of quenching is to obtain martensitic microstructures. Martensite is a highly unstable structure that will undergo different changes depending on the tempering conditions. This instability is attributed to the supersaturation of carbon atoms in the body-centred tetragonal crystal lattice. This supersaturation of carbon atoms provides the driving force for cementite formation, the strain energy associated with the dislocations is the driving force for recovery and the interfacial energy associated with the high amount of lath or plate boundaries is the driving force growth or coarsening of the ferrite matrix [12]. Thus, many factors can be responsible of the mechanical property changes developed when martensitic carbon steels are tempered. Tempering is usually divided in the following three stages [54–57]:

Stage I: the formation of a transition carbide and the lowering of the carbon content on the matrix martensite.

Stage II: the transformation of retained austenite to ferrite and cementite.

Stage III: the replacement of the transition carbide and low-carbon martensite by cementite and ferrite.

Tempering treatment causes a modification of the quenched martensite, leading to the formation of carbides that can retard softening kinetics and/or produce secondary hardening phases. Depending on the tempering temperature and the following maintenance time, different type of carbides can be distinguished. High temperature followed by long maintenance times can promote the formation of coarse grain boundary carbides that will affect the toughness behaviour in the ductile-brittle regime [58]. In contrast, when high heating rates are combined with shorter holding times, tempering leads to faster carbide nucleation kinetics, which results in a final microstructures with finer cementite particles [59, 60]. Therefore, induction tempering treatments can offer additional microstructural improvements. For that purpose, a proper selection of induction tempering parameters, such as, heat rates, holding times and carbide distributions becomes essential [12].

2.3. Metallurgical mechanisms during hot rolling

2.3.1. Softening processes

Hot rolling, is characterized by the application of several deformation passes separated by different periods of time. During these deformation passes and the corresponding interpass intervals, there is a competition between work hardening (dislocation storage) and softening (dislocation elimination) mechanisms. The deformation applied in a rolling pass is partially transformed into stored energy in the steel. In addition, this stored energy can be released by certain softening mechanisms such as recovery and recrystallization. Under some conditions, these softening mechanisms can be activated dynamically (during the application of deformation) or statically (during the interpass time). If the interpass time is long enough, once recrystallization is completed, grain growth may occur before the next deformation pass. The microstructural changes that can happen from pass to pass during hot rolling are illustrated in Figure 2.6. In microalloyed steels, the interactions between work hardening and softening usually make the evolution of microstructure more complicated, while the microalloying elements can precipitate during hot rolling [44].

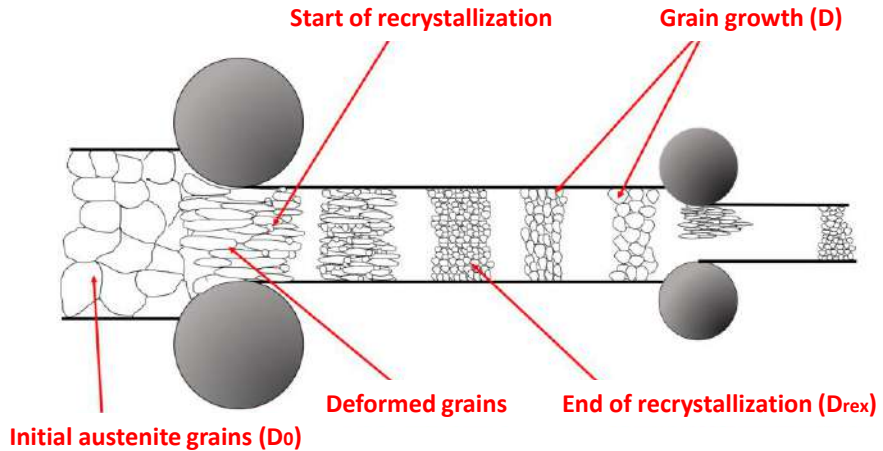


Figure 2.6. Microstructural changes during rolling from pass to pass [44].

2.3.1.1. Recovery

This phenomenon is the first softening process taking place when the material is deformed. Recovery is a combination of the processes acting prior to recrystallization that causes both the reduction of dislocation density and their reorganization into lower energy configurations, such as cells or equiaxed subgrains [61]. This processes can occur dynamically (during deformation) or statically (after deformation). Recovery is usually retarded by an increase in austenite grain size, a decrease in deformation temperature and an increase in Nb or Mo content [4].

2.3.1.2. Recrystallization

Recrystallization is the main softening process that can occur in austenite, before, during or after deformation. The combination of high temperature with accumulated strain leads to the activation of this phenomenon.

Dynamic recrystallization (DRX)

Dynamic recrystallization (DRX) could take place in austenite during deformation. DRX consists on the elimination of a large number of dislocations by the migration of grain boundaries and formation of new grains with a low dislocation density [62]. The new grains nucleate preferentially at existing grain boundaries and triple points. In addition, the initial austenite grain size, the amount of microalloying elements in solid solution and the deformation conditions (temperature and strain rate) can affect

dynamic recrystallization kinetics. Microalloying elements can delay dynamic recrystallization through the solute drag effect or precipitation. This is usually related to the pinning effect exerted by fine TiN and Nb precipitates or to the pinning effect of fine precipitates such as NbC [28].

Figure 2.7 schematically illustrates the changes that occur in the stress-strain curve due to dynamic recrystallization. After a rapid increase in the flow stress and once a critical strain, ϵ_c , is reached, DRX is activated. The new grains provide additional softening that promotes the flow stress to pass through a maximum, indicated by peak strain ϵ_p , before dropping to a steady-state, ϵ_{ss} , characterized by a constant stress [28, 46, 63].

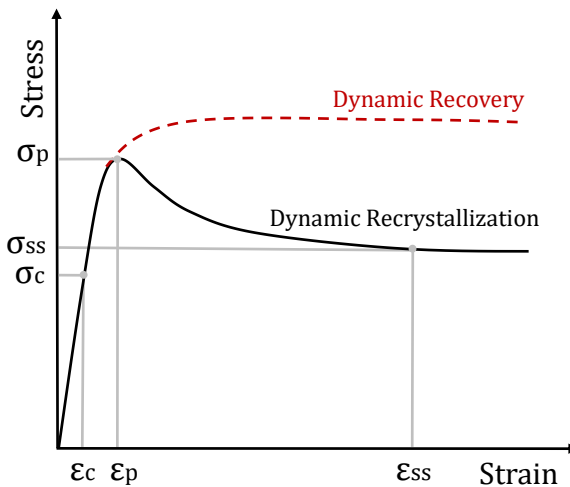


Figure 2.7. Scheme of start of dynamic recrystallization and its effect on stress-strain curve [64].

As dynamic recrystallization takes place during a given rolling pass, the nucleation and the grain growth occur simultaneously during strain application, resulting in a necklace of nucleation and limited grain growth, as shown in Figure 2.8. During deformation process, the recrystallized grains are formed around the austenite grain boundaries decorating the deformed grains. These new grains are deformed, until they reach required critical strain to undergo dynamic recrystallization. The new grains are formed around the initial grains forming a necklace [46].

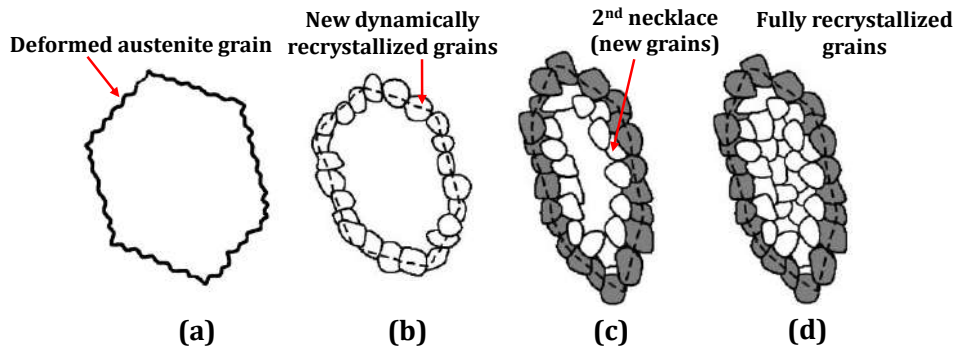


Figure 2.8. Scheme of nucleation of dynamic recrystallized grains [44].

A large number of previous studies reported that the size of the equiaxed austenite grain (D_{dyn}) is independent of the initial microstructure, being dependant only on the deformation conditions, such as the strain rate and deformation temperature.

These parameters are combined in the Zener-Hollomon parameter (Z), calculated as follows [63, 65]:

$$Z = \dot{\epsilon} \left(\frac{Q_{def}}{RT} \right) \quad 2.1$$

where $\dot{\epsilon}$ is the strain rate, Q_{def} the activation energy for deformation, R the gas constant (8.31 J/K.mol) and T the temperature.

Static recrystallization (SRX)

If the applied strain during hot rolling is smaller than the critical value ($\epsilon < \epsilon_c$), instead of dynamic recrystallization, static recrystallization (SRX) is activated during the interpass time. SRX is characterized by the nucleation and growth of new grains until the complete consumption of the deformed microstructure [20]. In the case of SRX, it is necessary to take into account both solute drag effect and precipitation. For instance, Nb microalloyed steels have a significant effect delaying recrystallization kinetics of the austenite by the presence of Nb in solid solution or due to the formation of strain-induced precipitates Nb (C,N) [25].

The evolution of static recrystallization kinetics can be described by a Avrami-type equation [66, 67]. A useful parameter to evaluate recrystallization kinetics is the time for 50% recrystallization, named as $t_{0.5}$ [68–70], which is affected by the initial grain size D_0 , and the processing parameters such as strain ϵ , strain rate $\dot{\epsilon}$, temperature T

and composition [38]. The general expression including all the parameters is described as follows:

$$t_{0.5X} = AD_0^m \varepsilon^{-p} \dot{\varepsilon}^{-q} \exp\left(\frac{Q_{srx}}{RT}\right) \quad 2.2$$

Where, A , m , p and q are constants and Q_{srx} is the activation energy for static recrystallization. All of them depend on the chemical composition of the steel. Several studies proposed different expressions in the literature to define $t_{0.5}$ in Nb microalloyed steels [71–74]. In particular, Dutta and Sellars [71] introduced a correcting factor to evaluate the contribution of Nb in solid solution on static recrystallization kinetics. Fernandez et al. [75, 76] studied the SRX kinetics of Nb and Ti microalloyed steels. Following this approach, Pereda et al. [26, 77] obtained the following equation for Nb and NbMo low carbon microalloyed steels (0.05%C):

$$t_{0.5X} = 9.92 \times 10^{-11} D_0 \varepsilon^{-5.6 D_0^{-0.15}} \dot{\varepsilon}^{-0.53} \exp\left(\frac{180000}{RT}\right) \exp\left[\left(\frac{275000}{T} - 185\right) ([\text{Nb}]_{\text{eff}})\right] \quad 2.3$$

$[\text{Nb}]_{\text{eff}} = [\text{Nb}]$ for Nb microalloyed steels

$[\text{Nb}]_{\text{eff}} = 1.19[\text{Nb}] + 0.09 [\text{Mo}]$ for 0.03% NbMo steels

$[\text{Nb}]_{\text{eff}} = 1.19[\text{Nb}] + 0.032 [\text{Mo}]$ for 0.06% NbMo steels

The equation was developed for Nb content between 0.03 and 0.06% and Mo content between 0 and 0.31%. The approach includes Nb effective term that considers the synergy effect of Nb and Mo in the delaying of recrystallization kinetics. The term related to Mo differs depending on the Nb content. For 0.03% Nb this term is about 0.09 and when Nb is increased to 0.06%, the Mo effect is reduced significantly, as the term decreases until 0.032. Therefore, Mo impact is reduced increasing Nb content, reflecting that a saturation of Mo occurs for high Nb levels.

2.3.1.3. Recrystallized grain size

Static recrystallization refines the grain size of the austenite. The statically recrystallized grain size, D_{rex} is related to the initial grain size, D_0 , which determines the density of nucleation sites and the deformation parameters such as strain and temperature. Equation 2.4 shows the general form of many equations proposed for the prediction of recrystallized grain size, in which the effect of temperature is not considered.

$$D_{\text{rex}} = A \cdot D_0^p \cdot \varepsilon^{-m} \quad \text{for } \varepsilon < \varepsilon_c \quad 2.4$$

Where A and m are material dependent constants, ε is the applied strain, D_0 is the initial austenite grain size and p is the strain exponent. Table 2.1 shows several equations reported in the literature for C-Mn steels and microalloyed with Nb.

Table 2.1. Static recrystallized austenite grain size equations for C-Mn steels and microalloyed with Nb.

Steel	Equation	
CMn	$D_{\text{rex}} = 0.743 \cdot D_0^{0.67} \cdot \varepsilon^{-1}$	Beynon et al. [68]
CMn-Nb	$D_{\text{rex}} = 1.1 \cdot D_0^{0.67} \cdot \varepsilon^{0.67}$	Sellars [78]
CMn-Nb	$D_{\text{rex}} = 1.4 \cdot D_0^{0.56} \cdot \varepsilon^{-1}$	Abad et al. [75]

With the aim of obtaining fine and homogeneous recrystallized austenite size and therefore, final microstructure refinement, an adequate definition of rolling passes becomes crucial. In this context, very fine recrystallized grains combined with low finishing temperatures to avoid their growth can be appropriate. In addition, the presence of elements in solid solution can also affect the microstructure evolution during rolling. For instance, TiN particles, with an adequate size and volume fraction, can entirely suppress grain growth during rolling [44].

2.3.2. Delay in softening kinetics

The following two mechanisms are proposed as responsible for promoting a delay in softening kinetics. The solute drag effect due to solute atoms and the pinning effect due to strain induced precipitates.

2.3.2.1. Solute drag effect

This phenomenon takes place when dissolved solute atoms are presented, either as segregations at grain boundaries or in a concentrated form such as clusters. These atoms can drastically reduce the mobility of grain boundaries. Lucke and Detert [79] proposed a model which takes into account the interaction between the solute atoms in solution and the moving grain boundaries. Further approaches developed by Cahn [17] Lucke and Stüwe [80], reported that due to the different size between the matrix and solute atoms, the impurities experiment an attracting or repulsive force towards the grain boundary. Moreover, the addition of impurities, can strongly affect the kinetics of recovery and recrystallization, as the elements in solid solution tend to form atmospheres associated with dislocations and grain boundaries, inhibiting their mobility [77].

2.3.2.2. Precipitate pinning

The retarding effect promoted by precipitates in recrystallization and grain growth processes is normally related to the decrease in the surface energy that they exert [81]. The precipitate replace part of the grain boundary area, impeding the movement of the boundary on the other side of the particle and thus, a supplementary effort to increase the boundary area is needed. In this process, the fraction and size of particles are the key factors.

Based on the expression developed by Zener [81], different models were proposed for the estimation of the precipitation pinning force (F_{pin}). Among the different approaches reported for different steel grades, the most suitable model to define F_{pin} it seems to be the following [82, 83]:

$$F_{pin} = \frac{3\gamma \cdot f_v^{0.66}}{\pi r} \quad 2.5$$

Where γ is the austenite grain boundary energy, f_v the precipitate volume fraction and r the precipitate radius.

When the pinning force exerted by precipitates exceeds the stored energy of the deformation, the recrystallization stops completely [84]. This is the situation of Nb (C,N) strain induced precipitates that appear during hot rolling [77, 85].

2.3.3. Precipitation

Precipitation is considered one of the factors controlling the properties of steels. During industrial processing, several microalloying elements can remain in solid solution. It is well known that microalloying elements like Nb, V or Ti have a strong affinity for elements such as C and N and that a small addition of these elements can provide a significant improvement of the mechanical properties on account of the formation of fine precipitates. Control of the size and volume fraction of precipitates plays an important role in improving the mechanical properties of the steel [86].

The nucleation and growth of these precipitates can take place during the liquid region, in the austenitic region and during or after phase transformation, depending on the composition of the steel and the applied thermomechanical cycle. Depending on the region that precipitation occurs (in the liquid, austenitic or ferritic region), the size, the volume fraction and the distribution of the precipitates can vary significantly, promoting considerable effects on different parameters that will affect the mechanical properties of the final product [87].

It is essential to maintain the microalloying elements in solid solution prior to hot rolling for ensuring precipitation. To that end, a suitable definition of the reheating temperature is required. In microalloyed steels, carbides and nitrides are supposed to be formed. The solubility of the formed nitride, carbide and carbonitrides needs to be taken into consideration since are related to the size and the volume fraction of the precipitates [44, 88]. The solubility products corresponding to Ti, V, Al and Nb are shown in Figure 2.9.

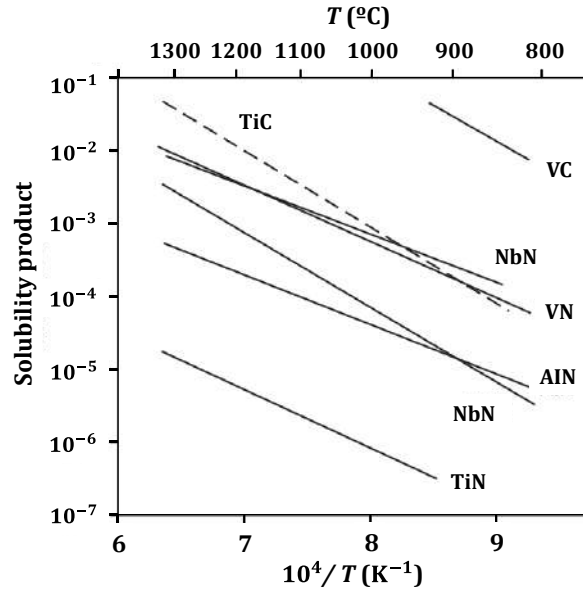


Figure 2.9. Solubility products of various nitrides and carbides in austenite [89].

As shown in Figure 2.9, nitrides are more stable than carbides and require higher temperatures to dissolve. Moreover, the most stable element is TiN, as it remains precipitated during reheating and prior to hot rolling. Therefore, the presence of fine TiN precipitates becomes essential when recrystallization controlled rolling processes are required, due its ability to prevent the grain boundary movement and thus inhibit the growth of recrystallized grains. In addition, VC shows the highest solubility. This type of particles tend to precipitate during or after phase transformation, promoting an important precipitation hardening effect. Furthermore, Nb displays intermediate solubility products. The presence of niobium in solid solution and in precipitate form presents an important influence on recrystallization kinetics and grain growth. Nb can also form fine precipitates able to improve tensile properties.

2.3.3.1. Types of precipitation

Depending on the temperature at which precipitation occurs, the size and the volume fraction of the precipitates can vary significantly, promoting different effects on the material. The precipitation of nitrides, carbides and carbonitrides of Nb or Ti usually is activated prior to hot rolling, during hot rolling and during or after phase transformation.

Precipitation prior to hot rolling

The aim of the preconditioning step is usually to obtain a complete dissolution of microalloying elements so that they can precipitate at lower temperatures. The formation of Nb precipitates for example, can control grain growth of the austenite. Nevertheless, some precipitates such as TiN particles can remain undissolved due to their high stability. High enough reheating temperatures are required to avoid the formation of coarse precipitates and consequently the loss of effective microalloying elements [84, 88]. The formation of fine nitride particles involves the control of austenite grain growth and promotes the delay on recrystallization kinetics.

Strain induced precipitation

Strain induced precipitation could interact with recrystallization after the application of deformation. While temperature decreases during rolling, the supersaturation in austenite is increased and the dislocation density generated during deformation promotes the precipitation of carbonitrides, mainly Nb (C,N) particles. These fine precipitates provide a very strong pinning force on the boundaries, delaying or even completely stopping the static recrystallization process [44, 90].

Precipitation during and after phase transformation

The precipitates formed during phase transformation tend to nucleate at the austenite-ferrite interface. This type of precipitation is named as *interphase precipitation* and is mainly characterized by the distribution of very fine precipitates organized in parallel rows. As in the case of C, microalloying elements seem to be more soluble in austenite than in ferrite and thus, during austenite-ferrite transformation, ferrite ejects the excess of alloying elements into the interface. While the interface moves forward the material, turns enriched in microalloying elements until achieves a certain concentration at which precipitation takes place. This process is repeated until continuous parallel rows of fine precipitates separated between them are formed. Moreover, the interphase precipitation is usually favoured with high initial transformation temperatures [87]. Yield strength values of about 300-400 MPa

are estimated for interphase precipitates, as the high concentration of the formed precipitates can obstruct the movement of dislocations [91, 92].

At lower temperatures and when interphase precipitation is not possible, randomly distributed fine precipitates can be formed in ferrite after phase transformation. This type of precipitates can provide significant hardening effect on the material [93].

2.3.4. Phase transformation

After conditioning of the austenite during hot rolling, cooling is applied after the last deformation pass and the austenite to ferrite phase transformation takes place during cooling. This step is very relevant, as different microstructures with diverse mechanical properties can be obtained depending on the selected cooling strategy.

Additional heat treatments such as tempering can be applied after cooling in order to achieve better mechanical properties. During this treatment, the microstructure can vary and other transformation products can be achieved. Tempering treatment changes the microstructure of the quenched martensite, promoting the formation of carbides that can retard softening kinetics and/or produce secondary hardening phases.

Furthermore, the transformation of austenite depends on the steel chemistry and the austenite conditioning. The changes performed during transformation are usually evaluated by means of CCT (Continuous Cooling Transformation) diagrams [44].

2.3.4.1. CCT diagrams

CCT curves provide information about the effects of selecting different cooling strategies on the final microstructure and thus, in the obtained mechanical properties. CCT curves mainly depend on the austenite characteristics such as, grain size, retained strain and the amount of elements in solid solution or precipitated [44]. From the dilatometry tests, CCT curves are defined, where after austenite conditioning the samples are cooled down at different continuous cooling rates. In the obtained diagrams, the initial and final transformation temperatures are determined and the achieved microstructures are analysed with the aim of verifying the phases formed for each cooling rate [94]. In most of the cases, hardness Vickers values are also added in the CCT curves. Several examples of this type of diagrams can be found in reference [33].

2.3.4.2. Transformation products

Several transformation products can be achieved depending on the considered cooling strategy. In quenched high strength steels, fully martensitic microstructures are desired. However, a brief description of other different phases including pearlite, ferrite or bainite are also detailed below.

Martensite

Martensitic microstructures are formed in steels when austenite is cooled down at high cooling rates. As-quenched martensitic microstructures have the highest hardness and strength that can be produced in a given steel.

Martensite formation and crystallography

The martensitic transformation takes place without carbon diffusion. C atoms do not have enough time to diffuse out of the crystal structure and thus, the transformation occurs by the massive movement of a large number of atoms, leading to a new component with the same carbon content as the starting austenite. The martensitic transformation, in the case of iron-carbon and carbon steels, requires a change in crystallographic lattice from face-centred cubic austenite (FCC) to body-centred tetragonal lattice (BCT). Therefore, martensite is considered a supersaturated solid solution of carbon with a body-centred tetragonal lattice (BCT).

In a slower cooling, during phase transformation, C atoms tend to diffuse from the octahedral positions of the austenite to the tetrahedral positions of the ferrite. Nevertheless, in the case of martensitic transformation, the high cooling rates promote the trapping of C atoms in octahedral positions of the ferritic structure, leading to the formation of internal stresses within the crystalline lattice, deforming it to form the BCT structure [87].

These deformations can produce a large number of dislocations, resulting in high levels of hardness and strength in martensite. However, this microstructure possesses a fundamentally metastable feature.

The shear mechanisms and absence of diffusion require close crystallographic coupling of the austenite and martensite: for example, close-packed planes of atoms in austenite $\{111\}_A$, become close-packed planes in martensite $\{110\}_M$. The relationship between the austenite and ferrite lattice was developed by Bain [95], who proposed a simple scheme to obtain the martensitic microstructure starting from austenite. Taking together two austenite cells (FCC structure), Figure 2.10, a martensitic cell can be obtained (BCT structure), after having subjected the resulting

cell to a contraction strain of $\approx 17\%$ along the $[001]_\gamma$ direction and at a uniform expansion strain of $\approx 12\%$ along the $(001)_\gamma$ plane.

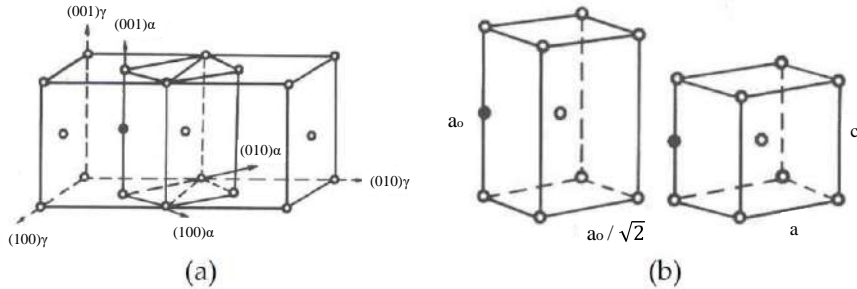


Figure 2.10. (a) The Bain model and (b) the BCT cell before (left) and after (right) of the deformations. White dots: iron atoms; the black dots: interstitial atoms [96].

Martensite transformation kinetics and morphologies

The start and finish martensitic transformation temperatures, are called M_s and M_f , respectively. The content of carbon and alloying elements strongly affects M_s temperatures, as shown in Equation 2.6 formulated by Andrews for low alloy steels (in weigh percentage) [97]. The higher the C content in the steel, the lower these temperatures.

$$M_s(^{\circ}\text{C}) = 539 - 423 \text{ C} - 30.4 \text{ Mn} - 12.1 \text{ Cr} - 17.7 \text{ Ni} - 7.5 \text{ Mo} \quad 2.6$$

In some cases, when M_f temperature is lower than the room temperature, during cooling, part of austenite might remain untransformed resulting in a *residual or retained austenite*. The percentage of this retained austenite depends not only on the temperature at which the steel is cooled to, but also on the amount of carbon and other alloying elements [47].

In steels, two distinct morphologies of martensite are known: lath martensite and plate martensite. The lath martensite is formed in low- and medium-carbon steels with low content of alloying elements (when M_s is high). Plate shaped martensite instead, is formed in high-carbon steels. Lath martensite crystals are very fine. In contrast, plate martensite tend to be much larger. Plate martensitic microstructures have larger amounts of retained austenite, as a consequence of low M_s temperatures. Retained austenite is also present in lath martensitic microstructures, but in smaller amounts than in high-carbon steels. The austenite is retained in thin layers between parallel crystals of martensite [98].

Tempered martensite

Given that martensite is a very hard and brittle phase, in most of the application, it is necessary to apply a heat treatment (in the range between 150 and 700 °C) after quenching. This process is named as tempering. Tempering may be performed at any temperature below the temperature at which austenite begins to form in a given steel. That temperature is defined as the lower critical temperature on heating, A_{C1} , and is 727 °C for iron-carbon alloys. Alloying elements such as Ni and Cr lower A_{C1} and Mo for example tend to raise A_{C1} [98].

If martensite is heated by means of tempering, the atoms acquire a minimum mobility and through a diffusion process tend to leave their positions in the BCT structure precipitating as carbides. In consequence and for high/long times, the martensitic microstructure is decomposed into ferrite and cementite, leading to a new microstructure known as *tempered martensite* [99].

The tempering treatment lowers the strength, but increases the fracture resistance, toughness and ductility of the material, the steel becomes more malleable and therefore, more suitable for industrial use.

Other transformation products

After austenization process and considering slower cooling rates, austenite leads to other different transformation products.

Ferrite

The ferritic microstructure forms at the highest temperatures and the slowest cooling rates and it is nucleated as grain-boundary allotriomorphs and grows into equiaxed grains [100]. Morphologically, ferrite usually is presented with equiaxed and polygonal geometry [87]. Growth of ferrite is controlled by rapid substitutional atom transfer across partially coherent boundaries and long-range diffusion of carbon atoms which are rejected from the growing ferrite [100].

Bainite

Bainitic microstructures are formed by the decomposition of austenite at temperatures above M_s , but below than the formation of pearlite. Bainitic transformation takes place through small coordinated displacements of the crystal lattice atoms, as the diffusivity of carbon across the interface becomes more complex at low transformation temperatures. Bainite grows by the formation of groups known as bundles while each bundle is composed of parallel thin flats of ferrite and

cementite with the same crystallographic orientation [93]. Nowadays, there is no unanimity in the mechanisms controlling bainite transformation. Some of the works proposed reconstructive mechanism [101], whilst other theories consider displacive mechanisms [102].

Pearlite

Pearlite is usually formed during the slow cooling of steels and is characterized by a laminar combination of ferrite and cementite (Fe_3C). Pearlitic microstructures are formed by eutectoid decomposition of austenite upon cooling and through diffusion of carbon atoms. While the growth of ferrite and cementite, C atoms tend to precipitate as Fe_3C , leading to the formation of parallel laths named as pearlite colonies. If this process is repeated, a plate of Fe_3C with a different orientation may nucleate, giving rise to a new colony [103, 104].

Retained martensite-austenite islands (MA islands)

During the grain growth of several transformation products, carbon is expelled from the grains, while the new phases cannot contain the same amount of C in solution as austenite. Therefore, the austenite next to those grains increases their carbon content and C-enriched austenite partially transforms into martensite forming martensite-austenite islands (MA islands) [105]. Before transformation, the excess of carbon in austenite can lead to the precipitation of carbides and thus avoid the formation of MA islands. In spite of this, the use of microalloying elements such as Nb or Mo stabilizes the austenite, preventing the formation of carbides and favouring the transformation of austenite to MA islands [87].

2.3.4.3. Phase transformation during DQ process

As mentioned before, the main objective of direct quenching (DQ) is to create fully martensitic microstructures through applying high cooling rates. Nevertheless, depending on rolling conditions and the alloy concept, undesirable soft phases like ferrite and bainite can be formed. Microalloying with molybdenum and/or boron reduces the critical cooling speed for martensite formation, while the combined addition of microalloying elements like Ti, Nb, Mo and B to carbon steels can provide an increase in strength due to microstructural refinement and precipitation hardening as well as hardenability and final microstructure modification. Moreover, the addition of B increases strength by obstructing ferrite nucleation at austenite grain boundaries and so encouraging the formation of bainitic/martensitic microstructures even at low cooling rates [106].

Hannula et al. [1] evaluated the effect of niobium on phase transformation and hardenability following DQ strategy. For that purpose, continuous cooling transformation (CCT) diagrams were defined. It has been reported that Nb can improve hardenability in solid solution, but the formation of niobium-carbides, can decrease the hardenability effect [107]. Three low carbon (~0.08wt.%) boron steels with different levels of Nb (0, 0.025 and 0.05 wt.%) were studied in reference [1]. In addition, two different thermomechanical cycles were applied in order to simulate different austenite conditions before direct quenching (austenite with and without accumulated strain). Figure 2.11 shows the CCT diagrams for all the specimens and both thermomechanical cycles.

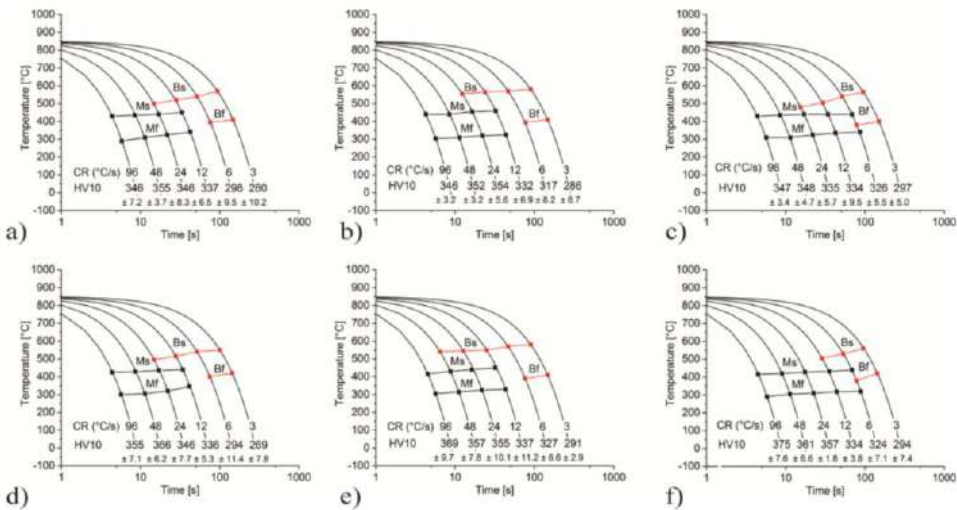


Figure 2.11. CCT diagrams of investigated steels (a,d) DQ, (b,e) DQ + 0.02Nb and (f,c) DQ + 0.05Nb. Upper row: no deformation; lower row: 3×0.2 prior deformation [1].

The authors did not observe a significant effect of Nb on phase transformation. Only at low cooling rates, Nb decreases the fraction of bainite, causing an increment of hardness values, as a consequence of improved hardenability of Nb-bearing steels.

In the same study, the effect of thermomechanical cycle was also analysed (Figure 2.11a, b and c correspond to non-deformed austenite and Figure 2.11d, e and f to austenite with accumulated strain). The CCT diagrams show that the accumulation of the austenite prior to transformation increases the hardness at high cooling rates, despite the phase transformation start temperatures are not largely affected.

H.J. Jun et al. [106] investigated the effects of deformation in two different low-carbon (0.05wt.%) steels, with and without boron alloy (A and B respectively).

Figure 2.12 shows the effect of accumulation of deformation in the austenite prior to transformation for both steels (boron free and boron steel). In both steels, the increase of A_{r3} is negligible when deformation is applied, due to recovery. However, in the alloy without boron, the deformation applied increased the A_{r1} temperature between 0.1 and 50 °C/s due to high diffusivity path formation. In boron added alloy, deformation did not affect A_{r3} and A_{r1} . In this study, it was observed that boron addition reduced A_{r3} and A_{r1} temperature ranges from 720–530 °C to 630–540 °C and from 500–400 °C to 480–400 °C, respectively. Therefore, it was demonstrated that boron addition can produce bainite ferrite and martensite, and effectively suppresses pearlite and ferrite formation even with deformation. Therefore, high strength can be achieved at a slow cooling rate in boron steels.

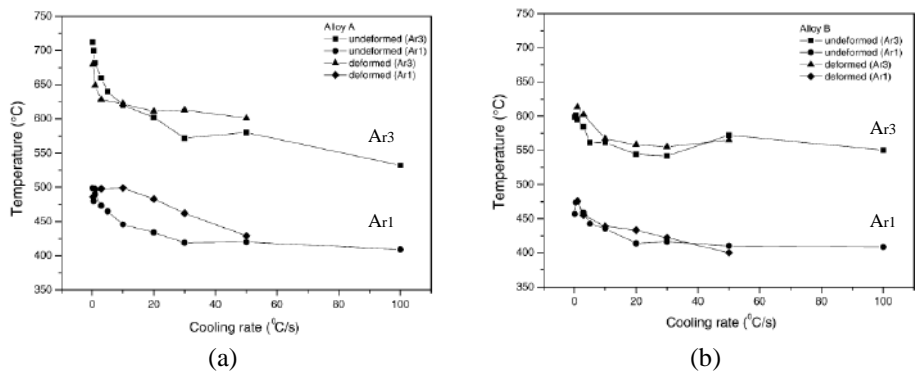


Figure 2.12. (a) A_{r3} and A_{r1} temperatures of (a) alloy A (without boron) and (b) alloy B (with boron) [106].

Concerning the effect of Mo addition, Futao Han et al. [108] reported the effect of Mo (0.20 wt.%) addition on boron (0.0023 wt.%) steels. Figure 2.13a and b show the CCT diagrams obtained for B and Mo-B steels. For B steel, martensite can be achieved for cooling rates higher than 20 °C/s, as shown Figure 2.13a. However, when Mo is added to the base composition, bainitic ferrite and martensite are formed at cooling rates higher than 3 °C/s and 10 °C/s, respectively (Figure 2.13b). This study demonstrates the effectiveness of Mo alloying for the enhancement of hardenability in boron-added steels, as decreases the transformation start and finish temperatures.

Figure 2.13c presents the variations in hardness as a function of cooling rate for both alloy-concepts. As expected, the hardness of Mo-B steel is higher than that of the B steel at entire range of cooling rates. As the effect of solid-solution strengthening is unremarkable in low-carbon steels, the increase in hardness is believed to originate

from the enhancement of hardenability. A. Terzic et al. [109] studied the phase transformation behaviour during continuous cooling of low-carbon boron steels with different B content additions. The strong effect of B on phase transformation was confirmed for boron contents of 29 and 51ppm.

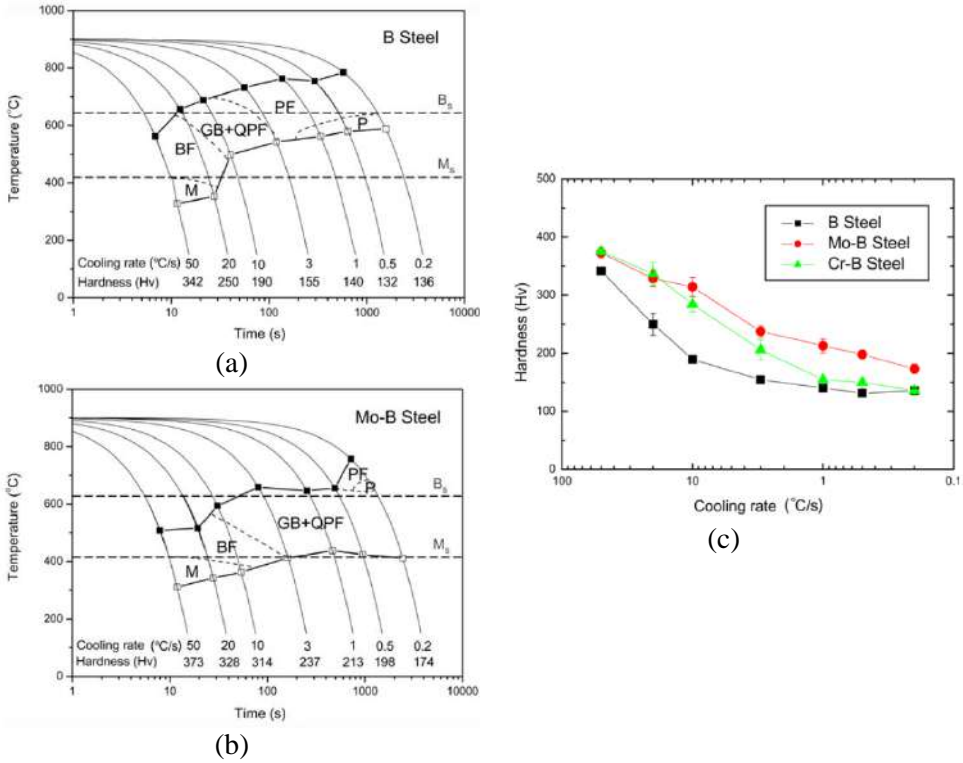


Figure 2.13. (a,b) CCT diagrams for the (a) B and (b) Mo-B steels and (c) Hardness plotted as a function of cooling rate for the B, Mo-B and Cr-B steels [108].

2.4. Relationship between microstructure and mechanical properties

An adequate combination of chemical composition and processing parameters is needed with the aim of obtaining the desired final microstructure and suitable strength and toughness properties [44].

2.4.1. Tensile properties

By means of tensile testing, a sample is subjected to a controlled tension until failure. Through these tests the applied force and the elongation can be measured and engineering stress-strain curves can be constructed in order to determine the tensile strength and yield strength of a steel. The tensile strength is defined as the maximum stress that a sample is capable to support before the rupture. In addition, the yield strength is described as the maximum stress that the sample is able to support until it starts to deform plastically.

In the following lines, different strengthening mechanisms affecting yield strength are defined.

2.4.1.1. Strengthening mechanisms

The yield strength (σ_y) of a steel can be determined by the addition of different strengthening mechanisms such as solid solution, grain size refinement, dislocation density, precipitation hardening and the presence of secondary phases (M/A islands). The yield strength of low carbon microalloyed steel grades can be calculated considering a linear sum of individual strengthening mechanisms according to Equation 2.7.

$$\sigma_y = \sigma_0 + \sigma_{ss} + \sigma_{gs} + \sigma_{\rho} + \sigma_{ppt} + \sigma_{M/A} \quad 2.7$$

Where, σ_0 is the friction stress, σ_{ss} the solid solution strengthening, σ_{gs} grain size refinement, σ_{ρ} is the dislocation hardening, σ_{ppt} the contribution of precipitation and $\sigma_{M/A}$ is the hardening due to secondary phases. In Figure 2.14 some of the different strengthening mechanisms included in Equation 2.7 are illustrated.

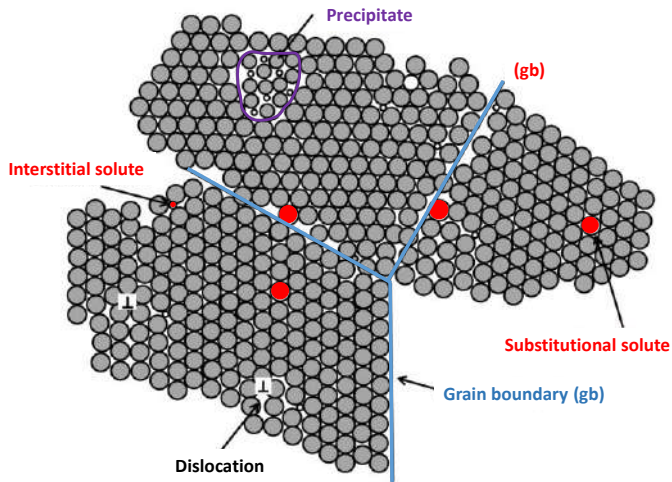


Figure 2.14. Scheme representing different strengthening mechanisms [44].

All these mechanisms are able to increase the strength of the material by obstructing or preventing dislocation movement during deformation. Dislocations are a linear defect within the crystal lattice and can be defined by specifying which atoms have lost their position relative to the defect-free lattice [87].

More details regarding each strengthening mechanism can be found in the following lines.

Solid solution

This hardening mechanism consists on the distortion of the crystal lattice when substitutional (occupying places of iron atoms in the lattice) or interstitial (in intermediate positions of the lattice) elements remain in solid solution, as illustrated in Figure 2.14. Substitutional elements such as, Mn, Ni, Cr, Al, Mo, Cu and Si are able to promote a slight distortion in the crystal lattice, resulting in a low strengthening effect. Therefore, large quantities are required in order to obtain a considerable effect in solid solution hardening. In addition, interstitial elements are characterized by their small size and thus, for being able to replace these positions. C and N are the most typical interstitial elements in steel. They usually generate a more notorious distortion which is more effective on the accumulation of dislocations [110, 111].

The contribution of each elements in solid solution to the yield strength is proportional to the concentration of each element, as shown in Equation 2.8.

$$\sigma_{ss}^i = k_i \cdot c_i \quad 2.8$$

Where σ_{ss}^i is related to the increase of strength due to solute i , c_i is the concentration of the solute i (in weight %), and k_i is the coefficient of hardening corresponding to solute i .

The effect of solid solution is usually calculated by considering the equation proposed by Pickering [48].

$$\sigma_{ss} = \sigma_0 + 32.3(\%Mn) + 83.2(\%Si) + 11(\%Mo) + 354(\%N_{free})^{0.5} \quad 2.9$$

Where σ_0 is the lattice fraction stress ($\sigma_0 = 53.9$ MPa) and the concentrations are expressed in weight %.

The use of elements to improve the strength of steels by solid solution is limited, as high contents are needed to obtain a significant effect, thus, the use of the solid solution as strengthening mechanism is reduced. Nevertheless, solid solution is usually considered as a complement to improve the strengthening mechanisms. The presence of elements in solid solution can alter the transformation start temperatures, changing the proportions of the new phases and promoting the refining of the final microstructure [93].

Grain size refinement

Grain refinement is considered the most efficient strengthening mechanism in HSLA steels. Through grain refinement, both the strength and toughness are improved without affecting weldability. In addition, grain size has a significant influence on the yield strength and ductile-brittle transition temperature, achieving considerable improvements while grain size decreases [112]. Fine microstructures usually show a higher specific grain boundary area, S_v , compared to coarse microstructures, being more effective as an obstacle in the dislocation movement and consequently, increasing strength.

For different type of microstructures (ferritic, bainitic and martensitic), the contribution of microstructural refinement has been widely estimated in the literature considering Hall-Petch type relationships [41]. Even though Hall-Petch equation was initially developed for high-angle misorientation, subsequently was extended to subgrains [113] and cell joints [114]. In microstructures with a high density of low angle boundaries, as in the case of bainitic microstructures, the effect of low and high angle boundaries needs to be quantified separately. For that purpose, Iza-Mendia et al. [115] proposed a new equation where both type of boundaries (low and high angle) are considered, see Equation 2.10. This approach was validated for a wide

range of microstructures such as ferritic-pearlitic, bainitic and martensitic microstructures.

$$\sigma_{gs} = 1.05\alpha M\mu\sqrt{b} \left[\sum_{2 \leq \theta_i \leq 15^\circ} f_i \sqrt{\theta_i} + \sqrt{\frac{\pi}{10}} \sum_{\theta_i \geq 15^\circ} f_i \right] d_{2^\circ}^{-1/2} \quad 2.10$$

Where, α is a constant, M is the Taylor factor, μ is the shear modulus and b is the magnitude of the Burgers vector ($\alpha=0.3$, $M=3$, $\mu=8 \cdot 10^4$ MPa y $b=2.5 \cdot 10^{-7}$ mm). θ_i is the average misorientation angle expressed in rads and f_i the relative frequency. Both parameters as well as the mean unit size considering low angle misorientation criteria (d_{2°) are obtained through EBSD technique.

Dislocation density

Dislocations are defined as crystalline defects or irregularities. The interaction between different dislocations can also obstruct their movement. The mentioned interactivity will have different effects, when the dislocations are in the same slip plane or not. The formation of a microstructure with higher dislocation density (for example bainite) could also improve tensile properties.

The contribution of dislocations to yield strength can be determined by the following equation [116]:

$$\sigma_p = \alpha M\mu b\sqrt{\rho} \quad 2.11$$

Where, α is the numeric factor representing the interactions between dislocations in the microstructure, M the Taylor factor, μ the shear modulus, b the Burgers vector and ρ the dislocation density.

In addition, in previously published papers the hardening due to dislocation density has been evaluated through Kernel Average Misorientation (KAM) obtained by EBSD, according to Equation 2.12 [117]. Based on this equation, the dislocation density (ρ) is estimated from Kernel Average Misorientation angle with respect to its neighbours (θ) [115].

$$\rho = \frac{2\theta}{u \cdot b} \quad 2.12$$

Where, u is the unit length associated with Kernel measurements. This length is usually related to the different conditions used while scanning, such as the step size and the number of neighbour.

The Kernel Average Misorientation is defined as the average misorientation between a point and its surrounding neighbours. As shown in Figure 2.15, this measurement is obtained considering the points situated at an equal distance to the step size (first neighbour) or at an equal distance to two or three times the step size (second and third neighbours respectively). Moreover, the image shows some previously mentioned parameters such as the misorientation angle (θ) and the length associated with the position of the neighbour (u), in this case, the third neighbour [93].

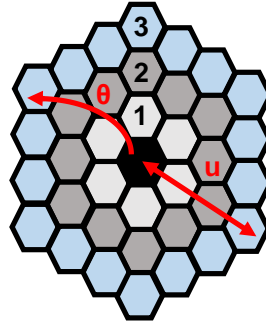


Figure 2.15. Schematic representation of Kernel parameters for the estimation of dislocation density (ρ) (third neighbour is considered) [93].

Concerning the dislocation density data available in the literature, there is no unanimity in the reported values. Bainitic and martensitic microstructures are characterized due to its high dislocation densities, which range between $3.77 \cdot 10^{14}$ and 10^{16} m^{-2} [118]. In ferritic microstructures, some authors affirm that polygonal ferrite contains a low density of dislocations, of around 10^{12} m^{-2} for CMn steels [119]. Other studies report that the dislocation density corresponding to microstructures composed by equiaxed ferrite, ranges from $3.7 \cdot 10^{13} \text{ m}^{-2}$ to $5 \cdot 10^{13} \text{ m}^{-2}$ [120, 121].

Precipitation hardening

Precipitation can play different roles in the improvement of yield strength depending on when and how precipitates are formed. In microalloyed steels, precipitation of fine precipitates can occur during or after phase transformation, hindering the movement of dislocations while deformation, and consequently increasing the strength of the material. In the case where the microstructure contains precipitates, the mechanism proposed by Orowan needs to be considered [122]. The model describes a process where a dislocation meets a group of precipitates and the dislocation tries to cross the region. As in microalloyed steels the particles are hard enough and non-deformable, the dislocation surrounds the precipitate so that

dislocation loops are formed around the precipitates. These loops, also can represent obstacles to the progress of other dislocations [123].

Based on the Orowan mechanism, Ashby proposed the Ashby-Orowan [124] equation (see Equation 2.13), able to predict the contribution of the precipitates based on the size (x) and volume fraction (f_v).

$$\sigma_{\text{ppt}} = 10.8 \cdot \frac{f_v^{0.5}}{x} \ln \left(\frac{x}{6.125 \cdot 10^{-4}} \right) \quad 2.13$$

According to this approach, a higher precipitate volume fraction as well as the precipitates size refinement leads to an increase in the contribution to yield strength [4].

Secondary phases

The presence of secondary phases such as MA islands can also hinder the movement of dislocations during deformation. The presence of these phases can be detrimental to the toughness of the material [125]. In addition, MA islands are able to increase the strength of the material due to its hardness. Their contribution to yield strength can be determined through the equation proposed by Bush et al. [126]:

$$\sigma_{\text{MA}} = 900 \cdot f_{\text{MA}} \quad 2.14$$

Where f_{MA} is the volumetric fraction of MA islands.

2.4.2. Toughness properties

Toughness is the ability of a material to absorb energy and plastically deform without fracturing. Although there are several parameters and techniques to measure toughness, Charpy test remains of the most common one for hot rolled products. Charpy tests performed at different temperatures provide a curve where the evolution of absorbed energy as a function of the testing temperature can be evaluated, as illustrated in Figure 2.16. In this curve, three regions can be distinguished: the *upper plateau* corresponding to completely ductile behaviour, the *lower plateau* where the fracture is totally brittle and the *transition* interval in which both ductile and brittle mechanisms are present [44].

In the transition regime, there is a competition between ductile and brittle mechanisms and the control of the characteristics involved in the brittle process can contribute to a considerable improvement in the toughness of the steel.

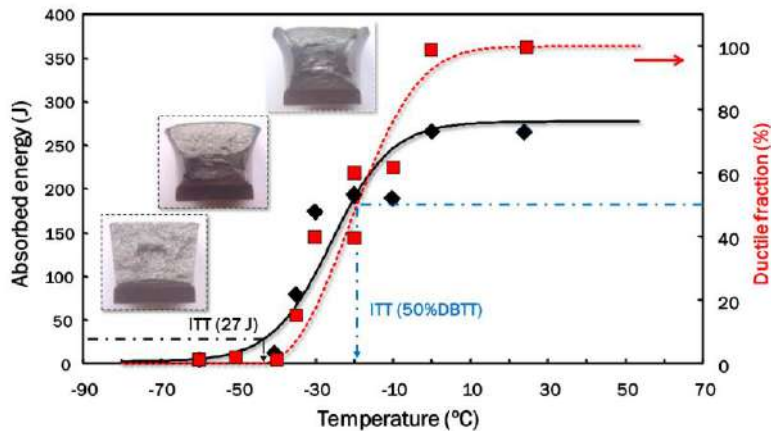


Figure 2.16. Schematics of a Charpy curve including absorbed energy and ductile fraction appearance as a function of testing temperature [44].

The brittle cleavage is attributed to the nucleation of a microcrack followed by its propagation in the surrounding matrix. The brittle process is usually divided into three different processes. In the first step, a microcrack is nucleated into a microstructural brittle fracture. The second step consists on the propagation of the microcrack to the surrounding matrix, while the third step corresponds to the propagation of the crack through the matrix. Different type of particles such as grain boundary carbides, non-metallic inclusions, complex oxides and coarse TiN nitrides can be responsible for the nucleation of microcracks in the matrix [127].

In addition, in a ductile fracture, high amount of plastic deformation is accumulated before the rupture. When the sample is subjected to an external stress, a microcrack nucleates due to the fracture of the particle-matrix interface, as in the brittle fracture. As a consequence of the applied stress, more microcracks are formed that grow and join the major crack, increasing continuously the main crack. This process is repeated until the total rupture of the sample is finished [111].

2.4.2.1. Contributions to toughness

Toughness is generally predicted by the ductile-brittle impact transition temperature. This parameter can be defined in different ways. Generally, the impact transition temperature (ITT), also called ductile-brittle transition temperature (DBTT), is defined as 50% fracture appearance transition temperature (ITT50%). In other situations, the ITT temperature corresponds to that associated with a certain absorbed energy, for example 27J.

As in the case of yield strength, several relationships for the estimation of ITT values as a function of microstructural parameters have been proposed in the literature [48, 128–130]. Most approaches were derived from analysing low-carbon ferrite-pearlite steels. Several works suggested that a parameter accounting the presence of coarse grains and microstructural heterogeneity is required for accurately predicting the ductile-brittle transition temperature [131, 132]. In that sense, Larzabal et al. [133] proposed a relationship allowing to predict ITT50% for low carbon Nb, NbMo and TiMo microalloyed steels, thereby taking into account the effect of microstructural heterogeneity and the presence of hard secondary phases like pearlite and MA islands (see Equation 2.15). This equation is applicable to ferritic-pearlitic and bainitic microstructures.

$$\text{ITT50\% (}^{\circ}\text{C)} = -11\text{Mn} + 42\text{Si} + 700 (N_{\text{free}})^{0.5} + 15 (\text{pct Pearlite} + \text{pct MA})^{\frac{1}{3}} + 0.26\Delta\sigma_y - 14(D_{15^{\circ}})^{-0.5} + 63 \left(\frac{D_{c20\%}}{D_{15^{\circ}}} \right)^{0.5} + 18(D_{\text{MA}})^{0.5} - 42 \quad 2.15$$

Where the first two terms are related to the solid solution contribution. N_{free} is the free nitrogen, the percent of secondary phases is the sum of the *fraction of pearlite* and *MA islands*, $\Delta\sigma_y$ is the term related to fine precipitation and dislocation density ($\Delta\sigma_y = \sigma_p + \sigma_{\text{ppt}}$), $D_{15^{\circ}}$ is the effective cleavage unit size, the influence of heterogeneity is represented by $D_{c20\%}/D_{15^{\circ}}$ factor and D_{MA} is the size of the formed MA islands.

2.4.3. Relationship between microstructure and tensile/toughness properties in high strength Q/Q&T steels

Recently, the relationship between martensite and obtained tensile/toughness properties have been analysed for high strength Q/Q&T steels. P. Uranga et al. [134] evaluated the impact of molybdenum on martensitic microstructures formed after hot rolling and direct quenching for boron steels. Considering different alloy concepts, they denoted that carbon is the dominant element providing strength to martensite (see Figure 2.17a). Regarding the effect of different elements on the hardenability, as shown in Figure 2.17b, for the same weight percentage added, they considered Mo to be the most powerful hardenability element (comparing to other typical alloys such as Mn, Cr and Ni). The authors suggest [134] that the basic Mn-B alloy concept cannot fulfil advanced requirements in terms of toughness and cracking resistance. Mo addition is required in order to ensure additional benefits regarding microstructural refinement, tempering resistance and delayed cracking resistance.

In reference [134], the influence of adding different Mo levels (0.25 and 0.5%Mo) and adding Mo-Nb is evaluated in terms of mechanical properties. They observed better strength and toughness properties with increasing molybdenum alloy content due to stronger austenite pancaking [134]. By means of Figure 2.17c and d they demonstrated this effect using the ratio of grain boundary area to volume (S_v) being a reference for the degree of austenite pancaking. With increasing Mo content, austenite pancaking becomes more pronounced and the tensile strength increases. Simultaneously, the impact transition temperature (T_{28f}) decreases considerably in the steels containing Mo. The combination of Nb and Mo results in even stronger austenite pancaking (S_v). In addition, as illustrated in Figure 2.18, the temper-induced strength drop is higher in the Mo-free steel. Nb-Mo alloy concept shows the highest tempering resistance. [134].

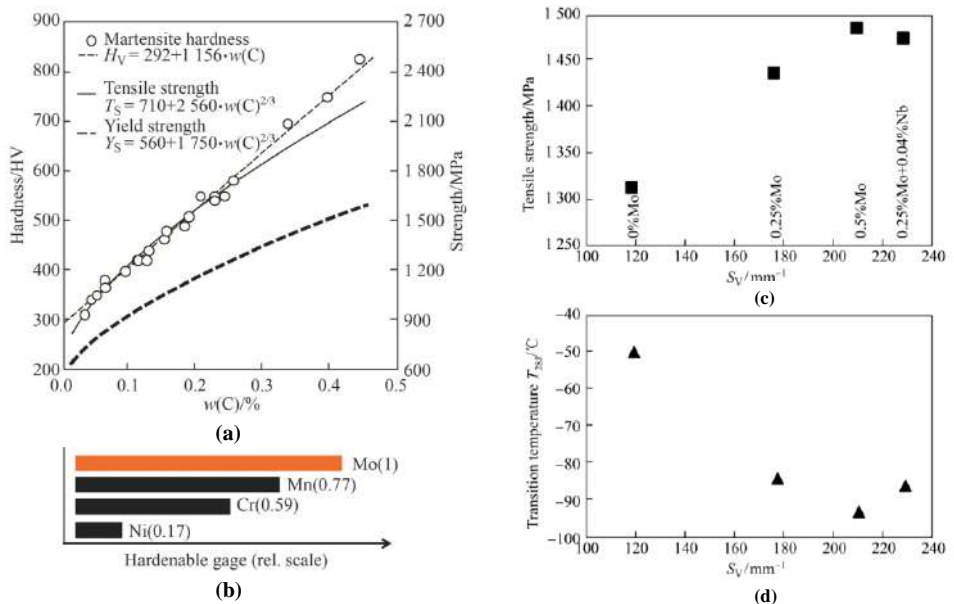


Figure 2.17. (a) Influence of carbon content on measured hardness and calculated strength. (b) Relative effect of alloying elements on hardening depth. (c,d) Influence of Mo and Nb-Mo synergy on strength and toughness [134].

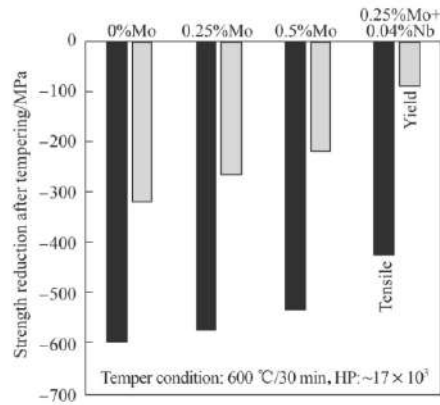


Figure 2.18. Reduction of yield and tensile strength after tempering treatment of directly quenched alloys [134].

Regarding the effect of boron in terms of tensile/toughness properties, Hannula et al. [31] studied the influence of adding B on a low-carbon Nb microalloyed martensitic steel. They demonstrated that removing boron considerably improves the toughness properties due to the formation of finer and more homogeneous martensitic microstructures. In another work, Hannula et al. [135] analysed the impact of adding Mo and Nb on the martensitic microstructure after DQ and DQ&T thermomechanical treatments. They observed that the addition of Nb and Mo (0.25 Mo-0.04 Nb) significantly improves the strength via an increased dislocation density and fine precipitation hardening. However, this steel shows worse toughness properties compared to 0.25 Mo steel due to intense precipitation hardening in the Nb-grade [11].

The effect of tempering treatment on directly quenched low alloy ultrahigh-strength steels has been widely studied in the literature in terms of microstructure and mechanical properties [9, 136]. Pallaspuuro et al. [136] reported that low ITT28J values can be achieved after direct quenching and that good toughness properties can be ensured without tempering treatment. Nevertheless, they observed a reduction in yield strength as well as an improvement in ductility and toughness after tempering. The improvement of toughness is generally attributed to the formation of more homogeneous martensitic microstructures with a low fraction of coarse grains [11, 136]. The positive effect of austenite pancaking on martensite homogeneity has also been reported by Sastamoinen et al. [51].

3. Summary of appended papers

This thesis is composed of five different papers published in the development of this research. The current investigation is organised in three main tasks, and each task is related to one or more appended papers. The structure of the current thesis is sequentially designed to first understand the combined effect of Nb, Mo and B on hot working behaviour. Afterwards, martensitic phase transformations have been studied and finally the relationship between the microstructure and the resulting tensile/toughness properties have been investigated for all chemical composition. Table 3.1 shows the chemical composition of the studied steels with 0.16% of C and approximately 20 ppm of boron. Besides a CMnB steel, three different microalloyed steels have been studied, microalloyed with Nb, Mo and NbMo. The Nb level is 0.026%, and Mo content is about 0.5%.

Table 3.1. Chemical composition of the studied steels (weight percent).

Steel	C	Si	Mn	Mo	Nb	B	Ti	N
CMnB	0.15	0.32	1.05	0.020	0.0003	0.0022	0.019	0.0051
CMnNbB	0.16	0.29	1.05	0.020	0.026	0.0019	0.022	0.0052
CMnMoB	0.16	0.28	1.07	0.51	0.0006	0.00022	0.025	0.0053
CMnNbMoB	0.16	0.31	1.08	0.52	0.026	0.0018	0.019	0.0052

3.1. Hot working behaviour

Paper I

I. Zurutuza, N. Isasti, E. Detemple, V. Schwinn, H. Mohrbacher, and P. Uranga, 2022, Effect of Nb and Mo on austenite microstructural evolution during hot deformation in Boron high strength steels, *Metallurgical and Materials Transactions A*, Vol. 53, pp. 1529-1539.

This paper is focused on the study of hot working behaviour of the studied steels. For that purpose, different type of torsion tests were performed in order to analyse the interaction between recrystallization and precipitation kinetics. The retardation

in recrystallization kinetics was modelled in all cases and measured kinetics agree with those predicted by equations previously developed for Nb-Mo microalloyed steels. The strain induced precipitation in the steels microalloyed with Nb was also characterized. Moreover, the fractional softening evolution during multipass rolling simulations was compared with MicroSim® model predictions, showing a good agreement with experimental results.

Paper II

I. Zurutuza, N. Isasti, E. Detemple, V. Schwinn, H. Mohrbacher, and P. Uranga, 2022, Effect of Dynamic Recrystallization on Microstructural Evolution in B Steels Microalloyed with Nb and/or Mo, *Materials*, Vol. 15, no. 4, 1424.

The dynamic recrystallization behaviour of Nb, Mo and NbMo microalloyed boron steels is analysed in this paper. Multipass torsion tests were performed for simulating plate hot rolling conditions followed by direct quenching. The results indicate that for Nb microalloyed steel, partial dynamic recrystallization occurs resulting in local clusters of fine-sized equiaxed grains dispersed within the pancaked austenitic structure. The activation of dynamic recrystallization results in the formation of soft bainitic phases within the martensitic matrix in the Nb grade. Conversely, the addition of Mo is shown to be an effective means of suppressing dynamic recrystallization. The circumstances initiating dynamic recrystallization were studied in more detail. Furthermore, the interference of the various alloying elements with the observed phenomena and the potential consequences of dynamic recrystallization before quenching were also discussed.

3.2. Phase transformation analysis

Paper III

I. Zurutuza, N. Isasti, E. Detemple, V. Schwinn, H. Mohrbacher, and P. Uranga, 2021, Effect of Quenching Strategy and Nb-Mo Additions on Phase Transformations and Quenchability of High-Strength Boron Steels, *JOM*, Vol. 73, no. 11, pp. 3158–3168.

In this paper, both direct quenching (DQ) and conventional quenching (CQ) processing routes were simulated by dilatometry tests and continuous cooling transformation (CCT) diagrams were built for all compositions. Based on the CCT diagrams, the impact of thermomechanical treatment on phase transformation, the resulting microstructure and hardness were evaluated. The results indicate that the addition of Mo and Nb-Mo suppresses the ferritic region and considerably shifts the CCT diagram to lower transformation temperatures. The combination of DQ strategy

and the Mo-alloying concept provides the best option to ensure hardenability and the formation of a fully martensitic microstructure, and to avoid the presence of soft phases in the centre of thick plates.

3.3. Relationship between microstructure and mechanical properties

Paper IV

I. Zurutuza, N. Isasti, E. Detemple, V. Schwinn, H. Mohrbacher, and P. Uranga, 2021, Effect of Nb and Mo additions in the microstructure/tensile property relationship in high strength quenched and quenched and tempered boron steels, *Metals*, Vol. 11, no. 1, 29.

This paper analyses the tensile properties of the studied steels. To that end, plane compression tests were performed consisting of two different thermomechanical cycles, quenching (Q) and quenching and tempering (Q&T). In order to evaluate the tensile behaviour, tensile tests for both quenched and quenched & tempered states and for all the steel grades were carried out. This work evaluates the complex interaction between the martensitic microstructure, the tempering treatment, the addition of microalloying elements and the resulting tensile properties. For that purpose, an exhaustive EBSD quantification was developed and the contribution of different strengthening mechanisms to yield strength was analysed. The optimum tensile properties are achieved combining Nb and Mo before and after tempering.

Paper V

I. Zurutuza, N. Isasti, E. Detemple, V. Schwinn, H. Mohrbacher, and P. Uranga, 2021, Toughness property control by Nb and Mo additions in high-strength quenched and tempered boron steels, *Metals*, Vol. 11, no. 1, 95.

Taking into account the results extracted in paper IV as a starting point, this study goes further and proposes a procedure for evaluating the contribution of different microstructural aspects on Charpy impact toughness. To that end, a detailed crystallographic characterization of tempered martensite was carried out using EBSD. Moreover, the existing equations for impact transition temperature (ITT50%) predictions were extended from ferrite-pearlite and bainitic microstructures to tempered martensite microstructures. The results show that microstructural refinement is the most beneficial factor for strength and toughness while unit size heterogeneity and fine precipitation has a particularly negative effect on ductile to-brittle transition behaviour.

4. Appended papers

Effect of Nb and Mo on Austenite Microstructural Evolution During Hot Deformation in Boron High Strength Steels



IRATI ZURUTUZA, NEREA ISASTI, ERIC DETEMPLE, VOLKER SCHWINN, HARDY MOHRBACHER, and PELLO URANGA

This work has focused on the study of hot working behavior of boron high strength steels microalloyed with different combinations of Nb and/or Mo. The role of Nb and Mo during the hot deformation of low carbon steels is well known: both mainly retard austenite recrystallization, leading to pancaked austenite microstructures before phase transformation and to refined room temperature microstructures. However, the design of rolling schedules resulting in properly conditioned microstructures, requires microstructural evolution models that take into account the effect of the different alloying elements. In this specific case, the effect that high levels of molybdenum (0.5 pct) have in the recrystallization delay was evaluated. In that respect, hot torsion tests were performed in this work to investigate the microstructural evolution during hot deformation of four boron steels, with different Nb (0.025 pct) and Mo (0.5 pct) combinations. The retardation in recrystallization kinetics was modeled in all cases and measured kinetics agree with those predicted by equations previously developed for Nb–Mo microalloyed steels with lower Mo concentrations (< 0.3 pct). The strain-induced precipitation in the Nb and Nb–Mo bearing steels was also characterized. Finally, the fractional softening evolution during multipass rolling simulations was compared with MicroSim® model predictions, showing a good agreement with experimental results.

<https://doi.org/10.1007/s11661-022-06618-0>

© The Author(s) 2022

I. INTRODUCTION

OVER the last years, new alloy concepts as well as innovative thermomechanical processing routes have been developed to fulfill the increasing mechanical property requirements for high-strength steels produced by direct quenching and subsequent tempering treatment. To achieve a good balance between strength and toughness, the combination of boron with microalloying elements (such as Nb, Mo or Nb–Mo) is a common practice.^[1–4] Besides selecting an optimum alloy concept, an appropriate design of rolling strategy becomes crucial for achieving pancaked austenite that promotes the

formation of refined microstructures and improves resulting mechanical properties. Recently, the effect of combining boron and microalloying elements on phase transformation has been investigated, to select the optimum alloy concept and processing route that ensures the formation of fully martensitic microstructure.^[5] Another relevant aspect that has to be considered is the strengthening due to grain size refinement that can be improved reaching a pancaked austenite before phase transformation. It is widely known that the addition of Nb and Mo delays softening kinetics, retards recrystallization of austenite and ensures the accumulation of deformation of the austenite prior to transformation.^[6] The addition of Nb and Mo increases the non-recrystallization temperature (T_n) and therefore, the strain is accumulated in austenite during the finishing passes of hot rolling.^[7,8] The retardation of the recovery and recrystallization of the austenite is related to the drag effect of Nb and Mo in solid solution and the pinning effect of Nb-rich strain induced precipitates. Depending on the interaction between driving and pinning forces, recrystallization can be partially retarded or fully hindered, promoting the refinement of the transformed room temperature microstructure.^[9] Even though the impact of adding Nb and Mo on recrystallization

IRATI ZURUTUZA, NEREA ISASTI, and PELLO URANGA are with the Materials and Manufacturing Division, CEIT-Basque Research and Technology Alliance (BRTA), 20018, Donostia-San Sebastián, Basque Country, Spain and with the Mechanical and Materials Engineering Department, Universidad de Navarra, Tecnun, 20018, Donostia-San Sebastián, Basque Country, Spain. Contact e-mail: puranga@ceit.es ERIC DETEMPLE and VOLKER SCHWINN are with the AG der Dillinger Hüttenwerke, Dillingen, Saar, Germany. HARDY MOHRBACHER is with the NiobelCon BV, 2970 Schilde, Belgium and with the Department of Materials Engineering (MTM), KU Leuven, 3001 Leuven, Belgium.

Manuscript submitted October 15, 2021; accepted January 26, 2022. Article published online February 18, 2022

kinetics was already investigated, the complex interaction between B, Nb and Mo, with higher molybdenum levels, and its effect on the austenite evolution during hot working is still unclear.

In the current work, different types of torsion tests were performed to analyze the interaction between recrystallization and precipitation kinetics for different high-strength medium carbon steels. In addition to evaluate the impact of chemical composition (synergy between B, Nb, Mo and Nb–Mo) and deformation temperature on static recrystallization of austenite, the competition between recrystallization, atoms in solid solution and strain-induced precipitates were analyzed during multipass deformation under continuous cooling conditions (in terms of T_{nr}). Finally, the applicability of the available austenite evolution models was studied.

II. MATERIALS AND METHODS

Table I shows the chemical composition of the studied steels containing 0.16 pct of C and 20 ppm of boron. Laboratory casts were produced for the present work. A reference CMnB steel was selected in addition to three different microalloyed steels with Nb, Mo and NbMo. Nb level is of 0.026 pct and Mo content about 0.5 pct. All the steels are alloyed with Ti to ensure the full effect of boron. All the grades show Ti/N ratios higher than the Ti/N stoichiometric ratio ($Ti/N = 3.42$).

Two different types of torsion tests were performed in a computer controlled torsion machine. Double twist torsion tests were carried out to define static recrystallization kinetics and multipass torsion tests in order to determine the evolution of fractional softening and the non-recrystallization temperature (T_{nr}). The torsion specimens are characterized by a central gauge section of 17 mm in length and a diameter of 7.5 mm.

The thermomechanical schedule in Figure 1 was defined for the double-twist torsion tests. In all cases, a soaking treatment was applied at 1200 °C for 10 minutes, for dissolving microalloying elements. Afterwards, deformation pass of 0.3 was applied at 1175 °C with the aim of refining the initial austenite grain size. After this deformation, the samples were cooled down to the deformation temperature. Two deformation passes were applied in the temperature range between 1100 °C and 850 °C and different interpass times were applied to evaluate the softening fractional evolution. Softening kinetics were recorded for a strain of 0.3. The full softening curve was obtained for the entire range of deformation temperatures (1100 °C, 1000 °C, 950 °C, 900 °C and 850 °C). The fractional softening (FS) for each condition was determined using the 2 pct offset method. It has been reported that, in the absence of strain-induced precipitation, this method excludes adequately the contribution of recovery to the overall softening.^[10,11] Torsion double twist technique shows several advantages when compared to the traditional double-hit compression tests.^[12] In addition, the initial austenite grain size (D_0) before the double twist torsion tests was measured. To that end, the samples were

quenched after reheating and applying a roughing pass at 1175 °C.

For the multipass torsion tests, the thermomechanical schedule included a soaking treatment at 1200 °C for 10 minutes. For CMnB and CMnNbB steels, 24 deformation passes were applied at decreasing temperatures in the 1100 and 640 °C range. For the steels containing Mo, deformation passes were applied from 1200 °C. The temperature decrease between passes was of 20 °C. Different strain per pass of 0.2 and 0.3 and interpass times of 5 and 15 seconds were selected. A strain rate of 1 s^{-1} was defined. The non-recrystallization temperature was defined considering the standard method proposed by Bai *et al.*^[13] Fractional softening calculated from the multipass torsion tests were compared with the Micro-Sim-PM® software results which simulates the microstructural evolution of austenite grain size distributions during hot working processes.

The specimens were characterized metallographically in the sub-surface longitudinal section, corresponding to 0.9 of the outer radius of the torsion specimen. The analysis of the austenitic structure was performed using optical microscopy (OM, LEICA DM15000 M, Leica microsystems). The specimens were etched by a solution of saturated picric acid and HCl to reveal the austenite grain boundaries in the quenched samples. Austenite grain size distributions were measured taking into account the mean equivalent diameter method. The measurements were carried out using the QWin v.2.3 image analysis software. For each steel grade, 400 to 600 austenite grains were measured. Concerning the analysis of softening kinetics, in selected conditions, the interaction between strain induced precipitation and recrystallization was analyzed. The study of the fine precipitates was performed using a transmission electron microscope (TEM, JEOL 2100) with a voltage of 200 kV and LaB₆ thermionic filament. To that end, carbon extraction replicas were obtained and strain induced precipitation analysis was carried out.

III. RESULTS AND DISCUSSION

A. Softening Kinetics

In Figure 2 the effect of chemical composition on the fractional softening curves for each deformation temperature can be evaluated. The kinetics of static recrystallization defined by an Avrami-type equation^[14] is used to fit the experimental data:

$$X_{\text{REX}} = 1 - \exp\left(-0.693 \left(\frac{t}{t_{0.5}}\right)^n\right) \quad [1]$$

The softening fraction (FS) can be replaced by the recrystallized fraction (X_{REX}), where t is the interpass time, $t_{0.5}$ is the time corresponding to 50 pct of the recrystallized volume and n is the Avrami exponent.

Several approaches for predicting the time of 50 pct recrystallization can be found in the literature. In a previous work,^[7] the following equation was deduced for low carbon Nb and Nb–Mo microalloyed steels

TABLE I. Chemical Composition of the Studied Steels (wt. pct)

Steel	C	Si	Mn	Mo	Nb	B	Ti	N	Ti/N
CMnB	0.15	0.32	1.05	0.020	0.0003	0.0022	0.019	0.0051	3.70
CMnNbB	0.16	0.29	1.05	0.020	0.026	0.0019	0.022	0.0052	4.32
CMnMoB	0.16	0.28	1.07	0.51	0.0006	0.0022	0.025	0.0053	4.63
CMnNbMoB	0.16	0.31	1.08	0.52	0.026	0.0018	0.019	0.0052	3.74

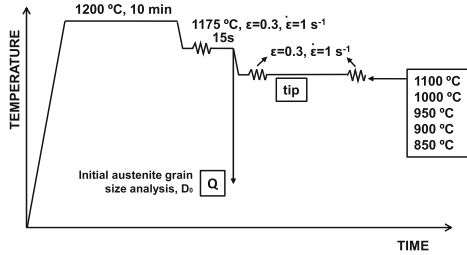


Fig. 1—Schematics of the thermomechanical cycles applied for the softening kinetics.

taking the effect of microalloying elements in solid solution, the deformation parameters (ϵ , $\dot{\epsilon}$, and T , strain, strain rate (s^{-1}) and temperature (K), respectively) and the initial austenite grain size (D_0) into account.

$$t_{0.5} = 9.92 \times 10^{-11} \cdot D_0 \cdot \epsilon^{-5.6D_0^{0.15}} \cdot \dot{\epsilon}^{-0.53} \cdot \exp\left(\frac{180,000}{RT}\right) \cdot \exp\left[\left(\frac{275,000}{T} - 185\right) \cdot [Nb]_{\text{eff}}\right] \quad [2]$$

$[Nb]_{\text{eff}} = [Nb]$ for Nb microalloyed steels.

$[Nb]_{\text{eff}} = 1.19[Nb] + 0.09[Mo]$ for 0.03 pct Nb-Mo microalloyed steels.

$[Nb]_{\text{eff}} = 1.19[Nb] + 0.032[Mo]$ for 0.06 pct Nb-Mo microalloyed steels.

The equation was developed for Nb and Nb-Mo low carbon (0.05 pct C) microalloyed steels with Nb content between 0.03 and 0.06 pct and Mo content between 0 and 0.31 pct. The approach includes a Nb effective term that considers the synergy between Nb and Mo in the delaying of recrystallization kinetics. The term related to Mo differs depending on the Nb content. For 0.03 pct Nb this term is about 0.09 and when Nb is increased to 0.06 pct, the Mo effect is reduced significantly, as the term decreases to 0.032. Therefore, the impact of Mo is reduced with increasing Nb content.

From the softening curves, the $t_{0.5}$ and the Avrami exponent n were calculated for the different deformation temperatures and steel grades. Additionally, the initial mean austenite grain sizes (D_0) were also quantified. In

Table II the experimental $t_{0.5}$ and n values determined from the softening curves, as well as D_0 measurements have been summarized. Concerning the initial mean austenite grain sizes (D_0), no significant differences are observed in the different steels. Mean initial grain sizes of 47, 59, 49 and 52 μm are measured for CMnB, CMnNbB, CMnMoB and CMnNbMoB steels, respectively.

As shown in Figure 2, for all deformation temperatures, the addition of microalloying elements affects the recrystallization kinetics. This effect is more pronounced as the deformation temperature decreases. In addition, Figure 2 suggests that the decrease of the deformation temperature promotes the delay of softening kinetics. Longer times are required for achieving fully recrystallized austenitic structure. When microalloying elements are added (Nb, Mo or Nb-Mo), even though very long times are applied (see Figures 2(d) and (e)), recrystallization is not completed for the lowest deformation temperatures of 900 °C and 850 °C. At the lowest deformation temperature of 850 °C, recrystallization interacts with deformation induced precipitation and atoms in solid solution in the steels containing Nb (CMnNbB and CMnNbMoB, see Figure 2(e)). However, in the CMnMoB steel, the retardation of the recrystallization kinetic is mainly attributed to the presence of Mo in solid solution. In the CMnNbB and CMnNbMoB grades, a plateau can be detected in the fractional softening curve if a deformation temperature of 850 °C is applied (see Figure 2(e)). This plateau is related to the presence of strain induced Nb precipitates that interact with recrystallization kinetics.^[15,16]

In Figure 3 the relation between predicted $t_{0.5}$ values by means of Eq. [2] and the experimental value is plotted for the current steels and deformation temperatures. The results indicate that reasonable prediction could be achieved in most cases considering the equation proposed by Pereda *et al.*^[7] The R2 score calculated for this dataset is of 0.77.

B. Analysis of Strain Induced Precipitates

Precipitation analysis was performed in the quenched samples for Nb and NbMo grades (deformation temperature of 850 °C and interpass time of 300 seconds), in order to confirm that the delaying of recrystallization can be justified by the presence of deformation induced precipitates in austenite. In Figure 4 several TEM images are presented at different magnifications for both Nb microalloyed steels (CMnNbB in Figures 4(a) through (c) and CMnNbMoB in Figures 4(d) through

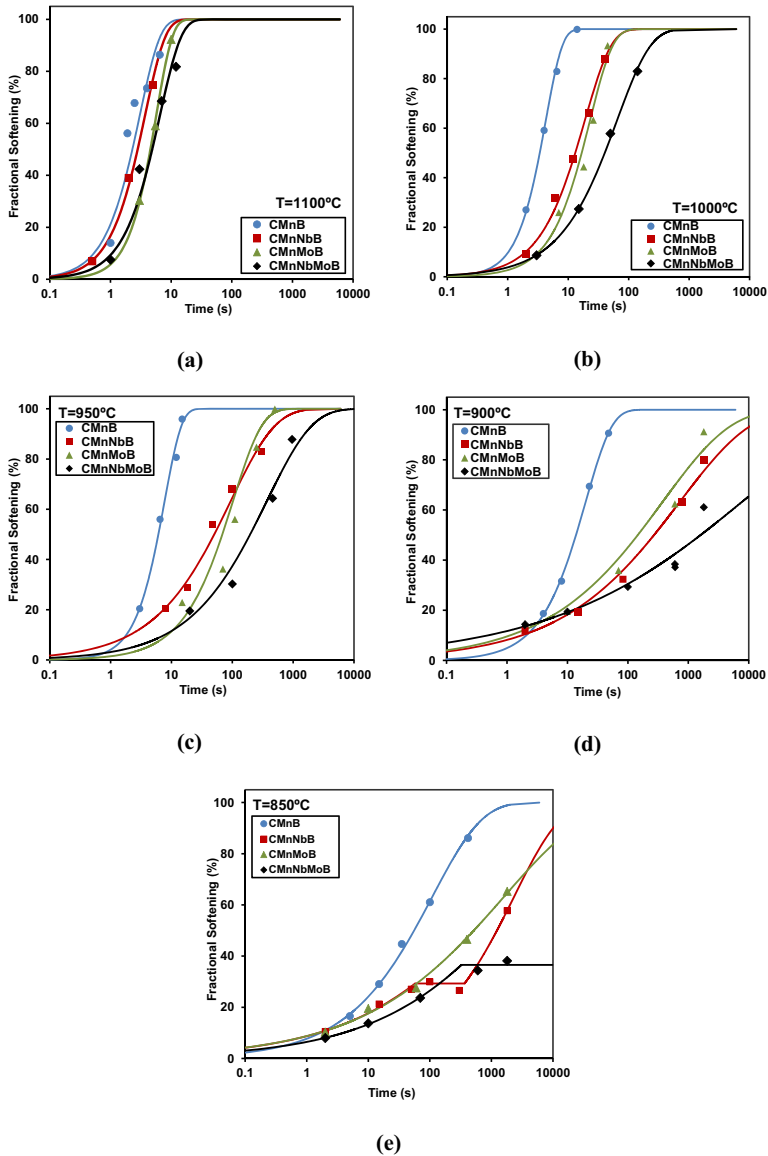


Fig. 2—Effect of the chemical composition on the softening behavior at (a) 1100 °C, (b) 1000 °C, (c) 950 °C, (d) 900 °C and (e) 850 °C.

(f). Different precipitate populations can be identified in both chemistries. In addition to non-dissolved Nb and Ti rich precipitates sized between 20 and 50 nm (see Figures 4(a) and (d)), finer strain induced precipitates are also observed (size below 10 nm, as shown in

Figures 4(b), (c), (e) and (f)). Spectral analysis (Figure 4(g)) reveals that these strain-induced precipitates are rich in Nb. These fine-sized Nb-based precipitates appear when deformation at low temperatures is applied. Their pinning effect on the austenite grain

Table II. Experimental $t_{0.5}$ and n Avrami Exponent Values, as Well as Initial Austenite Grain Sizes (D_0) Measured at Different Deformation Temperatures and Steel Grades

Steel	ϵ	D_0 (μm)	T_{def} ($^{\circ}\text{C}$)	$\dot{\epsilon}$ (s^{-1})	$t_{0.5}$ (s)	n
CMnB	0.3	47 ± 2	1100	1	2.3	1.3
			1000		3.4	1.6
			950		6.1	1.6
			900		7.7	1.0
			850		9.6	0.5
CMnNbB	0.3	59 ± 3	1100	1	2.8	1.3
			1000		13	1.0
			950		51	0.6
			900		70	0.4
			850		—	0.3
CMnMoB	0.3	49 ± 2	1100	1	4.6	1.6
			1000		17	1.1
			950		69	0.9
			900		95	0.5
			850		127	0.2
CMnNbMoB	0.3	52 ± 3	1100		4.9	1.2
			1000		41	0.8
			950	1	196	0.6
			900		273	0.2
			850		—	0.3

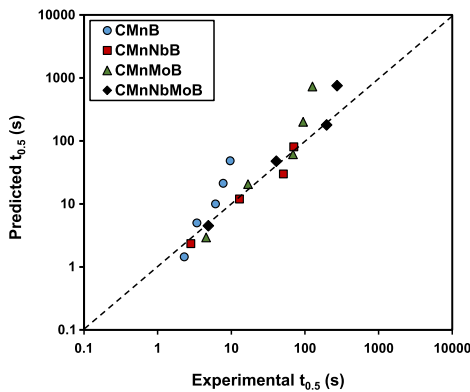


Fig. 3—Comparison between experimental and predicted time of 50 pct recrystallization ($t_{0.5}$) using Eq. 2.

boundaries causes a strong delay of the recrystallization kinetics and augments strain accumulation in austenite prior to transformation.

C. Multipass Torsion Tests

1. Definition of non-recrystallization temperature (T_{nr})

Multipass torsion tests were performed for two different deformation strains of 0.2 and 0.3 and interpass times of 5 and 15 seconds. The non-recrystallization temperature (T_{nr}) value was defined by means of multipass torsion tests for all the steel grades. Stress strain curves obtained from the torsion tests allowed calculating the mean flow stress (MFS), defined as the

area under the stress-strain curve divided by the pass strain, by numerical integration. The MFS for each deformation pass is plotted against the temperature in Figure 5 for an interpass time of 15 seconds. Thereby, the influence of the chemical composition of the steels on the MFS becomes apparent for both deformation strains. Two different regimes can be distinguished. In the initial regime at higher austenite temperature, complete recrystallization takes place between passes and the stress increase from pass to pass is only related to decreasing temperature and accordingly increasing yield strength of austenite. The second regime at lower austenite temperature is indicating strain accumulation caused by incomplete recrystallization.^[13] Following the standard procedure,^[10] the non-recrystallization temperature (T_{nr}) was determined as the intersection of linear fitted regression lines for the data points of either regime. Thus, non-recrystallization temperatures of 918 $^{\circ}\text{C}$, 956 $^{\circ}\text{C}$, 1003 $^{\circ}\text{C}$ and 1015 $^{\circ}\text{C}$ have been determined for CMnB, CMnNbB, CMnMoB and CMnNbMoB steels respectively, when a deformation of 0.2 and t_{ip} of 15 seconds is applied (see Figure 5(a)). An increase on the non-recrystallization temperatures is found for the higher deformation strain of 0.3. Steels with molybdenum alloying comprise the highest T_{nr} values especially when combined with Nb microalloying. Moreover, the molybdenum alloyed variants show a stronger impact of the deformation strain on the T_{nr} values. T_{nr} values measured for the different deformation conditions and all chemistries are summarized in Table III. For both interpass times, the lowest T_{nr} value was achieved for CMnB grade, followed by CMnNbB, CMnMoB and CMnNbMoB steels respectively. The reduction of interpass time, leads to higher T_{nr} values. This trend is observed for both deformation values.

These alloying effects on the non-recrystallization temperature may be related to two mechanisms being solute drag and particle pinning effect caused by strain induced precipitates. Molybdenum, niobium and titanium have a significantly larger atom size than iron and a tendency for segregating towards the austenite grain boundary. The drag effect by the alloying element is enhanced when the solute alloy atom has a large misfit with the matrix atom (Fe) and its self-diffusion coefficient is small. Calculations based on density functional theory have revealed furthermore that large-sized solute atoms have a high binding energy with the austenite grain boundary.^[17] This binding energy correlates with the activation energies necessary for static and dynamic recrystallization.^[18,19] Of the alloying elements considered in the current steels, niobium has the strongest binding energy followed by molybdenum and titanium. However, the solute drag effect also scales with the number of atoms, at least until saturation of the available grain boundary sites is reached. In that respect molybdenum clearly offers the greater potential since the element has much better solubility in austenite as compared to niobium and titanium having a similarly low solubility. Boron, being a smaller element, shows a lower binding energy.^[20–22] Some authors have also reported complex interactions between Nb and B affecting the recrystallization kinetics of Nb.^[23] In the

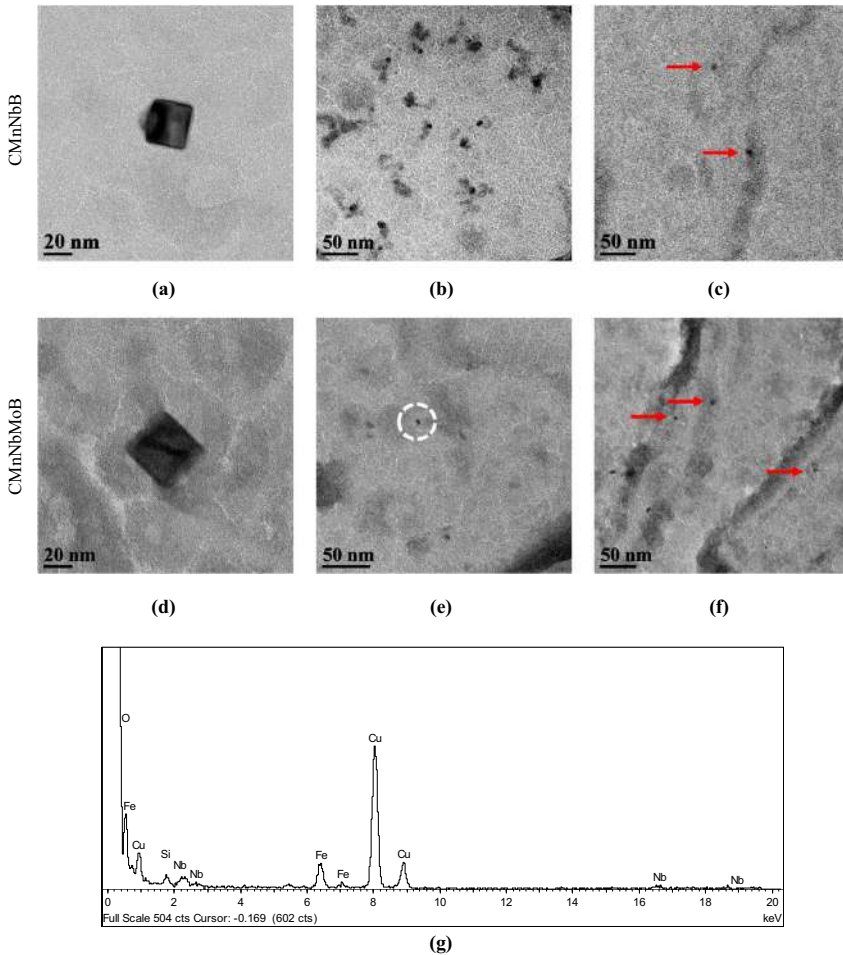


Fig. 4—Nb containing precipitates detected in the carbon replicas extracted from (a, b, c) CMnNbB and (d, e, f) CMnNbMoB steels after a deformation pass in 850 °C (interpass time of 300 s). (g) Microanalysis of the fine precipitate marked in (e) in a circle (the presence of Cu in the spectrum is due to the Cu grid of the carbon replica).

current paper, no effect of boron in static recrystallization kinetics was considered.

On the contrary, molybdenum by itself cannot form carbide precipitates in austenite contrary to niobium and titanium. In-situ formation of strain-induced precipitates exerts a pinning effect on austenite grain boundaries according to the well-known Zener theory.^[24] As already mentioned, the considered alloying elements (Mo, Nb, Ti) segregate towards austenite grain boundaries with decreasing temperature supported by the flow of vacancies.^[25,26] This leads to locally considerably higher concentration of these elements. Interstitial carbon and boron atoms show a similar boundary

segregation. Accordingly, the local solubility product of especially niobium can largely exceed the solubility limit facilitating strain-induced precipitation in the immediate boundary neighborhood. Titanium in the current steels is mostly consumed by forming TiN or Ti,Nb(C,N) particles after solidification.^[27] The near-stoichiometric (Ti/N) addition of titanium therefore leaves only a small amount available for forming strain-induced Ti particles (Table I). This residual Ti amount is largest in the CMnMoB steel being approximately 60 mass ppm while it is only 15 mass ppm in the CMnNb steel.

Based on these two mechanisms the measured T_{nr} values in Table III can be interpreted. In the CMnB steel

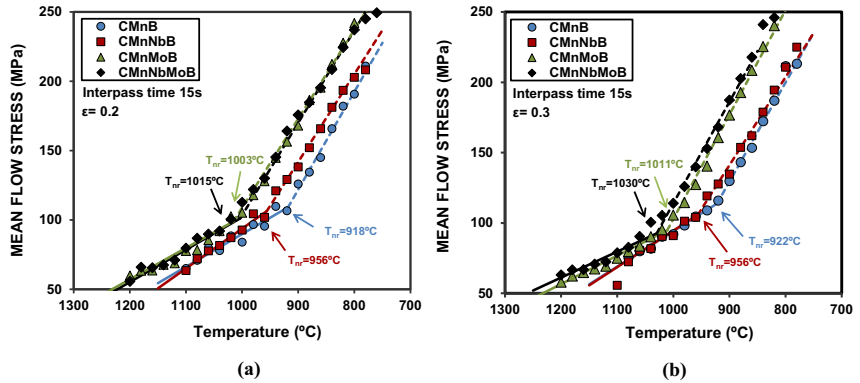


Fig. 5—Mean flow stress derived from multipass torsion tests as a function of temperature for (a) 0.2 and (b) 0.3 strain levels and an interpass time of 15 s.

Table III. T_{nr} Measured From Multipass Torsion Tests for Both Interpass Times (5 and 15 s), Both Deformation Levels (0.2 and 0.3) and All Chemical Compositions

Steel	Interpass Time (s)	ϵ	T_{nr} (°C)	Interpass Time (s)	ϵ	T_{nr} (°C)	ΔT_{nr} (5/15)
CMnB	5	0.2	955	15	0.2	918	37
	5	0.3	947	15	0.3	922	25
CMnNbB	5	0.2	980	15	0.2	956	24
	5	0.3	984	15	0.3	956	28
CMnMoB	5	0.2	1010	15	0.2	1003	7
	5	0.3	1030	15	0.3	1011	19
CMnNbMoB	5	0.2	1024	15	0.2	1015	9
	5	0.3	1049	15	0.3	1030	19

the formation of carbide particles is unlikely since only a very small residual amount of Ti is present. Therefore, any delay of recrystallization must be related to solute drag by the two segregating interstitials carbon and boron. With longer interpass time, this drag effect is increasingly overcome leading to considerably lower T_{nr} . The higher pass strain increases the driving force for recrystallization yet this effect on the T_{nr} is rather small especially for the longer interpass time. The addition of niobium increases T_{nr} considerably by around 35 °C for both interpass times. It is reasonable to assume that for the shorter interpass time the contribution by solute drag is more relevant. The longer interpass time facilitates the formation of precipitates exerting an additional pinning effect while the solute drag effect diminishes. The addition of molybdenum results in a very significant increase of T_{nr} as compared to the CMnB steel. This must be related to strong solute drag due to the rather high amount of solute molybdenum in this steel. Additionally, an influence of the pass strain is evident especially for the shorter interpass time. This could be explained by the higher defect density induced by the larger pass strain facilitating a more pronounced segregation of molybdenum atoms towards the grain

boundary. The solute drag effect caused by Mo is also sustained for the longer interpass time reflecting in a smaller decrease of T_{nr} relative to the Mo-free steels. By adding niobium and molybdenum in combination T_{nr} is further increased. This can be attributed to the solute drag effect of niobium.^[28] However, the incremental increase in T_{nr} by Nb in the Mo-alloyed is smaller than in the Mo-free steel. It is uncertain whether niobium precipitation already occurs at the generally higher T_{nr} temperatures of the Mo-alloyed steel. The small amount of residual titanium in these steels does not appear to have a significant influence on the recrystallization behavior.

2. Comparison between experimental anisothermal fractional softening and predicted by MicroSim® model

The experimental work was complemented by the advanced modeling tool MicroSim-PM®. This plate mill model allows predicting the evolution of austenite conditioning and can be a very useful tool for designing the optimum combination of rolling schedule and alloy composition.^[29] In the present study MicroSim-PM® software was used for predicting the recrystallized fraction of austenite from pass to pass and estimating

the evolution of Fractional Softening (FS) during plate hot rolling simulation. This analysis supports the understanding of the mechanisms involved and the interaction between precipitation and recrystallization in each alloy composition. MicroSim-PM® requires the initial austenite grain size distribution as an input and returns the size distributions for recrystallized and unrecrystallized fractions at the onset of subsequent rolling passes. For that purpose, the model assumes the interaction between different mechanisms acting during the interpass time, such as, static and metadynamic recrystallization, grain growth and Nb(C,N) strain induced precipitation. The equations implemented in the model are developed from industrially produced plates for plain CMn, Nb and NbMo microalloyed steels and adapted for a wide range of initial austenite grain sizes.

The fractional softening curves predicted by the model for the various steel compositions are plotted as a function of temperature for a deformation strain of 0.3 and an interpass time of 15 seconds in Figure 6. In addition, based on the results extracted from the multipass torsion tests, experimental FS results are overlaid in each graph for comparison. For determination of the fractional softening, anisothermal interpass conditions were assumed, considering the approach proposed by Liu and Akben^[30] shown in Eq. [3].

$$\text{FS (pct)} = \frac{\sigma_m^i - \sigma_y^{i+1} \frac{\sigma_0^i}{\sigma_0^{i+1}}}{\sigma_m^i - \sigma_0^i} \cdot 100 \quad [3]$$

where σ_m^i and σ_y^{i+1} are the maximum and the yield stresses for both, the i th (at temperature T_i) and the $(i + 1)$ st (at temperature T_{i+1}) passes, respectively, while σ_0^i and σ_0^{i+1} are the yield stresses of a fully recrystallized material for the i th and $(i + 1)$ st passes. The stresses σ_m^i and σ_y^{i+1} were derived from the pass-to-pass flow curves, while σ_0^i and σ_0^{i+1} were determined from the relationship derived from the values of the yield stresses measured in the stress-strain curves corresponding to the range of complete recrystallization. The yield stresses were determined by the 2 pct offset method.

In addition, experimental T_{nr} values calculated from multipass torsion tests (as reported in Table III) are indicated in Figure 6 (see the results shown in Section III-C-1). Evidently the softening behavior differs depending on the alloy concept. The decrease of softening in the microalloyed steels starts at higher austenite temperatures as expected. While at high temperatures the reduced softening could be related to the solute drag effect, strain induced precipitation in the Nb microalloyed variants becomes the dominating mechanism at lower austenite temperatures.

In general the model predicts the fractional softening behavior reasonably well for the different steel grades. The best match between the model prediction and experimental data is found for the CMnMoNbB steel. For the CMnMoB steel the model overestimates fractional softening below temperatures of approximately 980 °C while it underestimates FS at higher

temperatures. The experimental data indicate that solute drag by Mo becomes particularly strong at lower austenite temperatures, potentially supported by precipitation of residual Ti. In the CMnNbB steel the degree of FS is larger than predicted especially at temperatures below T_{nr} . In an earlier study on the same steels it has been observed that dynamic recrystallization can occur in this alloy variant during deformation passes at lower austenite temperatures.^[2] Such dynamic recrystallization was however completely suppressed in the CMnNbMoB alloy variant. The present data on the CMnNbMoB alloy variant (Figure 7(d)) support this earlier observation.

The effect of deformation strain and interpass time on the temperature evolution of FS is analyzed for the CMnNbB variant in Figure 7, again comparing predicted and experimental data. For the lower strain of 0.2 complete recrystallization is not even achieved during the initial deformation passes at high austenite temperatures for both interpass times (Figures 7(a) and (c)). The lower strain and thus the reduced driving force cannot sufficiently overcome the Nb solute drag effect preventing complete softening. Clearly, the solute drag effect is strongest for the shorter interpass time. Increasing the strain to 0.3 (Figures 7(b) and (d)), recrystallization approaches completeness for the longer interpass time. Comparing the experimental data to the MicroSim-PM® simulation results, it appears that the model correctly predicts the influence of deformation conditions (strain and interpass time) on the evolution of the austenite fractional softening along the pass schedule.

IV. CONCLUSIONS

The analysis of recrystallization kinetics and double twist torsion test results performed on four different variants of typical direct quenching steel alloy designs indicated that additions of Nb, Mo and Nb + Mo severely delay the softening kinetics at lower deformation temperatures. This is due to increasing solute drag on the austenite grain boundary by segregated alloying elements. Even if the solute drag effect of Nb per unit mass is the highest one, molybdenum has the most pronounced effect due to the higher number of solute atoms with the current compositions.

Nb microalloying shows a dual effect by providing solute drag at higher austenite temperature and grain boundary pinning by strain induced Nb precipitates at lower austenite temperature. The presence of Nb-rich strain induced precipitates has been confirmed by microscopic analysis. The accuracy of an established constitutive equation predicting the time for achieving 50 pct recrystallization was confirmed to be also valid for higher Mo levels used in some of the current steels.

Multipass torsion tests indicated that the solute drag effect is more dominant at shorter interpass time. It diminishes at longer interpass time but clearly less pronouncedly for the molybdenum alloyed variants. The variation of deformation strain also has more influence

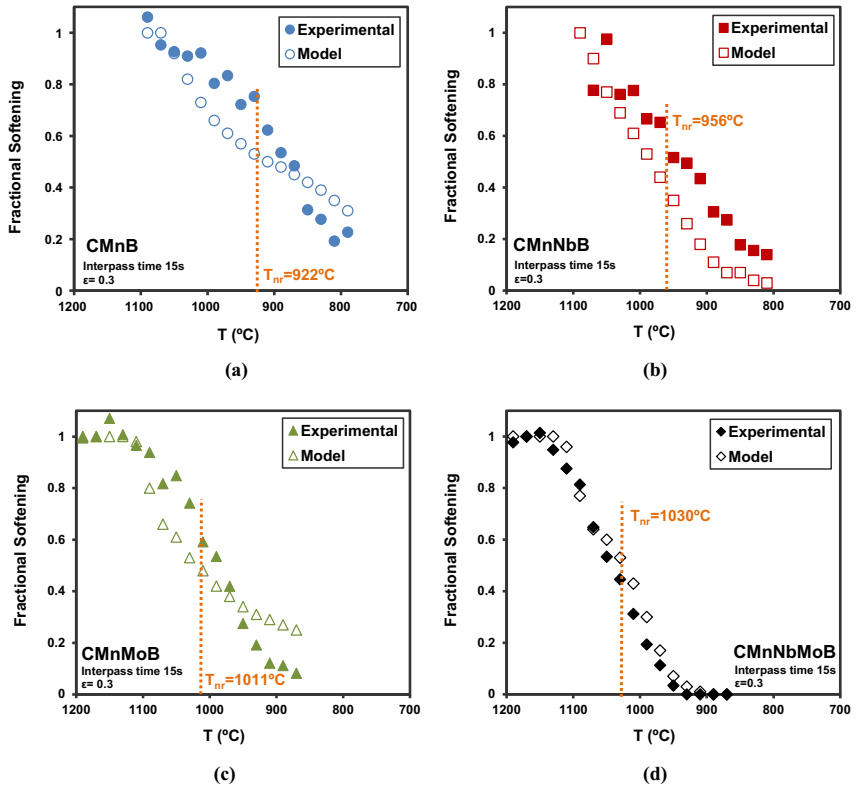


Fig. 6—Comparison between experimental fractional softening curves obtained from multipass torsion tests and those predicted by MicroSim-PM® (interpass time of 15 s and strain of 0.3): (a) CMnB, (b) CMnNbB, (c) CMnMoB and (d) CMnNbMoB. Non-recrystallization temperature (T_{nr}) as obtained in Fig. 5 is also indicated.

on the non-recrystallization temperature in the molybdenum alloyed variants. The larger deformation strain had apparently however no significant effect on the strain-induced precipitation of niobium at either interpass time in the present steels.

The combined addition of niobium and molybdenum results in synergetic behavior. At higher austenite temperatures, both niobium and molybdenum exert a strong solute drag effect. At lower austenite temperatures, niobium partially precipitates and in combination with solute drag exerted by molybdenum completely suppresses fractional softening, even under the larger deformation strain and for the longer interpass time.

MicroSim-PM® software was employed for predicting the recrystallized fraction of austenite from pass to pass and estimating the evolution of fractional softening during plate hot rolling simulation. Even though the software was so far mainly used and optimized for standard microalloyed HSLA steels, predictions of fractional softening for the current direct quenching steel alloys showed reasonably good agreement with the experimental behavior. Nevertheless, improvements in the underlying constitutive equations to better account for the austenite grain boundary segregation behavior of molybdenum and boron should be implemented.

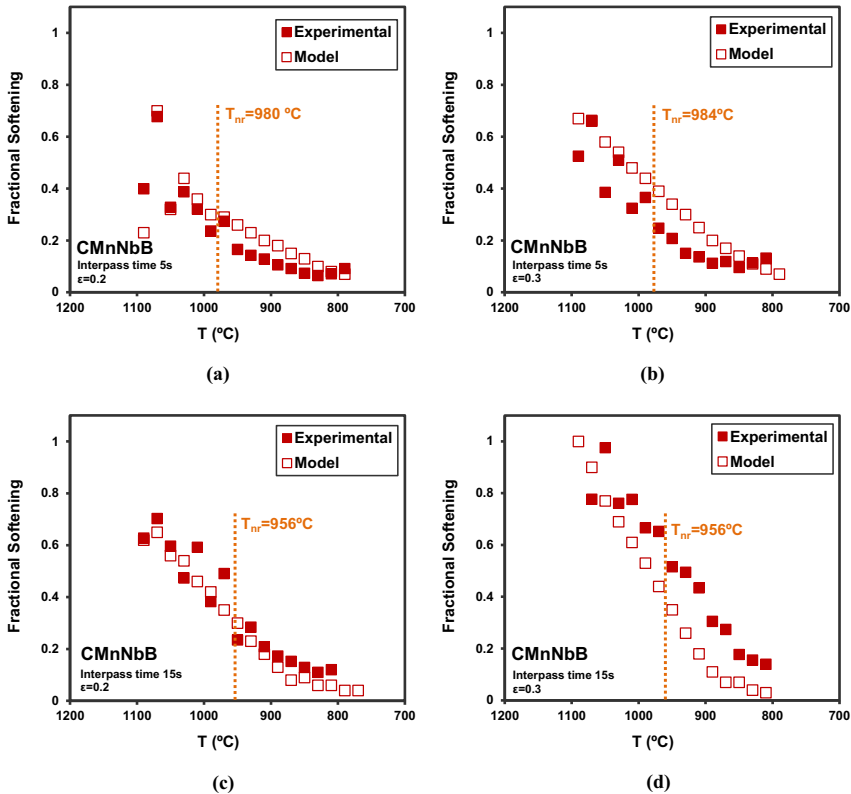


Fig. 7—Comparison between experimental fractional softening curves obtained from multipass torsion tests and predicted by MicroSim-PM® for CMnNbB steel: (a) $\varepsilon = 0.2$, $t_{ip} = 5$ s, (b) $\varepsilon = 0.2$, $t_{ip} = 15$ s, (c) $\varepsilon = 0.3$, $t_{ip} = 5$ s and (d) $\varepsilon = 0.3$, $t_{ip} = 15$ s. Non-recrystallization temperature (T_n) as obtained in Fig. 5 is also indicated.

ACKNOWLEDGMENTS

The authors would like to acknowledge the International Molybdenum Association (IMOA) for funding this project.

CONFLICT OF INTEREST

The authors declare that they have no conflict of interest.

FUNDING

Open Access funding provided thanks to the CRUE-CSIC agreement with Springer Nature.

OPEN ACCESS

This article is licensed under a Creative Commons Attribution 4.0 International License, which permits use, sharing, adaptation, distribution and reproduction in any medium or format, as long as you give appropriate credit to the original author(s) and the source, provide a link to the Creative Commons licence, and indicate if changes were made. The images or other third party material in this article are included in the article's Creative Commons licence, unless indicated otherwise in a credit line to the material. If material is not included in the article's Creative Commons licence and your intended use is not permitted by statutory regulation or exceeds the permitted use, you will need to obtain permission directly from the copyright holder. To view a copy of this licence, visit <http://creativecommons.org/licenses/by/4.0/>.

REFERENCES

1. I. Zurutuza, N. Isasti, E. Detemple, V. Schwinn, H. Mohrbacher, and P. Uranga: *Metals*, 2021, vol. 11(1), art. no. 29. <https://doi.org/10.3390/met11010029>.
2. I. Zurutuza, N. Isasti, E. Detemple, V. Schwinn, H. Mohrbacher, and P. Uranga: *Metals*, 2021, vol. 11(1), art. no. 95. <https://doi.org/10.3390/met11010095>.
3. H. Mohrbacher: *Metals*, 2018, vol. 8(4), art. no. 234. <https://doi.org/10.3390/met8040234>.
4. X.L. He, M. Djahazi, J.J. Jonas, and J. Jackman: *Acta Met. Mater.*, 1991, vol. 39(10), pp. 2295–308. [https://doi.org/10.1016/0956-7151\(91\)90012-P](https://doi.org/10.1016/0956-7151(91)90012-P).
5. I. Zurutuza, N. Isasti, E. Detemple, V. Schwinn, H. Mohrbacher, and P. Uranga: *JOM.*, 2021, vol. 73, pp. 3158–68. <https://doi.org/10.1007/s11837-021-04773-0>.
6. M.G. Akben, B. Bacroix, and J.J. Jonas: *Acta Metall.*, 1983, vol. 31(1), pp. 161–74. [https://doi.org/10.1016/0001-6160\(83\)90076-7](https://doi.org/10.1016/0001-6160(83)90076-7).
7. B. Pereda, B. López and J.M. Rodríguez-Ibabe: *Int. Conf. Microalloyed Steels Process Microstruct. Prop. Perform. Proc.*, Pittsburgh, PA, USA, July 2007, pp. 151–59.
8. C. Klinkenberg, K. Hulka, and W. Bleck: *Steel Res. Int.*, 2004, vol. 75, pp. 746–54. <https://doi.org/10.1002/srin.200405837>.
9. E.J. Palmiere, C.I. García, and A.J. DeArdo: *Metall. Mater. Trans. A.*, 1996, vol. 27A, pp. 951–60. <https://doi.org/10.1007/BF02649763>.
10. A.I. Fernandez, B. Lopez, and J.M. Rodriguez-Ibabe: *Scripta Mater.*, 1999, vol. 40(5), pp. 543–49. [https://doi.org/10.1016/S1359-6462\(98\)00452-7](https://doi.org/10.1016/S1359-6462(98)00452-7).
11. L. Llanos, B. Pereda, and B. Lopez: *Metall. Mater. Trans. A.*, 2015, vol. 46A, pp. 5248–65. <https://doi.org/10.1007/s11661-015-3066-2>.
12. T.J. Ballard, J.G. Speer, K.O. Findley, and E. De Moor: *Sci. Rep.*, 2021, vol. 11, art. no. 1495. <https://doi.org/10.1038/s41598-021-81139-1>.
13. D.Q. Bai, S. Yue, W.P. Sun, and J.J. Jonas: *Metall. Mater. Trans. A.*, 1993, vol. 24A, pp. 2151–59. <https://doi.org/10.1007/BF02648589>.
14. S. Vervynckt: *Control of the Non-Recrystallization Temperature in High Strength Low Alloy (HSLA) Steels*, Ghent University, Ghent, Belgium, 2010. <http://hdl.handle.net/1854/LU-4333753>.
15. S.F. Medina and A. Quispe: *ISIJ Int.*, 2001, vol. 41(7), pp. 774–81. <https://doi.org/10.2355/isijinternational.41.774>.
16. B. Pereda, J.M. Rodríguez-Ibabe, and B. Lopez: *ISIJ Int.*, 2008, vol. 48(10), pp. 1457–66. <https://doi.org/10.2355/isijinternational.48.1457>.
17. M. Hoerner, J. Speer, and M. Eberhart: *ISIJ Int.*, 2017, vol. 57(10), pp. 1847–50. <https://doi.org/10.2355/isijinternational.ISIJINT-2017-096>.
18. S. Medina and J. Mancilla: *ISIJ Int.*, 1996, vol. 36(8), pp. 1063–69. <https://doi.org/10.2355/isijinternational.36.1063>.
19. M. Akben, T. Chandra, P. Plassiard, and J.J. Jonas: *Acta Metall.*, 1984, vol. 32(4), pp. 591–601. [https://doi.org/10.1016/0001-6160\(84\)90070-1](https://doi.org/10.1016/0001-6160(84)90070-1).
20. L. Karlsson and H. Norden: *Le J. Phys. Colloq.*, 1986, vol. 47(C7), pp. C7-257–62. <https://doi.org/10.1051/jphyscol:1986744>.
21. J.E. Morral and W.F. Jandeska: *Metall. Mater. Trans. A.*, 1980, vol. 11A, pp. 1628–29. <https://doi.org/10.1007/BF02654530>.
22. W.F. Jandeska and J.E. Morral: *Metall. Trans.*, 1972, vol. 3(11), pp. 2933–37. <https://doi.org/10.1007/BF02652863>.
23. X.L. He, M. Djahazi, J.J. Jonas, and J. Jackman: *Acta Metall. Mater.*, 1991, vol. 39(10), pp. 2295–308. [https://doi.org/10.1016/0956-7151\(91\)90012-P](https://doi.org/10.1016/0956-7151(91)90012-P).
24. L.J. Cuddy and J.C. Raley: *Metall. Mater. Trans. A.*, 1983, vol. 14A, pp. 1989–95. <https://doi.org/10.1007/BF02662366>.
25. H. Mohrbacher and T. Senuma: *Metals*, 2020, vol. 10(7), art. no. 853. <https://doi.org/10.3390/met10070853>.
26. Y. Li, D. Ponge, P.P. Choi, and D. Raabe: *Scripta Mater.*, 2015, vol. 96, pp. 13–16. <https://doi.org/10.1016/j.scriptamat.2014.09.031>.
27. J. Weibel, A. Herges, D. Britz, E. Detemple, V. Flaxa, H. Mohrbacher, and F. Mücklic: *Metals*, 2020, vol. 10(2), art. no. 243. <https://doi.org/10.3390/met10020243>.
28. N. Maruyama, R. Uemori, and M. Sugiyama: *Mater. Sci. Eng. A.*, 1998, vol. 250(1), pp. 2–7. [https://doi.org/10.1016/S0921-5093\(98\)00528-0](https://doi.org/10.1016/S0921-5093(98)00528-0).
29. X. Azpeitia, N. Isasti, P. Uranga, J.M. Rodríguez Ibabe, D.G. Stalheim and M. Rebellato: *Procs. 2nd International Symposium on the Recent Developments in Plate Steels*, AIST, Orlando, FL, 3–6 June, 2018, pp. 83–91.
30. W.J. Liu and M.G. Akben: *Can. Metall. Q.*, 1987, vol. 26(2), pp. 145–53. <https://doi.org/10.1179/cmqr.1987.26.2.145>.

Publisher's Note Springer Nature remains neutral with regard to jurisdictional claims in published maps and institutional affiliations.

Article

Effect of Dynamic Recrystallization on Microstructural Evolution in B Steels Microalloyed with Nb and/or Mo

Irati Zurutuza ^{1,2}, Nerea Isasti ^{1,2}, Eric Detemple ³ , Volker Schwinn ³, Hardy Mohrbacher ^{4,5} 
and Pello Uranga ^{1,2,*} 

- ¹ Materials and Manufacturing Division, CEIT-Basque Research and Technology Alliance (BRTA), 20018 Donostia-Saint Sebastian, Basque Country, Spain; izurutuza@ceit.es (I.Z.); nisasti@ceit.es (N.I.)
- ² Mechanical and Materials Engineering Department, Universidad de Navarra, Tecnun, 20018 Donostia-Saint Sebastian, Basque Country, Spain
- ³ Aktien-Gesellschaft der Dillinger Hüttenwerke, 66763 Dillingen/Saar, Germany; Eric.Detemple@dillinger.biz (E.D.); Volker.Schwinn@dillinger.biz (V.S.)
- ⁴ NiobelCon BV, 2970 Schilde, Belgium; hm@niobelcon.net
- ⁵ Department of Materials Engineering (MTM), KU Leuven, 3001 Leuven, Belgium
- * Correspondence: puranga@ceit.es; Tel.: +34-943-212-800

Abstract: The dynamic recrystallization behavior of ultra-high strength boron-microalloyed steels optionally alloyed with niobium and molybdenum is analyzed in this paper. Multipass torsion tests were performed to simulate plate rolling conditions followed by direct quenching. The influence of alloy composition on the transformed microstructure was evaluated by means of EBSD, thereby characterizing the morphology of the austenite grain morphology after roughing and finishing passes. The results indicated that for Nb-microalloyed steel, partial dynamic recrystallization occurred and resulted in local clusters of fine-sized equiaxed grains dispersed within the pancaked austenitic structure. A recrystallized austenite fraction appeared and transformed into softer phase constituents after direct quenching. The addition of Mo was shown to be an effective means of suppressing dynamic recrystallization. This effect of molybdenum in addition to its established hardenability effects hence safeguards the formation of fully martensitic microstructures, particularly in direct quenching processes. Additionally, the circumstances initiating dynamic recrystallization were studied in more detail, and the interference of the various alloying elements with the observed phenomena and the potential consequences of dynamic recrystallization before quenching are discussed.

Keywords: austenite conditioning; multipass torsion tests; dynamic recrystallization; Nb–Mo microalloyed steels



Citation: Zurutuza, I.; Isasti, N.; Detemple, E.; Schwinn, V.; Mohrbacher, H.; Uranga, P. Effect of Dynamic Recrystallization on Microstructural Evolution in B Steels Microalloyed with Nb and/or Mo. *Materials* **2022**, *15*, 1424. <https://doi.org/10.3390/ma15041424>

Academic Editor: Ivo Schindler

Received: 26 January 2022

Accepted: 10 February 2022

Published: 15 February 2022

Publisher's Note: MDPI stays neutral with regard to jurisdictional claims in published maps and institutional affiliations.



Copyright: © 2022 by the authors. Licensee MDPI, Basel, Switzerland. This article is an open access article distributed under the terms and conditions of the Creative Commons Attribution (CC BY) license (<https://creativecommons.org/licenses/by/4.0/>).

1. Introduction

Ultra-high strength steel with a martensitic microstructure is the preferred material for structural applications requiring an extreme load-bearing capacity or superior wear resistance. Martensitic steels are traditionally produced by conventional quenching (CQ), where the steel is reheated from ambient temperature back into austenite before quenching. Direct quenching (DQ) is an increasingly often practiced variant for processing ultra-high strength steel that enables cost and capacity optimization in steel mills [1]. The DQ method typically applies fast cooling to conditioned austenite, while the CQ method acts on a normalized (equiaxed) austenite microstructure. Accordingly, the martensite substructure originating from the DQ process develops within a pancaked austenite microstructure [2].

The microstructural homogeneity of austenite before quenching is related to recrystallization phenomena occurring along the entire austenite hot working process. An inhomogeneous prior austenite microstructure is detrimental for the toughness and (particularly) ductile-to-brittle transition temperature of the quenched steel [2,3]. Microstructural heterogeneity in austenite can be generated at different stages during the hot working

process. Alloy additions of boron, niobium, and molybdenum induce strong solute drag on austenite boundaries, thus delaying austenite recrystallization at temperatures between 1000 and 1100 °C [4]. If the austenite temperature during the last passes of recrystallizing rolling (roughing) drops into that range, the recrystallization of austenite, especially in the plate center, may not completely occur and individual non-recrystallized grains may not be as refined as the recrystallized ones. This heterogeneity cannot be removed by subsequent austenite conditioning (pancaking), resulting in pancaked grains of different thicknesses. Only a complete normalization, as occurs under CQ conditions, results in a homogeneous austenite microstructure.

On the other hand, strong austenite conditioning, which is typically connoted with high reduction ratio and low finishing temperatures, can trigger dynamic recrystallization in part of a microstructure. This event produces a fraction of very fine equiaxed austenite grains. It has been shown that the application of large deformation strain at low austenite temperature and the presence of dynamically recrystallized austenite compromises the hardenability effect related to boron microalloying [2,5–8]. The hardenability related to molybdenum alloying, however, appears to be much more robust under the same processing conditions. Although the impacts of Nb and Mo in dynamic recrystallization kinetics have been already analyzed, the synergetic effect of Nb, Mo and B for higher Mo contents needs to be further explored. Therefore, the authors of the current study investigates the circumstances initiating dynamic recrystallization in more detail. The interference of the various alloying elements (Mo, Nb, and B) with the observed phenomena and potential consequences of dynamic recrystallization before quenching are discussed.

2. Materials and Methods

The chemical composition of the boron-microalloyed steel designs using individual or combined Nb and Mo additions is listed in Table 1. Boron was stopped from forming boron nitride with an appropriate microalloy addition of titanium. The CMnB steel was used as a reference and for comparison based on previous papers.

Table 1. Chemical composition of the steels investigated in this work (in weight percent).

Steel	C	Si	Mn	Mo	Nb	B
CMnB	0.15	0.32	1.05	-	-	0.0022
CMnNbB	0.16	0.29	1.05	-	0.026	0.0019
CMnMoB	0.16	0.28	1.07	0.5	-	0.0022
CMnNbMoB	0.16	0.31	1.07	0.5	0.026	0.0018

Multipass torsion tests were performed to carry out hot rolling simulations followed by direct quenching. The torsion samples comprised a reduced central gauge section of 17 mm in length with a diameter of 7.5 mm. The torsion specimens were subjected to the thermomechanical deformation schedule shown in Figure 1. After soaking at 1200 °C for 10 min, allowing for the nearly complete dissolution of the microalloying elements B and Nb, five deformation passes with the austenite temperature gradually decreasing from 1170 to 1150 °C were executed in order to re-produce the roughing stage. In the roughing passes, a deformation strain of 0.2 at a strain rate of 2 s⁻¹ and an interpass time of 6 s was applied. Between roughing and finishing, the material was held for 360 s, allowing for cooling to a finishing-start temperature of 880 °C. Eight finish deformation passes, each applying a strain of 0.2, were applied with a strain rate of 5 s⁻¹. The finish deformation sequence ended at 830 °C. Subsequent slow cooling (1 °C/s) until 790 °C was followed by accelerated cooling at a rate of approximately 30 °C/s down to ambient temperature.

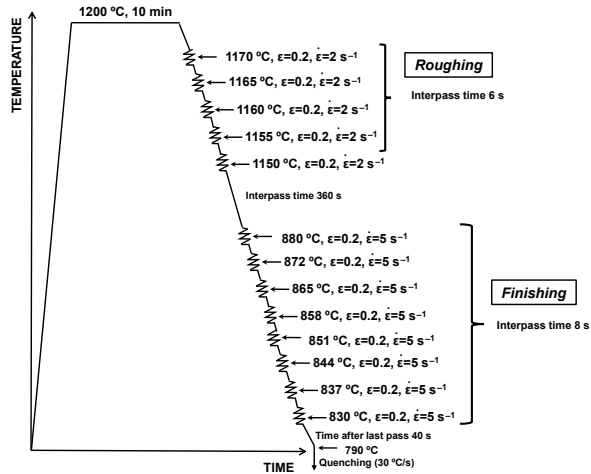


Figure 1. Schematics of multipass thermomechanical cycle employed with the torsion testing machine for simulating plate hot rolling.

Two specific hot torsion schedules (Figure 2) were designed to evaluate the influence of the alloying elements Nb and Mo on the occurrence of dynamic recrystallization and to verify under which conditions this mechanism was triggered during finishing deformation passes. Both thermomechanical cycles started from reheating at 1200 °C for 10 min, followed by five roughing passes, similar to the ones defined for the hot rolling simulation (Figure 1). In one schedule (Figure 2a), the samples were cooled down to 850 °C after the last roughing pass, when 8 finish deformation passes were isothermally applied with a strain of 0.2, a strain rate of 5 s⁻¹ and an interpass time of 1 s. The other schedule (Figure 2b) consisted of one large deformation cycle at 850 °C, with a strain of 4 and a strain rate of 5 s⁻¹. Both schedules were followed by quenching to room temperature with a rate of approximately 30 °C/s.

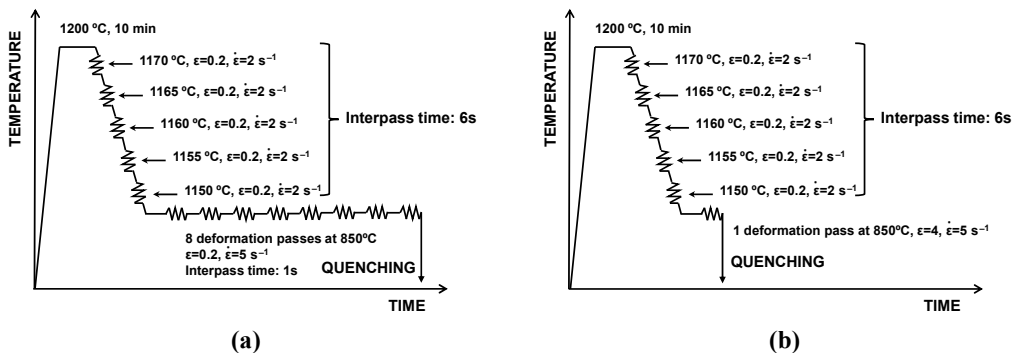


Figure 2. Thermomechanical schedules employed at the torsion testing machine for analyzing dynamic recrystallization phenomena: (a) roughing simulation followed by 8 deformation passes at 850 °C ($\epsilon = 0.2$ and $\dot{\epsilon} = 5 \text{ s}^{-1}$) and (b) roughing simulation followed by a deformation pass at 850 °C ($\epsilon = 4$ and $\dot{\epsilon} = 5 \text{ s}^{-1}$).

The quenched martensitic microstructures were metallographically characterized in the sub-surface longitudinal section, corresponding to 0.9 of the outer radius of the torsion specimen. The analysis of the austenite structure was performed after etching in 2% Nital by optical microscopy (OM, LEICA DM1500 M, Leica microsystems, Wetzlar, Germany), and the quantification of microstructural features was performed via electron backscattered diffraction (EBSD). The EBSD samples were polished down to 1 μm , and the final polishing was performed with colloidal silica. EBSD was performed on the equipment with a camera NORDLYS II (Oxford Instruments, Abingdon, UK), a well as an acquisition program and data analysis, OXFORD HKL CHANNEL 5 PREMIUM coupled to the JEOL JSM-7100 F FEG-SEM (JEOL Ltd., Tokyo, Japan). A scan step size of 0.2 μm was used, and a total scanned area of $140 \times 140 \mu\text{m}^2$ was defined for characterization of martensitic microstructure. The EBSD scans were analyzed by means of TSL OIM™ Analysis 5.31 software (EDAX, Mahwah, NJ, USA).

Besides analyzing the direct quenched martensite, the austenitic structures prior to martensite transformation were also characterized after etching in a solution of saturated picric acid HCl. Due to the highly deformed austenitic microstructure, the reconstruction of austenite was carried out by means of EBSD. For reconstructing the austenite prior to transformation, a scan step size of 1 μm and a total scanned area of $500 \times 500 \mu\text{m}^2$ were defined. The analysis of strain-induced precipitation was also performed in the sub-surface longitudinal section of the torsion specimen using a transmission electron microscope (TEM, JEOL 2100, JEOL Ltd., Tokyo, Japan) with a voltage of 200 kV and LaB6 thermionic filament. This analysis was done using carbon extraction replicas.

3. Results

3.1. Characterization of the Direct Quenched Martensitic Microstructure after Plate Hot Rolling Simulation

The microstructures of the direct quenched steels following the hot deformation illustrated in Figure 1 are shown in Figure 3a–c. While the Mo and NbMo added steels exhibited fully martensitic microstructures, the CMnNbB steel comprised clusters consisting of non-polygonal ferrite within the martensitic microstructure. The presence of the ferrite phase resulted in a rather low hardness of 290 HV. The Mo- and NbMo-alloyed steels had much higher hardness values of 394 and 422 HV, respectively.

EBSD analysis was performed in the same specific locations corresponding to the optical images. Figure 3d–f shows grain boundary maps, in which low angle (between 2° and 15°) and high angle boundaries ($>15^\circ$) are represented by red and black colors, respectively. Grain boundary maps corresponding to the three steel grades confirm the formation of a very fine-sized and complex microstructure. The presence of a substructure is reflected in a high density of low angle boundaries. However, in the CMnNbB steel (Figure 3d), some areas are clearly lacking this substructure, thus indicating that a softer phase was formed within the otherwise martensitic matrix. The mean unit sizes considering both tolerance angles ($D2^\circ$ and $D15^\circ$) are indicated in the grain boundary maps. The CMnMoB and CMnNbMoB steels showed similar mean unit sizes, $D2^\circ$ and $D15^\circ$, of about 0.9 and 1.3 μm , respectively. However, for CMnNbB grades, slightly coarser mean unit sizes of 1.1 and 1.5 μm were found for $D2^\circ$ and $D15^\circ$, respectively. The kernel average misorientation (KAM) maps shown in Figure 3g–i reflect the presence of highly dislocated microstructures such as martensite and bainite (red- and yellow-colored areas, respectively). Yet in the CMnNbB steel, larger islands with lower dislocation density (blue and green colored areas) can be seen; these represent softer ferritic phases. The KAM value increased from 1.38° in CMnNb steel to 1.57° in the CMnMoB and CMnNbMo steels. In Figure 3j–l, the unit size distributions considering low and high angle misorientation criteria (boundaries between 2° and 15° and boundaries higher than 15° , respectively) are plotted for the three steels. For both misorientation criteria, a finer unit size distribution can be observed in the CMnNbMoB steel compared to the CMnNbB steel.

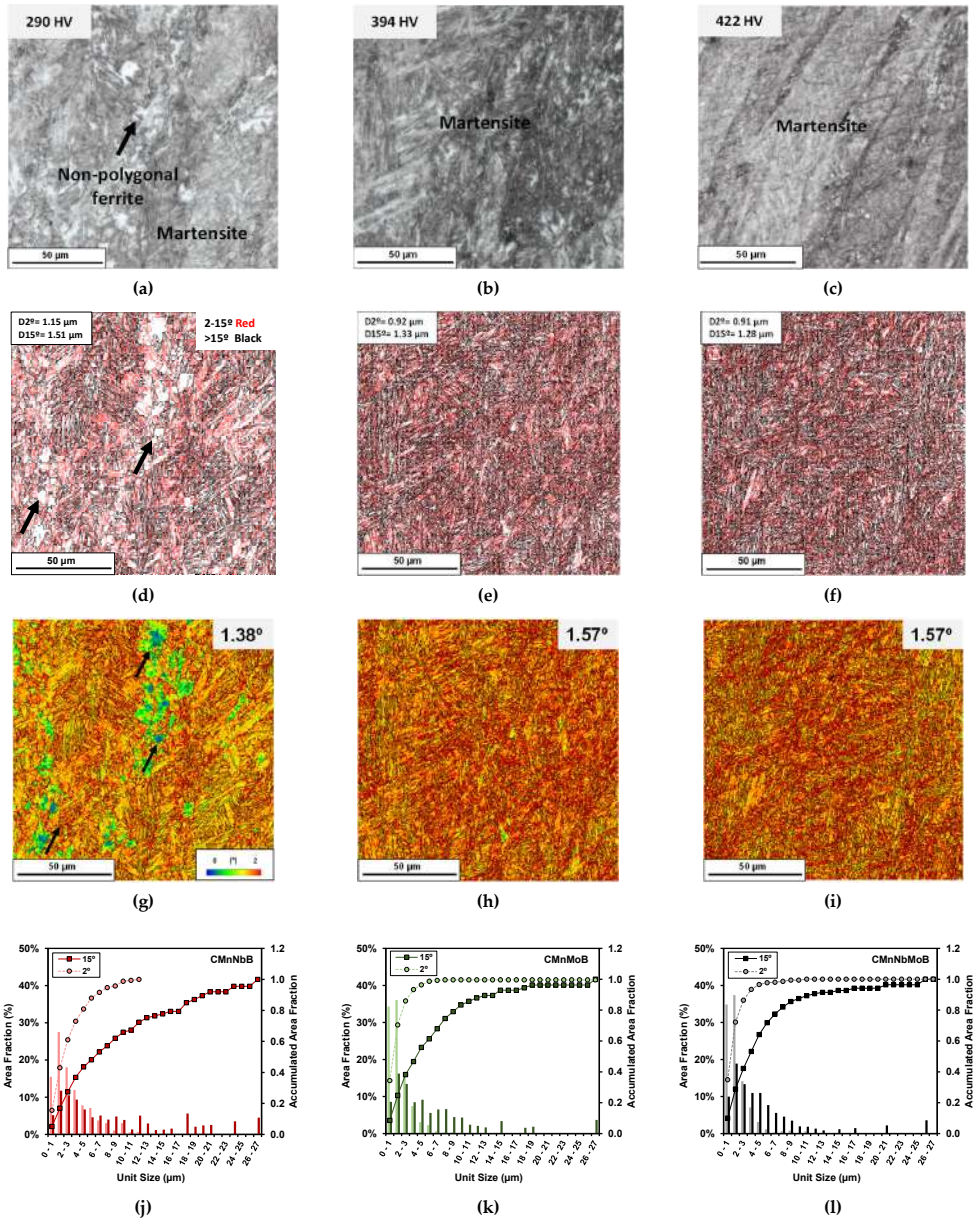


Figure 3. (a–c) Optical images, (d–f) grain boundary maps, and (g–i) kernel maps obtained for (a,d,g) CMnNbB, (b,e,h) CMnMoB, and (c,f,i) CMnNbMoB steels. (j–l) Unit size distributions measured for Nb, Mo, and NbMo grades, respectively (low and high angle misorientation criteria are considered).

3.2. Impact of Adding Nb and Mo on Austenite Conditioning

As the final martensitic features are strongly influenced by the austenite morphology prior to phase transformation, the characterization of the prior austenitic structure was analyzed (Figure 4). However, hot rolling simulations generating extremely deformed austenite hinder quantitative characterization. In all steel alloys, the microstructure comprised highly elongated austenite grains (Figure 4a,c,e). The accumulation of deformation was most pronounced for the combined addition of Nb and Mo (Figure 4e,f). Analyzing the optical images obtained at higher magnifications (Figure 4b,d,f) revealed a fraction of fine equiaxed grains in the CMnNbB grade, as indicated with red arrows in Figure 4b. These must have resulted from localized dynamic recrystallization occurring during final deformation. In the Mo-bearing steel grades, such equiaxed grains were not observed (see Figure 4d,f).

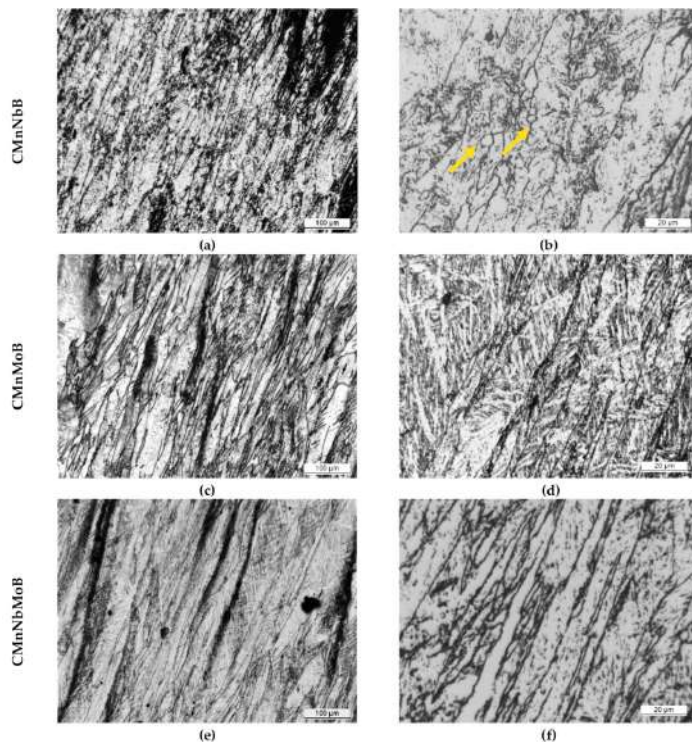


Figure 4. Optical micrographs at different magnifications ((a,c,e) and (b,d,f), at low and high magnifications, respectively) corresponding to all steel grades after the multipass torsion test (etched by Picric acid).

EBSD inverse pole figure (IPF) maps obtained on the martensitic microstructures (Figure 5a–c) allowed for the reconstruction of the prior austenite grain structure (Figure 5d–f) according to a procedure defined in [9,10]. The reconstruction confirmed the presence of elongated austenite grains in all steels. In agreement with the optical microscopy analysis, the reconstructed austenite structure of the CMnNbB steel demonstrated a fraction of very fine equiaxed grains.

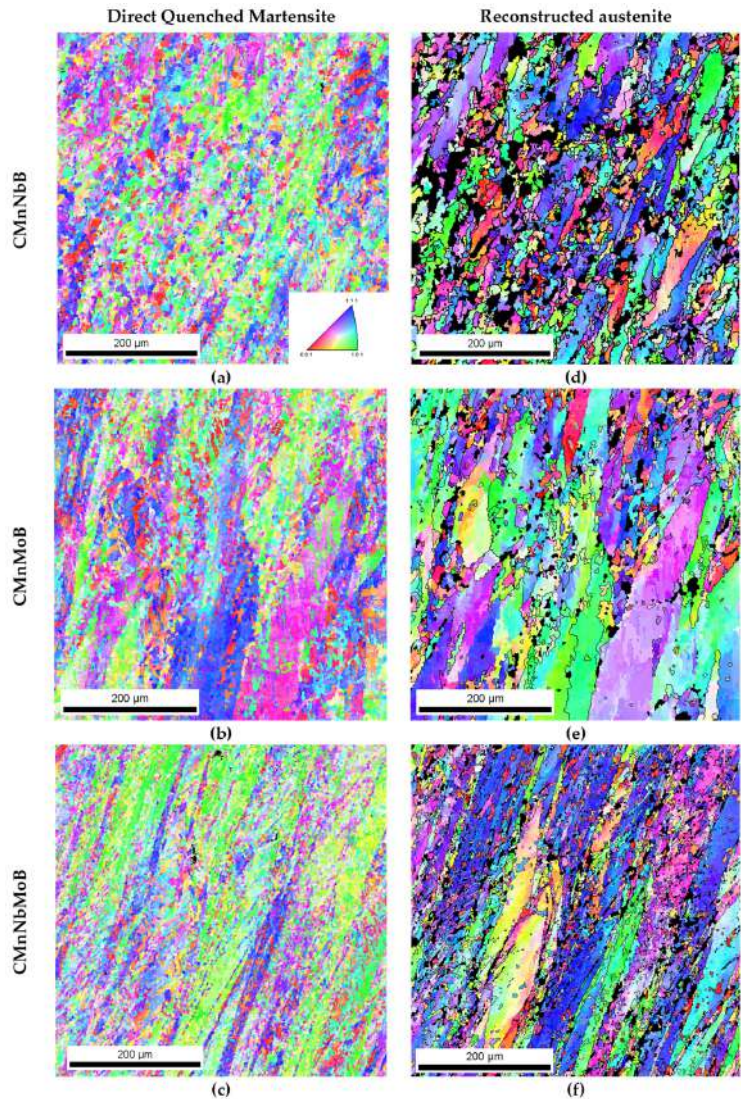


Figure 5. (a–c) IPF maps corresponding to the martensitic microstructure and (d–f) Reconstructed austenite microstructures for different steel grades.

When deforming Nb-microalloyed steels at austenite temperatures below T_{nr} , strain-induced precipitates can be formed, delaying static recrystallization and promoting strain accumulation prior to transformation. Usually, the pinning effect of these strain-induced particles is assumed to be strong enough to block any further static recrystallization during conventional hot deformation sequences. Carbon extraction replicas of the CMnNbB steel were analyzed with TEM, as shown in Figure 6, where different precipitate populations can be identified. Precipitates composed of Nb and Ti of relatively larger size (Figure 6a) were

likely undissolved particles existing prior to the soaking treatment. Additionally, strain-induced precipitates in the size range between 10 and 30 nm were observed (Figure 6b–d). The microanalysis shown in Figure 6e shows that Nb and Ti comprised these carbide particles. These strain-induced precipitates efficiently blocked static recrystallization during the finishing passes.

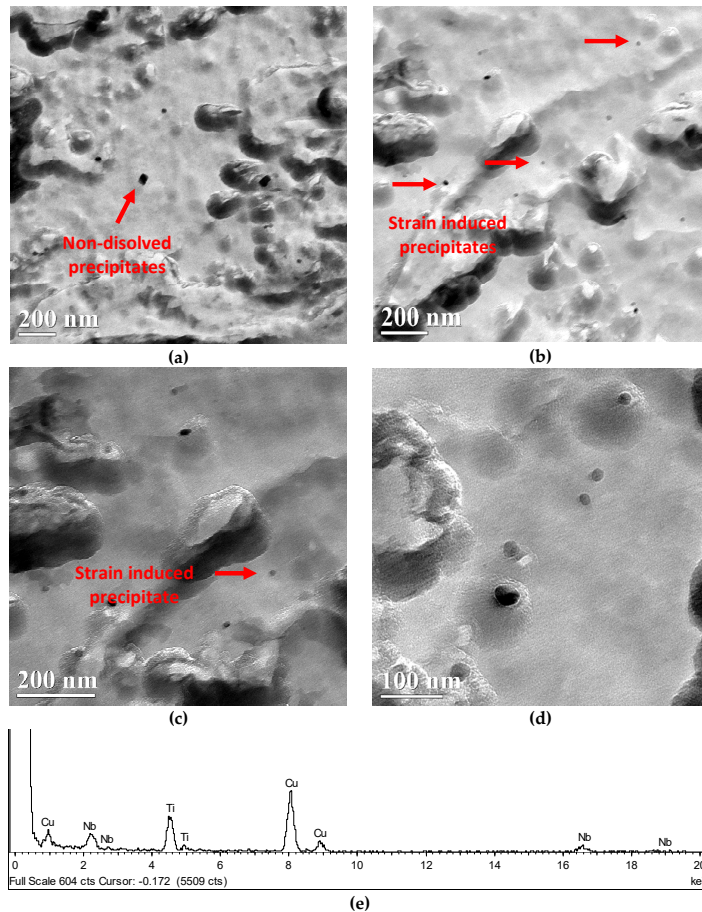


Figure 6. (a–d) Presence of non-dissolved Nb–Ti precipitates and strain-induced fine precipitates (NbTi-rich) in CMnNbB steel after plate hot rolling simulation and DQ. (e) Microanalysis of the strain-induced precipitate marked in (c) with a red arrow (the presence of Cu in the spectrum is associated with the grid holding of the carbon replica).

Molybdenum, on the other hand, does not precipitate in austenite due to its high solubility even for the current addition of 0.5 mass% [11]. Hence, the observed austenite pancaking in the CMnMoB steel must have primarily been caused by a strong solute drag effect acting on the grain boundaries. The absence of fine-sized equiaxed austenite grains in the microstructure of that steel suggests that the presence of strain-induced precipitates is not decisive for the avoidance of dynamic recrystallization.

3.3. Analysis of Dynamic Recrystallization Onset

The deformation schedule specified in Figure 2a was designed to provoke dynamic recrystallization in the investigated steels. The resulting stress–strain curves in Figure 7a–c indicate that the peak stress was reached during the fifth deformation pass for the Nb-microalloyed steels and during the seventh deformation pass for the CMnMoB steel. The molybdenum-alloyed steels reached a higher peak stress than the CMnNbB steel. The stress–strain curve reveals a transition from continuous yielding to pronounced yielding in the second pass for the Nb-microalloyed steels. This could have been related to the strain-induced precipitation of Nb. The Nb-free steel only showed this yielding phenomenon during later passes. Potentially, Ti or B formed precipitates in that steel since molybdenum does not form carbides in austenite due to its good solubility. Analyzing the austenite grain structure after eight deformation passes (Figure 8a–c) revealed a fraction of extremely fine-sized equiaxed austenite grains within the pancaked austenite matrix of all steels, as indicated with red arrows in Figure 8a. The recrystallized austenite grains were clustered in areas where austenite pancakes were particularly thin. Apparently, molybdenum alloying could not completely prevent the initiation of dynamic recrystallization. However, molybdenum significantly suppressed the volume fraction of recrystallized austenite grains during the simulated plate rolling schedule (Figure 5).

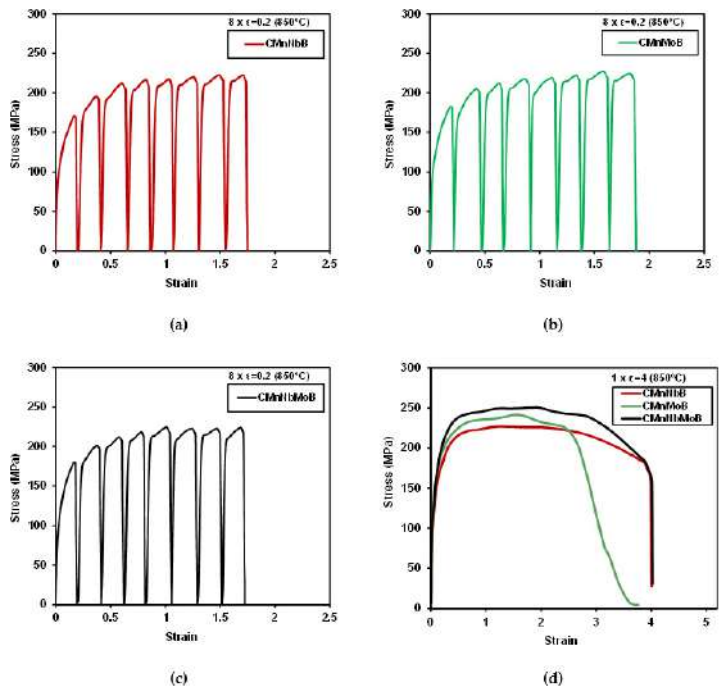


Figure 7. (a–c) Stress–strain curves for 8 deformation passes of $\epsilon = 0.2$ (CMnNbB, CMnMoB, and CMnNbMoB grades, respectively) and (d) one deformation pass of $\epsilon = 4$ at 850°C .

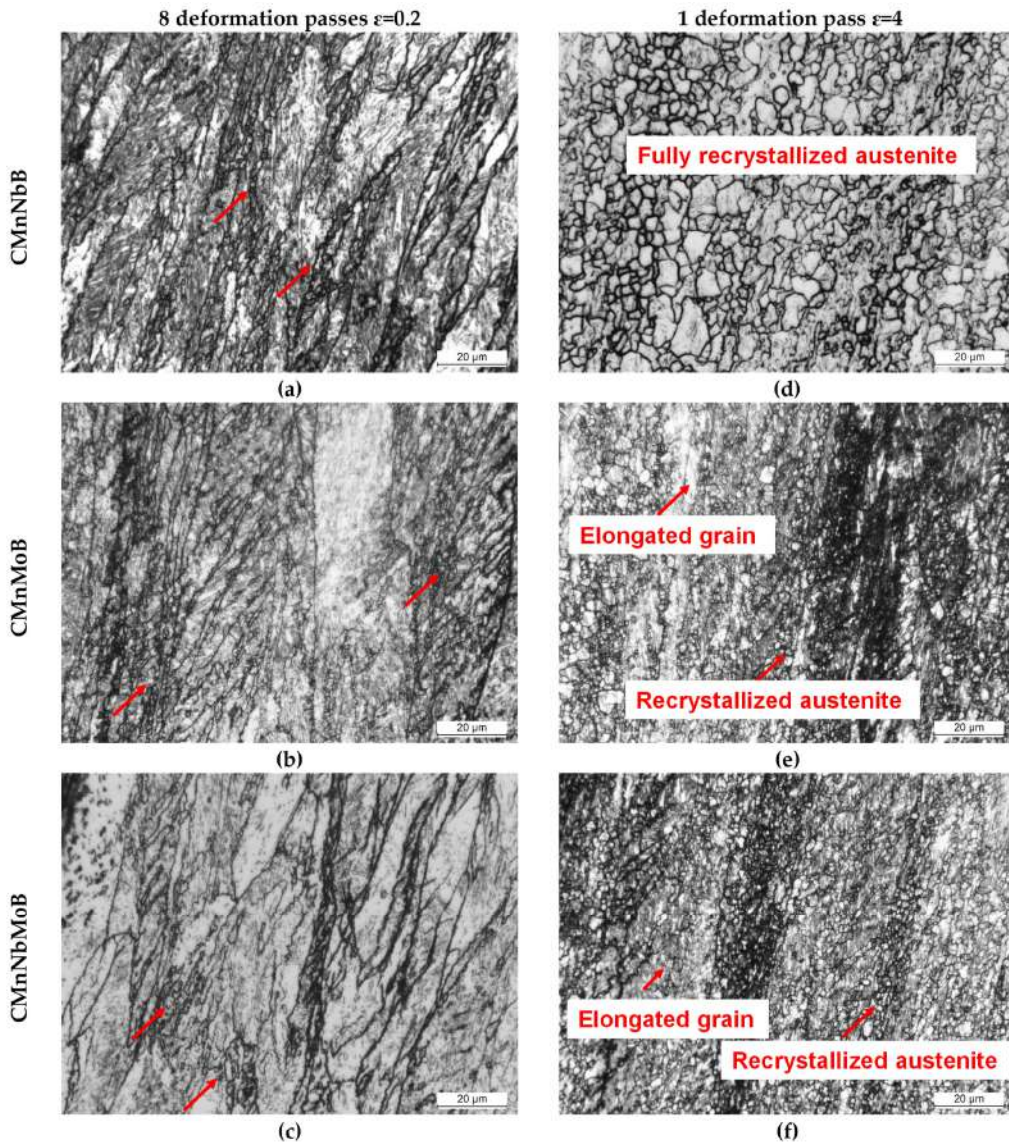


Figure 8. Optical images corresponding to the austenitic structure obtained after the thermomechanical cycle shown in Figure 2: (a–c) Roughing simulation and 8 deformation passes of 0.2 at 850 °C (see Figure 2a); (d–f) roughing simulation and 1 deformation pass of 4 at 850 °C (see Figure 2b). Dynamically recrystallized grains are indicated with red arrows.

This effect was further elucidated after applying a large strain during a single deformation pass according to Figure 2b. The stress–strain curves of all three steels reveal continuous yielding (Figure 7d). The mean flow stress increased in the order of CMnNbB,

CMnMoB, and CMnMoNbB steels. The austenite grain structure after the large deformation cycle (Figure 8d–f) reflected the nearly complete recrystallization in the CMnNbB steel, which showed fine-sized equiaxed grains with sizes of up to around 10 μm . The molybdenum-alloyed steels, however, presented a mixed microstructure consisting of elongated grains and recrystallized grains. The recrystallized grains were extremely fine-sized, typically smaller than 3 μm . This observation again indicates that molybdenum alloying did not completely prevent the initiation of dynamic recrystallization. For analyzing the critical strain triggering dynamic recrystallization, single pass deformation cycles were interrupted at lower strain values. Dynamically recrystallized grains were not found for a strain of $\epsilon = 1$ (Figure 9a,b). At the strain of peak stress, ϵ_p (being 1.26 and 1.30 for the CMnNbB and CMnNbMoB steels, respectively), dynamic recrystallization did occur (Figure 9c,d). The critical strain, ϵ_c , triggering dynamic recrystallization was determined to be 1.08 and 1.1 for the CMnNbB and CMnNbMoB steels, respectively. The ratio of critical strain to peak strain was around 0.85 for both steels; this ratio is in the range of those reported in the literature for C–Mn and microalloyed steels [12]. Thus, the critical strain was obviously not significantly influenced by molybdenum alloying. However, molybdenum appeared to strongly obstruct the nucleation and growth of austenite grains under dynamic recrystallization conditions.

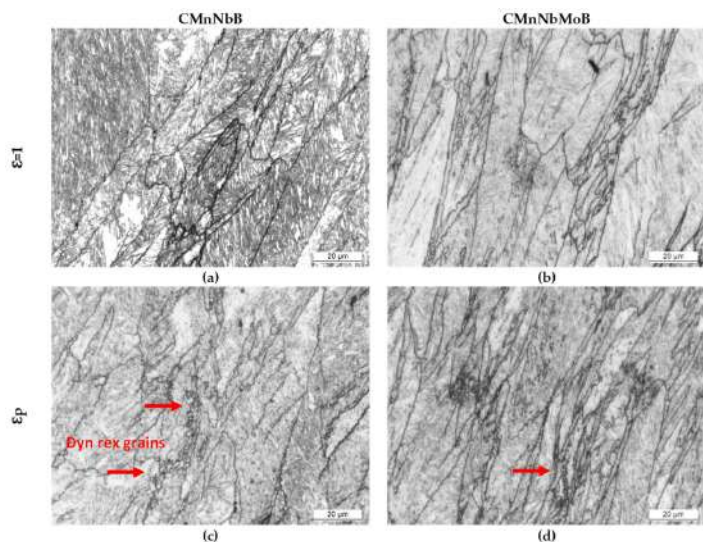


Figure 9. Optical micrographs after (a,b) $\epsilon = 1$ and (c,d) ϵ_p deformation passes for: (a,c) CMnNbB and (b,d) CMnNbMoB steel grades (dynamically recrystallized grains are indicated with red arrows).

4. Discussion

The kinetics of dynamic recrystallization is influenced by the initial austenite grain size and the Zener–Hollomon parameter defined as $Z = \dot{\epsilon} \exp(Q_{\text{def}}/RT)$, where Q_{def} is the activation energy, R is the gas constant, $\dot{\epsilon}$ is the strain rate, and T is the absolute temperature [13]. For coarse grain sizes, DRX kinetics is delayed due to the reduction of the amount of available nucleation sites as the grain boundary area per unit volume is decreased. No significant difference regarding the initial average austenite grain size after roughing simulation was observed in the studied steels. The measured values were approximately 50 μm in all steels. Therefore, the main influencing factor in the kinetics of DRX in the present experiments must have been the Zener–Hollomon parameter. Since the

strain rate and deformation temperature were equal in all experiments, the activation energy was the main criterion accounting for the observed differences. The solutes having variable influence on the activation energy were Nb and Mo. Most of the Ti was bound in TiN, and a residual fraction participated in strain-induced NbC particles, so the residual solute amount of Ti was negligibly small. Solute Mo is known to impede the movement of high angle grain boundaries due to solute drag [14]. Schambron et al. [15] experimentally demonstrated that the activation energy for DRX correlates with Mo content (in mass percent) by a factor of 323 kJ/mol. Hence, the studied Mo content of 0.5 mass% increased the activation energy by 160 kJ/mol. Niobium is considered the most potent element in retarding DRX by solute drag [13]. However, under the applied hot deformation conditions, Nb partially precipitated and thereby lowered its solute content. From previous experiments on the same steels, it was concluded that the amount of soluble Nb after quenching hot worked steel is below 0.01 mass%. Strain-induced precipitates, on the other hand, are not very effective in suppressing DRX. Accordingly, DRX is expected to more likely occur in the CMnNbB steel, in agreement with the present experimental observations. Boron has been claimed to facilitate a softening effect due to its non-equilibrium grain boundary segregation [16,17]. A similar effect must have occurred in all investigated steels because the boron content was nominally identical.

The T_{nr} temperatures for the current steels were previously determined as 955, 980, 1010, and 1024 °C for the CMnB, CMnNbB, CMnMoB, and CMnNbMoB steels, respectively [4]. Accordingly, all finishing temperatures shown in the current experiments were below T_{nr} . Though the Nb- and/or Mo-alloyed steels presented a pronouncedly pancaked austenite structure (Figure 5), the CMnB base steel comprised a completely equiaxed austenite microstructure with a generally fine average grain size (Figure 10). Due to this refinement, the total austenite grain boundary area per material volume was significantly increased. It was shown by de Rosa et al. [18] that boron segregation to austenite grain boundaries occurs extremely quickly and even during the quenching cycle. Several studies using atom probe tomography [19,20] have indicated a high concentration of boron in the immediate vicinity of austenite grain boundaries while the grain interior away from the boundaries becomes nearly depleted of boron. When boron segregation proceeds during austenite conditioning, additionally supported by a strong flux of vacancies towards the austenite boundaries, it is possible that no diffusible boron is left for covering the new austenite grain boundaries generated by dynamic recrystallization. Earlier investigations on the current and other boron-alloyed steels [2,6–8] revealed that the hardenability effect related to boron is weakened when applying substantial strain immediately before quenching. In CCT diagrams reported in the previous works, the ferrite and bainite phase fields are then shifted towards shorter times and higher transformation temperatures under direct quenching conditions.

In the CMnNbB steel, DRX fully occurred only when large strain ($\epsilon = 4$) was applied. Thus, under conditions representing a TMCP rolling schedule, pancaked grains with accumulated strain could coexist with fine-sized recrystallized grains. The strain accumulation increased the driving force for transformation while the recrystallized grain fraction was exposed to insufficient boron protection, as described before. The presence of ferrite colonies (Figure 3) in the former partially recrystallized austenite area indicated an early transformation, probably due to insufficient boron protection. The combination of both effects further extended the ferrite phase field under direct quenching conditions compared to completely recrystallized CMnB steel [6].

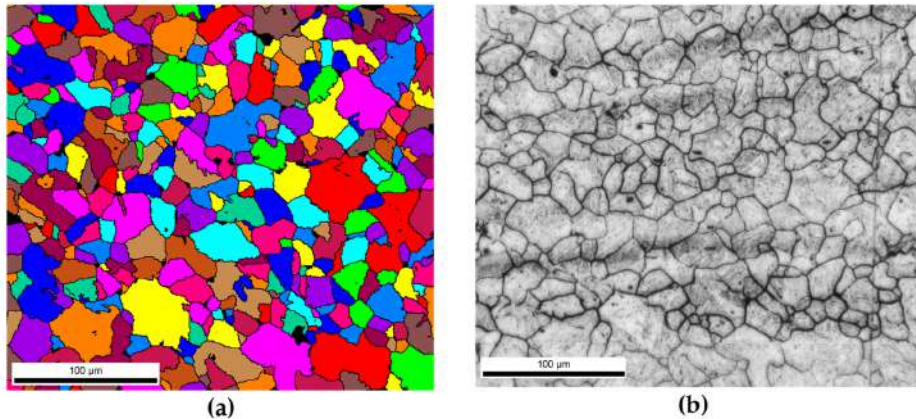


Figure 10. (a) Reconstructed austenite by EBSD and (b) optical image corresponding to austenite obtained after picric acid for CMnB steel grade.

The molybdenum-alloyed steels showed high strain accumulation without causing obvious dynamic recrystallization for the simulated rolling schedule (Figure 4). Their hardenability is much better than that of the Mo-free variants [6]. Ferrite formation was substantially retarded to a similar extent for direct quenching and conventional quenching conditions. That means the ferrite-suppressing effect of molybdenum was not measurably influenced by the presence of accumulated strain. This behavior is in good agreement with the results of Hannula et al. [7] who investigated the hardenability of very similar DQ steel alloys. Their results indicated the formation very fine-grained equiaxed austenite decorating the boundaries of much larger pancaked austenite grains when finish rolling at 800 °C. Such necklace structures gradually disappeared when molybdenum was added to the CMnB steel in amounts of 0.25 and 0.5 mass%. They were generally absent when applying less severe austenite pancaking and using a higher finish rolling temperature of 900 °C. However, despite severe pancaking and strain accumulation at the low finishing temperature, full hardenability was achieved in the molybdenum-alloyed steels in contrast to the CMnB steel. Like boron, molybdenum is strongly segregating at austenite grain boundaries [19,20]. Yet, a sufficiently high concentration level remained in the grain interior due to the comparably high molybdenum alloy addition. Accordingly, the Zener–Hollomon parameter had to have been significantly increased in the region near the grain boundary.

The micrographs of Figure 4 indicate that the austenite microstructure was not homogeneously deformed after the simulated rolling schedule but comprised a considerable range of austenite pancake thicknesses. Dynamic recrystallization was found to primarily initiate in the zones of most narrow pancakes. This was similar in all investigated steels (Figure 8a–c). The stress–strain curve for large deformation (Figure 7d) reveals that the stress initially increased to a relatively broad peak stress and then slowly declined to a steady state at large strain. In the steady state, the recrystallized grains generally grew in the CMnNbB steel, while they remained much finer in the molybdenum-alloyed steels (Figure 8 d–f). The observed features suggest geometric dynamic recrystallization (GDRX) as the acting mechanism [21]. In this mechanism, the impingement of serrated austenite pancake boundaries occurred when the pancake thickness approached 1–2 sub-grain size dimensions. Furthermore, the micrographs in Figure 9 indicate that GDRX did not instantaneously occur upon reaching the critical stress. The narrow ends of pancakes show the first appearance of ultrafine equiaxed grains in agreement with the model of de Pari and Misiolek [22], suggesting the gradual progress of GDRX with increasing strain. The steady state sub-grain size decreased with the increasing Zener–Hollomon parameter in

the molybdenum-alloyed steels compared to the CMnNbB steel. In areas where extremely thin pancakes were clustered prior to GDRX, the molybdenum concentration must have been increased due to the close proximity of boundary segregation profiles. Therefore, the recrystallized grain size remained smaller in these areas, while it was larger in areas of formerly thicker pancakes. Petterson et al. [23], using hot torsion tests, showed that the critical strain for GDRX is directly related to the initial grain size and inversely related to the sub-grain size. Both features were similar in the currently discussed steels, as were the observed critical strains regardless of the Zener–Hollomon parameter. The critical strain triggering GDRX under deformation in compression was indicated to become smaller than that in torsion [23], which is of relevance when considering industrial rolling.

The occurrence of partial GDRX before quenching has additional implications for martensitic transformation behavior. Experimental and theoretical studies [24–26] have indicated that the martensite-start temperature rapidly decreases for prior austenite grain sizes below 10 μm . Equiaxed grains originating from GDRX have sizes in the order of 1 μm and hence transform at lower temperature than surrounding austenite pancakes. The delayed transformation of the ultrafine austenite grains during quenching can thus lead to the buildup of residual stress because the dilatation caused by the martensitic transformation cannot be accommodated by plastic deformation in the previously transformed martensitic matrix. Such residual stresses typically result in unwanted quench distortion [27] and can have a negative impact regarding hydrogen-induced delayed cracking [28].

5. Conclusions

The current study has confirmed that dynamic recrystallization (DRX) can occur in direct quenching steels during austenite conditioning at low temperatures. After applying a typical TMCP deformation-temperature schedule to standard CMnB steel, DRX resulted in a fully equiaxed microstructure. The microalloying of niobium (0.026%) to such steel produced pancaked austenite with the localized appearance of very fine equiaxed austenite grains originating from DRX. The addition of molybdenum (0.5%) completely suppressed DRX under the same TMCP conditions. This effect of molybdenum was related to a significant increase of the Zener–Hollomon parameter.

Specific austenite conditioning, applying larger strain at low austenite temperature, demonstrated that the molybdenum-alloyed steel could experience DRX, resulting in ultrafine austenite grains. The progress of DRX and the austenite grain size was evidently smaller than in the niobium-microalloyed steel without molybdenum addition.

The initiation of DRX in the niobium- and molybdenum-added steels was related to the mechanism of geometrical DRX (GDRX). GDRX appeared to occur when the thickness of individual austenite pancakes was approaching the dimension of 1–2 sub-grains and proceeded gradually. Under a large single-pass strain ($\epsilon = 4$), DRX was completed in the Nb-microalloyed steel but not in the molybdenum-alloyed steels. The larger Zener–Hollomon parameter in the latter steels resulted in a smaller size of the recrystallized grains.

The presence of fine-grained austenite generated by DRX was shown to produce soft phases upon quenching under an industrial cooling rate of 30 $^{\circ}\text{C}/\text{s}$. It was argued that the sudden and late increase of the austenite grain boundary area caused by DRX could weaken the hardenability effect related to boron.

Molybdenum alloying acts twofold—by its high inherent hardenability effect and by avoiding DRX.

The presence of fine-grained austenite originating from DRX within a partially coarser microstructure is expected to cause non-synchronous martensite transformation, with the fine grains transforming at lower temperature. This phenomenon can induce residual stresses that lead to quench distortion and should be investigated in a dedicated study.

Author Contributions: I.Z. carried out the experiments and wrote the manuscript; N.I. supervised the results, analyzed the data and wrote the manuscript; E.D., V.S. and H.M. contributed to the interpretation of the data and edited the manuscript; P.U. managed the project and edited the manuscript. All authors have read and agreed to the published version of the manuscript.

Funding: This research received funding by the International Molybdenum Association (IMOA).

Institutional Review Board Statement: Not applicable.

Informed Consent Statement: Not applicable.

Data Availability Statement: The data presented in this study are available on request from the corresponding author. The data are not publicly available due to project confidentiality.

Acknowledgments: The authors would like to acknowledge the International Molybdenum Association (IMOA) for funding this project.

Conflicts of Interest: The authors declare no conflict of interest.

References

- Uranga, P.; Shang, C.-J.; Senuma, T.; Yang, J.-R.; Guo, A.-M.; Mohrbacher, H. Molybdenum alloying in high-performance flat-rolled steel grades. *Adv. Manuf.* **2020**, *8*, 15–34. [\[CrossRef\]](#)
- Hannula, J.; Kömi, J.; Porter, D.A.; Somani, M.C.; Kajjalainen, A.; Suikkanen, P.; Yang, J.R.; Tsai, S.P. Effect of Boron on the Strength and Toughness of Direct-Quenched Low-Carbon Niobium Bearing Ultra-High-Strength Martensitic Steel. *Metall. Mater. Trans. A* **2017**, *48*, 5344. [\[CrossRef\]](#)
- Zurutuza, I.; Isasti, N.; Detemple, E.; Schwinn, V.; Mohrbacher, H.; Uranga, P. Toughness Property Control by Nb and Mo Additions in High-Strength Quenched and Tempered Boron Steels. *Metals* **2021**, *11*, 95. [\[CrossRef\]](#)
- Zurutuza, I.; Isasti, N.; Detemple, E.; Schwinn, V.; Mohrbacher, H.; Uranga, P. Effect of Nb and Mo on austenite microstructural evolution during hot deformation in Boron high strength steels. *Metall. Mater. Trans. A* **2022**, *accepted*. [\[CrossRef\]](#)
- Bai, D.Q.; Yue, S.; Maccagno, T.M.; Jonas, J.J. Effect of Deformation and Cooling Rate on the Microstructures of Low Carbon Nb–B Steels. *ISIJ Int.* **1998**, *38*, 371–379. [\[CrossRef\]](#)
- Zurutuza, I.; Isasti, N.; Detemple, E.; Schwinn, V.; Mohrbacher, H.; Uranga, P. Effect of Quenching Strategy and Nb-Mo Additions on Phase Transformations and Quenchability of High-Strength Boron Steels. *JOM* **2021**, *73*, 3158–3168. [\[CrossRef\]](#)
- Hannula, J.; Porter, D.A.; Kajjalainen, A.; Kömi, J. Evaluation of Mechanical Properties and Microstructures of Molybdenum and Niobium Microalloyed Thermomechanically Rolled High-Strength Press Hardening Steel. *JOM* **2019**, *71*, 2405–2412. [\[CrossRef\]](#)
- Ali, M.; Nyo, T.; Kajjalainen, A.; Javaheri, V.; Tervo, H.; Hannula, J.; Kömi, J. Incompatible effects of B and B+Nb additions and inclusions characteristics on the microstructures and mechanical properties of low-carbon steels. *Mater. Sci. Eng. A* **2021**, *819*, 141453. [\[CrossRef\]](#)
- Sanz, L.; López, B.; Pereda, B. Characterization of Austenite Microstructure from Quenched Martensite Using Conventional Metallographic Techniques and a Crystallographic Reconstruction Procedure. *Metals* **2018**, *8*, 294. [\[CrossRef\]](#)
- Sanz, L.; Pereda, B.; López, B. Validation and Analysis of the Parameters for Reconstructing the Austenite Phase from Martensite Electron Backscatter Diffraction Data. *Metall. Mater. Trans. A* **2017**, *48*, 5258–5272. [\[CrossRef\]](#)
- Pavlina, E.J.; Speer, J.G.; Van Tyne, C.J. Equilibrium solubility products of molybdenum carbide and tungsten carbide in iron. *Scr. Mater.* **2012**, *66*, 243–246. [\[CrossRef\]](#)
- Bellavoine, M.; Dumont, M.; Drillet, J.; Hébert, V.; Maugis, P. Combined Effect of Heating Rate and Microalloying Elements on Recrystallization During Annealing of Dual-Phase Steels. *Metall. Mater. Trans. A* **2018**, *49*, 2865–2875. [\[CrossRef\]](#)
- Fernandez, A.I.; Uranga, P.; López, B. Dynamic Recrystallization behaviour covering a wide austenite grain size range in Nb and Nb-Ti microalloyed steels. *Mater. Sci. Eng. A* **2003**, *361*, 367–376. [\[CrossRef\]](#)
- Pereda, B.; Fernández, A.I.; López, B.; Rodríguez-Ibabe, J.M. Effect of Mo on Dynamic recrystallization behavior of Nb-Mo microalloyed steels. *ISIJ Int.* **2007**, *47*, 860–868. [\[CrossRef\]](#)
- Schambron, T.; Dehghan-Manshadi, A.; Chen, L.; Gooch, T.; Killmore, C.; Pereloma, E. Effect of Mo on Dynamic Recrystallization and Microstructure Development of Microalloyed Steels. *Met. Mater. Int.* **2017**, *23*, 778–787. [\[CrossRef\]](#)
- López-Chipres, E.; Mejía, I.; Maldonado, C.; Bedolla-Jacuinde, A.; El-Wahabi, M.; Cabrera, J.M. Hot flow behavior of boron microalloyed steels. *Mater. Sci. Eng. A* **2008**, *480*, 49–55. [\[CrossRef\]](#)
- Gao, Y.L.; Xue, X.X.; Yang, H. Effect of boron concentration on dynamic recrystallization behavior of low-carbon steel. *Acta Metall. Sin. Engl. Lett.* **2015**, *28*, 931–939. [\[CrossRef\]](#)
- Da Rosa, G.; Maugis, P.; Portavoce, A.; Drillet, J.; Valle, N.; Lentzen, E.; Hoummada, K. Grain-boundary segregation of boron in high-strength steel studied by nano-SIMS and atom probe tomography. *Acta Mater.* **2020**, *182*, 226–234. [\[CrossRef\]](#)
- Li, Y.J.; Ponge, D.; Choi, P.; Raabe, D. Segregation of boron at prior austenite grain boundaries in a quenched martensitic steel studied by atom probe tomography. *Scr. Mater.* **2015**, *96*, 13–16. [\[CrossRef\]](#)
- Mohrbacher, H.; Senuma, T. Alloy optimization for reducing delayed fracture sensitivity of 2000 MPa press hardening steel. *Metals* **2020**, *10*, 853. [\[CrossRef\]](#)
- Huang, K.; Logé, R.E. A review of dynamic recrystallization phenomena in metallic materials. *Mater. Des.* **2016**, *111*, 548–574. [\[CrossRef\]](#)
- De Pari, L., Jr.; Misiolek, W.Z. Theoretical predictions and experimental verification of surface grain structure evolution for AA6061 during hot rolling. *Acta Mater.* **2008**, *56*, 6174–6185. [\[CrossRef\]](#)

23. Pettersen, T.; Holmedal, B.; Nes, E. Microstructure development during hot deformation of aluminum to large strains. *Metall. Mater. Trans. A* **2003**, *34*, 2737–2744. [[CrossRef](#)]
24. García-Junceda, A.; Capdevila, C.; Caballero, F.G.; De Andres, C.G. Dependence of martensite start temperature on fine austenite grain size. *Scr. Mater.* **2018**, *58*, 134–137. [[CrossRef](#)]
25. Yang, H.S.; Bhadeshia, H.K.D.H. Austenite grain size and the martensite-start temperature. *Scr. Mater.* **2009**, *60*, 493–495. [[CrossRef](#)]
26. Guimarães, J.R.C.; Rios, P.R. Martensite start temperature and the austenite grain-size. *J. Mater. Sci.* **2010**, *45*, 1074–1077. [[CrossRef](#)]
27. Tobie, T.; Hippenstiel, F.; Mohrbacher, H. Optimizing gear performance by alloy modification of carburizing steels. *Metals* **2017**, *7*, 415. [[CrossRef](#)]
28. Eliaz, N.; Shachar, A.; Tal, B.; Eliezer, D. Characteristics of hydrogen embrittlement, stress corrosion cracking and tempered martensite embrittlement in high-strength steels. *Eng. Fail. Anal.* **2002**, *9*, 167–184. [[CrossRef](#)]



ADVANCED HIGH-STRENGTH STEELS

Effect of Quenching Strategy and Nb-Mo Additions on Phase Transformations and Quenchability of High-Strength Boron Steels

IRATI ZURUTUZA,^{1,2} NEREA ISASTI,^{1,2} ERIC DETEMPLE,³
 VOLKER SCHWINN,³ HARDY MOHRBACHER,^{4,5}
 and PELLO URANGA ^{1,2,6}

1.—Materials and Manufacturing Division, CEIT-Basque Research and Technology Alliance (BRTA), 20018 Donostia/San Sebastián, Basque Country, Spain. 2.—Mechanical and Materials Engineering Department, Universidad de Navarra, 20018 Donostia/San Sebastián, Basque Country, Spain. 3.—AG der Dillinger Hüttenwerke, 66763 Dillingen/Saar, Germany. 4.—NiobelCon BV, 2970 Schilde, Belgium. 5.—Department of Materials Engineering (MTM), KU Leuven, 3001 Leuven, Belgium. 6.—e-mail: puranga@ceit.es

The application of direct quenching after hot rolling of plates is being employed in the production of ultra-high-strength hot rolled plates. When heavy gauge plates are produced, the complexity involve in achieving high cooling rates in the plate core is increased and the formation of undesirable soft phases within martensite is common. In the current paper, both direct quenching and conventional quenching (DQ and CQ) processing routes were reproduced by dilatometry tests and continuous cooling transformation (CCT) diagrams were built for four different high-strength boron steels. The results indicate that the addition of Mo and Nb-Mo suppresses the ferritic region and considerably shifts the CCT diagram to lower transformation temperatures. The combination of DQ strategy and the Mo-alloying concept provides the best option to ensure hardenability and the formation of a fully martensitic microstructure, and to avoid the presence of soft phases in the center of thick plates.

INTRODUCTION

The practice of direct quenching (DQ) after hot rolling is gaining importance in industry in the production of high-strength plates.¹ The DQ process avoids the re-austenitization step that is usual for the conventional quenching (CQ) procedure, enabling significant energy savings to be made, and leading to economic benefits and productivity improvements.^{2–4} In CQ, the rolled material is cooled down to room temperature and reheated before being quenched. However, DQ strategy is based on the application of fast cooling immediately after a thermomechanically controlled hot rolling process. This is an efficient process used to improve the strength and toughness of steels by pancaking the austenite below the recrystallization stop tem-

perature (RST) prior to quenching.⁵ In addition, given that the reheating process is obsolete, DQ strategy could prove to be beneficial in preserving microalloying elements in solid solution that in turn could precipitate during subsequent tempering treatment.⁵ The main objective of DQ is to create entirely martensitic microstructures by applying the highest possible cooling rate. Although cooling rates above 100°C/s could be reached through current cooling facilities, the effective cooling rate for thicker gauges at the plate core is considerably lower and so ensuring full martensitic structures throughout the thickness becomes challenging.⁶ Therefore, depending on rolling conditions and the alloy concept, there may be a risk of forming undesirable soft phases such as ferrite and bainite. Furthermore, residence time in the cooling device may be excessively long in the case of thicker

(Received March 18, 2021; accepted June 18, 2021;
 published online July 6, 2021)

gauges, lowering the output of the rolling mill. In this case, applying the CQ process might prove to be economically more attractive.

Alloying with molybdenum and/or boron effectively helps reduce the critical cooling speed for martensite formation, while the combined addition of microalloying elements such as Ti, Nb, Mo, and B to carbon steels may provide an increase in strength through microstructural refinement and precipitation hardening as well as hardenability and final microstructural modification.⁷⁻⁹ The use of B as an alloying element increases strength by obstructing ferrite nucleation at austenite grain boundaries, thus encouraging the formation of bainitic/martensitic microstructures even at low cooling rates.¹⁰ The combined addition of B and Nb as well as Mo in turn encourages the segregation of boron into the austenite grain boundaries, thus ensuring the effectiveness of boron with regard to hardenability.¹¹⁻¹⁴ Microalloying of Nb is standardly used for retarding austenite recrystallization during rolling, both by solute drag and by strain-induced precipitation.^{15,16} This leads to an accumulation of deformation in austenite, ensuring grain size refinement of the final microstructure and improving mechanical properties.¹⁷ Molybdenum alloying increases strength and toughness properties in carbon steels due to the effect it has on encouraging the formation of low-temperature transformation products such as bainite and martensite,¹⁸ and by avoiding temper embrittlement. Besides the direct effects of molybdenum, the combination of Nb and Mo leads to pronounced synergetic effects, while Mo significantly contributes to austenite pancaking by solute drag during hot rolling. This effect is even greater in combination with niobium, as the martensitic substructures are formed in the previously pancaked austenite grains,^{6, 19,20} combining drag and strain-induced precipitation mechanisms. Molybdenum also delays precipitation of niobium during austenite conditioning, making a higher amount of solute niobium available for precipitation during tempering treatment.

Recently, the impact of adding Nb and Mo to the microstructure and tensile/toughness properties was evaluated in high-strength quenched and tempered boron steels.^{21,22} In these studies, the addition of 0.5% Mo to a 0.16% CMnB base alloy was proven to be crucial in ensuring yield strength values above 900 MPa and low ductile-to-brittle transition temperatures after direct quenching and tempering treatment (600°C during 300 s). The results shown in references²¹ and²² suggest that the most relevant contribution to strength and toughness was related to microstructural refinement. Additional refinement is associated with austenite conditioning, which can be achieved by combining Mo with 0.025% Nb.

Given that direct quenching is a relatively new process in plate production, the metallurgical effects of Mo and Nb alloying on high-strength direct-

quenched boron steels have not been widely reported in the literature and further knowledge regarding its effect on phase transformation is needed. To this end, DQ and CQ strategies were simulated by dilatometry tests in the current study. Continuous cooling transformation (CCT) diagrams were derived for all compositions and the impact of thermomechanical treatment on phase transformation, the resulting microstructure and hardness was evaluated accordingly. Finally, the feasibility of the direct quenching strategy was evaluated, and the optimum alloy concept/thermomechanical cycle selected.

EXPERIMENTAL PROCEDURE

Four carbon steels containing 0.16% C and 20 ppm boron were selected, three of them microalloyed with Nb, Mo, and NbMo. The Nb level was 0.026% and Mo content 0.5%. All the steels were alloyed with Ti to ensure the full effect of boron. Table I shows the chemical composition of the steels.

Uniaxial compression tests were performed in a Bähr DIL805A/D quenching and deformation dilatometer, with solid cylinders of 5 mm in diameter and 10 mm in length being used. The specimens were subjected to two different thermomechanical schedules (direct quenching and conventional quenching) in order to simulate different rolling and cooling strategies, represented schematically in Fig. 1. Both cycles included reheating treatment at 1200°C for 10 min followed by two deformation passes of a 0.3 strain and at a strain rate of 1 s^{-1} at 1175°C and 1050°C, in order to obtain a fine recrystallized austenite. As for the direct quenching (DQ) cycle (Fig. 1a), a third deformation pass of $\epsilon = 0.3$ was applied below the non-recrystallization temperature at 870°C, with the aim of accumulating deformation in the austenite prior to phase transformation. Finally, continuous cooling was applied ranging from 0.1°C/s to maximum cooling (0.1°C/s, 0.5°C/s, 1°C/s, 2°C/s, 5°C/s, 10°C/s, 20°C/s, 50°C/s, 100°C/s and maximum cooling). Regarding conventional quenching strategy (CQ), following the first two deformation passes at 1175°C and 1050°C, the specimens were then cooled down slowly (1°C/s) to room temperature. Afterwards, a second austenitization treatment was

Table I. Chemical composition of the steels studied (wt.%)

Steel	C	Si	Mn	Mo	Nb	B
CMnB	0.15	0.32	1.05	–	–	0.0022
CMnNbB	0.16	0.29	1.05	–	0.026	0.0019
CMnMoB	0.16	0.28	1.07	0.5	–	0.0022
CMnNbMoB	0.16	0.31	1.07	0.5	0.026	0.0018

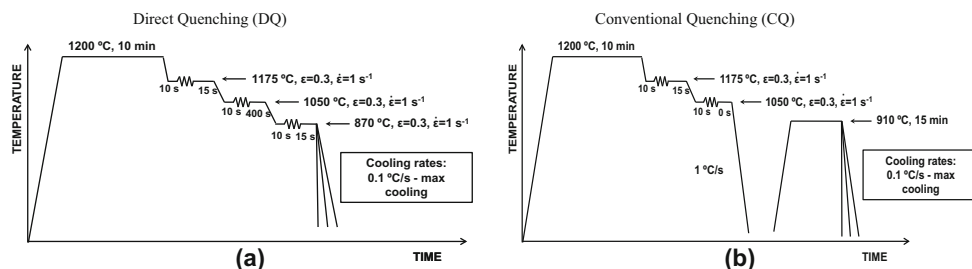


Fig. 1. Thermomechanical schedules. (a) Direct quenching and (b) conventional quenching performed using the dilatometer.

applied at 910 °C for 15 min and, finally, controlled cooling was applied at cooling rates from 0.1 °C/s to maximum cooling.

Initial and final transformation temperatures were calculated from the dilatation curves,²³ and the lever rule was applied to the dilatometry curves in order to measure evolution of the transformed fraction.²⁴ This rule relies on extrapolating the linear expansion behavior from the temperature regions where no transformation occurs and subsequently assuming proportionality between the fraction of decomposed austenite and the length change observed.²⁵ In the current study, the transformation start and finish temperatures were defined as being represented at 5 and 95% transformed fractions, while for their part, the dilatometry specimens were sectioned along their longitudinal axis by selecting the region corresponding to a maximum area fraction of nominal strain and reduced strain gradient.^{25,26}

The transformed microstructures obtained from the dilatometry samples were etched in 2% Nital and the austenite prior to transformation was revealed by etching in a solution of saturated picric acid and HCl. Samples were characterized by optical microscopy (OM, LEICA DM15000 M, Leica microsystems) and field-emission gun scanning electron microscopy (FEGSEM, JEOL JSM-7100F). In addition, the austenite grain sizes prior to transformation were measured using the mean equivalent diameter method, with all specimens finally undergoing the Vickers hardness test, using a 1-kg load.

RESULTS AND DISCUSSION

Phase Transformations

Austenite Conditioning

Table II summarizes the austenite grain size parameters measured for all chemical compositions and thermomechanical cycles. Together with the average grain size, D_v , calculated as the average equivalent area diameter, values for surface area

per unit volume, S_v , and grain thickness (for DQ cycles) values were also reported. In the case of direct quenched CMnB steel, the austenitic structure could not be properly reconstructed, due to the formation of a bainitic/martensitic microstructure rather than a fully martensitic one. Consequently, a reliable austenite grain size measurement was not possible in that case. In the case of all alloys and in terms of D_v , the DQ process results in coarser mean austenite grain size than in the CQ process. After DQ processing, austenite morphology in the Mo and Nb alloyed steels is pancaked, whereas this is rather equiaxed in the case of the CMnB base alloy. This results in closest values for both S_v and thickness measurements, especially in the case of Mo bearing grades. Conversely, the CQ process normalizes the microstructure, leading to equiaxed austenite grain morphology in all steel alloys subject to research. The re-austenitizing condition applied in the current study (910 °C/900 s) prevents significant austenite grain growth before quenching, resulting in relatively smaller average austenite grain size. Furthermore, the addition of molybdenum causes a significant reduction in mean austenite grain size in the DQ processed steels. This is related to more pronounced pancaking of the austenite due to strong solute drag by molybdenum during austenite conditioning. In CQ processed steels, however, molybdenum alloying appears to have the opposite effect, as the average austenite grain size is slightly larger than in the Mo-free steels. On one side, boron segregation at the grain boundary suppresses nucleation of the new phase by reducing the grain boundary energy. On the other side, molybdenum reduces the interface mobility between ferrite and austenite.²⁷ During re-transformation, austenite nucleates from carbon-rich phase (pearlite) and at grain boundaries, especially at triple points. If the latter is delayed due to solute boron and low interface mobility, the nuclei from the carbon-rich phase have more room to grow by experiencing less growth competition. The reduction of grain size at higher austenite temperature can be due to Mo

Table II. Austenite grain quantification for all steel grades and thermomechanical cycles

Steel	DQ			CQ	
	D_7 (μm)	S_v (μm^{-1})	Thickness (μm)	D_7 (μm)	S_v (μm^{-1})
CMnB	–	–	–	19 ± 1	0.10
CMnNbB	45 ± 5	0.04	37 ± 4	23 ± 2	0.11
CMnMoB	32 ± 3	0.07	23 ± 2	25 ± 2	0.10
CMnNbMoB	32 ± 4	0.07	22 ± 2	25 ± 2	0.07

solute drag, as was demonstrated by Militzer et al.²⁸ However, this requires molybdenum to diffuse sufficiently to the austenite grain boundaries, which depends on the diffusional range at a given re-heat temperature and time. For the reheating conditions in the current manuscript, the diffusional range is much too small in comparison with grain diameters, so this effect could be negligible. It should be noted that industrially practiced re-austenitizing conditions typically use somewhat higher temperatures and longer times. Niobium microalloying was found to be very effective in limiting austenite grain coarsening by boundary pinning under such treatment conditions, having a beneficial effect on toughness of the quenched steel.²⁹

Final Microstructure and Vickers Hardness

Figure 2 shows an example of the microstructures obtained by optical and FEGSEM microscopy of the CMnMoB steel after DQ processing and cooling rates of 0.1°C/s, 5°C/s, and 50°C/s. The lowest cooling rate (0.1°C/s) produces a microstructure that mainly contains ferrite and bainite (see Fig. 2a). Ferrite formation is suppressed at higher cooling rates in the case of this particular steel. Second phases such as MA islands and pearlite are dispersed in the ferrite matrix (Fig. 2d) at a slow cooling rate, while when an intermediate cooling rate of 5°C/s is applied, the microstructure becomes predominantly bainitic (see Fig. 2b and e). From a cooling rate of 50°C/s the microstructure becomes fully martensitic (Fig. 2c and f), with this microstructural evolution generally being similar among all the steels and cycles applied, albeit with significant differences regarding the critical cooling rates required to induce the microstructural changes observed.

Analysis of the hardness evolution as a function of the cooling rate (Fig. 3) identifies two plateaus and a transition range. At low cooling rates, the hardness is on a low level and only slightly increasing with the cooling rate, whereas hardness saturates on an upper plateau at higher cooling rates. The maximum hardness of full martensite with a carbon content of 0.15% is calculated to be around 465 HV,²⁹ while the upper plateau value approaches 420 HV, remaining below the calculated maximum—likely due to self-tempering. In the case of the Mo-alloyed steels, the plateau values are

lower following the CQ process than after the DQ process. The CMnMoB steel clearly achieves the highest hardness at a given cooling rate irrespective of the process variant, and the critical cooling rates marking the end of the lower plateau as well as the onset of the upper plateau are significantly lowered by alloying of the molybdenum. In the case of CMnMoB steel cooling rates above 20°C/s, the formation of a fully martensitic microstructure is established, and in that of the NbMo grade, lower hardness values are measured than for Mo steel. When Nb is added to a Mo microalloyed steel, higher strain accumulation is achieved in the austenite, leading to an increase in the ferrite nucleation sites, which encourages a faster nucleation of the bainitic laths and increases the critical cooling rate required to obtain pure martensite. As for the CMnB and CMnNbB steels, a gradual change from ferrite-pearlite microstructures to more bainitic ones causes a slight hardness increment for cooling rates up to 20°C/s, although rates above 100°C/s are needed to obtain a fully martensitic microstructure in the Mo-free steels. In the case of the CMnMoB steel and cooling rates above 20°C/s, the hardness remains almost constant (around 420 HV), this being attributed to the formation of a fully martensitic microstructure. Therefore, the addition of molybdenum decreases the critical cooling rate in order to create martensitic microstructures.

From a practical point of view, hardness after direct or conventional quenching will be lower in industrial samples due to two factors. First, as final plate thickness increases the through-thickness temperature gradients and cooling rate differences from surface to center will be higher. Second, the auto-tempering process will be enhanced in thicker gauges, reducing the hardness levels in quenched samples towards the centerline areas.

Alloy and Processing Effects on CCT Diagrams

Figure 4 shows CCT diagrams for all the alloys subject to research and both quenching processes. The molybdenum alloyed steels reveal a clear shift of the ferrite phase field towards longer times, and the bainite phase field is also depressed. It is important to note that boron microalloying by itself cannot fully prevent ferrite formation in these steels at technically realistic cooling rates, as only in combination with molybdenum alloying can there be

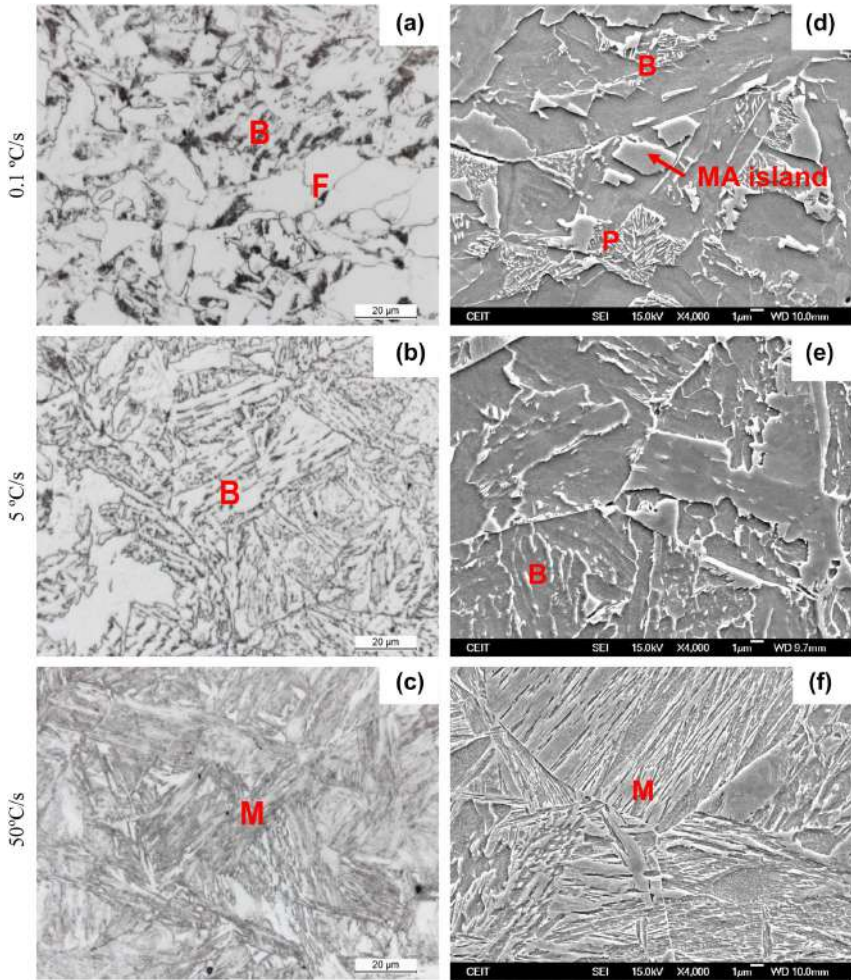


Fig. 2. Optical (a–c) and FEGSEM (d–f) micrographs of the CMnMoB steel grade after direct quenching.

sufficient suppression of ferrite nucleation. The major impact of molybdenum alloying on hardenability relies on two effects. Firstly, molybdenum reduces the nucleation rate of allotriomorphic ferrite somewhat independently of temperature in the range of diffusional transformations, as demonstrated by Kinsman and Aaronson.³⁰ Secondly, a major solute drag effect acts on the carbon-rich interphase boundaries that attract molybdenum, due to its high binding energy with carbon.

The segregation of solute B atoms at the austenite grain boundaries also efficiently suppresses the nucleation of allotriomorphic ferrite, although this effect is lost when boron forms $Fe_{23}(C, B)_6$ or Fe_2B precipitates.^{12–14} The formation of such boride precipitates is encouraged by higher boron addition; therefore, the optimum boron addition range for hardenability is particularly narrow, namely 5–15 ppm, and the boron addition of 20 ppm in these steels already carries the risk of $Fe_{23}(C, B)_6$ precipitation. Recent work by Ishikawa et al.³¹ has

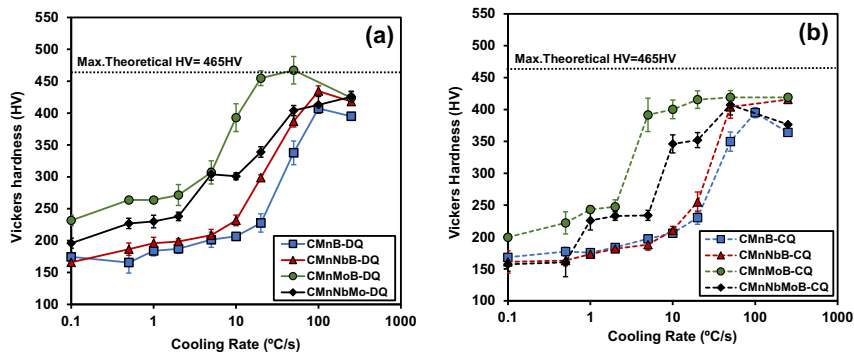


Fig. 3. Vickers hardness as a function of cooling rate for (a) direct quenching (DQ) and (b) conventional quenching (CQ) cycles.

indicated that the addition of 20 ppm B to 0.15% C-Mn steel reduces the critical cooling rate to around 50 °C/s in Mo-free steel under CQ conditions, this being in line with current data. For its part, the addition of 0.5% Mo was shown to reduce the critical cooling rate to below 20 °C/s, which is also congruent with current data, while the hardenability synergy between the two alloying elements was noted in the fact that molybdenum additions below 0.75% suppress precipitation of $Fe_{23}(C, B)_6$.³¹

The formation of carbon-rich phases such as pearlite and MA particles can only be observed for the slowest cooling rates in Mo-free steels. For its part, the diffusion-based partitioning of carbon required is greatly suppressed by the presence of molybdenum and, hence, pearlite does not form in Mo-alloyed steels.

The effect of niobium microalloying on transformation behavior is ambiguous as, on the one hand, niobium that remains solute in austenite after hot rolling is known to lower the transformation temperature, encouraging the formation of bainite or acicular ferrite; on the other hand, accumulated strain energy related to the recrystallization-inhibiting effect of niobium is a driving force behind accelerated transformation. In a recent study on the same steels,²² it was also shown that severe austenite conditioning that triggers dynamic recrystallization results in austenite grain boundaries being insufficiently protected by segregated boron, while the addition of molybdenum was found to suppress dynamic recrystallization.

In the present CCT diagrams it is evident that Nb microalloying in the DQ process encourages ferrite formation more than CMnB steel (Fig. 4a versus b). Similarly, for the CQ cycle, the ferritic formation is suppressed for lower cooling rates in CMnB steel than for CMnNb steel (Fig. 4e versus f). In the Mo+Nb alloyed steel under DQ processing conditions, early ferrite formation is also completely

suppressed (Fig. 4b versus d), whereas the bainite start temperature is increased, and the nose is shifted towards shorter times when compared with the Mo-only steel (Fig. 4d versus c). The same comparison under CQ processing conditions indicates that the bainite phase fields are nearly identical and that only the ferrite phase field is moved to shorter times (Fig. 4g versus h).

In a previous paper, activation of dynamic recrystallization was reported in the case of CMnNbB steel,²² with formation of these recrystallized grains during deformation at low temperatures, leading to the transformation from austenite to polygonal ferritic grains in a bainitic matrix. Even if deformation below T_{nr} is lower in this case, similar mechanisms could be the source of the effects observed in the DQ process. The co-addition of molybdenum successfully suppresses dynamic recrystallization and thus prevents early ferrite formation. However, the strain accumulation still encourages bainite formation, while in the CQ process strain accumulation is absent. Unlike molybdenum at the current addition level, niobium does precipitate during the CQ reheating cycle to near completeness, while moderately accelerated ferrite formation in Nb microalloyed steels is potentially caused by co-precipitation of boron with niobium. For its part, niobium has the capacity to form NbB_2 precipitates which are stable at austenitizing temperature,³² although a detailed analysis using high-resolution TEM and atom probe tomography would be needed to confirm this assumption.

Effect of Quenching Process on Quenchability

It was evidently demonstrated that the addition of Mo is crucial for increasing hardenability and ensuring fully martensitic microstructures after quenching. Fig. 5 shows the comparison between the CCT diagrams corresponding to the CMnB and CMnMoB steels and DQ process. In the case of the

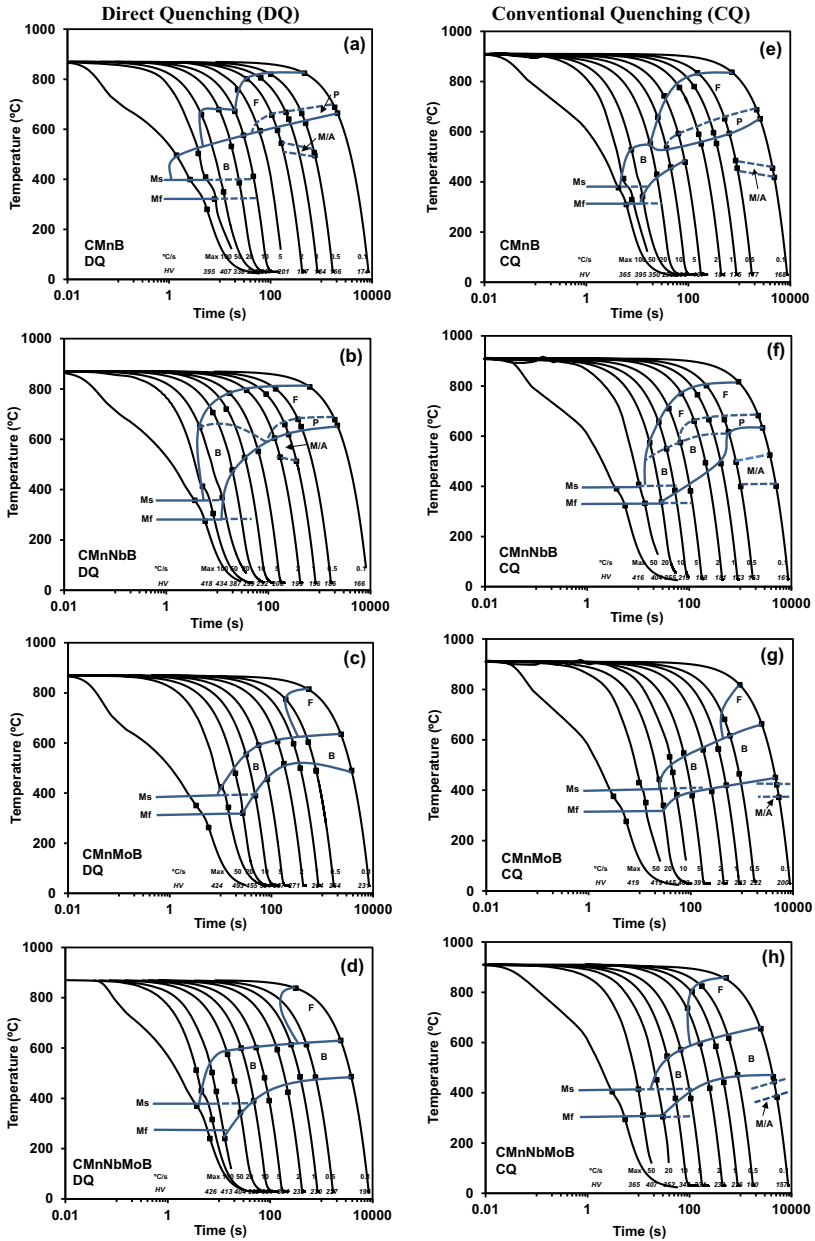


Fig. 4. CCT diagrams corresponding to (a, e) CMnB, (b, f) CMnNbB, (c, g) CMnMoB and (d, h) CMnNbMoB steels obtained from DQ (a–d) and CQ (e–h) cycles.

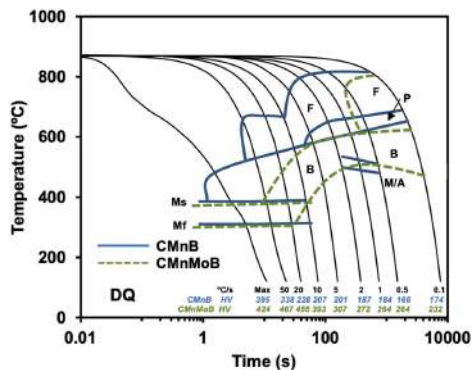


Fig. 5. Comparison between CCT diagrams corresponding to CMnB and CMnMoB steels and the direct quenching (DQ) cycle.

CMnB steel, bainitic-martensitic microstructures are formed, and a fully martensitic microstructure cannot be ensured even though maximum cooling is applied. However, in the case of the Mo steel, the martensitic phase becomes dominant at cooling rates above 20°C/s. Therefore, at 50°C/s, a significantly harder microstructure is formed in the case of Mo-alloyed steel compared with CMnB base steel (467 HV versus 338 HV), this being associated with the formation of martensite instead of bainite.

During industrial production of thick plates, the cooling rate in the center of the plate thickness will be significantly slower than at the surface of the plate, even though accelerated cooling is applied. For a typical final plate thickness in the range of 15–20 mm, the cooling rate is expected to vary between 20°C/s and 50°C/s. Thus, Fig. 6a shows the effect of chemical composition on the evolution of a transformed fraction for a cooling rate of 20°C/s in order to evaluate the feasibility of the different alloy concepts used in DQ processing. This is supported by Fig. 6b–e, which shows optical micrographs of the respective final microstructures.

The highest transformation temperatures are observed in the CMnB steel. When Nb is added, the transformation kinetics are initially similar to that of the CMnB steel, while with progressive transformation, the rate becomes increasingly delayed, shifting the microstructure to a higher fraction of bainite (Fig. 6b versus c). Alloying of 0.5% molybdenum shifts the transformation curve by approximately 200°C towards lower temperatures. The martensite start temperature for the current alloys was calculated to be around 440 °C, with molybdenum alloying having only a marginal impact.³³ Thus, the CMnMoB steel almost completely transforms below the martensite start temperature while nonetheless experiencing some self-tempering. For its part, the CMnMoNbB steel shows a fraction of about 20% transformation in

the bainite region, before martensite transformation starts. This is also reflected in the micrographs (Fig. 6d versus e), insofar as hardness measurements of these microstructures resulted in values of 227.7 HV, 298.7 HV, 454.7 HV, and 339 HV for the CMnB, CMnNbB, CMnMoB, and CMnNbMoB steels, respectively. The value of the fully martensitic CMnMoB steel is thus slightly below the theoretical maximum hardness of 465 HV of martensite containing 0.15% C, due to self-tempering.

The effect of the quenching process on the transformation start temperatures is evaluated in Fig. 7, in order to define appropriate processing windows for full martensite transformation. In this figure, the effect of the cooling rate on transformation start temperature is only considered in the case of intermediate and high cooling rates (above 10°C/s). In the case of the CMnB grade, a completely martensitic microstructure is only obtained by the CQ process and then for cooling rates above 100°C/s. In CMnNbB steel, martensite formation requires cooling rates above 50°C/s in the CQ process and 100°C/s in the DQ process. Such high cooling rates are, however, not obtainable under industrial conditions, especially when heavier plate gauges are being produced. With the addition of 0.5% Mo, the critical cooling rate required for full martensite formation is reduced to much lower values of between 20 and 30°C/s for both DQ and CQ processes, with the combined addition of Nb and Mo suppressing the formation of ferrite for all cooling rates above 10°C/s (Fig. 7d). With the DQ process, this alloy encourages partial bainite formation for industrially relevant cooling rates, resulting in a bainite-martensite mixed microstructure. The transformation start temperatures observed in Fig. 7 are in agreement with the Vickers hardness evolution as a cooling rate function, as shown in Fig. 3.

CONCLUSION

This study analyzed the phase transformation behavior of 0.15% C-MnB steels that simulate direct (DQ) and conventional (CQ) quenching processes, in the course of which it became evident that boron microalloying would be insufficient for the purpose of obtaining a fully martensitic microstructure at industrially achievable cooling rates.

The addition of 0.5% molybdenum allowed the critical cooling rate to be reduced to a reasonably low level, while martensite hardness did not reach the theoretical maximum hardness of 465 HV due to self-tempering occurring below the martensite start temperature of approximately 440 °C in these alloys.

The excellent hardenability in the 0.5% Mo-alloyed steel is related to intrinsic effects of molybdenum that reduce the ferrite nucleation rate and exert major solute drag on the carbon-enriched

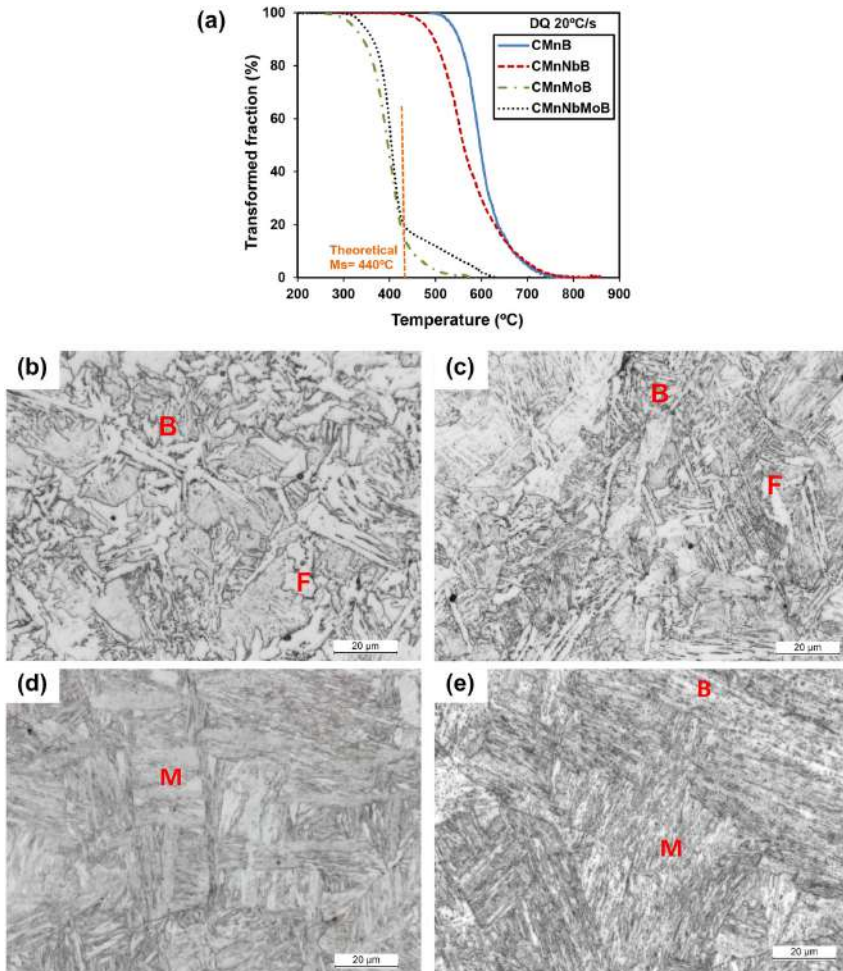


Fig. 6. (a) Evolution of transformed fraction for the 20°C/s cooling rate and DQ cycle. Optical micrographs corresponding to (b) CMnB, (c) CMnNbB, (d) CMnMoB, and (e) CMnNbMoB steels.

interphase area. Furthermore, molybdenum enhances the efficiency of boron by preventing partial precipitation into $Fe_{23}(B, C)_6$. Particularly in the DQ process, molybdenum alloying suppresses dynamic recrystallization, thus enhancing the probability of boron-depleted new austenite grain boundaries.

Identical steel alloys are less hardenable under DQ conditions than under CQ conditions, and this is due to accumulated strain and a larger total grain boundary surface of pancaked austenite offering

more nucleation sites for ferrite in the DQ process. Both effects are further encouraged by niobium microalloying.

In the CQ process, niobium microalloying moderately encourages ferrite formation, despite equiaxed austenite morphology and an absence of accumulated strain. It was speculated that niobium could trap part of the solute boron by co-precipitation, although this possibility has to be researched in detail in a future study. NbC precipitates, however, are considered beneficial in an industrial CQ

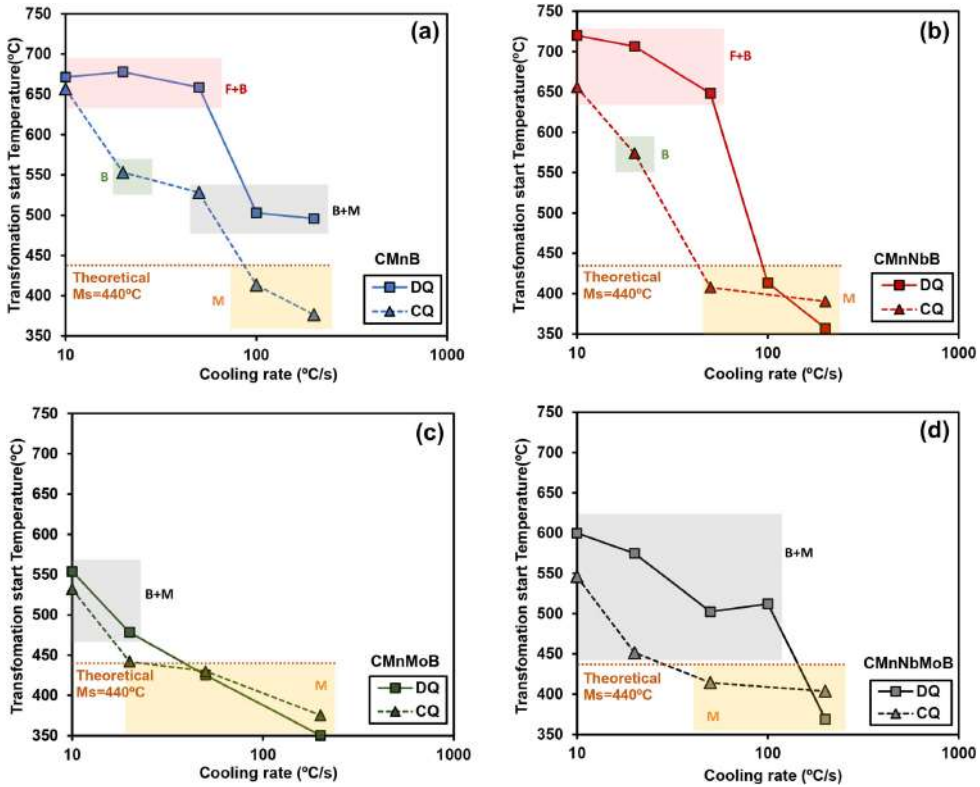


Fig. 7. Effect of cooling rate on transformation start temperature when direct quenching and conventional quenching cycles are applied for (a) CMnB, (b) CMnNbB, (c) CMnMoB, and (d) CMnNbMoB steels.

process, as these temperature-stable particles may efficiently control austenite grain size before quenching by boundary pinning. As such, combined alloying of niobium with molybdenum provides sufficient hardenability, particularly in CQ processes.

ACKNOWLEDGEMENTS

The authors would like to express their gratitude to the International Molybdenum Association (IMO) for funding this project.

CONFLICT OF INTEREST

The authors declare that they have no conflicts of interest.

OPEN ACCESS

This article is licensed under a Creative Commons Attribution 4.0 International License, which per-

mits use, sharing, adaptation, distribution and reproduction in any medium or format, as long as you give appropriate credit to the original author(s) and the source, provide a link to the Creative Commons licence, and indicate if changes were made. The images or other third party material in this article are included in the article's Creative Commons licence, unless indicated otherwise in a credit line to the material. If material is not included in the article's Creative Commons licence and your intended use is not permitted by statutory regulation or exceeds the permitted use, you will need to obtain permission directly from the copyright holder. To view a copy of this licence, visit <http://creativecommons.org/licenses/by/4.0/>.

REFERENCES



1. J. Hannula, J. Kömi, D.A. Porter, M.C. Somani, A. Kajalainen, P. Suikkanen, J.R. Yang, and S.P. Tsai, *Metall. Mater. Trans.* 48, 5344. <https://doi.org/10.1007/s11661-017-4295-3> (2017).

2. A. Saastamoinen, A. Kaijalainen, T.T. Nyo, P. Suikkanen, D. Porter, and J. Kömi, *Mater. Sci. Eng.* 760, 346. <https://doi.org/10.1016/j.msea.2019.06.018> (2019).
3. J. Kömi, P. Karjalainen, and D. Porter, in *Encyclopaedia of Iron, Steel and Their Alloys*, ed. by R. Colás and G.E. Totten, (Boca Raton, CRC Press, 2016), p. 1109. <https://doi.org/10.1081/E-EISA-120049737>.
4. A.J. Kaijalainen, P.P. Suikkanen, T.J. Linnell, L.P. Karjalainen, J.I. Kömi, and D.A. Porter, *J. Alloys Compd.* 577, S642. <https://doi.org/10.1016/j.jallcom.2012.03.030> (2013).
5. Z.J. Xie, C.J. Shang, X.L. Wang, X.P. Ma, S.V. Subramanian, and R.D.K. Misra, *Mater. Sci. Eng.* 727, 200. <https://doi.org/10.1016/j.msea.2018.04.086> (2018).
6. P. Uranga, C.-J. Shang, T. Senuma, J.-R. Yang, A.-M. Guo, and H. Mohrbacher, *Adv. Manuf.* 8, 15. <https://doi.org/10.1007/s40436-019-00285-y> (2020).
7. H. Mohrbacher, International seminar on applications of Mo in steels, ed. by CISRI and IMOA (Beijing, China, 2010), p. 74.
8. N. Isasti, D. Jorge-Badiola, M.L. Taheri, B. López, and P. Uranga, *Metall. Mater. Trans.* 42, 3729. <https://doi.org/10.1007/s11661-011-0624-0> (2011).
9. G.I. Garcia, Int. Conf. Microalloying '95, (ISS, Warrendale, PA, 1995), p. 365.
10. A. Larrañaga-Otegui, B. Pereda, D. Jorge-Badiola, and I. Gutiérrez, *Metall. Mater. Trans.* 47, 3150. <https://doi.org/10.1007/s11661-016-3465-z> (2016).
11. D.T. Llewellyn, *Ironmak. Steelmak.* 20, 338. (1993).
12. K.A. Taylor, *Metall. Trans.* 23, 107. <https://doi.org/10.1007/BF02660858> (1992).
13. G. Shigesato, T. Fujishiro, and T. Hara, *Metall. Mater. Trans.* 45, 1876. <https://doi.org/10.1007/s11661-013-2155-3> (2014).
14. Y.J. Li, D. Ponge, P. Choi, and D. Raabe, *Scripta Mater.* 96, 13. <https://doi.org/10.1016/j.scriptamat.2014.09.031> (2016).
15. C.L. Miao, C.J. Shang, G.D. Zhang, and S.V. Subramanian, *Mater. Sci. Eng.* 527, 4985. <https://doi.org/10.1016/j.msea.2010.04.039> (2010).
16. C.R. Hutchinson, H.S. Zurob, C.W. Sinclair, and Y.J.M. Brechet, *Scripta Mater.* 59, 635. <https://doi.org/10.1016/j.scriptamat.2008.05.036> (2008).
17. N. Isasti, D. Jorge-Badiola, M.L. Taheri, and P. Uranga, *Metall. Mater. Trans.* 44, 3552. <https://doi.org/10.1007/s11661-013-1738-3> (2013).
18. P. Cizek, B.P. Wynne, C.H.J. Davies, and P.D. Hodgson, *Metall. Mater. Trans.* 46, 407. <https://doi.org/10.1007/s11661-014-2601-x> (2015).
19. J. Hannula, D.A. Porter, and A. Kaijalainen, *JOM.* 71, 2405. <https://doi.org/10.1007/s11837-019-03478-9> (2019).
20. H. Mohrbacher, in *International Symposium on the Recent Development in Plate Steels, Winter Park, Colorado* (2011), p. 169–178.
21. I. Zurutuza, N. Isasti, E. Detemple, V. Schwinn, H. Mohrbacher, and P. Uranga, *Metals.* 11, 29. <https://doi.org/10.3390/met11010029> (2021).
22. I. Zurutuza, N. Isasti, E. Detemple, V. Schwinn, H. Mohrbacher, and P. Uranga, *Metals.* 11, 95. <https://doi.org/10.3390/met11010095> (2021).
23. C. Garcia de Andres, F.G. Caballero, C. Capdevila, and L.F. Alvarez, *Mater. Charact.* 48, 101. [https://doi.org/10.1016/S1044-5803\(02\)00259-0](https://doi.org/10.1016/S1044-5803(02)00259-0) (2002).
24. R. Petrov, L. Kestens, and Y. Houbaert, *Mater. Charact.* 53, 51. <https://doi.org/10.1016/j.matchar.2004.07.005> (2004).
25. P.A. Manohar, T.R. Chandra, and C.R. Killmore, *ISIJ Int.* 36, 1486. <https://doi.org/10.2355/isijinternational.36.1486> (1996).
26. ABAQUS Reference Manuals: Dassault Systemes, Providence, RI, (2009).
27. F. Togashi, and T. Nishizawa, *J. Jpn. Inst. Metals.* 40, 12. (1976).
28. M. Militzer, in *Comprehensive Materials Processing*, ed. by S. Hashmi, G.F. Batalha, C.J. Van Tyne, and B. Yilbas (Elsevier Ltd., Amsterdam, 2014), Vol. 1, p. 191. <https://doi.org/10.1016/B978-0-08-096532-1.00115-1>.
29. H. Mohrbacher, *Metals.* 8, 234. <https://doi.org/10.3390/met8040234> (2018).
30. K.R. Kinsman and H.I. Aaronson, *Transformation and Hardenability in Steels* (Climax Molybdenum Co., Ann Arbor, 1967), p. 39.
31. K. Ishikawa, H. Nakamura, R. Homma, M. Fujioka, and M. Hoshino, *ISIJ Int.* 58, 551. <https://doi.org/10.2355/isijinternational.ISIJINT-2017-579> (2018).
32. V.T. Witusiewicz, A.A. Bondar, U. Hecht, J. Zollinger, and T.Y. Velikanov, *J. Alloys Compd.* 587, 234. <https://doi.org/10.1016/j.jallcom.2013.10.142> (2014).
33. S.M.C. van Bohemen, *Mater. Sci. Technol.* 28, 487. <https://doi.org/10.1179/1743284711Y.0000000097> (2012).

Publisher's Note Springer Nature remains neutral with regard to jurisdictional claims in published maps and institutional affiliations.

Article

Effect of Nb and Mo Additions in the Microstructure/Tensile Property Relationship in High Strength Quenched and Tempered Boron Steels

Irati Zurutuza ^{1,2}, Nerea Isasti ^{1,2}, Eric Detemple ³, Volker Schwinn ³, Hardy Mohrbacher ^{4,5}  and Pello Uranga ^{1,2,*} 

- ¹ Materials and Manufacturing Division, CEIT-Basque Research and Technology Alliance (BRTA), 20018 Donostia/San Sebastián, Basque Country, Spain; izurutuza@ceit.es (I.Z.); nisasti@ceit.es (N.I.)
- ² Tecnum, Mechanical and Materials Engineering Department, Universidad de Navarra, 20018 Donostia/San Sebastián, Basque Country, Spain
- ³ AG der Dillinger Hüttenwerke, 66763 Dillingen/Saar, Germany; Eric.Detemple@dillinger.biz (E.D.); Volker.Schwinn@dillinger.biz (V.S.)
- ⁴ NiobelCon BV, 2970 Schilde, Belgium; hm@niobelcon.net
- ⁵ Department of Materials Engineering (MTM), KU Leuven, 3001 Leuven, Belgium
- * Correspondence: puranga@ceit.es; Tel.: +34-943212800

Abstract: Recently, advanced thermomechanical hot rolling schedules followed by direct quenching are being developed in order to avoid reheating and quenching treatment after hot rolling to eliminate an energy and cost consuming step. The use of boron as an alloying element is a widely known practice in high strength medium carbon steels to increase the strength due its potential for delaying phase transformation and improving hardenability. In addition, a significant synergetic effect on hardenability could be reached combining B with microalloying elements (adding Nb, Mo or Nb-Mo). With the purpose of exploring the effect of microalloying elements and thermomechanical rolling schedule, laboratory thermomechanical simulations reproducing plate mill conditions were performed using ultra high strength steels micro-alloyed with Nb, Mo, and Nb-Mo. To that end, plane compression tests were performed, consisting of an initial preconditioning step, followed by several roughing and finishing deformation passes and a final quenching step. After fast cooling to room temperature, a tempering treatment was applied. In the present paper, the complex interaction between the martensitic microstructure, the tempering treatment, the addition of microalloying elements, and the resulting tensile properties was evaluated. For that purpose, an exhaustive EBSD quantification was carried out in both quenched as well as quenched and tempered states for all the steel grades and the contribution of different strengthening mechanisms on yield strength was analyzed. Highest tensile properties are achieved combining Nb and Mo, for both quenched (Q) and quenched and tempered states (Q&T), reaching yield strength values of 1107 MPa and 977 MPa, respectively. Higher tempering resistance was measured for the Mo-bearing steels, making the CMnNbMoB steel the one with the lowest softening after tempering. For CMnB grade, the yield strength reduction after tempering of about 413 MPa was measured, while for NbMo micro-alloyed steel, yield strength softening is considerably reduced to 130 MPa.

Keywords: martensite; Q + T steels; thermomechanical simulations; tensile properties; microalloying elements



Citation: Zurutuza, I.; Isasti, N.; Detemple, E.; Schwinn, V.; Mohrbacher, H.; Uranga, P. Effect of Nb and Mo Additions in the Microstructure/Tensile Property Relationship in High Strength Quenched and Tempered Boron Steels. *Metals* **2021**, *11*, 29. <https://doi.org/10.3390/met11010029>

Received: 4 December 2020

Accepted: 23 December 2020

Published: 25 December 2020

Publisher's Note: MDPI stays neutral with regard to jurisdictional claims in published maps and institutional affiliations.



Copyright: © 2020 by the authors. Licensee MDPI, Basel, Switzerland. This article is an open access article distributed under the terms and conditions of the Creative Commons Attribution (CC BY) license (<https://creativecommons.org/licenses/by/4.0/>).

1. Introduction

In response to the market requirements for highest strength and good impact resistance, plate steels are usually quenched and tempered for a large variety of applications. Boron is an efficient microalloying element, commonly used in high strength medium carbon Quenched (Q) and quenched and tempered (Q&T) steels, in substitution for more

expensive elements. The addition of B increases strength, ensures hardenability, and promotes the formation of bainitic/martensitic microstructures. The pronounced segregation of B to the austenite grain boundary delays the nucleation of ferrite, which is the basis for its strong effect on hardenability [1–4]. In order to safeguard high efficiency in terms of hardenability, it is essential to maintain boron in solution and to avoid strong plastic deformation immediately before quenching. Avoiding traces of softer phases as well as establishing good homogeneity of the microstructure are essential for ensuring the best mechanical properties of the final product.

A synergetic effect on hardenability by combined alloying of B and Nb, as well as B and Mo [5–8] is widely reported in the literature. The potential loss of solute boron by formation of ferro-boron carbides ($\text{Fe}_{23}(\text{C},\text{B})_6$) especially in the austenite grain boundary area is prevented by the formation of Nb or Mo carbides. Since Nb and Mo are well established as alloying elements in low carbon steel plates with yield strength levels above 500 MPa, the synergetic effect with boron is simultaneously provided. The major function of Nb addition is to strongly delay static recrystallization kinetics of the austenite, via solute drag and strain-induced precipitation [9,10]. This allows for the accumulation of deformation in austenite during finish rolling, resulting in grain size refinement of the final microstructure and thus improving mechanical properties [11,12]. Mo is usually added to steels when ultrahigh strength is requested. Through this addition, the formation of low-temperature transformation products such as bainite and martensite can be achieved [5]. It should be noted that molybdenum's hardenability mechanism is complementary to that of boron. Molybdenum also delays Nb precipitation in austenite while promoting a finer-sized and more copious NbC precipitate formation during or after transformation. This results in more pronounced precipitation hardening [11,13]. The effects of solute Nb and Mo on the austenite-to-ferrite transformation are similar. Both delay the phase transformation [14] and particularly obstruct pearlite formation [15], thus promoting bainite formation. This effect is standardly used when producing advanced high strength low alloy (HSLA) steels with increased toughness [16–18]. The synergetic effect of the addition of both elements has been primarily investigated in low carbon steels and ferritic/bainitic final microstructures ($\text{C} < 0.10\%$) [12]. However, in high strength steels with an increased carbon content ($\sim 0.15 \div 0.2\%$ C) and complex martensitic microstructures, a deeper understanding of these mechanisms is needed to optimize the synergetic effect of both elements. In this context, the present work will investigate the synergetic effect of B, Nb, and Mo in martensitic microstructures on the tensile properties.

Q and Q/T steels are usually produced by conventional quenching (CQ) routes in which the hot rolled plate is reheated to austenite in a separate process. Lately, the direct quenching (DQ) route after thermomechanical controlled processing is being used increasingly often. In the DQ process, the conditioned austenitic microstructure is subjected to high cooling rate immediately after hot rolling, promoting the transformation into martensite. The DQ route has economic and operational advantages over the CQ route, as it removes logistic bottlenecks and allows producing higher volumes of ultrahigh strength steel.

From a microstructural point of view, differences between the DQ and CQ processed products are expected. None withstanding that both products have martensitic microstructure, the difference is seen in the underlying prior austenite grain structure. In the CQ route the austenite grain morphology before quenching is equiaxed as cooling down and reheating result in a normalizing effect. The DQ process is quenching a conditioned austenite structure directly into martensite. Thus, austenite pancaking and heterogeneities related to recrystallization phenomena are being preserved in the martensitic microstructure. Austenite pancaking results in anisotropic mechanical properties of the final martensite particularly reflecting in differences of toughness and bendability between rolling and transverse direction [17]. Thermomechanical processing must be carefully designed to obtain an optimum pancaked austenite structure resulting in refined final grain size. Particular attention must be attributed to avoiding inhomogeneous austenite size and morphology as to ensure a good balance between tensile and toughness properties [19–21].

This paper analyzes the relationship between quenched martensite, quenched and tempered microstructures, and tensile properties in four different steels. To that end, tensile tests were performed for all the chemistries and both quenched and quenched and tempered states. In the current study, plane strain compression tests were performed for simulating DQ process. The impact of different strengthening mechanisms on the yield strength was calculated and a model able to evaluate the different strengthening contributions was developed for martensitic microstructures. The yield strength of martensitic microstructures composes of a combination of different strengthening mechanisms, such as solid solution hardening, grain size refinement, strain hardening and precipitation hardening. In addition, the role of carbon in solid solution is evaluated.

2. Materials and Methods

The chemical compositions of the laboratory cast steels are listed in Table 1. All the steels contain about 0.16% of carbon and 20 ppm of boron. They are alloyed with Ti to ensure the full effect of B. In addition to the plain CMnB steel, three different micro-alloyed steels are also included which are micro-alloyed with Nb, Mo and NbMo. The Nb and Mo contents are set to 0.026%Nb and 0.5%, respectively.

Table 1. Chemical composition of the studied steels (weight percent).

Steel	C	Si	Mn	Mo	Nb	B
CMnB	0.15	0.32	1.05	-	-	0.0022
CMnNbB	0.16	0.29	1.05	-	0.026	0.0019
CMnMoB	0.16	0.28	1.07	0.5	-	0.0022
CMnNbMoB	0.16	0.31	1.07	0.5	0.026	0.0018

Plane strain compression tests were performed in order to simulate the direct quenching and tempering treatments (see the thermomechanical schedule in Figure 1). For each chemistry, two laboratory tests were performed, one for simulating Q and another one for reproducing Q + T cycle. For that purpose, rectangular plane strain compression specimens were used (60 mm long, 30 mm wide, and 22 mm thick). Firstly, a preconditioning step consisting of soaking at 1200 °C for 10 min followed by a deformation pass ($\epsilon = 0.2$ at 1 s^{-1}) at 1140 °C was carried out to minimize the presence of coarse austenite grains. Afterwards, the samples were cooled down at a constant rate of $1 \text{ }^\circ\text{C/s}$ to room temperature. In a recently published work, and following the same hot working strategy, it was observed that the roughing and finishing passes were not able to refine the austenitic structure at reheating temperature [22]. Therefore, the preconditioning step was essential for ensuring a homogeneous and fine austenite prior to martensite transformation. Then, the plane compression specimens were reheated at 1200 °C for 10 min in order to ensure the dissolution of Nb in the CMnNbB and CMnNbMoB steels, followed by three roughing deformation passes ($\epsilon = 0.2$ at 2 s^{-1}) with an interpass time of 3 s at decreasing temperature in the 1140–1120 °C range. After a holding time of 360 s, the finishing passes were completed applying four deformation passes of 0.2 at 5 s^{-1} with an interpass time of 8 s in the 851 and 830 °C range. In order to simulate plate quenching conditions after the last deformation pass, an air–water mixture was employed. A cooling strategy of two steps was applied cooling down at $30 \text{ }^\circ\text{C/s}$ to 300 °C and then, at $10 \text{ }^\circ\text{C/s}$ down to room temperature. Finally, for the Q + T samples, a tempering treatment was performed at 600 °C for 15 min.

Due to sample/tool geometry and friction, a heterogeneous strain distribution through section is developed in the plane compression specimens [23]. Therefore, with the aim of avoiding strain gradients, the sample employed for microstructural characterization was cut from the central part of the plane compression specimen. The microstructures were characterized after etching in 2% Nital by optical microscopy (OM, LEICA DM15000 M, Leica microsystems, Wetzlar, Germany) and field-emission gun scanning electron microscopy (FEG-SEM, JEOL JSM-7100F, Tokyo, Japan). Carbide size and density measurements were carried out by FEG-SEM (considering equivalent diameter method). In all cases,

between 200 and 450 particles were measured. Additionally, a more detailed microstructural characterization was performed using electron backscattered diffraction (EBSD), and crystallographic features were quantified for all the steel grades and both Q and Q + T states. For that purpose, the samples were polished down to 1 μm , and the final polishing was performed with colloidal silica. Orientation imaging was carried out on the equipment with a camera NORDLYS II (Oxford Instruments, Abingdon, UK) and with an acquisition program and data analysis, OXFORD HKL CHANNEL 5 PREMIUM coupled to the JEOL JSM-7100 F (FEG-SEM). A scan step size of 0.2 μm was defined and the total scanned area was about 140 $\mu\text{m} \times 140 \mu\text{m}$. The EBSD scans were analyzed by means of TSL OIMTM Analysis 5.31 software (TSL OIM Analysis 5.31 software (EDAX, Mahwah, NJ, USA)). The study of the fine precipitates was performed using a Transmission Electron Microscope (TEM, JEOL 2100, JEOL Ltd., Tokyo, Japan) with a voltage of 200 kV and LaB₆ thermionic filament. To that end, carbon extraction replicas were obtained, and precipitation analysis was carried out.

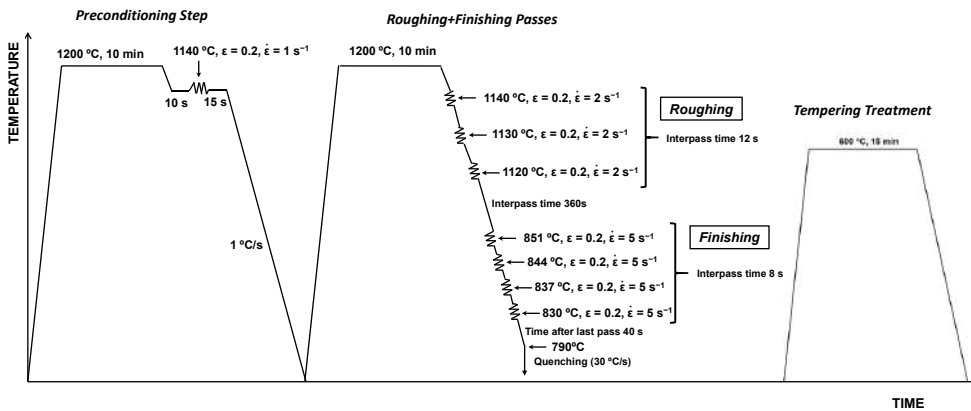


Figure 1. Schematics of the applied plane strain compression cycle.

Tensile tests were performed at room temperature in an Instron testing machine (INSTRON 5982, Instron, Grove City, PA, USA) under strain control (using an engineering strain rate of 10^{-3} s^{-1}). Cylindrical tensile specimens with a gauge length of 17 mm and a diameter of 3 mm were machined from the central area of the plane strain compression specimens. Finally, Vickers hardness was also measured in all specimens, using a 1-Kg load. In the present study, the average value of six hardness measurements is reported.

3. Results and Discussion

3.1. Microstructural Characterization

The microstructures obtained after quenching for all steel grades are shown in Figure 2 (optical microscopy) and Figure 3 (FEG-SEM). For the quenched state, fully martensitic microstructures are observed for all chemical compositions. Additionally, very fine carbides are also distinguished in the martensitic matrix (see Figure 3a–d), which are assumed to have formed by self-tempering during the final step of the accelerated cooling. The FEG-SEM images shown in Figure 3 allow us to compare the microstructures of the different alloys in quenched and quenched and tempered samples. The tempering treatment leads to the formation of carbides, which, depending on the steel grade, differ considerably (see Table 2) in size and spatial distribution. For Mo containing steels MC, M₂C, M₆C, and M₂₃C₆ type carbides were formed, whereas Nb forms only MC type carbides. It is obvious that molybdenum alloying results in finer-sized carbide particles as well as a higher particle density. In the tempered martensite, different type of carbides can be differentiated (see Figure 3), some of them pre-

precipitate at the prior austenite grain boundaries and other carbides precipitate away from the austenite boundaries (within the prior austenite grains). Furthermore, the particle density is much lower considering carbides located at prior austenite grain boundaries. Again, this is clearly more pronounced in the molybdenum alloyed steels. The total carbide area fraction of both type of carbides increases with the alloy content. Molybdenum alloying has in this respect the dominating impact.

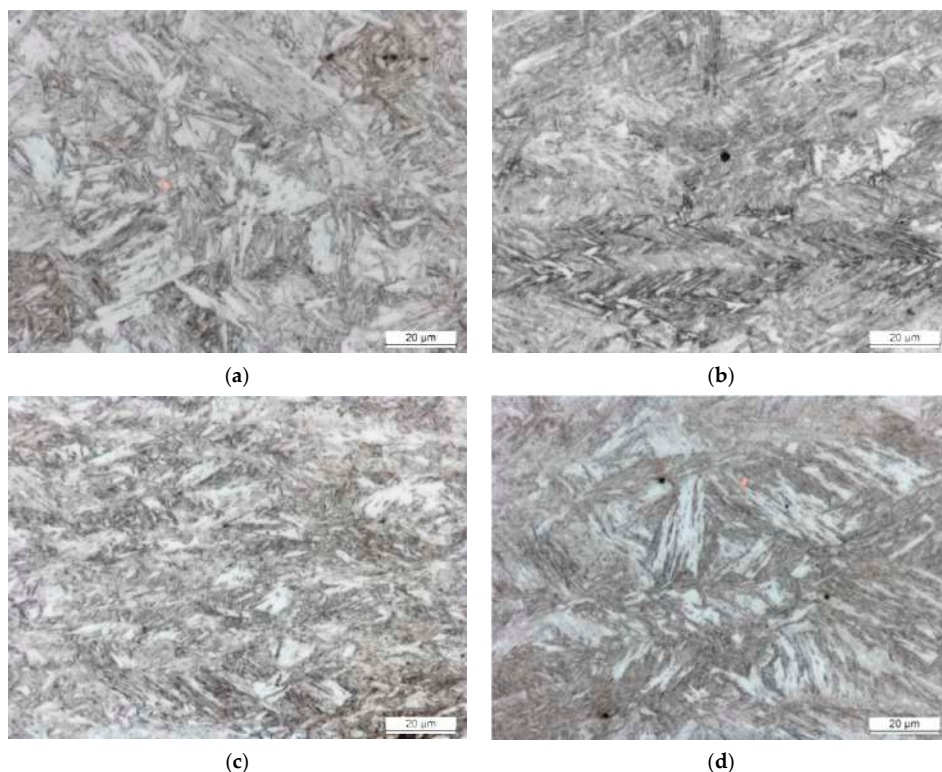


Figure 2. Optical micrographs after quenching (Q state) corresponding to (a) CMnB, (b) CMnNbB, (c) CMnMoB, and (d) CMnNbMoB steels.

Table 2. Measured mean carbide sizes and carbide densities considering both type of carbides (carbides located at prior austenite grain boundaries and inside prior austenite grains).

Steel	Carbides Located at Prior Austenite Grain Boundaries		Carbides Located Inside Prior Austenite Grains	
	Carbide Size (nm)	Area Fraction (%)	Carbide Size (nm)	Area Fraction (%)
CMnB	113.6 ± 3.9	0.18	103.8 ± 4.3	0.33
CMnNbB	115.3 ± 3.9	0.16	105.9 ± 4.4	0.41
CMnMoB	91.4 ± 5.4	0.29	59.4 ± 3.1	0.91
CMnNbMoB	80.4 ± 3.8	0.31	66.8 ± 2.9	1.26

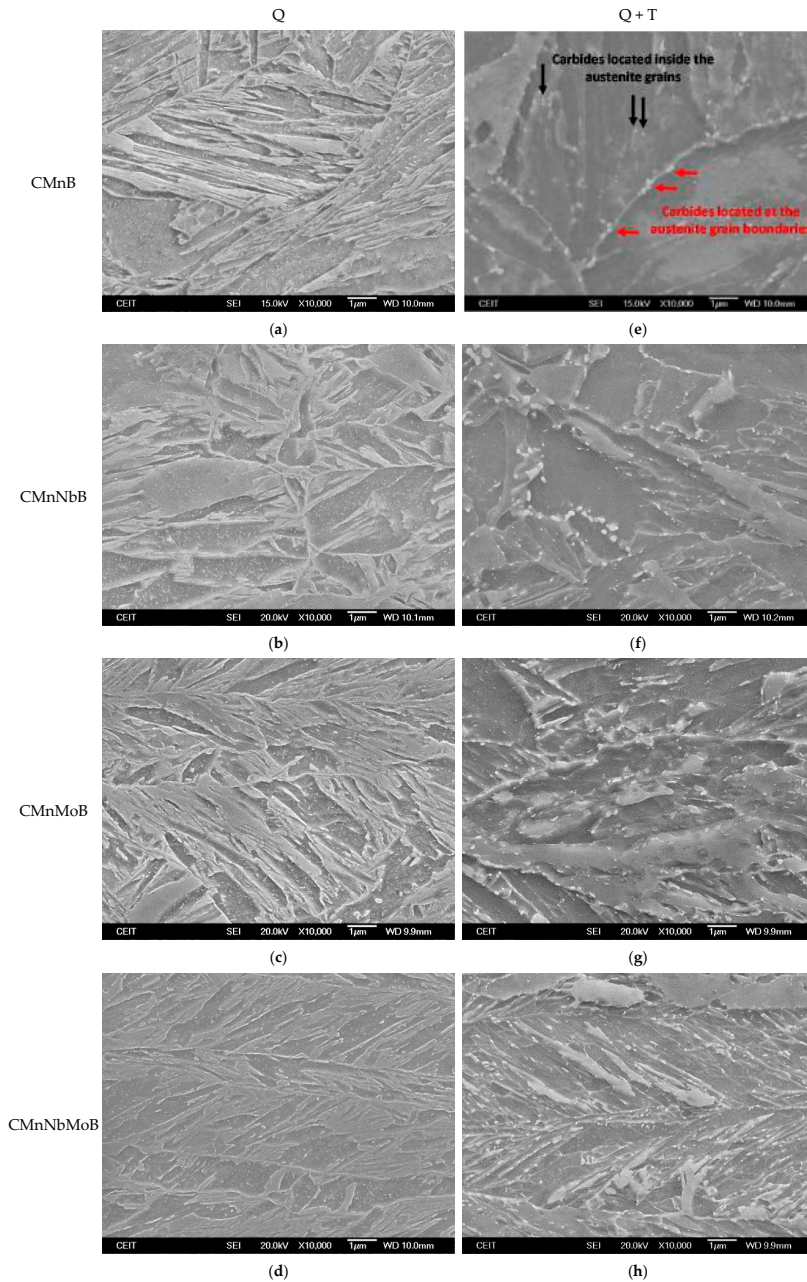


Figure 3. FESEM micrographs corresponding to (a–d) Q and (e–h) Q + T conditions for (a,e) CMnB, (b,f) CMnNbB, (c,g) CMnMoB steel, and (d,h) CMnNbMoB steels.

3.1.1. Quantification of Unit Sizes by Means of EBSD

Besides the qualitative characterization by means of conventional observation techniques, a quantitative crystallographic characterization was carried out using EBSD technique. In Figure 4 the IPF (Inverse Pole Figure) maps corresponding to the different steels and both Q and Q + T states are presented. Regarding the effect of chemistry, the addition of microalloying elements promotes microstructural refinement. The coarsest martensitic structure is observed in the CMnB grade before and after tempering (see Figure 4a,e). The formation of a very fine martensitic microstructure is observed in the Mo containing steels (Figure 4c,d,g,h). Moreover, the EBSD maps corresponding to Mo and NbMo micro-alloyed steels show that the transformation takes place from a heavily deformed austenitic structure, as the prior austenite pancaked structure is clearly reflected. In order to confirm this fact, samples were etched by picric acid and completely different austenite conditioning could be identified depending on the chemical composition as shown in a previous study [22]. In the CMnB steel, an equiaxed and homogeneous austenite grain structure is observed. For the CMnNbB steel, a mixed structure consisting of pancaked and dynamically recrystallized fine grains is found. The Mo containing grades comprise a fully pancaked austenite microstructure showing a high degree of strain accumulation [22]. Tempering of the CMnB steel modifies the microstructure to slightly coarser grain size as compared to the quenched state (Figure 4a,e). On the contrary, the microstructure of the micro-alloyed steels appears not to be altered by the tempering treatment (see Figure 4). This can be related to the well-known potency of Mo and Nb of strongly obstructing recrystallization at temperatures below 650 °C.

In Figure 5, the grain boundary maps related to (a,c) CMnB and (b,d) CMnMoB steels are shown. Low angle boundaries, between 2 and 15° are drawn in red, whereas the high angle boundaries, higher than 15° are represented in black. The influence of adding Mo is evidently reflected in Figure 5. Significantly finer microstructures are being achieved when Mo is added, considering both misorientation criteria. Additionally, Mo alloying augments the low angle boundary density (drawn in red), in the quenched steel and retains it even during tempering (Figure 5b,d). On the contrary, tempering of the CMnB steel evidently results in a significant reduction of the low angle boundary density (Figure 5a,c). Additionally, a slight coarsening of the microstructure for the CMnB steel is observed during the heat treatment.

The unit sizes were quantitatively determined from these EBSD scans in both, Q and Q + T states, for all steel grades. For quantifying the mean grain size, different misorientation criteria were considered, measuring the unit sizes with low and high tolerance angles. The effective grain size was calculated as the equivalent circle diameter corresponding to the individual grain area. In Figure 6, the mean grain size considering low and high angle misorientation criteria (boundaries between 2° and 15° and boundaries higher than 15°, respectively) are plotted for Q and Q + T states. Regarding the evolution of 2° mean unit size, for both Q and Q + T samples, slightly finer D_{2°} are achieved when microalloying elements are added. Considering the high angle boundary misorientation criteria, a similar trend is detected. The addition of microalloying elements causes a reduction of mean unit sizes, and largely prevents coarsening by the tempering treatment. Such coarsening, however, occurs in the CMnB steel where D_{2°} increases from 1.08 in the quenched state to 1.26 µm after tempering. The NbMo steel comprises the smallest D_{2°} unit size of around 0.87 µm in Q as well as Q + T condition.

3.1.2. Dislocation Density Estimation Based on Kernel Average Misorientation

The impact of tempering treatment and chemical composition on the Kernel Average Misorientation (KAM) maps is compared in Figure 7 for the CMnB and CMnNbMoB grades. KAM is widely employed for dislocation density evaluation [12,24]. Regarding the effect of chemistry, the addition of microalloying elements leads to the increment of KAM values. For the Q condition, KAM value increases from 1.2° to 1.35°, when Nb and Mo are added (see Figure 7a,c).

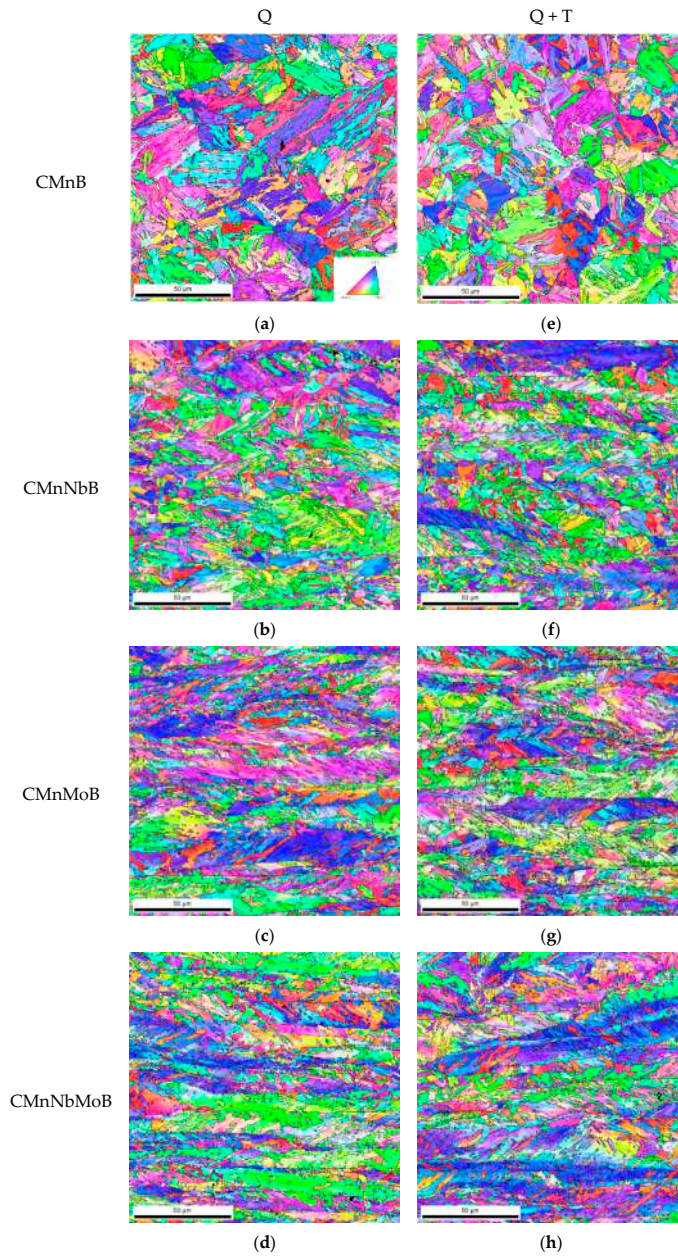


Figure 4. Inverse Pole Figure (IPF) maps corresponding to (a–d) Q and (e–h) Q + T states.

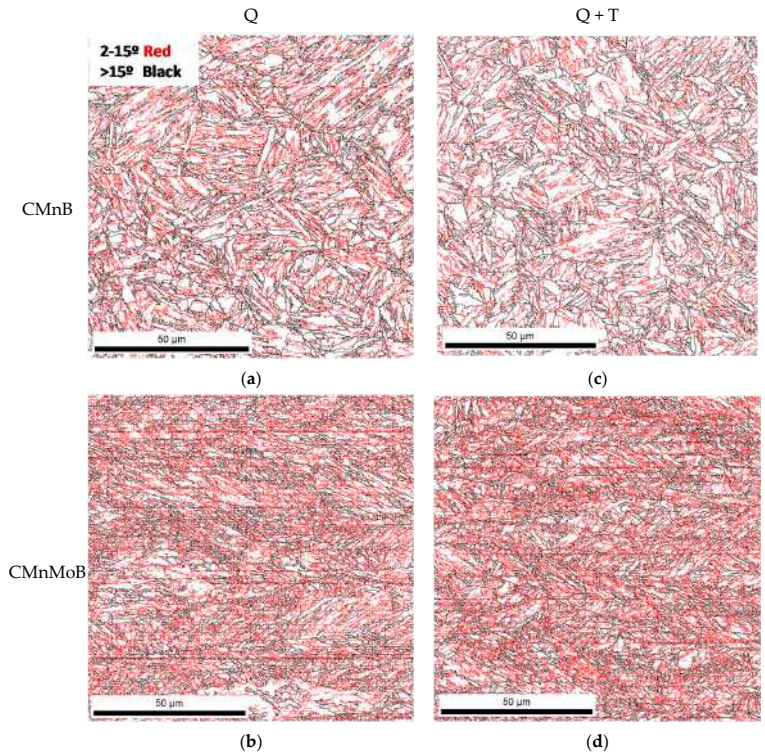


Figure 5. Influence of tempering on the Grain Boundary maps related to (a,c) CMnB and (b,d) CMnMoB.

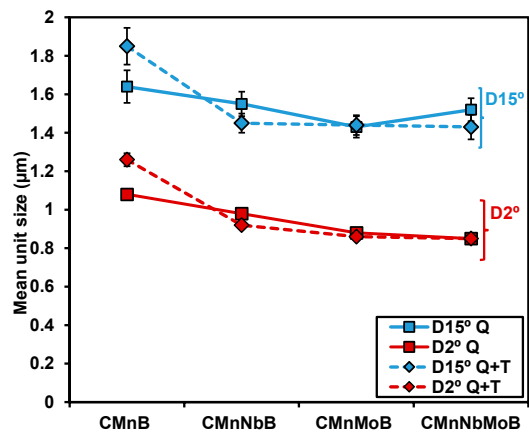


Figure 6. Mean Unit Sizes considering different misorientation criteria (tolerance angle of 2° and 15°) for both conditions: Q and Q + T cycles.

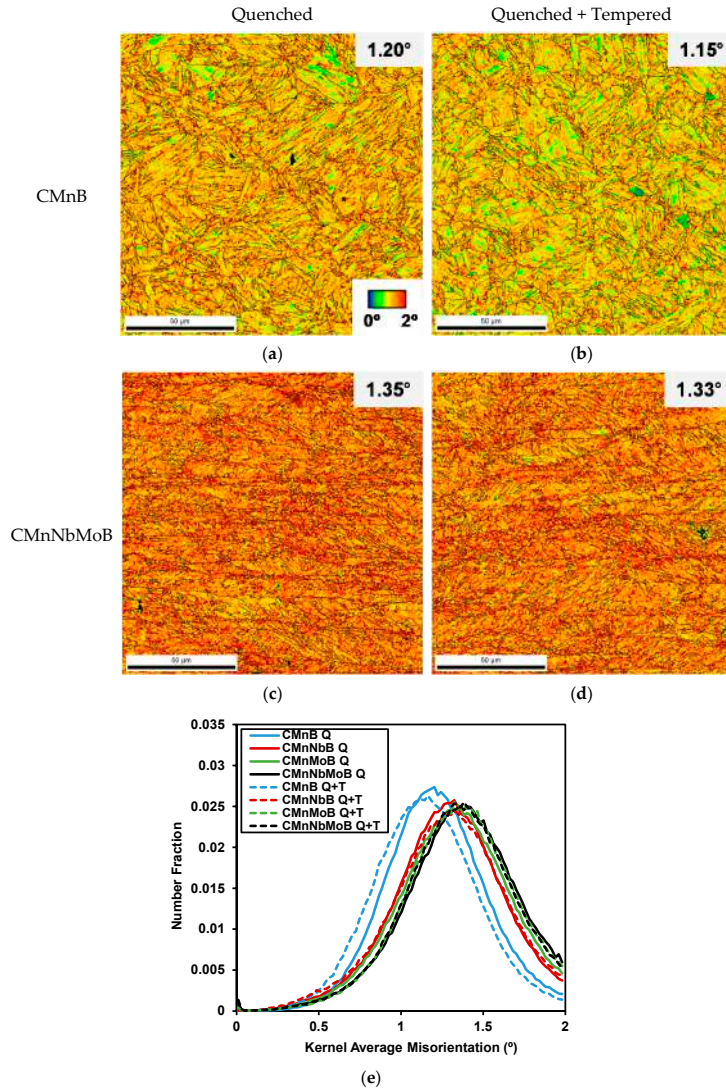


Figure 7. Kernel Average Misorientation maps corresponding to different steels ((a,b) CMnB and (c,d) CMnNbMoB) and both conditions: (a,c) Q and (b,d) Q + T states. (e) KAM distributions corresponding to all the steel grades and both states.

Analyzing the effect of tempering treatment, different behavior is noticed depending on the chemical composition. In the CMnB steel, slightly different KAM maps are observed when Q and Q + T states are compared (see Figure 7a,b). For the CMnNbMoB though, KAM parameter remains unmodified. Similar average KAM values are measured before and after heat treatment (see Figure 7c,d, KAM values of approximately 1.3°). For CMnNbB steel, similar KAM values are quantified for both conditions (of 1.28°), while for CMnMoB

grade, KAM values of 1.30° and 1.34° are measured, for Q and Q + T, respectively. Besides the average value, the effect of tempering on the KAM distributions are plotted in Figure 7e for all the steels. No impact of tempering is observed on Kernel Average Misorientation distributions for the micro-alloyed steels (Nb, Mo, and Nb-Mo). In the CMnB grade meanwhile, the tempering treatment slightly shifts the KAM distribution to lower values. The Kernel map in the Q state presents more regions in red-orange colors and the Q + T image shows some blue-green areas (see Figure 7a,b).

3.1.3. Fine Precipitation Analysis on Mo Containing Steels and Q + T State by TEM

Niobium, titanium, boron, and molybdenum have the potential of precipitating as carbides or nitrides. When such precipitates are formed in the bcc lattice, they can add to strength depending on particle size and amount. Titanium being a strong nitride former is added in the current quenchable steels mainly to protect boron from forming nitrides. Considering the Ti:N ratios in the current steels, most of the added Ti is tied as insoluble TiN particles. It is well-established that part of the added Nb co-precipitates with TiN particles and is thus not available for its actually intended metallurgical effects. Such TiN and Ti,Nb(C,N) precipitates typically have a coarse size and do not contribute to strength. TiN particles with cubic morphology having sizes up to the lower micrometer range could be detected in all current steels.

TEM analysis of replicas from both Mo-alloyed steels (CMnMoB and CMnNbMoB) after tempering revealed the presence of coarser-sized precipitates with complex composition. For the CMnMoB grade, these precipitates are carbo-nitrides rich in Ti and Mo, while for the CMnNbMoB steel the precipitates are rich in Ti-Mo-Nb. In some cases, co-precipitation is also observed, where the nucleation of smaller carbonitride (rich in Nb and small fraction of Ti, Mo) is detected on pre-existing TiN particles.

A population of fine-sized precipitates having diameters of less than 10 nm is detected in the CMnMoB and CMnNbMoB steels, as shown in Figure 8a,b, respectively. For the CMnNbMoB steel (Figure 8b,c), the share of fine precipitates appears to be higher and sizes below 5 nm are found. These particles are rich in Mo as indicated by the XPS spectrum in Figure 8c. The quenched condition does not allow precipitation of Mo for kinetic reasons contrary to the tempering condition. A variety of Mo containing carbide phases can be formed during tempering depending on time and temperature as well as Mo concentration [25]. The latter is not homogeneous as Mo is usually segregated to prior austenite grain boundaries where it was found to have concentration peaks in the order of 3 times the average bulk concentration [4,26]. Furthermore, Mo can segregate to substructure boundaries during tempering. Under the current tempering condition, the Mo diffusion range is limited to below 30 nm, thus not allowing strong concentration enhancement. The observed fine-sized precipitates are likely represented by MC and M_2C type. MC type particles are typical for the microalloying elements Nb and Ti of which small amounts can still be solute at the onset of tempering in the present steels. It has been demonstrated that Mo clusters can nucleate such MC carbides, even representing the dominant fraction when these MC particles are ultra-fine in size [27]. The synergistic effects of molybdenum refining the size of the micro-alloy precipitates and simultaneously enhancing the MC particle volume fraction has also been reported [11,13]. M_2C grows at the expense of cementite (M_3C) that has previously formed at lower temperatures. Upon long tempering times M_2C type particles adopt a needle-shaped morphology [28,29], which due to the short tempering are not seen in the present steels. On the other hand, Mo can participate in coarser-sized particles of type M_6C or $M_{23}C_6$ located near to M_3C particles at both, large and small angle boundaries [25].

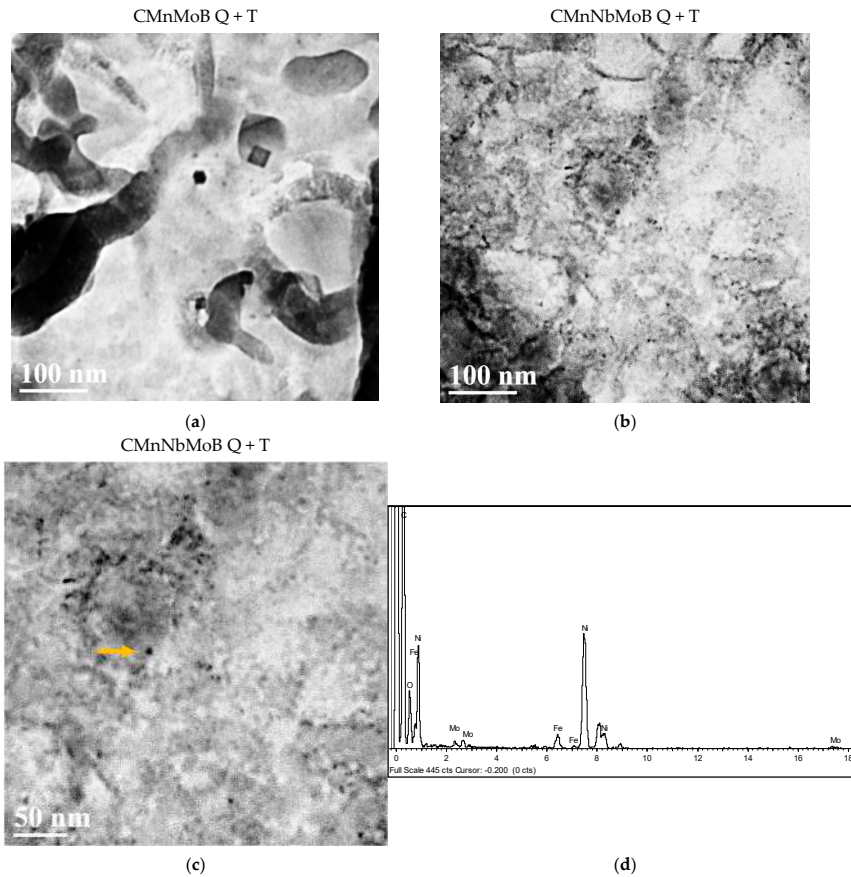


Figure 8. TEM micrographs corresponding to (a) CMnMoB and (b,c) CMnNbMoB grades and Q + T state (d) Microanalysis of the fine precipitate marked in (c) (the presence of Ni in the spectrum originates from the grid holding the carbon replica).

3.2. Interaction between Microstructure and Tensile Properties

3.2.1. Hardness Measurements

Figure 9 compares average Vickers hardness values obtained for each chemical composition before and after tempering treatment. Considering first the quenched condition, the CMnB steel comprises the lowest hardness as expected. The sole addition of Nb and Mo raises the hardness by 16.2 HV and 45.2 HV, respectively. However, combined alloying of Nb and Mo does not result in further significant hardness increase over the Mo-only addition. Tempering generally leads to a major loss of hardness. The hardness drop is largest in the CMnB steel amounting to 187 HV. The additions of Nb and Mo reduce the hardness loss to 163 HV and 131 HV, respectively. The combined addition of Mo and Nb further reduces the hardness loss to 114 HV. Accordingly, beyond the individual contributions of Nb and Mo to tempering resistance a significant synergetic effect is observed when both alloying elements are combined.

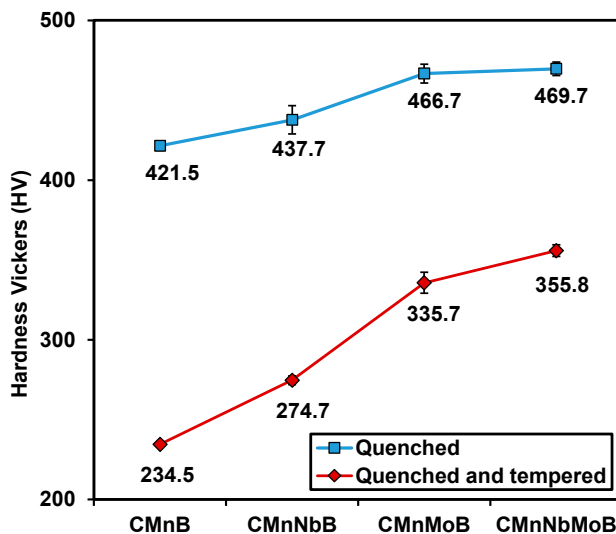


Figure 9. Hardness measurements for all steel grades for Q and Q + T cycles.

3.2.2. Tensile Properties

The tensile behavior of the quenched steels shows “round-house” curves with high and continuous work hardening immediately after yielding as typically observed for martensitic steels (Figure 10). The CMnB steel has the lowest strength and largest total elongation. The steels with Mo addition reach the highest strength level of over 1400 MPa tensile strength (Table 3). The Mo and Nb combined alloyed steel not only comprises the highest strength but also shows better total elongation than the steels alloyed with either Nb or Mo. Tempering drastically changes the tensile behavior (Figure 10). Tensile strength is significantly reduced to values in the range of 700 to 1034 MPa, depending on the alloy concept. The strength reduction comes along with improvement of total elongation except for the Mo + Nb steel, showing lower elongation compared to the quenched condition. The observed differences between the various alloys are manifested mainly in the extent of post-uniform elongation after tempering. The yield-to-tensile ratio (YTR) is in the range of 0.75 to 0.78 reflecting the good work hardening potential in the quenched condition. Tempering affects the tensile strength much more than the yield strength. Accordingly, the YTR increases to values between 0.88 and 0.95. The Mo alloyed steels have the highest YTR after tempering, regardless of whether Nb is added or not. The losses in yield and tensile strength after tempering are compared in Figure 11. The smaller strength loss and high YTR suggest that Mo not only provides high tempering resistance but also recovers strength by secondary hardening. The Nb alloyed steel shows indications of secondary hardening as well yet it has clearly lower tempering resistance as compared to the Mo-added steels. The lower post-uniform elongation after tempering in the steels alloyed with Mo and/or Nb could be related to the carbide particle population described in Section 3.1. Particularly the higher carbide fraction located at low angle boundaries has the potential of generating more microstructural damage during the work hardening phase making post-uniform yielding less stable. Additionally, it must be taken into account that the stress level at the end of the work hardening phase in these steels is also significantly higher, promoting the cracking of carbide particles.

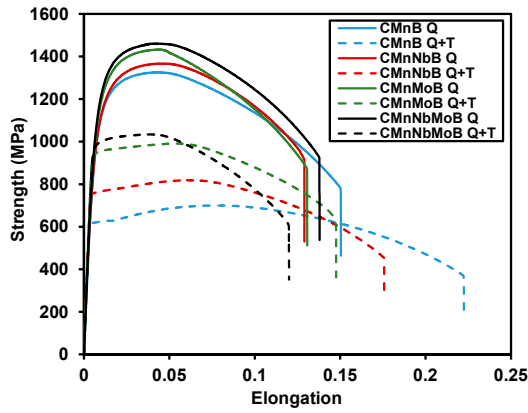


Figure 10. Tensile curves in Q and Q + T cycles for all steel grades.

Table 3. Tensile properties measured before and after tempering treatment for all the chemistries (YTR: yield-to-tensile ratio).

Steel	Cycle	Yield Strength (MPa)	Tensile Strength (MPa)	YTR	Homogeneous Elongation	Total Elongation
CMnB	Q	1030	1325	0.78	0.05	0.15
	Q + T	617	700	0.88	0.08	0.22
CMnNbB	Q	1026	1366	0.75	0.04	0.12
	Q + T	757	818	0.93	0.07	0.17
CMnMoB	Q	1075	1432	0.75	0.04	0.13
	Q + T	943	991	0.95	0.06	0.15
CMnNbMoB	Q	1107	1460	0.76	0.04	0.14
	Q + T	977	1034	0.95	0.03	0.12

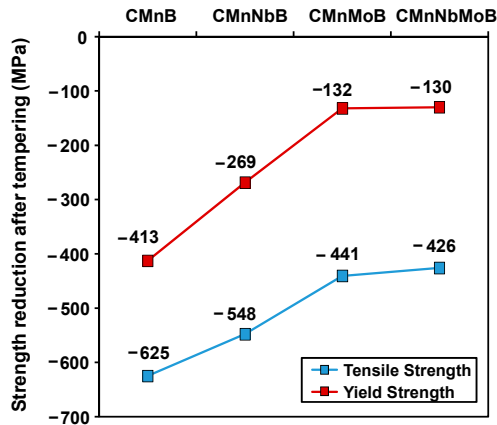


Figure 11. Reduction of yield strength and tensile strength after tempering treatment.

3.3. Estimation of the Contribution of Strengthening Mechanisms on Yield Strength

Based on the information obtained from the EBSD characterization, the contribution of different strengthening mechanisms to yield strength was estimated for all investigated conditions. The yield strength of low carbon micro-alloyed steel grades can be calculated considering a linear sum of individual strengthening mechanisms, such as solid solution (σ_{ss}), unit size refinement (σ_{gs}), and dislocation density (σ_{ρ}) according to Equation (1). For martensitic microstructures, however, a further contribution termed “unaccounted strength” (σ_{us}) must be added. This contribution accounts for the effect of carbon in solid solution. In this study, the individual contributions of the each strengthening mechanisms have been estimated by means of different approaches reported in the literature (see the summary of the used equations in Table 4).

$$\text{Yield Strength (MPa)} = \sigma_{ss} + \sigma_{gs} + \sigma_{\rho} + \sigma_{us} \tag{1}$$

Table 4. Summary of the used equations for estimating the contribution of different strengthening mechanisms.

Solid Solution	$\sigma_{ss} = \sigma_0 + 32.3(\%Mn) + 83.2(\%Si) + 11(\%Mo) + 354(\%N_{free})^{0.5}$	[30]
Grain Size	$\sigma_{gs} = 1.05\alpha M\mu\sqrt{b} \left[\sum_{2 \leq \theta_i \leq 15^\circ} f_i \sqrt{\theta_i} + \sqrt{\frac{\pi}{10}} \sum_{\theta_i \geq 15^\circ} f_i \right] d_2^{-\frac{1}{2}}$	[31]
Dislocation Density	$\rho = \frac{2\theta}{u \cdot b}, \sigma_{\rho} = \alpha M\mu b\sqrt{\rho}$	[24,32]

The effect of solid solution was calculated by means of the equation proposed by Pickering [31] (see Table 4). For martensitic microstructures, the contribution of microstructural refinement has been extensively estimated in the literature by considering the Hall–Petch type relationships [5]. However, there is no unanimity in the definition of the effective grain size acting as an obstacle on dislocation movement in a martensitic matrix. Some authors consider the packet size as the effective gain size in lath martensite [33,34], while other works state that block size controls the strength [35,36]. Hannula et al. [37] showed that the effective grain size can be determined by measuring high angle misorientation boundaries (higher than 15°) through EBSD technique and they concluded that its square root correlates well with the measured yield strength. The equation proposed by Iza-Mendia et al. [31], where both types of boundaries (low and high angle) are considered and balanced by their fraction (see Table 4) is the approach selected in the present analysis. This approach was validated for a wide range of microstructures (ferritic-pearlitic, bainitic and martensitic microstructures). Low and high angle boundary fractions (f_i), as well as mean unit size considering low angle misorientation criteria (d_2°) were calculated by EBSD technique for the different steel grades and both states. Finally, hardening due to dislocation density was evaluated through Kernel Average Misorientation obtained by EBSD scans, according to the equations shown in Table 4 [24,32]. More details regarding the considered assumptions as well as the followed procedure can be found in Refs. [12,38].

For estimating the contribution of unaccounted strength (σ_{us}), the difference between the experimental yield strength (measured by tensile tests) and the rest of the terms (related to solid solution, grain size refinement, and dislocation density) was calculated. For the quenched state, σ_{us} is associated with the impact the carbon in solid solution, while for tempered state, this term can also account for the strengthening effect of nanosized precipitates formed by Nb and Mo during tempering treatment.

In Table 5 and Figure 12a,b, the values for the different strengthening mechanisms are shown for both Q and Q + T conditions, respectively. For verification, the experimental yield strength values obtained by tensile tests are represented by the red dots in the figure. Regarding the quenched state, similar contribution due to solid solution are estimated

for all the steels. The results suggest that the most relevant strengthening mechanism is associated with the unit sizes. Contributions ranging from 472 to 528 MPa are quantified, for CMnB and CMnNbMoB steels, respectively. No significant effect on the hardening related to dislocation density is apparent from adding microalloying elements as this contribution only increases from 114 to 121 MPa at the most. The hardening due to carbon in solid solution is associated in the unaccounted strength (σ_{us}), as explained earlier. This contribution is calculated as the difference between experimental yield strength and the sum of all other contributions. Values higher than 300 MPa are quantified in all the cases for the unaccounted strength (σ_{us}). A similar procedure was also considered in other works [39].

Table 5. Individual contributions of strengthening mechanism to yield strength.

Steel	Cycle	Solid Solution (MPa)	Grain Size (MPa)	Dislocation Density (MPa)	Unaccounted Strength (MPa)
CMnB	Q	115	472	114	329
	Q + T	115	448	112	0
CMnNbB	Q	112	496	118	300
	Q + T	112	516	118	11
CMnMoB	Q	117	516	119	323
	Q + T	117	520	121	185
CMnNbMoB	Q	120	528	121	338
	Q + T	120	508	120	229

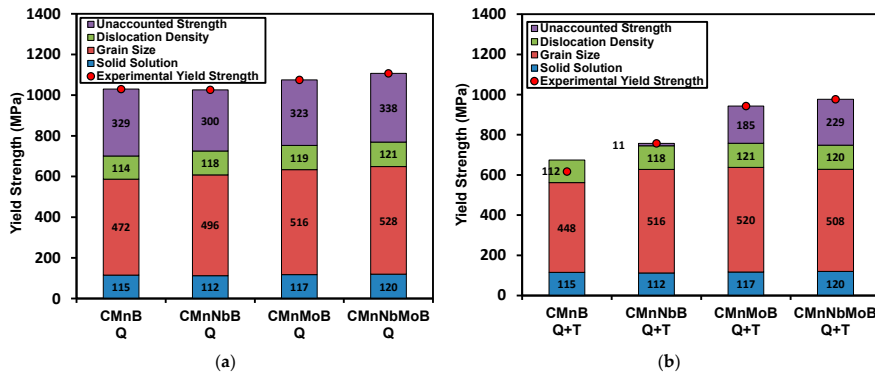


Figure 12. Contribution of different strengthening mechanisms (solid solution, grain size, dislocation density and unaccounted strength) to the yield strength: (a) Q and (b) Q + T states.

The contributions of individual strengthening mechanisms to yield strength after tempering treatment are presented in Figure 12b. No considerable impact of the tempering treatment is seen for the contributions by solid solution, unit size and dislocation density. In CMnB steel, the unit size contribution is estimated to be slightly lower after tempering, due to the observed coarsening of the microstructure (see Figures 5 and 6). The experimentally observed yield strength drop after tempering is dominantly controlled by the unaccounted strength term and in this respect, molybdenum displays its marked effect of tempering resistance as already mentioned earlier. For the CMnB and Nb-only alloyed steel the unaccounted strength drops to a marginal level after tempering. This can be associated with thermally activated diffusion of carbon during tempering and the lack of carbon in interstitial solution remaining after tempering in the CMnB and CMnNbB steels. Conversely, in the Mo-bearing steels, a high contribution of the unaccounted strength

is calculated after tempering. This could be related to a lack of complete diffusion of carbon out of the martensite lattice and/or by the formation of very fine precipitates during the tempering treatment. In Figure 13, the unaccounted strength values predicted for all the steels and both conditions are plotted together. For the as-quenched martensite, an important hardening due to carbon in solid solution is estimated and the increase in MPa is similar in all the chemistries (329, 300, 323 and 338 MPa, in the CMnB, CMnNbB, CMnMoB, and CMnNbMoB steels, respectively). For the Q + T condition, unaccounted strength terms of 185 and 229 MPa are estimated, for the CMnMoB and CMnNbMoB steels, respectively.

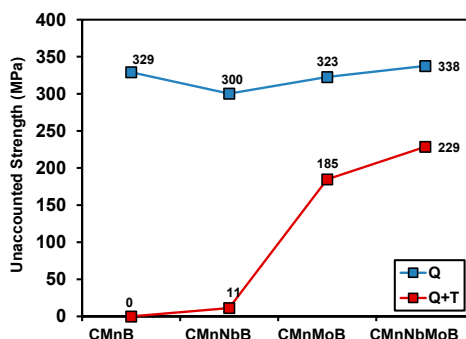


Figure 13. Contribution of unaccounted strength to the yield strength for both Q and Q + T conditions.

It is reasonable to relate the unaccounted strength seen in the tempered condition of the present steels (Figure 12) to precipitation strengthening. The CMnB base steel does not contain free microalloying elements before the tempering stage and thus the unaccounted strength is zero. Niobium in the CMnNbB steel can be in solid solution to a small amount before tempering. Considering that part of the Nb was trapped in insoluble particles and another part was forming strain-induced precipitates during austenite conditions, it is reasonable assuming the available amount of solute Nb being less than 0.01%. The applied tempering condition is not suitable to allow a complete precipitation of Nb [40] so the resulting low precipitation strengthening effect could be indeed represent the unaccounted strength of 11 MPa. Molybdenum, on the contrary, is nearly fully solute at the onset of tempering providing theoretically sufficient feedstock for precipitates to raise yield strength in the order of 200 MPa. Based on the precipitation analysis performed by TEM, it can be indeed concluded that intense fine precipitation takes place during tempering treatment for both Mo containing grades. However, due to the fine size of these particles, the quantification of size and volume fraction of these precipitates becomes very complex and therefore, the straight-forward estimation of the contribution by fine precipitation is difficult. However, based on the Ashby–Orowan mechanism, one can estimate the average interparticle spacing that would result the observed unaccounted strength values of 180–230 MPa [41]. Accordingly, the resulting values for inter particle spacing should be in the range of 40–60 nm. It appears from the TEM micrographs (Figure 8) that particle spacing in that range is indeed existing. Moreover, the calculated diffusion ranges for Mo and Nb being 30 and 20 nm, respectively, under the applied tempering conditions are also congruent with such particle interspacing. The higher unaccounted strength in the CMnNbMoB steel would then again indicate a synergetic effect by which Mo promotes the precipitation of Nb adding around 50 MPa to yield strength over the Mo-only variant [42,43].

Molybdenum, upon tempering, also appears forming larger-sized precipitates of the M_6C and $M_{23}C_6$ type which can explain the particle distributions described in Section 3.1. The observation that the large-sized particle density is higher at small-angle boundaries

could be due to local concentration of molybdenum and carbon. The formation of M_2C type precipitates requires rather high Mo and C concentrations that are more likely occurring at large-angle boundaries. Expectedly less pronounced Mo and C segregation at small-angle boundaries should favor Mo participating in M_6C and $M_{23}C_6$ formation [25].

Effect of Composition and Tempering Treatment on Work Hardening Rate

Finally, in order to find a reasonable correlation between the work hardening parameter and ductility of the material, the stress-strain behavior was analyzed using the Hollomon approach [44,45]. From the tensile curves shown in Figure 10, the work hardening rate ($d\sigma/d\varepsilon$) was calculated before and after quenching. In Figure 14 the work hardening rate is plotted as a function of true strain for all the chemistries and both quenched as well as tempered samples. Initially, for both, the Q and Q + T states, the work hardening rate is relatively high and decreases drastically in the early stage of the deformation. In this region, work hardening of the quenched sample is significantly higher compared to the tempered sample. In the quenched steels, no significant effect of alloying is observed in the work hardening behavior while this is clearly the case in tempered condition (see Figure 14). The CMnB steel exposes Lüders deformation without work hardening immediately after dislocations have been unlocked. The steel alloyed with Nb and/or Mo, however, maintain work hardening in that strain range, be it at a much lower level than in quenched condition. The observed differences could be explained by an increasing population density of nano-precipitates in the CMnNbB towards the CMnNbMo containing steels. According to the Ashby–Orowan mechanism [46], mobile dislocations passing an array of precipitates produce Orowan loops enhancing dislocation density and reducing the mean-free particle interspace, thus generating work hardening. The back-stress of the dislocation loops can induce cracking of larger carbide particles and cause quicker progress of failure after passing homogeneous elongation. This is assumed to be the reason for the reduced post-uniform elongation, of the CMnMoB and especially the CMnNbMoB steels as mentioned earlier.

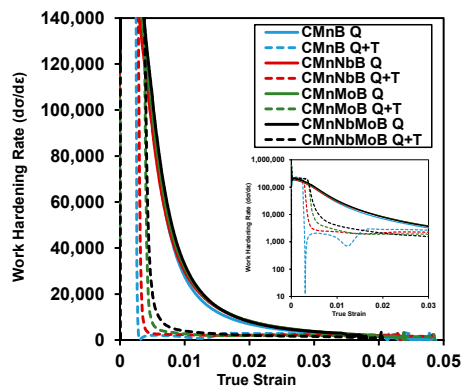


Figure 14. Work hardening rate as a function of true strain for all samples after Q and Q + T treatments.

4. Conclusions

Modifications of a baseline CMnB steel concept using Mo and Nb alloying have been investigated regarding their effects on microstructure and tensile properties in plate steel of 1000 MPa yield strength level, processed via a direct quenching route.

In as-quenched condition, the CMnB baseline alloy concept achieves the minimum specified yield strength (960 MPa) by reasonable margin while alloying of 0.5%Mo and 0.5%Mo–0.025%Nb provide an additional yield strength margin of 45 and 75 MPa, respectively. The enhancement of tensile strength is in the range of 110–140 MPa in the modified alloys.

Upon tempering (600 °C/900 s), the CMnB steel experiences a large drop of yield and tensile strength in the order of 400 MPa and 600 MPa, respectively. The CMnNbMoB steel, however, still meets the minimum required specified tensile properties.

The excellent tempering resistance in the CMnNbMoB steel can be due to individual and synergetic effects by molybdenum and niobium. Detailed EBSD analysis revealed that the small niobium addition is highly efficient in retaining the extremely fine large-angle and small-angle unit sizes present in the quenched condition during tempering, while the CMnB steel shows measurable coarsening of these. Molybdenum alloying establishes a particularly fine-sized low-angle grain boundary structure in the quenched steel that is retained even after tempering.

The strength loss caused by redistribution and precipitation of interstitial carbon during tempering accounts for approximately 320 MPa in all investigated steels. A major part of that strength loss is compensated by precipitation strengthening in the Mo-alloyed steels. Ultra-fine Mo-rich precipitates have been identified by TEM. Experimental data and theoretical estimations suggest that precipitation strengthening accounts for approximately 200 MPa gain in yield strength. While the small available amount of Nb by itself contributes only around 10 MPa to precipitation strengthening, the synergy between Mo and Nb adds around 50 MPa over the Mo-only effect.

The presence of ultra-fine precipitates and their particularly strong effect on yield strength reflects in a very high yield-to-tensile ratio of 0.95 after tempering. Nevertheless, the Mo-alloyed steels maintain continuous yielding after tempering whereas the CMnB steel shows features of Lüders elongation.

Author Contributions: I.Z. carried out the experiments and wrote the manuscript; N.I. supervised the results, analyzed the data and wrote the manuscript; E.D., V.S. and H.M. contributed to the interpretation of the data and edited the manuscript; P.U. managed the project and edited the manuscript. All authors have read and agreed to the published version of the manuscript.

Funding: This research received funding by the International Molybdenum Association (IMOA).

Institutional Review Board Statement: Not applicable.

Informed Consent Statement: Not applicable.

Data Availability Statement: Data sharing not applicable.

Acknowledgments: The authors would like to acknowledge the International Molybdenum Association (IMOA) for funding this project.

Conflicts of Interest: The authors declare no conflict of interest.

References

1. Llewellyn, D.T. Nitrogen in Steels. *Ironmak. Steelmak.* **1993**, *20*, 338–343.
2. Taylor, K.A. Grain-boundary segregation and precipitation of boron in 0.2 percent carbon steels. *Met. Mater. Trans. A* **1992**, *23*, 107–119. [[CrossRef](#)]
3. Shigesato, G.; Fujishiro, T.; Hara, T. Grain Boundary Segregation Behavior of Boron in Low-Alloy Steel. *Met. Mater. Trans. A* **2014**, *45*, 1876–1882. [[CrossRef](#)]
4. Li, Y.; Ponge, D.; Choi, P.; Raabe, D. Segregation of boron at prior austenite grain boundaries in a quenched martensitic steel studied by atom probe tomography. *Scr. Mater.* **2015**, *96*, 13–16. [[CrossRef](#)]
5. Mohrbacher, H. Property Optimization in As-Quenched Martensitic Steel by Molybdenum and Niobium Alloying. *Metals* **2018**, *8*, 234. [[CrossRef](#)]
6. Larrañaga-Otegui, A.; Pereda, B.; Jorge-Badiola, D.; Gutiérrez, I. Austenite Static Recrystallization Kinetics in Microalloyed B Steels. *Met. Mater. Trans. A* **2016**, *47*, 3150–3164. [[CrossRef](#)]
7. He, X.; Djahazi, M.; Jonas, J.; Jackman, J. The non-equilibrium segregation of boron during the recrystallization of Nb-treated HSLA steels. *Acta Met. Mater.* **1991**, *39*, 2295–2308. [[CrossRef](#)]
8. Hulka, K.; Kern, A.; Schrieffer, U. Application of Niobium in Quenched and Tempered High-Strength Steels. *Mater. Sci. Forum* **2005**, *500–501*, 519–526. [[CrossRef](#)]
9. Miao, C.; Shang, C.; Zhang, G.; Subramanian, S. Recrystallization and strain accumulation behaviors of high Nb-bearing line pipe steel in plate and strip rolling. *Mater. Sci. Eng. A* **2010**, *527*, 4985–4992. [[CrossRef](#)]

10. Hutchinson, C.; Zurob, H.; Sinclair, C.; Brechet, Y. The comparative effectiveness of Nb solute and NbC precipitates at impeding grain-boundary motion in Nb steels. *Scr. Mater.* **2008**, *59*, 635–637. [[CrossRef](#)]
11. Isasti, N.; Jorge-Badiola, D.; Taheri, M.L.; Uranga, P. Microstructural and precipitation characterization in Nb-Mo microalloyed steels: Estimation of the contributions to the strength. *Met. Mater. Int.* **2014**, *20*, 807–817. [[CrossRef](#)]
12. Larzabal, G.; Isasti, N.; Rodriguez-Ibabe, J.; Uranga, P. Evaluating Strengthening and Impact Toughness Mechanisms for Ferritic and Bainitic Microstructures in Nb, Nb-Mo and Ti-Mo Microalloyed Steels. *Metals* **2017**, *7*, 65. [[CrossRef](#)]
13. Lee, W.-B.; Hong, S.-G.; Park, C.-G.; Park, S.-H. Carbide precipitation and high-temperature strength of hot-rolled high-strength, low-alloy steels containing Nb and Mo. *Met. Mater. Trans. A* **2002**, *33*, 1689–1698. [[CrossRef](#)]
14. Togashi, F.; Nishizawa, T. Effect of Alloying Elements on the Mobility of Ferrite/Austenite Interface. *J. Jpn. Inst. Met.* **1976**, *40*, 12–21. [[CrossRef](#)]
15. Coldren, A.P.; Eldis, G.T. Using CCT Diagrams to Optimize the Composition of an As-Rolled Dual-Phase Steel. *JOM* **1980**, *32*, 41–48. [[CrossRef](#)]
16. Cizek, P.; Wynne, B.P.; Davies, C.H.J.; Hodgson, P.D. The Effect of Simulated Thermomechanical Processing on the Transformation Behavior and Microstructure of a Low-Carbon Mo-Nb Linepipe Steel. *Met. Mater. Trans. A* **2015**, *46*, 407–425. [[CrossRef](#)]
17. Isasti, N.; Jorge-Badiola, D.; Taheri, M.L.; Lopez, B.; Uranga, P. Effect of Composition and Deformation on Coarse-Grained Austenite Transformation in Nb-Mo Microalloyed Steels. *Met. Mater. Trans. A* **2011**, *42*, 3729–3742. [[CrossRef](#)]
18. Olasolo, M.; Uranga, P.; Rodriguez-Ibabe, J.; López, B. Effect of austenite microstructure and cooling rate on transformation characteristics in a low carbon Nb-V microalloyed steel. *Mater. Sci. Eng. A* **2011**, *528*, 2559–2569. [[CrossRef](#)]
19. Kajjalainen, A.J.; Suikkanen, P.; Linnell, T.J.; Karjalainen, L.P.; Kömi, J.; Porter, D.A. Effect of austenite grain structure on the strength and toughness of direct-quenched martensite. *J. Alloys Compd.* **2013**, *577*, S642–S648. [[CrossRef](#)]
20. Opiela, M.; Grzegorzczak, B. Thermo-mechanical Treatment of Forged Products of Ti-V-B Microalloyed Steel. In Proceedings of the Metal 2013, 22nd International Conference on Metallurgy and Materials, Brno, Czech Republic, 15–17 May 2013; Tanager Ltd.: Ostrava, Czechia, 2013; pp. 796–801.
21. Siwecki, T. Improving Mechanical Properties on High-Strength Steel Plate by Optimizing the Direct Quenching Process. In Proceedings of the International Symposium on the Recent Developments in Plate Steels, Winter Park, CO, USA, 19–22 June 2011.
22. Zurutuza, I.; Isasti, N.; Detemple, E.; Schwinn, V.; Mohrbacher, H.; Uranga, P. Effect of Thermomechanical Strategy and Mo-Nb-B Alloying Additions on High Strength Medium Carbon Q/Q&T Steels. In Proceedings of the Materials Science and Technology 2019 (MS&T19) Conference, Portland, OR, USA, 29 September–3 October 2019; pp. 1401–1408. [[CrossRef](#)]
23. Uranga, P.; Gutiérrez, I.; López, B. Determination of recrystallization kinetics from plane strain compression tests. *Mater. Sci. Eng. A* **2013**, *578*, 174–180. [[CrossRef](#)]
24. Calcagnotto, M.; Ponge, D.; Demir, E.; Raabe, D. Orientation gradients and geometrically necessary dislocations in ultrafine grained dual-phase steels studied by 2D and 3D EBSD. *Mater. Sci. Eng. A* **2010**, *527*, 2738–2746. [[CrossRef](#)]
25. Zhou, T.; Babu, R.P.; Hou, Z.; Odqvist, J.; Hedström, P. Precipitation of multiple carbides in martensitic CrMoV steels—Experimental analysis and exploration of alloying strategy through thermodynamic calculations. *Materialia* **2020**, *9*, 100630. [[CrossRef](#)]
26. Mohrbacher, H.; Senuma, T. Alloy Optimization for Reducing Delayed Fracture Sensitivity of 2000 MPa Press Hardening Steel. *Metals* **2020**, *10*, 853. [[CrossRef](#)]
27. Seol, J.-B.; Na, S.-H.; Gault, B.; Kim, J.-E.; Han, J.-C.; Park, C.-G.; Raabe, D. Core-shell nanoparticle arrays double the strength of steel. *Sci. Rep.* **2017**, *7*, srep42547. [[CrossRef](#)]
28. Yamasaki, S.; Bhadeshia, H.K.D.H. Modelling and characterisation of Mo₂C precipitation and cementite dissolution during tempering of Fe–C–Mo martensitic steel. *Mater. Sci. Technol.* **2003**, *19*, 723–731. [[CrossRef](#)]
29. Fujita, N.; Bhadeshia, H. Precipitation of molybdenum carbide in steel: Multicomponent diffusion and multicomponent capillary effects. *Mater. Sci. Technol.* **1999**, *15*, 627–634. [[CrossRef](#)]
30. Pickering, F.B.; Gladman, T. *Metallurgical Developments in Carbon Steels*; Special Report No. 81; Iron and Steel Institute: London, UK, 1963.
31. Iza-Mendia, A.; Gutiérrez, I. Generalization of the existing relations between microstructure and yield stress from ferrite-pearlite to high strength steels. *Mater. Sci. Eng. A* **2013**, *561*, 40–51. [[CrossRef](#)]
32. Kubin, L.; Mortensen, A. Geometrically necessary dislocations and strain-gradient plasticity: A few critical issues. *Scr. Mater.* **2003**, *48*, 119–125. [[CrossRef](#)]
33. Tomita, Y.; Okabayashi, K. Effect of microstructure on strength and toughness of heat-treated low alloy structural steels. *Met. Mater. Trans. A* **1986**, *17*, 1203–1209. [[CrossRef](#)]
34. Wang, C.; Wang, M.; Shi, J.; Hui, W.; Dong, H. Effect of Microstructure Refinement on the Strength and Toughness of Low Alloy Martensitic Steel. *J. Mater. Sci. Technol.* **2007**, *23*, 659–664.
35. Morito, S.; Ohba, T. Crystallographic Analysis of Characteristic Sizes of Lath Martensite Morphology. In *Fundamentals of Martensite and Bainite toward Future Steels with High Performance*; Furuhashi, T., Tsuzaki, K., Eds.; ISIJ: Tokyo, Japan, 2007; pp. 57–62.
36. Morris, J.J.W. On the Ductile-Brittle Transition in Lath Martensitic Steel. *ISIJ Int.* **2011**, *51*, 1569–1575. [[CrossRef](#)]
37. Hannula, J.; Kömi, J.; Porter, D.A.; Somani, M.C.; Kajjalainen, A.; Suikkanen, P.; Yang, J.-R.; Tsai, S.-P. Effect of Boron on the Strength and Toughness of Direct-Quenched Low-Carbon Niobium Bearing Ultra-High-Strength Martensitic Steel. *Met. Mater. Trans. A* **2017**, *48*, 5344–5356. [[CrossRef](#)]

38. Isasti, N.; Jorge-Badiola, D.; Taheri, M.L.; Uranga, P. Microstructural Features Controlling Mechanical Properties in Nb-Mo Microalloyed Steels. Part I: Yield Strength. *Met. Mater. Trans. A* **2014**, *45*, 4960–4971. [[CrossRef](#)]
39. Hutchinson, B.; Hagström, J.; Karlsson, O.; Lindell, D.; Tornberg, M.; Lindberg, F.; Thuvander, M. Microstructures and hardness of as-quenched martensites (0.1–0.5%C). *Acta Mater.* **2011**, *59*, 5845–5858. [[CrossRef](#)]
40. Mohrbacher, H.; Yang, J.-R.; Chen, Y.-W.; Rehl, J.; Hebesberger, T. Metallurgical Effects of Niobium in Dual Phase Steel. *Metals* **2020**, *10*, 504. [[CrossRef](#)]
41. Ashby, M.F. *Physics of Strength and Plasticity*; Argon, A.S., Ed.; MIT Press: Cambridge, MA, USA, 1969; p. 113.
42. Larzabal, G.; Isasti, N.; Rodriguez-Ibabe, J.M.; Uranga, P. Precipitation Strengthening by Induction Treatment in High Strength Low Carbon Microalloyed Hot-Rolled Plates. *Met. Mater. Trans. A* **2018**, *49*, 946–961. [[CrossRef](#)]
43. Huang, B.M.; Yang, J.-R.; Yen, H.W.; Hsu, C.H.; Huang, C.Y.; Mohrbacher, H. Secondary hardened bainite. *Mater. Sci. Technol.* **2014**, *30*, 1014–1023. [[CrossRef](#)]
44. Xie, Z.; Ren, Y.; Zhou, W.; Yang, J.; Shang, C.; Misra, R. Stability of retained austenite in multi-phase microstructure during austempering and its effect on the ductility of a low carbon steel. *Mater. Sci. Eng. A* **2014**, *603*, 69–75. [[CrossRef](#)]
45. Colla, V.; De Sanctis, M.; DiMatteo, A.; Lovicu, G.; Solina, A.; Valentini, R. Strain Hardening Behavior of Dual-Phase Steels. *Met. Mater. Trans. A* **2009**, *40*, 2557–2567. [[CrossRef](#)]
46. Kamikawa, N.; Sato, K.; Miyamoto, G.; Murayama, M.; Sekido, N.; Tsuzaki, K.; Furuhashi, T. Stress-strain behavior of ferrite and bainite with nano-precipitation in low carbon steels. *Acta Mater.* **2015**, *83*, 383–396. [[CrossRef](#)]

Article

Toughness Property Control by Nb and Mo Additions in High-Strength Quenched and Tempered Boron Steels

Irati Zurutuza ^{1,2}, Nerea Isasti ^{1,2}, Eric Detemple ³ , Volker Schwinn ³, Hardy Mohrbacher ^{4,5}  and Pello Uranga ^{1,2,*} 

- ¹ CEIT-Basque Research and Technology Alliance (BRTA), Materials and Manufacturing Division, 20018 Donostia/San Sebastián, Basque Country, Spain; izurutuza@ceit.es (I.Z.); nisasti@ceit.es (N.I.)
- ² Mechanical and Materials Engineering Department, Universidad de Navarra, Tecnun, 20018 Donostia/San Sebastián, Basque Country, Spain
- ³ AG der Dillinger Hüttenwerke, 66763 Dillingen/Saar, Germany; Eric.Detemple@dillinger.biz (E.D.); Volker.Schwinn@dillinger.biz (V.S.)
- ⁴ NiobelCon BV, 2970 Schilde, Belgium; hm@niobelcon.net
- ⁵ Department of Materials Engineering (MTM), KU Leuven, 3001 Leuven, Belgium
- * Correspondence: puranga@ceit.es; Tel.: +34-943-212-800

Abstract: The synergetic effect on hardenability by combining boron with other microalloying elements (such as Nb, Mo and Nb + Mo) is widely known for high-strength medium carbon steels produced by direct quenching and subsequent tempering treatment. The improvement of mechanical properties could be reached through optimization of different mechanisms, such as solid solution hardening, unit size refinement, strain hardening, fine precipitation hardening and the effect of carbon in solid solution. The current study proposes a procedure for evaluating the contribution of different microstructural aspects on Charpy impact toughness. First, the effect that austenite conditioning has on low-temperature transformation unit sizes and microstructural homogeneity was analysed for the different microalloying element combinations. A detailed crystallographic characterization of the tempered martensite was carried out using electron backscattered diffraction (EBSD) in order to quantify the effect of unit size refinement and dislocation density. The impact of heterogeneity and presence of carbides was also evaluated. The existing equations for impact transition temperature (ITT_{50%}) predictions were extended from ferrite-pearlite and bainitic microstructures to tempered martensite microstructures. The results show that microstructural refinement is most beneficial to strength and toughness while unit size heterogeneity has a particularly negative effect on ductile-to-brittle transition behaviour. By properly balancing alloy concept and processing, steel having a yield strength above 900 MPa and low impact transition temperature could be obtained by direct quenching and tempering.

Keywords: martensite; thermomechanical simulations; toughness properties; microalloying elements



Citation: Zurutuza, I.; Isasti, N.; Detemple, E.; Schwinn, V.; Mohrbacher, H.; Uranga, P. Toughness Property Control by Nb and Mo Additions in High-Strength Quenched and Tempered Boron Steels. *Metals* **2021**, *11*, 95. <https://doi.org/10.3390/met11010095>

Received: 21 December 2020
Accepted: 1 January 2021
Published: 5 January 2021

Publisher's Note: MDPI stays neutral with regard to jurisdictional claims in published maps and institutional affiliations.



Copyright: © 2021 by the authors. Licensee MDPI, Basel, Switzerland. This article is an open access article distributed under the terms and conditions of the Creative Commons Attribution (CC BY) license (<https://creativecommons.org/licenses/by/4.0/>).

1. Introduction

Quenching and tempering treatments are well established for achieving a favourable combination of strength and toughness properties for a wide range of applications. In quenched and tempered steels, packet size and particle distribution as well as brittle intergranular fracture modes by grain boundary segregation of impurities in ferrite (temper embrittlement) or precipitates in austenite are of importance. Anisotropy of toughness arises from banded structures especially when non-metallic inclusions such as MnS are stretched out [1].

Cooling installations in modern rolling mills allow for direct quenching from the rolling heat with the option of self-tempering or offline tempering. This approach is economically attractive. It has to be considered, however, that properties can be anisotropic, in this case due to austenite pancaking [2].

For ensuring full transformation into martensite of especially heavier gages under technically feasible cooling rates, hardenability-increasing alloying elements have to be used. The use of boron microalloying is common practice for achieving through hardening low- and medium-carbon manganese steels. However, boron must be segregated as the solute to the austenite grain boundary before quenching. Titanium microalloying protects the loss of solute boron as BN by forming more stable TiN. Furthermore, combined alloying of Nb and B as well as Mo and B has been described in the literature as enhancing boron's hardenability effect [2–6]. Both elements prevent boron from forming boron carbides ($\text{Fe}_{23}(\text{C},\text{B})_6$) in the austenite grain boundaries that would reduce solute boron's effect of obstructing ferrite nucleation [7].

Usually, the tempering treatment softens the martensitic microstructure, thereby promoting an improvement of toughness and ductility [8,9]. However, the role of the different microstructural features must be taken into account in order to avoid brittle fracture behaviour [10]. Since the martensite substructure forms within the austenite grains prior to quenching [11], austenite conditioning has a significant impact on achieving an optimal balance of strength and toughness [12]. Several works analyse the role of the microstructure prior to austenitizing in terms of mechanical properties, and different ways of refining grain size have been proposed in the literature [13–15]. Thermomechanical treatment can affect the size and shape of the final martensite and the level of segregation at grain boundaries, favouring intergranular fracture. When microalloying elements are added, strong pancaking of austenite can be reached. A significant synergetic effect of combining Nb and B on recrystallization delay has been reported in several works [16]. The addition of Nb is widely used to delay the static recrystallization kinetics of austenite through two different mechanisms: solute drag and strain-induced precipitation [17]. This promotes the accumulation of deformation on the austenite prior to phase transformation, leading to microstructural refinement of the resulting microstructure and ensuring enhancement of both tensile and toughness properties [18].

In order to evaluate the effect of austenite conditioning in terms of microstructural homogeneity and toughness properties, austenitic structure characterization has to be performed. For equiaxed and polygonal austenite, analysis and quantification of the austenite grain size distribution usually relies on optical microscopy, yet for highly deformed austenitic structures, the austenite grain boundaries cannot be properly revealed by optical microscopy. Consequently, the use of the electron backscattered diffraction (EBSD) technique for reconstructing the prior austenite from the martensitic microstructure has become an essential tool for reliable quantitative characterization. In this respect, efforts on the development of several austenite reconstruction methods have been made recently [19–21].

Previous studies evaluated the effect of tempering treatment on directly quenched low-alloy ultrahigh-strength steels in terms of microstructure and mechanical properties [22,23]. Pallaspuro et al. [23] reported that low-impact transition temperatures at which 28 J of impact energy is reached (ITT_{28J}) can be achieved after direct quenching and that good toughness properties can be ensured without tempering treatment. However, they observed a reduction in yield strength and an improvement in ductility as well as toughness after tempering. They noticed a clear beneficial effect of microstructural homogeneity in martensite [23]. The presence of coarser effective grain sizes reflects the longer tailing out of unit size distributions curves. These result in the deterioration of toughness properties. The improvement of toughness observed for the direct quenched as compared to the reheated and quenched states is attributed to the formation of more homogeneous martensitic microstructures with a lower fraction of coarse grains [23]. The positive effect of austenite pancaking on martensite homogeneity has also been reported by Saastamoinen et al. [24]. In addition, they concluded that the effective grain size at 90% cut-off in the cumulative grain size distribution is the key criterion controlling toughness properties for both the Direct Quenching (DQ) and DQ+tempering (DQ+T) processing strategies. Regarding the effect of boron in terms of tensile/toughness properties, Hannula et al. [12] studied the influence of adding boron to a low-carbon Nb microalloyed martensitic steel. It was

demonstrated that removing boron significantly improved the toughness properties due to the formation of a finer and more homogeneous martensitic microstructure in the B-free steel. In another work, Hannula et al. [25] analysed the impact of adding Mo and Nb on the martensitic microstructure and mechanical properties of laboratory-rolled DQ and DQ+T plates. They observed that the addition of Mo and Nb improves the strength considerably (0.25 Mo–Nb) via an increased dislocation density and fine precipitation hardening. However, 0.25 Mo–Nb steel shows worse toughness properties compared to 0.25 Mo steel due to intense precipitation hardening in the Nb-grade. Even though upgrading tensile properties could be reached through optimization of different strengthening mechanisms, toughness properties could be impaired. In this context, the exact interaction between toughness properties and the different microstructural features has to be better understood. Effort has been made in that respect regarding toughness properties in ferritic and non-polygonal bainitic microstructures [26–29].

Several relationships have been proposed in the literature for quantitatively predicting the impact transition temperatures [28–31]. Most of the proposed approaches consider the impact of solid solution, pearlite fraction, dislocation density and fine precipitation (both represented by the $\Delta\sigma_y$ term), carbide thickness (t) and unit size refinement. The transition temperature can be represented by different definitions, one of them being the fracture appearance transition temperature (ITT50%). Most approaches were derived from analysing low-carbon ferrite-pearlite steels. These equations account for microstructural grain size heterogeneities. Several works suggested that a parameter accounting for the presence of coarse grains and microstructural heterogeneity is required for accurately predicting the ductile-to-brittle transition temperature [32,33]. In that sense, Larzabal et al. [34] proposed a relationship (Equation (1)) to predict ITT50% for low-carbon Nb, NbMo and TiMo microalloyed steels, thereby taking into account the effect of microstructural heterogeneity and the presence of hard secondary phases such as pearlite and Martensite-austenite (MA) islands. This relationship is applicable to ferritic-pearlitic and bainitic microstructures [34].

$$ITT50\%(^{\circ}C) = -11Mn + 42Si + 700(N_{free})^{0.5} + 15(pct\ Pearlite + pct\ MA)^{\frac{1}{3}} + 0.26\Delta\sigma_y - 14(D_{15^{\circ}})^{-0.5} + 63\left(\frac{D_{20\%}}{D_{15^{\circ}}}\right)^{0.5} + 18(DMA)^{0.5} - 42 \quad (1)$$

where $D_{15^{\circ}}$ is the high angle boundary unit size, $D_{20\%}$ is the cut-off unit size at the 80% area fraction in a grain size distribution and DMA is the average MA island size.

The present study aims to modify and extend this relationship for use in martensitic steels. In this context, the relationship between microstructure and toughness properties is analysed in four different boron microalloyed carbon–manganese steels after direct quenching and tempering treatment. The strength properties of the same steels have been recently published [35]. A model predicting the yield strength has been proposed and validated for both the quenched and tempered martensitic conditions incorporating the interaction between the quenched microstructure, the tempering treatment and the addition of microalloying elements [35]. Specific effects related to alloying of niobium and molybdenum have been revealed as well. For understanding the toughness properties, Charpy tests are performed with the same alloys in direct quenched and tempered conditions. Based on elaborate microstructural characterization, a modified relationship for predicting ITT50% is defined and validated. This platform allows for the definition of optimized alloy concepts and processing strategies for obtaining superior strength and toughness properties in tempered martensitic steels.

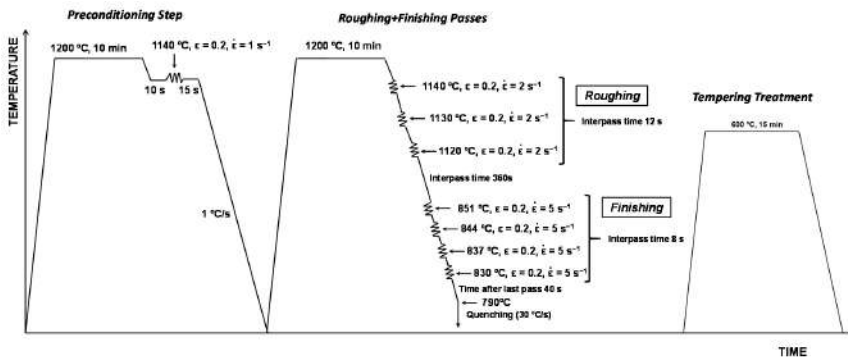
2. Materials and Methods

Table 1 shows the chemical composition of the selected medium carbon steels with 0.16% of C and 20 ppm of boron. Besides a CMnB steel, three different microalloyed steels were also studied, microalloyed with Nb, Mo and NbMo. The Nb level is 0.026%, and Mo content is about 0.5%.

Table 1. Chemical composition of the studied steels (weight percent).

Steel	C	Si	Mn	Mo	Nb	B
CMnB	0.15	0.32	1.05	-	-	0.0022
CMnNbB	0.16	0.29	1.05	-	0.026	0.0019
CMnMoB	0.16	0.28	1.07	0.5	-	0.0022
CMnNbMoB	0.16	0.31	1.07	0.5	0.026	0.0018

Plane strain compression tests were carried out in order to simulate the plate hot rolling process followed by direct quenching and subsequent tempering treatments. Deformation by plane strain compression was carried out in a servo-hydraulic machine equipped with an induction furnace for reheating. After this stage, the specimen was automatically transferred to a resistance furnace that was set at the deformation temperature and inside which the tools were kept hot. The specimen temperature was continuously monitored by an inserted thermocouple. Rectangular samples 60 mm long, 30 mm wide and 22 mm thick were used with a tool width of 15 mm. The cycle started with a preconditioning step, with the purpose of ensuring the refinement of the as-cast austenitic structure and minimizing the presence of coarse austenite grains at the reheating temperature (see the thermomechanical schedule in Figure 1). Then, the plate hot rolling simulation was carried out based on reheating at 1200 °C for 10 min followed by three roughing deformation passes ($\epsilon = 0.2$ at 2 s^{-1} and an interpass time of 3 s) at decreasing temperature in the interval between 1140 and 1120 °C. Subsequently, after holding for 360 s, 4 finishing passes were applied (strain of 0.2 at 5 s^{-1} with an interpass time of 8 s) in the temperature range between 851 and 830 °C. Finally, accelerated cooling was applied until room temperature (cooling rate of about 30 °C/s above 300 °C and below a cooling rate of approximately 10 °C/s). Afterwards, a tempering treatment was carried out at 600 °C for 15 min. Full details of the thermomechanical schedule can be found in Reference [35].

**Figure 1.** Schematics of the applied plane strain compression cycle.

Plane compression samples show that heterogeneous strain distribution through thickness was associated with the geometry and friction of the sample/tool [36]. Therefore, the specimens used for the microstructural characterization and Charpy tests were machined from the centre of the plane strain compression samples, with the purpose of minimizing strain gradients along the section of the plane strain compression samples.

Different characterization techniques were employed for microstructural characterization, such as optical microscopy (OM, LEICA DM15000 M, Leica microsystems) and field-emission gun scanning electron microscopy (FEGSEM, JEOL JSM-7100F). Besides analysing the martensitic microstructure after etching with Nital 2%, the austenitic structures were also characterized after etching in a solution of saturated picric acid and HCl

after polishing. For crystallographic unit sizes, measurements of the martensitic microstructure electron backscattered diffraction (EBSD) technique were employed. Additionally, EBSD data were used for reconstruction of the prior austenite grain orientation, and the approach described in [19,20] was applied. EBSD sample preparation consisted of a conventional polishing route, using diamond liquids down to 1 µm and final polishing with colloidal silica. EBSD was performed on the equipment with a camera NORDLYS II with an acquisition program and data analysis, OXFORD HKL CHANNEL 5 PREMIUM coupled to the JEOL JSM-7100 F (FEG-SEM). The selected step size and scanned area varied depending on the required resolution. A scan step size of 0.2 µm and a total scanned area of 140 × 140 µm were defined for unit size quantification. For reconstructing the austenite prior to transformation, higher scanned area of 300 × 300 µm² was used and a step size of 0.5 µm was defined. Two different crystallographic unit sizes were defined based on low- and high-angle boundaries. Low-angle units were defined for grain boundary misorientation between 2 and 15°, whereas high-angle unit sizes were set for a grain boundary misorientation higher than 15°.

Regarding toughness property evaluation, Charpy sub-size specimens (approximately 4 × 10 × 55 mm³) were machined from the central part of the plane strain compression samples, and Charpy tests were carried out within a −120 to 40 °C test temperature range (Tinius Olsen Model Impact 104 pendulum impact tester with maximum capacity of 410 J). The proportionality rule shown in Equation (2) can be assumed for these Charpy specimen thicknesses [28].

$$K_{v10} = \frac{10}{B} K_{vB} \tag{2}$$

where K_{v10} and K_{vB} are the absorbed impact energy for 10 mm and B sample thickness, respectively. For determining the impact transition curves, the modified hyperbolic tangent fitting algorithm suggested by Wallin was considered [37].

3. Results and Discussion

3.1. Mechanical Behaviour

In Table 2, upper-shelf energies (US) as well as the transition temperatures for an impact energy value of 27 J (ITT27 J) and the temperature at which the sample shows a 50% ductile–brittle appearance (ITT50%) are shown. Yield strength and tensile strength values previously reported in [35] are included. Figure 2 shows the comparison between the impact transition curves measured in each chemical composition (ductile fraction is plotted as a function of test temperature). Slightly better toughness properties are observed in CMnNb and CMnMoB steels compared to the CMnB grade one. ITT50% values of −66, −75 and −84 °C were quantified for the CMnB, CMnNbB and CMnMoB grades, respectively. Conversely, when Nb and Mo were added simultaneously, the impact transition curve shifted to higher temperatures, showing worse toughness properties (an ITT50% of −10 °C was measured in NbMo microalloyed steel).

Table 2. US (Upper-Shelf Energy), ITT27J, ITT50%, yield strength and tensile strength values measured from Charpy and tensile tests.

Steel	US (J)	ITT 27 J (°C)	ITT 50% (°C)	Yield Strength (MPa)	Tensile Strength (MPa)
CMnB	108	−63	−66	617	700
CMnNbB	112	−59	−75	757	818
CMnMoB	97	−80	−84	943	991
CMnNbMoB	82	−1	−10	977	1034

Detailed fractographic examination was performed on the tested Charpy samples (fracture surfaces were analysed) with the aim of evaluating possible cleavage crack-initiation sites and microstructural features in their vicinity. In Figure 3, cleavage initiation sites are shown at different magnifications for CMnNbB and CMnMoB steels (test temperature of

–100 °C and –120 °C, respectively). In the martensitic microstructures, crack initiators are not easy to detect. However, differences in the facet sizes are observed depending on the chemistry. Coarser facets are noticed in the CMnNbB grade steel (see Figure 3a) whereas CMnMoB shows the finest facets (see Figure 3c). Additionally, fracture surfaces were analysed after Nital 2% etching in order to better distinguish the microstructural features controlling the fracture. In both steels, some inclusions, such as coarse Ti nitride particles, were identified in the crack-initiation regions, as shown in Figure 3b,d.

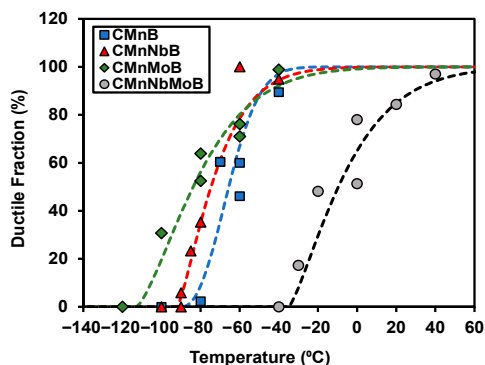


Figure 2. Effect of the addition of microalloying elements on toughness properties (ductile fraction as a function of test temperature).

3.2. Microstructural Characterization

3.2.1. Analysis of the Prior Austenitic Structure

Optical micrographs illustrating the parent austenite grain structures are shown in Figure 4. A completely different austenite morphology is noticed depending on the alloy composition. In CMnB steel, equiaxed austenite grains are observed, as shown in Figure 4a. In the Nb-added alloy, a combination of pancaked and very small equiaxed grains is observed. The small grains originate from dynamic recrystallization (DRX) due to the accumulated strain reflected on the high degree of pancaking. For Mo-containing grades, a strong accumulation of deformation on austenite is reflected by a fully pancaked microstructure (see Figure 4c,d, for CMnMoB and CMnNbMoB, respectively).

The delay that molybdenum and niobium exert on dynamic recrystallization kinetics is associated with two different phenomena. On the one hand, the solute drag of both Mo and Nb impedes the mobility of high-angle boundaries [38–40]. On the other hand, dynamic recrystallization could be affected by the impact of Mo on the Nb carbonitride precipitation. It is reported that molybdenum reduces the diffusivity of carbon in austenite [41], lowering the available C and consequently reducing Nb(C,N) formation. Therefore, a higher content of Nb remains in solution, impeding grain boundary mobility. Nb in solid solution has a stronger effect than Nb-based precipitates in hindering the movement of grain boundaries during DRX [42].

For highly deformed austenitic structures, the austenite grain boundaries are not properly revealed by chemical etching, and therefore, characterization of the austenitic structure by optical microscopy becomes more complex. In this respect, the use of the EBSD technique for reconstruction of the prior austenite has become an essential tool for characterizing and quantifying the austenitic structure from the orientation relationships between the parent austenite and final martensite [19,20]. Figure 5 shows the results for the reconstruction technique applied to CMnB and CMnNbMoB steels. The applied methodology starts by performing an EBSD scan in a selected area (see Figure 5a,e for CMnB and CMnNbMoB steels, respectively). EBSD maps and optical micrographs are aligned with the compression

deformation direction parallel to the vertical axis. From the martensitic microstructures, the parent austenite grain structure prior to transformation is calculated. In order to validate the austenite reconstruction procedure, the samples were subsequently etched by picric acid and analysed by optical microscopy in the same region where the EBSD scan was performed, as illustrated in Figure 5c,g. Additionally, the austenite grains were manually drawn in each case with the purpose of quantifying the austenite grain size distribution in the same area by OM. Figure 5d,h presents the comparison between austenite grain size distributions measured by the EBSD technique (considering a tolerance angle of 10° , as previously proposed in [20]) and by optical microscopy (considering equivalent diameter method). Analysing Figure 5d,h confirms that quite similar austenite size distributions are achieved by both techniques (EBSD and OM).

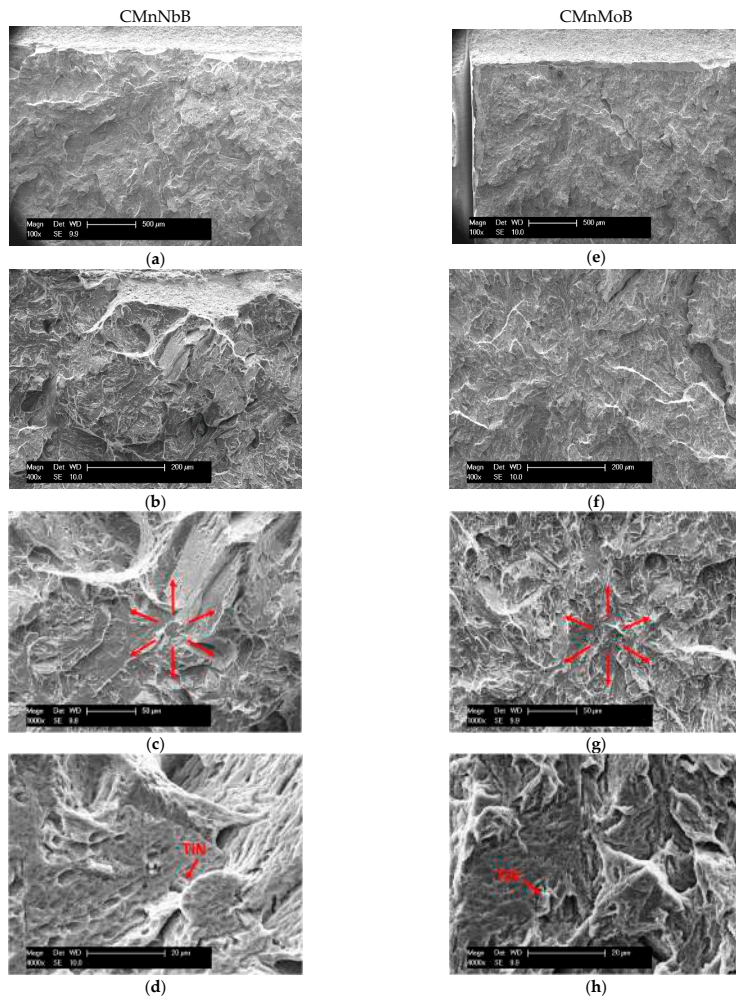


Figure 3. Fracture surfaces at different magnifications showing the crack-initiation site: (a–d) CMnNbB (test temperature of -100°C) and (e–h) CMnMoB (test temperature of -120°C).

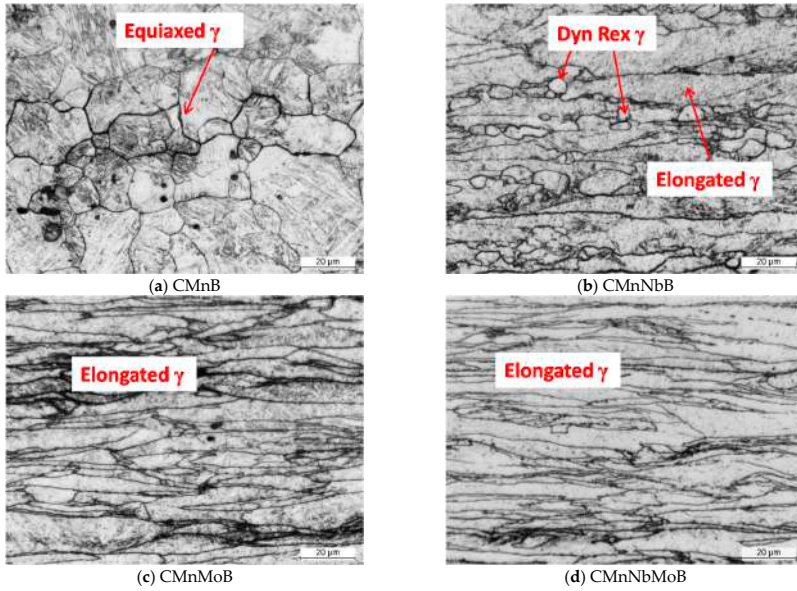


Figure 4. Optical micrographs of the austenite structure after quenching corresponding to (a) CMnB, (b) CMnNbB, (c) CMnMoB and (d) CMnNbMoB steels (picric acid etching is used).

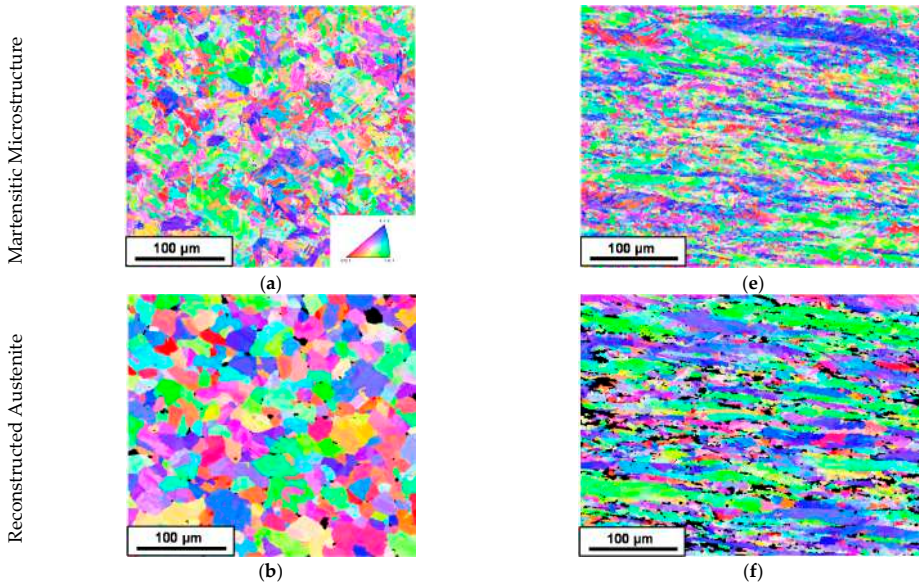


Figure 5. Cont.

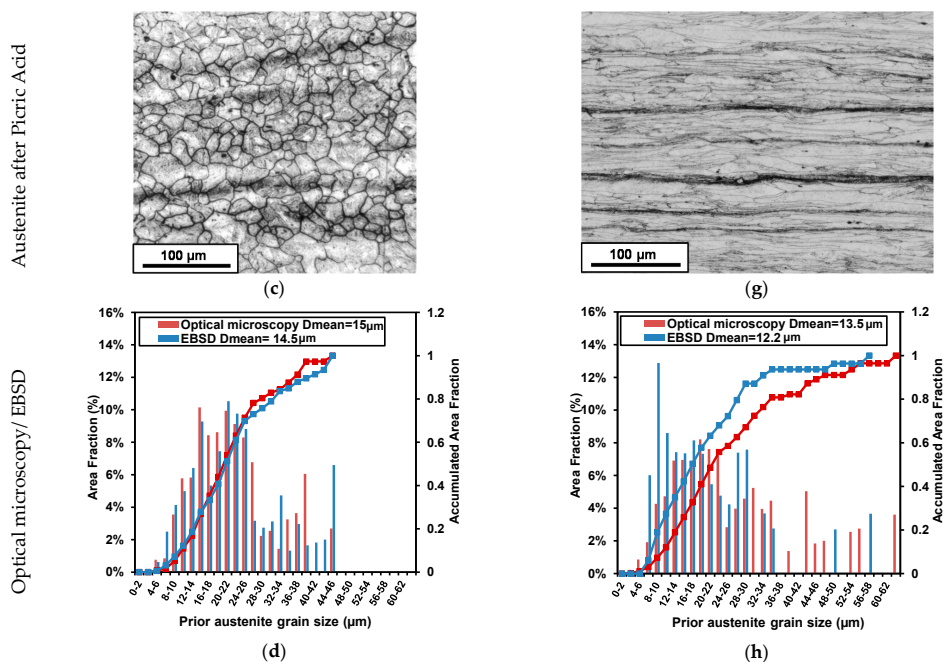


Figure 5. (a,e) Martensitic microstructure, (b,f) reconstructed austenite by electron backscattered diffraction (EBSD), (c,g) optical images corresponding to austenite obtained after picric acid, (d,h) austenite size distributions measured by optical microscopy and EBSD technique for (a–d) CMnB and (e–h) CMnNbMoB steels (Applied strain direction, equivalent to rolling direction (RD), is considered for Inverse Pole Figure (IPF) representation).

3.2.2. Quantification of Mean unit Sizes and Microstructural Homogeneity

High-resolution EBSD scans were also carried out to measure martensite unit sizes. High-angle boundaries act as effective obstacles to cleavage fracture, and therefore, the effective unit size affecting toughness properties was defined by a threshold of 15° ($D15^\circ$). Figure 6a,b shows the grain boundary maps corresponding to Nb and NbMo microalloyed steels, respectively. Low-angle boundaries, between 2° and 15° , are shown in red, whereas high-angle boundaries ($>15^\circ$) are drawn in black. In both steel grades, complex microstructures as well as very fine unit sizes can be distinguished. When Mo is added to Nb microalloyed steel, an increase in the low-angle boundaries is apparent and the martensitic matrix presents a more pronounced substructure (see Figure 6b). For evaluating the density of different boundary types, the grain boundary length per unit area was calculated [43]. Concerning low-angle boundaries between 2° and 15° , grain boundary length values per unit area of 0.98, 1.55, 1.79 and $1.98 \mu\text{m}^{-1}$ are measured for CMnB, CMnNbB, CMnMoB and CMnNbMoB steels, respectively. The low-angle boundary density increases with the addition of microalloying elements, reaching the highest density in the NbMo-microalloyed grade.

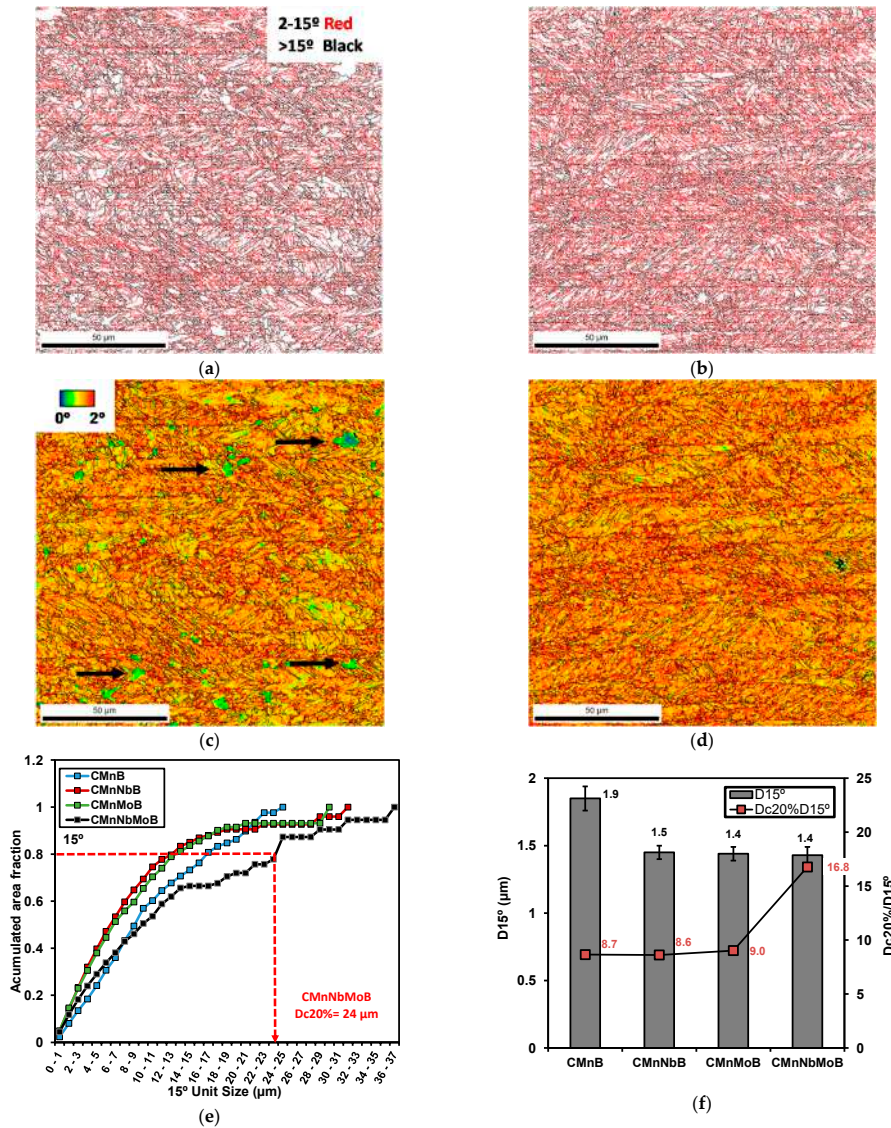


Figure 6. (a,b) Grain boundary maps and (c,d) Kernel maps corresponding to (a,c) Nb and (b,d) NbMo grades, (e) comparison between the unit size distributions taking into account 15° misorientation criteria and (f) D15° and Dc20%/D15° values measured for each steel grade.

Additionally, the dislocation density is evaluated from Kernel Average Misorientation (KAM) maps [34,44]. For the calculation of KAM maps, misorientation lower than 2° is assumed and the third neighbour is selected. Figure 6c,d shows the Kernel maps corresponding to Nb- and NbMo-microalloyed steels, respectively. For the CMnNbMo

steel (see Figure 6d), the KAM map is mainly coloured by yellow-orange, reflecting the presence of a highly dislocated tempered martensite. However, in the Nb-microalloyed steel (see Figure 6c), in addition to regions represented in yellow-orange, some grains coloured by blue-green can be clearly distinguished (see black arrows in Figure 6c), showing the presence of grains with lower dislocation density in the martensitic matrix. This is attributed to the formation of non-polygonal ferritic islands within the martensitic microstructure of the CMnNbB steel. Furthermore, these ferritic grains are characterized by the lack of substructure, as can be clearly observed in the grain boundary map shown in Figure 6a.

Within the softer ferritic phase, low angle boundaries (drawn in red) are absent (see Figure 6a). The presence of non-polygonal ferritic islands inside a martensitic matrix cannot be due to a lack of a cooling rate. It rather indicates that the obstruction of ferrite nucleation by solute boron was locally not effective. Since solute boron must be segregated to the austenite grain boundary for deploying this effect, it is reasonable to assume that an insufficient amount of boron was present in part of the grain austenite boundaries. It also appears that, in the CMnNbB steel, where this phenomenon is observed, the very small equiaxed dynamically recrystallized austenite islands (Figure 4b) coincide with these ferritic islands revealed in Figure 6c. It is possible that, at the instant of dynamic recrystallization, insufficient solute boron was left in the austenite matrix for segregation to these newly formed austenite grain boundaries, rendering a higher density of nucleation sites for ferrite formation.

Distribution diagrams of high-angle boundary unit sizes are plotted in Figure 6e for the different alloys. The measurements suggest that the addition of both Nb and Mo is beneficial as these elements promote the formation of finer unit sizes. However, when Nb and Mo are added in combination, a substantial fraction of coarser unit sizes appears in the distribution diagram, indicating the presence of mixed prior austenite grain sizes. This inhomogeneous austenite grain structure must originate from austenite conditioning. Principally, the two-stage deformation schedule applied in this study refines austenite grains by multiple recrystallizations during the first stage at higher temperature. The second deformation stage at lower temperature pancakes the formerly equiaxed austenite grains. Accordingly, size inhomogeneities can occur when an inhomogeneous grain structure is produced during the first deformation stage, for instance, by partial recrystallization provoking individual grains growing to larger sizes. Oppositely, dynamic recrystallization during severe pancaking in the second rolling stage can produce very fine austenite grains, which were observed in the CMnNbB steel (Figure 4b).

In Mo- and NbMo-microalloyed steels, austenite exhibits a pronounced pancake morphology prior to quenching caused by solute drag of Mo atoms and particle pinning related to Nb-based precipitates. A finer austenite thickness leads to finer effective grain size, resulting in improved tensile and toughness properties. By applying direct quenching after austenite conditioning, the martensite packet size is directly related to the austenite pancake thickness [45]. In Table 3, the Sv parameter related to the austenite boundary area per unit volume as well as the average austenite pancake thickness measured by optical microscopy are summarized. In addition, mean unit sizes quantified by EBSD technique are shown. The lowest Sv value is found for CMnB steel, and the coarsest austenite thickness is obtained. When Nb and/or Mo are added, the Sv parameter increases significantly, leading to a clear reduction of the austenite thickness. For CMnMoB grade steel, the Sv parameter reaches a maximum and the austenite thickness is the lowest. The strong accumulation of austenite deformation prior to transformation induces considerable refinement of the resulting martensitic microstructure. The lowest mean unit sizes ($D2^\circ$ and $D15^\circ$ values) are measured when Nb and Mo are added in combination, despite the smaller Sv parameter and larger austenite thickness compared to CMnMoB grade steel.

Table 3. Measured Sv parameter (grain boundary area per unit volume) and average austenite thickness for the different alloys: mean unit sizes were quantified by EBSD considering low- and high-angle misorientation criteria.

Steel	Sv (μm^{-1})	Austenite Thickness (μm)	D2° (μm)	D15° (μm)
CMnB	0.13	12.9 ± 0.8	1.26 ± 0.03	1.85 ± 0.1
CMnNbB	0.24	5.5 ± 0.2	0.92 ± 0.01	1.45 ± 0.05
CMnMoB	0.30	4.9 ± 0.2	0.86 ± 0.1	1.44 ± 0.05
CMnNbMoB	0.23	6.9 ± 0.4	0.85 ± 0.01	1.43 ± 0.06

In Figure 6f, the mean unit sizes measured for each steel grade are plotted together, assuming high-angle misorientation criteria (higher than 15°). The heterogeneity of the microstructure is measured by the Dc20% parameter [34], which is considered a useful criterion for defining the tail-out length of a size distribution curve. It corresponds to the cut-off unit size at the 80% area fraction in a grain size distribution, as indicated in Figure 6e. The ratio of Dc20%/D15° shown in Figure 6f increases considerably for the CMnNbMoB, indicating the presence of a more heterogeneous microstructure. The Dc20%/D15° ratios for the other alloys are nearly identical and approximately half of that found in the CMnNbMoB steel. From the data, it can be concluded that the inhomogeneity must have been generated during the first deformation stage. Djahazi et al. [46] demonstrated that the addition of boron to a Nb-microalloyed steel accelerates the precipitation of Nb(C,N) and induces it to occur at higher temperatures. Additionally, boron and molybdenum segregating to grain boundaries and dislocations can retard recrystallization after deformation. It is thus possible that particularly the combined alloying of niobium, molybdenum and boron already impedes recrystallization at rather high deformation temperatures [47], resulting in individual unrecrystallized austenite grains growing in size.

3.2.3. Quantification of Carbide Size and Area Fraction

Tempering treatment causes modification of the quenched martensite, leading to the formation of carbides. In Figure 7, FEGSEM images at high magnifications of the different steel alloys are presented. Depending on the chemistry, the impact of tempering differs considerably, and slightly coarser carbides are identified in CMnB grade steels (Figure 7a) and finer carbides are detected in the steels containing Mo (Figure 7c,d). In the tempered martensite, different types of carbides can be clearly distinguished [8]. Part of these carbides precipitates within the laths (at lath boundaries or other low-angle boundaries), while the other carbide fractions precipitate at high-angle boundaries, such as the prior austenite grain boundaries as well as martensite packet or block boundaries (Figure 7c). The latter carbides are generally coarser than those precipitating within the laths.

The carbide size and area fraction were evaluated for all alloys, taking into account both types of carbides located at low-angle (LAB) and high-angle (HAB) boundaries. The carbide size distributions shown in Figure 8 confirm that, for all alloys, the carbides located at high-angle boundaries are coarser than the carbides located at low-angle boundaries. Generally, coarser carbide size distributions are found in CMnB and CMnNbB steel as compared to the two alloys containing Mo. The carbides located at low-angle boundaries in the Mo-alloyed steels have approximately half the size compared to those in Mo-free steels. Furthermore, a higher area fraction of carbides is measured in the Mo-containing grades. Therefore, it can be concluded that Mo alloying promotes refinement of carbides and an increase in volume fraction. It was outlined in a previous paper [35] on the same steels that molybdenum participates in carbides of the MC, M₂C, M₆C and M₂₃C₆ types while Nb forms only MC-type carbides.

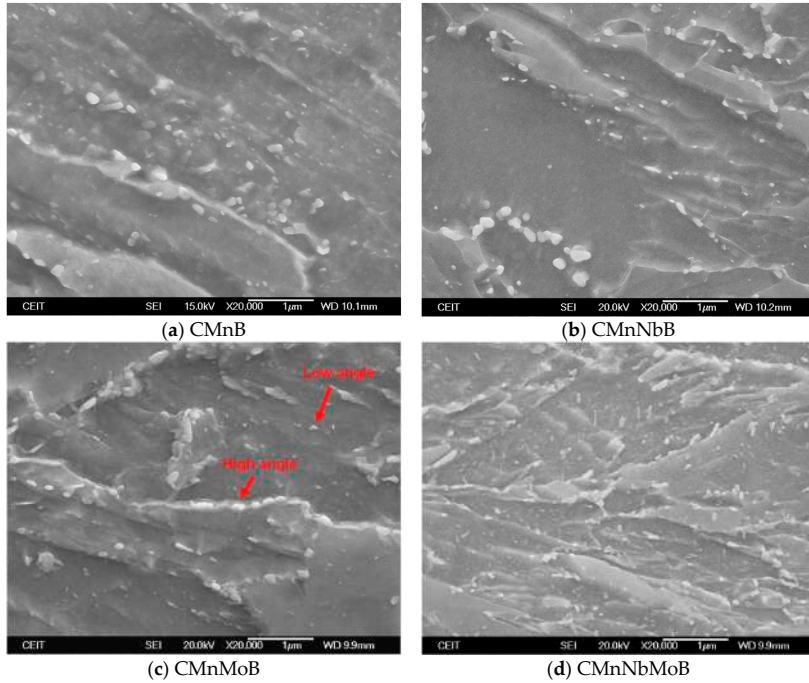


Figure 7. Field-emission gun scanning electron microscopy (FEGSEM) micrographs corresponding to (a) CMnB, (b) CMnNbB, (c) CMnMoB and (d) CMnNbMoB steels.

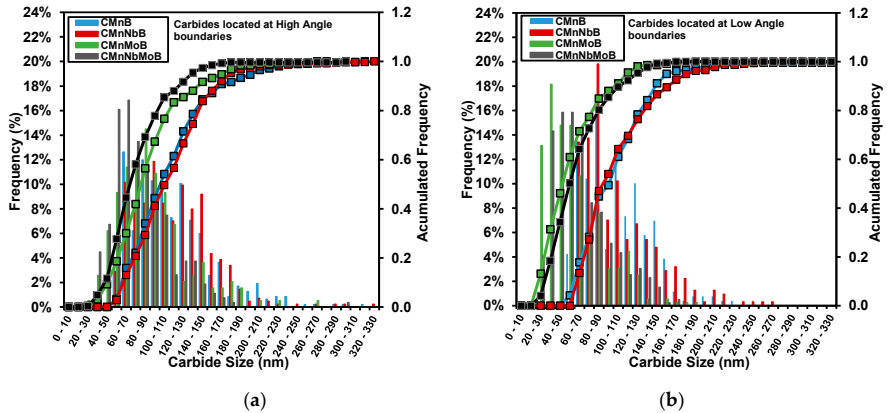


Figure 8. Comparison between carbide size distributions corresponding to the different steels and considering both grain boundaries: (a) carbides located at high-angle boundaries and (b) carbides located at low-angle boundaries.

As both carbide populations, i.e., at high- and low-angle boundaries, are considered to have similar detrimental effects on toughness, only the total carbide population is taken into account for further interpretation. The characteristics of the total carbide population

in the four alloys are summarized in Table 4. In addition to carbide size refinement caused by the addition of Mo and NbMo, a clear increment of carbide density is detected when molybdenum is added. A synergy between Mo and Nb with regard to carbide area fraction is apparent.

Table 4. Measured mean carbide sizes and carbide densities considering total carbide population (sum of high-angle and low-angle boundaries).

Steel	Carbide Size (nm) (Total Carbide Population)	Area Fraction (%) (Total Carbide Population)
CMnB	110.1 ± 3	0.54
CMnNbB	111.3 ± 2.9	0.60
CMnMoB	70.6 ± 3	1.46
CMnNbMoB	72.3 ± 2.4	1.72

3.2.4. Additional Contributions to Toughness

Besides the influence of effective unit size and carbide population and among the different microstructural aspects, the presence of secondary hard phases, hardening due to dislocation density and fine precipitation, as well as the strengthening associated with carbon in solid solution have impacts on toughness. In the following paragraphs, a more detailed study of each of these influencing factors will be considered.

(1) Presence of hard secondary phases

Concerning the differences in the final microstructures depending on alloy composition, the presence of non-polygonal ferrite is also observed when Nb is added. In the FEGSEM image shown in Figure 9a, ferritic regions can be clearly distinguished in the martensitic matrix. Within the observed softer phase, martensite-austenite (MA) islands are also detected, as shown in Figure 9a. It is commonly known that hard secondary phases, such as MA islands, can have a detrimental effect on toughness properties [48]. Accordingly, the quantification of MA size and fraction is required [49].

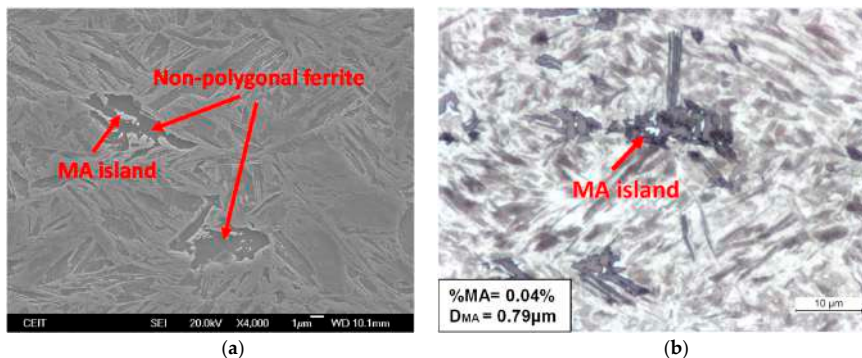


Figure 9. Presence of non-polygonal ferrite within martensitic matrix and martensite-austenite (MA) islands in CMnNbB steel: (a) FEGSEM micrograph and (b) optical image after LePera colour etching.

In the current work, MA island volume fraction as well as MA mean size (D_{MA}) were determined by quantitative metallography on optical micrographs (using the mean equivalent diameter method) after colour etching in LePera reagent [50]. In Figure 9b, an optical micrograph after colour etching is shown. Martensitic matrix and regions composed of non-polygonal ferrite are in brown, whereas MA islands can be distinguished in white. A low fraction of MA islands is measured in CMnNbB steel, approximately 0.04%, and

mean MA size is about 0.79 μm . In the other alloys, an MA microconstituent has not been detected. The formation of these MA islands must be a consequence of the ferrite growth explaining the close proximity of these phases. Since the carbon solubility in ferrite is very small, carbon partitions with growth of the ferrite phase are enriched in a residual austenite phase. The relative sizes of these microstructural features allow for the estimation that the carbon content in the MA phase should be indeed high enough ($>0.8\%$) for stabilizing austenite at ambient temperature after quenching. It has to be pointed out, however, that these MA islands should also decompose by the tempering treatment.

(2) Hardening due to dislocation density, fine precipitation and carbon in solid solution

Modification of mechanical properties caused by dislocation density and fine precipitation in ferrite-pearlite and bainitic microstructures is represented by a $\Delta\sigma_y$ term ($\Delta\sigma_y = \Delta\sigma_p + \Delta\sigma_{ppt}$). The effect of $\Delta\sigma_y$ on toughness can vary depending on the source. An effect of $0.45\text{ }^\circ\text{C}\cdot\text{MPa}^{-1}$ is observed by Pickering [51] for a ferritic phase, while a value of $0.26\text{ }^\circ\text{C}\cdot\text{MPa}^{-1}$ is observed for the bainitic constituent. In a recently published work, the contribution of $\Delta\sigma_y$ to ITT50% has also been determined to be $0.26\text{ }^\circ\text{C}\cdot\text{MPa}^{-1}$ [34].

In the analysis published in Reference [35], the hardening caused by solute carbon and fine precipitation is included in the unaccounted strength term. Figure 10 shows their contribution to yield strength for the different chemistries. Dislocation strengthening (σ_p) slightly increases when microalloying elements are added, increasing from 112 to 121 MPa for CMnB and Mo-microalloyed steel, respectively. The contribution related to unaccounted strength (σ_{us}) is nearly negligible for CMn and Nb steels, whilst for Mo containing grades, the impact of this contribution is considerably higher (185 and 229 MPa, for CMnMoB and CMnNbMoB, respectively). This larger yield strength could be attributed to the formation of ultrafine Mo-based precipitates during the tempering treatment that was also observed by TEM analysis. The synergy between Mo and Nb further enhances this precipitation strengthening effect.

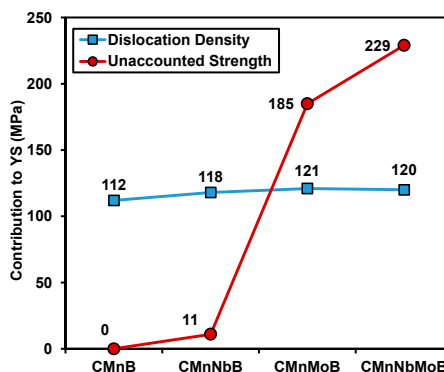


Figure 10. Dislocation density and unaccounted strength values corresponding to all steel grades.

3.3. Quantitative Relationship between Microstructure and Transition Temperature

A recent study on low carbon Nb-, NbMo- and TiMo-microalloyed steels [34] proposed an equation for predicting the impact transition temperature (ITT50%), taking into account the effect of microstructural heterogeneity and the presence of hard secondary phases such as MA islands (Equation (1)). In addition to the effect of chemical composition, the positive effect of refining cleavage unit size, the detrimental effect of heterogeneity, and MA size and fraction were taken into account. For considering the negative effect of heterogeneity, the ratio between Dc20% and 15° mean unit size was added in the equation.

Based on Equation (1) [34] which was developed for ferritic-pearlitic and bainitic microstructures, a modified relationship was worked out for predicting the impact transition temperature in medium carbon ultrahigh-strength steels with tempered martensitic microstructure (Equation (3)). This modified approach included contributions by dislocation hardening, σ_p , and unaccounted strength, σ_{us} . Moreover, in this equation, the harmful effect of carbides was also considered. Following the approach by Mintz et al. [29], an additional term considering the impact of carbide size, t , was introduced.

$$\text{ITT}_{50\%} = -11(\% \text{Mn}) + 42(\% \text{Si}) + 700(\% \text{N}_{\text{free}})^{0.5} + 15(\% \text{MA})^{\frac{1}{3}} + 18(D_{\text{MA}})^{0.5} - 14(D_{15^\circ})^{-0.5} + 0.26(\sigma_p + \sigma_{us}) + 63\left(\frac{D_{20\%}}{D_{15^\circ}}\right)^{0.5} + 112(t)^{0.5} \quad (3)$$

Predicted ITT_{50%} values based on Equation (3) are compared to experimental ones in Figure 11 for all alloys. The excellent agreement suggests that the modified relationship not only is appropriate for predicting transition temperatures of tempered martensitic microstructures but also allows for the identification of major influencing effects.

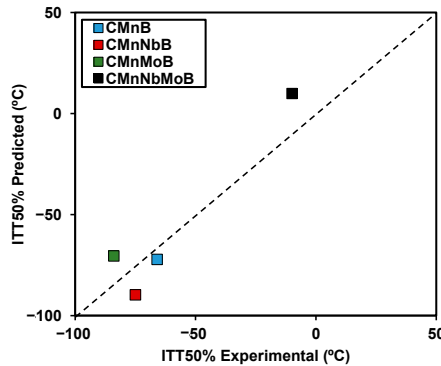


Figure 11. Correlation between predicted ITT_{50%} considering Equation (3) and the experimental ITT_{50%} measured by Charpy tests.

3.4. Comparative Evaluation of Strengthening versus Transition Temperature

With the aid of Equation (3), the individual effects on the transition temperature in the current four alloy design can be analysed. Using the data for the various strengthening mechanisms in these alloys reported in a recent paper [35], vector diagrams have been constructed (Figure 12) according to the procedure proposed by Gladman [52]. Since the base composition for all four alloys is identical, the first three terms in Equation (3) do not account for any of the observed differences. Nitrogen is mostly bound into TiN particles in these alloys to protect boron. Hence, nitrogen is not expected to make a contribution to ITT_{50%}. The contributions by Mn and Si lead to a strength increase by around 115 MPa without changing the transition temperature.

The MA phase was identified to be present in CMnNbB steel only. Its contribution to strength is marginal, but it does increase the ITT_{50%}. Due to decomposition of the MA phase by tempering, it is expected to act similarly to the other temper carbides located at high- and low-angle boundaries, thus increasing the transition temperature.

The clearly biggest contribution to strength originates from microstructural refinement according to the Hall–Petch relationship. The generally extremely fine-grained structure of martensite in the current steels accounts for a yield strength increase of 450–520 MPa correlating in that range with the severity of austenite conditioning (Table 3) [6]. Simultaneously, the transition temperature significantly decreases with the strength increase, manifesting this well-established and unique benefit of microstructural refinement.

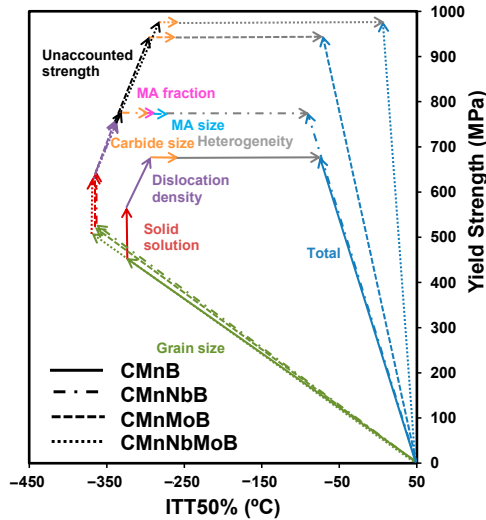


Figure 12. Relative contribution of different strengthening mechanisms (grain size, solid solution, dislocation density, unaccounted strength, presence of MA and heterogeneity) on both strength and toughness properties.

Other mechanisms such as dislocation strengthening and precipitation strengthening (denoted as unaccounted strength) cause an increase in transition temperature, which however is largely overcompensated by the microstructural refinement. Thus, the strategy for strengthening of first maximizing grain refinement before employing other mechanisms typically results in an improved ductile-to-brittle transition behaviour.

The main deleterious effect on the ductile-to-brittle behaviour in current steels is related to the heterogeneity in grain size distribution. Especially, the 20% fraction of largest grains is harmful to ITT50%, whereas its impact on strength is neutral. Large grains are more sensitive to cleavage at higher temperature than smaller ones. Simultaneously, the starting cracks caused by cleaving of larger individual grains are more likely to propagate. The fraction of very small prior austenite grains in the CMnNbB steel resulting from dynamic recrystallization is thus not expected to negatively affect ITT50%. However, the coexistence of very fine and larger grains can cause a serious level of residual stress in quenched steels, leading to macroscopic distortion [53]. The occurrence of very fine grains by dynamic recrystallization was found to be suppressed in current steels by sufficient alloying of molybdenum. This Mo-based effect has also been confirmed by other studies [39].

4. Conclusions

It was demonstrated in the current study that steel having a yield strength of over 900 MPa and appreciably low ductile-to-brittle transition temperature (ITT50%) can be produced by direct quenching from the rolling heat followed by short tempering treatment (600 °C for 300 s). The use of molybdenum in a 0.15%CMnB base alloy is essential for reaching these targets.

The largest contribution to strength and toughness originates from martensite microstructural refinement. Significant refinement is inherent to the martensitic substructure. Additional refinement is related to austenite conditioning, which can be achieved by Nb microalloying (0.025%), Mo alloying (0.5%) or a combination of both.

The most harmful effect on ITT50% is related to microstructural heterogeneity and more particularly to the fraction of largest prior austenite grains. This heterogeneity was quantitatively determined from an EBSD-based austenite reconstruction procedure. The combined addition of Mo and Nb causes the most pronounced heterogeneity, which apparently is caused by incomplete recrystallization during the high-temperature deformation (roughing) stage. Optimizing the processing towards achieving a high degree of microstructural homogeneity therefore appears to be a more important target than solely focusing on maximum refinement.

Molybdenum was confirmed to suppress dynamic recrystallization occurring during austenite conditioning in the CMnB and the Nb-only alloyed steels. The very fine equiaxed austenite grains showed the tendency to transform into ferrite due to the absence of boron on the grain boundary. In that respect, molybdenum can be considered to have an indirect contribution to hardenability in addition to its well-known direct transformation-retarding effect.

Author Contributions: I.Z. carried out the experiments and wrote the manuscript; N.I. supervised the results, analysed the data and wrote the manuscript; E.D., V.S. and H.M. contributed to the interpretation of the data and edited the manuscript; P.U. managed the project and edited the manuscript. All authors have read and agreed to the published version of the manuscript.

Funding: This research received funding by the International Molybdenum Association (IMOA).

Institutional Review Board Statement: Not applicable.

Informed Consent Statement: Not applicable.

Data Availability Statement: Data sharing not applicable.

Acknowledgments: The authors would like to acknowledge the International Molybdenum Association (IMOA) for funding this project.

Conflicts of Interest: The authors declare no conflict of interest.

References

1. Berns, H. On Toughness of Quenched and Tempered Steels. *Z. Werkstofftech* **1978**, *9*, 189–204. [[CrossRef](#)]
2. Mohrbacher, H. Property Optimization in As-Quenched Martensitic Steel by Molybdenum and Niobium Alloying. *Metals* **2018**, *8*, 234. [[CrossRef](#)]
3. Mohrbacher, H. Synergies of niobium and boron microalloying in molybdenum based bainitic and martensitic steel. *Fundam. Appl. Mo Nb Alloy. High Perform. Steels* **2014**, *1*, 83–108.
4. Larrañaga-Otegui, A.; Pereda, B.; Jorge-Badiola, D.; Gutierrez, I. Austenite Static Recrystallization Kinetics in Microalloyed B Steels. *Metall. Trans. A* **2016**, *47*, 3150–3164. [[CrossRef](#)]
5. He, X.L.; Djahazi, M.; Jonas, J.J.; Jackman, J. The non-equilibrium segregation of boron during the recrystallization of Nb-treated HSLA steels. *Acta Met. Mater.* **1991**, *39*, 2295–2308. [[CrossRef](#)]
6. Hulka, K.; Kern, A.; Schrieffer, U. Application of Niobium in Quenched and Tempered High-Strength Steels. *Mater. Sci. Forum* **2005**, *500–501*, 519–526. [[CrossRef](#)]
7. Sharma, M.; Ortlepp, I.; Bleck, W. Boron in Heat-Treatable Steels: A Review. *Steel Res. Int.* **2019**, *90*, 1900133. [[CrossRef](#)]
8. Revilla, C.; López, B.; Rodriguez-Ibabe, J.M. Carbide Size Refinement by Controlling the Heating Rate during Induction in a Low Alloy Steel. *Mater. Des.* **2014**, *62*, 296–304. [[CrossRef](#)]
9. Krauss, G. Martensite in steel: Strength and structure. *Mater. Sci. Eng. A* **1999**, *273*, 40–57. [[CrossRef](#)]
10. Linaza, M.A.; Rodriguez-Ibabe, J.M.; Urcola, J.J. Determination of the energetic parameters controlling cleavage fracture initiation in steels. *Fatigue Fract. Eng. Mater. Struct.* **1997**, *20*, 619–632. [[CrossRef](#)]
11. Maki, T.; Tsuzaki, K.; Tamura, I. The morphology of the strengthening of lath martensite in steels. *Trans. Iron Steel Inst. Jpn.* **1980**, *20*, 207–215. [[CrossRef](#)]
12. Hannula, J.; Kömi, J.; Porter, D.A. Effect of boron on the strength and toughness of direct-quenched low-carbon niobium bearing ultra-high-strength martensitic steel. *Metall. Mat. Trans. A* **2017**, *48*, 5344–5356. [[CrossRef](#)]
13. Prawoto, Y.; Jasmawati, N.; Sumeru, K. Effect of prior austenite grain size on the morphology and mechanical properties of martensite in medium carbon steel. *J. Mater. Sci. Technol.* **2012**, *28*, 461–466. [[CrossRef](#)]
14. Furuhashi, T.; Kikumoto, K.; Saito, H.; Sekine, T.; Ogata, T.; Morino, S. Phase transformation from fine-grained austenite. *ISIJ Int.* **2008**, *48*, 1038–1045. [[CrossRef](#)]

15. Khani Sanij, M.H.; Ghasemi Banadkouki, S.S.; Mashreghi, A.R.; Moshrefifar, M. The effect of single and double quenching and tempering heat treatments on the microstructure and mechanical properties of AISI 4140 steel. *Mater. Des.* **2012**, *42*, 339–346. [[CrossRef](#)]
16. Laasraoui, A.; Jonas, J.J. Recrystallization of Austenite after Deformation at High Temperatures and Strain Rates-Analysis and Modeling. *Metall. Trans. A* **1991**, *22*, 151–160. [[CrossRef](#)]
17. Hutchinson, C.R.; Zurob, H.S.; Sinclair, C.W.; Brechet, Y.J.M. The comparative effectiveness of Nb solute and NbC precipitates at impeding grain-boundary motion in Nb steels. *Scripta Mater.* **2008**, *59*, 635–637. [[CrossRef](#)]
18. Isasti, N.; Jorge-Badiola, D.; Taheri, M.L.; Uranga, P. Microstructural and precipitation characterization in Nb-Mo microalloyed steels, estimation of the contributions to the strength. *Met. Mater. Int.* **2014**, *20*, 807–817. [[CrossRef](#)]
19. Sanz, L.; López, B.; Pereda, B. Characterization of Austenite Microstructure from Quenched Martensite Using Conventional Metallographic Techniques and a Crystallographic Reconstruction Procedure. *Metals* **2018**, *8*, 294. [[CrossRef](#)]
20. Sanz, L.; Pereda, B.; López, B. Validation and Analysis of the Parameters for Reconstructing the Austenite Phase from Martensite Electron Backscatter Diffraction Data. *Metall. Mater. Trans. A* **2017**, *48*, 5258–5272. [[CrossRef](#)]
21. Germain, L.; Gey, N.; Mercier, R.; Blaineau, P.; Humbert, M. An advanced approach to reconstructing parent orientation maps in the case of approximate orientation relations: Application to steels. *Acta Mater.* **2012**, *60*, 4551–4562. [[CrossRef](#)]
22. Kajjalainen, A.; Pallaspuro, S.; Porter, D.A. Tempering of direct quenched low-alloy ultra-high-strength steel, Part I—Microstructure. *Adv. Mater. Res.* **2014**, *922*, 316–321. [[CrossRef](#)]
23. Pallaspuro, S.; Kajjalainen, A.; Limnell, T.; Porter, D. Tempering of Direct Quenched Low-Alloy Ultra-High-Strength Steel, Part II—Mechanical Properties. *Adv. Mater. Res.* **2014**, *922*, 580–585. [[CrossRef](#)]
24. Saastamoinen, A.; Kajjalainen, A.; Porter, D.; Suikkanen, P.; Yang, J.-R.; Tsai, Y.-T. The effect of finish rolling temperature and tempering on the microstructure, mechanical properties and dislocation density of direct-quenched steel. *Mater. Charact.* **2018**, *139*, 1–10. [[CrossRef](#)]
25. Hannula, J.; Kajjalainen, A.; Porter, D.; Somani, M.; Kömi, J. Evaluation of Mechanical Properties and Microstructures of Direct-Quenched and Direct Quenched and Tempered Microalloyed Ultrahigh-Strength Steels. *Steel Res. Int.* **2020**, 2000451. [[CrossRef](#)]
26. Isasti, N.; Badiola, D.J.; Taheri, M.L.; Uranga, P. Microstructural features controlling mechanical properties in Nb-Mo microalloyed steels. Part II: Impact toughness. *Metall. Mater. Trans. A* **2014**, *45*, 4972–4982. [[CrossRef](#)]
27. Irvine, K.J.; Pickering, F.B.; Gladman, T. Grain-refined C-Mn steels. *J. Iron Steel Inst.* **1967**, *205*, 161–182.
28. Mintz, B.; Peterson, G.; Nassar, A. Structure-property relationships in ferrite-pearlite steels. *Ironmak. Steelmak.* **1994**, *21*, 215–222.
29. Mintz, B.; Morrison, W.B.; Jones, A. Influence of carbide thickness on impact transition temperature of ferritic steels. *Met. Technol.* **1979**, *6*, 252–260. [[CrossRef](#)]
30. Gutierrez, I. Effect of microstructure on the impact toughness of Nb-microalloyed steel: Generalisation of existing relations from ferrite-pearlite to high strength microstructures. *Mater. Sci. Eng. A* **2013**, *571*, 57–67. [[CrossRef](#)]
31. Pickering, F.B.; Gladman, T. Metallurgical Developments in Carbon Steels. *ISI Spec. Rep.* **1963**, *81*, 42.
32. From, A.; Sandstrom, R. Influence of mixed grain size distributions on the toughness in high and extra high strength steels. *Mater. Charact.* **1999**, *42*, 111–122. [[CrossRef](#)]
33. Hanamura, T.; Yin, F.; Nagai, K. Ductile-brittle transition temperature of ultrafine ferrite/cementite microstructure in a low carbon steel controlled by effective grain size. *ISIJ Int.* **2004**, *44*, 610–617. [[CrossRef](#)]
34. Larzabal, G.; Isasti, N.; Rodriguez-Ibabe, J.M.; Uranga, P. Evaluating Strengthening and Impact Toughness Mechanisms for Ferritic and Bainitic Microstructures in Nb, Nb-Mo and Ti-Mo Microalloyed Steels. *Metals* **2017**, *7*, 65. [[CrossRef](#)]
35. Zurutuza, I.; Isasti, N.; Detemple, E.; Schwinn, V.; Mohrbacher, H.; Uranga, P. Effect of Nb and Mo Additions in the Microstructure/Tensile Property Relationship in High Strength Quenched and Quenched and Tempered Boron Steels. *Metals* **2021**, *11*, 29. [[CrossRef](#)]
36. Uranga, P.; Gutierrez, I.; Lopez, B. Determination of recrystallization kinetics from plane strain compression tests. *Mater. Sci. Eng. A* **2013**, *578*, 174–180. [[CrossRef](#)]
37. Wallin, K. *Modified Tank Fitting Algorithm Charpy Impact Data*; Research Seminar on Economical and Safe Application of Modern Steels for Pressure Vessels: Aachen, Germany, 2003.
38. Schambron, T.; Dehghan-Manshadi, A.; Chen, L.; Gooch, T.; Killmore, C.; Pereloma, E. Effect of Mo on Dynamic Recrystallization and Microstructure Development of Microalloyed Steels. *Met. Mater. Int.* **2017**, *23*, 778–787. [[CrossRef](#)]
39. Pereda, B.; Fernández, A.I.; López, B.; Rodriguez-Ibabe, J.M. Effect of Mo on Dynamic recrystallization behavior of Nb-Mo microalloyed steels. *ISIJ Int.* **2007**, *47*, 860–868. [[CrossRef](#)]
40. Medina, S.F.; Hernandez, C.A. General expression of the Zener-Hollomon parameter as a function of the chemical composition of low alloy and microalloyed steels. *Acta Mater.* **1996**, *44*, 137–148. [[CrossRef](#)]
41. Lee, W.B.; Hong, S.G.; Park, C.G.; Park, S.H. Carbide precipitation and high-temperature strength of hot-rolled high strength, low alloy steels containing Nb and Mo. *Metall. Mater. Trans. A* **2002**, *33*, 1689–1698. [[CrossRef](#)]
42. Mejía, I.; Salas-Reyes, A.E.; Bedolla-Jacuinde, A.; Calvo, J.; Cabrera, J.M. Effect of Nb and Mo on the hot ductility behavior of a high-manganese austenitic Fe-21Mn-1.3Al-1.5Si-0.5C TWIP steel. *Mat. Sci. Eng. A* **2014**, *616*, 229. [[CrossRef](#)]
43. Larzabal, G.; Isasti, N.; Rodriguez-Ibabe, J.M.; Uranga, P. Effect of Microstructure on Post-Rolling Induction Treatment in a Low C Ti-Mo Microalloyed Steel. *Metals* **2018**, *8*, 694. [[CrossRef](#)]

44. Calcagnotto, M.; Ponge, D.; Demir, E.; Raabe, D. Orientation gradients and geometrically necessary dislocations in ultrafine grained dual-phase steels studied by 2D and 3D EBSD. *Mater. Sci. Eng. A* **2010**, *257*, 2738–2746. [CrossRef]
45. Uranga, P.; Shang, C.-J.; Senuma, T.; Yang, J.-R.; Guo, A.-M.; Mohrbacher, H. Molybdenum alloying in high-performance flat-rolled steel grades. *Adv. Manuf.* **2020**, *8*, 15–34. [CrossRef]
46. Djahazi, M.; He, X.L.; Jonas, J.J.; Sun, W.P. Nb(C, N) Precipitation and Austenite Recrystallization in Boron-Containing High-Strength Low-Alloy Steels. *Metall. Mater. Trans. A* **1992**, *23*, 2111–2120. [CrossRef]
47. Mohrbacher, H. Mo and Nb alloying in plate steels for high-performance applications. Proc. International Symposium on the Recent Developments in Plate Steels. *Int. Symp. Recent Dev. Plate Steels* **2011**, 169–179. Available online: https://www.researchgate.net/profile/Hardy_Mohrbacher/publication/333661101_Mo_and_Nb_Alloying_in_Plate_Steels_for_High-Performance_Applications/links/5cfb6da24585157d159b1ad7/Mo-and-Nb-Alloying-in-Plate-Steels-for-High-Performance-Applications.pdf (accessed on 30 December 2020).
48. Kim, Y.M.; Shin, S.Y.; Lee, H.; Hwang, B.; Lee, S.; Kim, N.J. Effects of molybdenum and vanadium addition on tensile and charpy impact properties of API X70 linepipe steels. *Metall. Mater. Trans. A* **2007**, *38*, 1731–1742. [CrossRef]
49. Mohseni, P.; Solberg, J.K.; Karlsen, M.; Akselsen, O.M.; Østby, E. Cleavage fracture initiation at M-A constituents in intercritically coarse-grained heat-affected zone of a HSLA steel. *Metall. Mater. Trans. A* **2014**, *45*, 384–394. [CrossRef]
50. LePera, F.S. Improved etching technique for the determination of percent martensite in high-strength dual-phase steels. *Metallography* **1979**, *12*, 263–268. [CrossRef]
51. Pickering, F.B. The optimization of microstructures in steel and their relationship to mechanical properties. In *Hardenability Concepts with Applications to Steel*; Doane, D.V., Kirkaldy, J.S., Eds.; AIME: New York, NY, USA, 1978; pp. 179–228.
52. Gladman, T. *The Physical Metallurgy of Microalloyed Steels*, 2nd ed.; The Institute of Materials: London, UK, 1997; pp. 62–68.
53. Tobie, T.; Hippenstiel, F.; Mohrbacher, H. Optimizing Gear Performance by Alloy Modification of Carburizing Steels. *Metals* **2017**, *7*, 415. [CrossRef]

5. Discussion

5.1. Hot working behaviour

Analysis of hot working behaviour becomes crucial when plate hot rolling schedule needs to be optimized. A relevant aspect that has to be considered is the strengthening due to grain size refinement that can be improved reaching a pancaked austenite before phase transformation. It is widely known that the addition of Nb and Mo delays softening kinetics, retards recrystallization of austenite and ensures the accumulation of deformation of the austenite prior to transformation. Even though the impact of adding Nb and Mo on recrystallization kinetics was already investigated, the complex interaction between B, Nb and Mo, with higher molybdenum levels, and its effect on the austenite evolution during hot working is still unclear. Therefore, in the frame of the current thesis, different type of torsion tests were performed in order to analyse the interaction between recrystallization and precipitation kinetics.

5.1.1. Analysis of softening kinetics: Double-hit torsion tests

The influence of deformation temperature adding microalloying elements on static recrystallization kinetics was evaluated and for that purpose double-hit torsion tests were performed. The results suggest that the decrease of the deformation temperature promotes the delay of softening kinetics. Longer times are required for achieving fully recrystallized austenitic structure. When microalloying elements are added, recrystallization is not completed for the lowest deformation temperature of 850 °C (see Figure 5.1a). At the lowest deformation temperature, recrystallization interacts with deformation induced precipitation and atoms in solid solution in the steels containing Nb. As a consequence, in the CMnNbB and CMnNbMoB grades, a plateau is detected in the fractional softening curve, as illustrated in Figure 5.1a. Considering the precipitation analysis performed by TEM, in addition to non-dissolved Nb and Ti rich precipitates sized between 20 and 50 nm, finer strain induced precipitates rich in Nb (sized below 10 nm) have been also detected. Their pinning effect on the austenite grain boundaries causes a strong delay on the recrystallization kinetics and increases strain accumulation in austenite prior to transformation. However, in the CMnMoB steel, the retardation of the

recrystallization kinetic is mainly attributed to the presence of Mo in solid solution (see Figure 5.1a).

Taking into consideration several approaches for predicting the time of 50% recrystallization reported in the literature, Pereda et al. [26] deduced an equation for low carbon Nb and Nb-Mo microalloyed steels (Nb content between 0 and 0.06% and Mo content between 0 and 0.31%).

In the current work, the validity of this equation for higher molybdenum contents (0.5%Mo) was evaluated. In Figure 5.1b, the relation between predicted $t_{0.5}$ values (considering Equation 4.1) and the experimental value is plotted for the current steels and deformation temperatures. The results indicate that reasonable prediction is achieved in most cases considering the equation proposed by Pereda et al. [26].

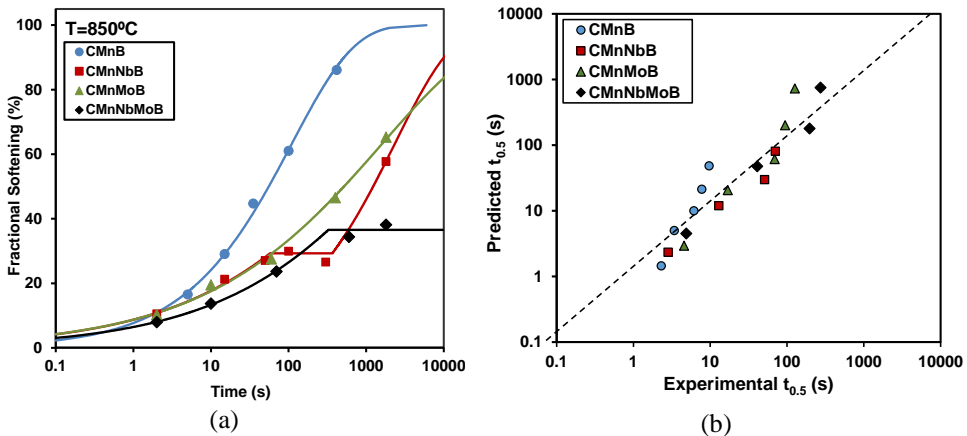


Figure 5.1. (a) Effect of chemical composition on the softening behaviour at 850 °C and (b) comparison between experimental and predicted time of 50% recrystallization $t_{0.5}$ concerning Equation 4.1.

5.1.2. Determination of non-recrystallization temperature (T_{nr}): Multipass torsion tests

The non-recrystallization temperature (T_{nr}) value has been defined by means of multipass torsion tests. The impact of adding microalloying elements on the increment of T_{nr} is clear. As an example, Figure 5.2a shows the mean flow stress as a function of temperature for a deformation level of 0.3 and an interpass time of 15s. Two different regimes can be distinguished. In the initial regime at high temperature, complete recrystallization takes place between passes and the stress increase from pass to pass is only related to decreasing temperature and accordingly increasing

yield strength of austenite. The second regime at lower austenite temperature is indicating strain accumulation caused by incomplete recrystallization [137]. Following the standard procedure [138], the non-recrystallization temperature (T_{nr}) was determined as the intersection of linear fitted regression lines for the data points of either regime. It can be observed that the addition of microalloying elements increases T_{nr} considerably. Steels with molybdenum alloying comprise the highest T_{nr} values especially when combined with Nb microalloying.

The effect of Nb and Mo on the non-recrystallization temperature may be related to two mechanisms, being solute drag and particle pinning effect caused by strain induced precipitates [139]. Mo, Nb and Ti have a significantly larger atom size than iron and a tendency for segregating towards the austenite grain boundary. For CMnB and CMnMoB steels, the delay on recrystallization could be mainly related to solute drag effect. On the other hand, in-situ formation of strain-induced precipitates observed in the Nb containing steels (CMnNbB and CMnNbMoB) exerts a pinning effect on austenite grain boundaries according to the well-known Zener theory [140].

Furthermore, MicroSim-PM® software was employed for predicting the recrystallized fraction of austenite from pass to pass and estimating the evolution of Fractional softening (FS) during plate hot rolling simulation [141]. In general, the model correctly predicts the influence of deformation conditions (strain and interpass time) on the evolution of the austenite fractional softening for all steel grades. The best match between the model prediction and experimental data is found for the CMnMoNbB steel, as shown in Figure 5.2b. However, for the Nb alloyed steel, see Figure 5.2c, the degree of FS is larger than predicted specially at temperatures below T_{nr} . This must be related to the activation of dynamic recrystallization kinetics in this alloy variant during deformation passes at lower austenite temperatures. Dynamic recrystallization phenomenon will be analysed in detail in the following chapter. Even though the software was so far mainly used and optimized for standard microalloyed HSLA steels, predictions of fractional softening for the current direct quenching steel alloys showed reasonably good agreement with the experimental behaviour. Nevertheless, improvements in the underlying constitutive equations to better account for the austenite grain boundary segregation behaviour of molybdenum and boron, as well as dynamic recrystallization should be implemented.

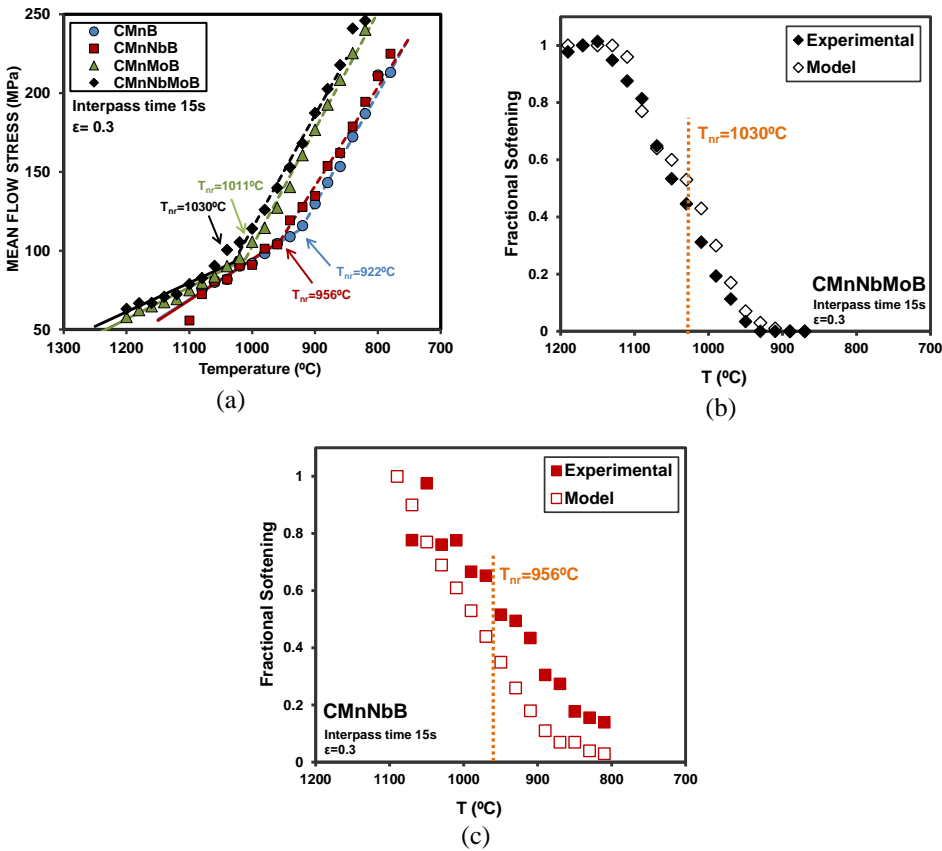


Figure 5.2. (a) Mean Flow Stress delivered from multipass torsion tests as a function of temperature for 0.3 strain level and an interpass time of 15s and (b,c) comparison between experimental fractional softening curve obtained from multipass torsion tests and the one predicted by MicroSim-PM® (interpass time of 15s and strain of 0.3) for (b) CMnNbMoB and (c) CMnNbB steels.

5.1.3. Dynamic recrystallization analysis: Plate hot rolling simulations by torsion tests

In the current work, the impact of adding Nb, Mo and Nb-Mo on dynamic recrystallization was analysed. For that purpose, multipass torsion tests have been performed to carry out plate hot rolling simulations followed by direct quenching for CMnNbB, CMnMoB and CMnNbMoB steel grades.

After plate hot rolling and subsequent direct quenching simulation, differences in the morphology of the microstructure are detected. While Mo and NbMo alloyed steels exhibit fully martensitic microstructures, in the CMnNbB steel clusters consisting

on non-polygonal ferritic within the martensitic microstructure are observed. The presence of the ferrite phase results in rather low hardness of 290 HV compared to Mo and NbMo alloyed steels, 394 and 422 HV respectively. The grain boundary maps obtained by EBSD confirm the formation of very fine-sized and complex microstructures for both Mo containing steels. However, in Nb alloyed steel, the formation of soft phases within the otherwise martensitic matrix can be observed (see Figure 5.3a). In the Kernel Average Misorientation (KAM) map corresponding to CMnNbB steel, larger islands with lower dislocation density (blue and green coloured areas) are seen, representing softer ferritic phases, Figure 5.3b.

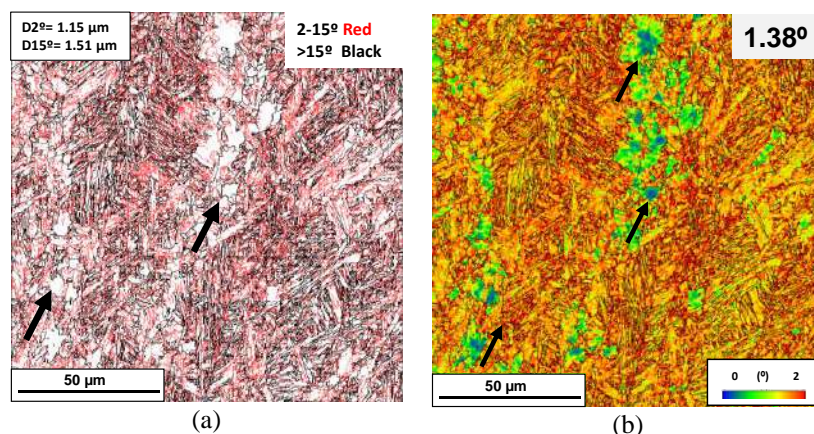


Figure 5.3. (a) Grain boundary and (b) Kernel maps corresponding to CMnNbB steel after plate hot rolling simulation by torsion tests.

As the final martensitic features are strongly influenced by the austenite morphology prior to phase transformation, the prior austenitic structure was also analysed. In all steel alloys, highly elongated austenite grains are observed, being the accumulation of deformation most pronounced for the combined addition of Nb and Mo. However, in CMnNbB grade, in addition to elongated austenite grains a fraction of fine equiaxed grains is formed, as illustrated in Figure 5.4a and b. This is resulting from localised dynamic recrystallization occurring during final deformation. The EBSD inverse pole figure maps (IPF) obtained on the martensitic microstructures (see Figure 5.4c), allowed to reconstruct the prior austenite grain structure according to a procedure defined in references [137, 142]. The reconstruction confirms the presence of elongated austenite grains in all steels and in agreement with the optical microscopy analysis, the reconstructed austenite structure of Nb steel shows a fraction of very fine equiaxed grains within the elongated grains (see reconstructed austenite in Figure 5.4c).

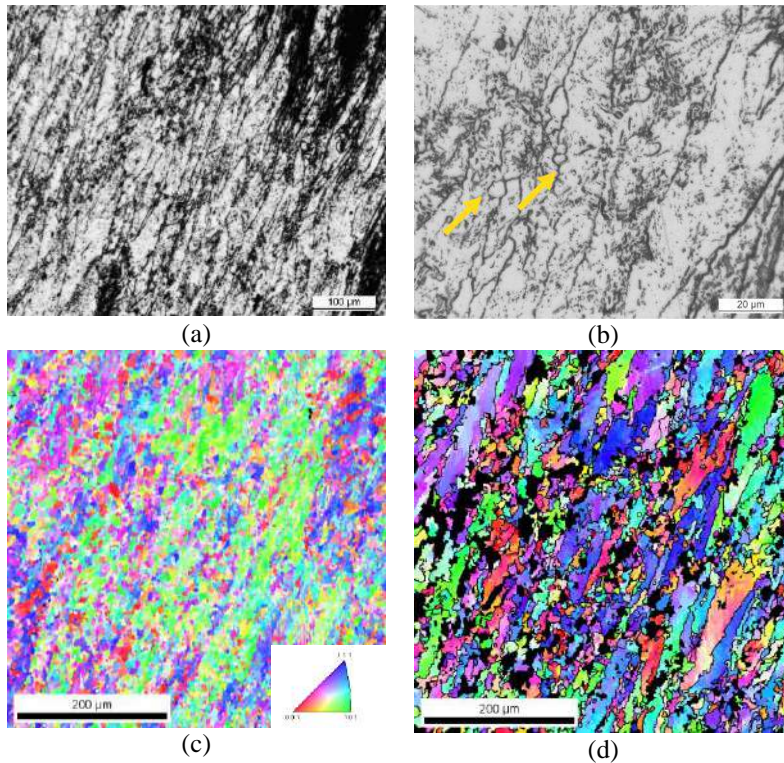


Figure 5.4. (a,b) Optical micrographs showing the activation of dynamic recrystallization in Nb steel. (c) IPF map of the martensitic microstructure and (d) reconstructed austenitic microstructure corresponding to CMnNbB steel.

In the Mo bearing steel grades, such equiaxed grains are not observed. Therefore, it can be stated that the addition of molybdenum (0.5%) completely suppresses DRX under the same conditions. This effect of molybdenum was related to a significant increase of the Zener-Hollomon parameter. The main influencing factor in the kinetics of DRX in the present experiments must be the Zener-Hollomon parameter. Solute Mo is known to impede the movement of high angle grain boundaries due to solute drag [28]. Niobium is considered being the most potent element in retarding DRX by solute drag [63]. However, under the applied hot deformation conditions Nb partially precipitates thereby lowering its solute content. Strain-induced precipitates, are not very effective in suppressing DRX. Accordingly, DRX is expected to occur more likely in the CMnNbB steel in agreement with the present experimental observations.

In addition, the circumstances initiating dynamic recrystallization have been studied in more detail. In order to promote dynamic recrystallization in the investigated steels, after roughing step, a large deformation is applied ($\epsilon=4$). As shown in Figure 5.5a, the austenite grain structure reflects nearly complete recrystallization in the Nb alloyed steel showing fine-sized equiaxed grains having sized up to around 10 μm . The molybdenum alloyed steels, however, present a mixed microstructure consisting of elongated and extremely fine-sized recrystallized gains (Figure 5.5b). This observation indicates that Molybdenum alloying does not completely prevent the initiation of DRX. However, in the Mo containing steels, the progress of DRX and the austenite grain size is evidently smaller than in the niobium microalloyed steel without molybdenum addition. The larger Zener-Hollomon parameter in the Mo steels results in a smaller size of the recrystallized grains.

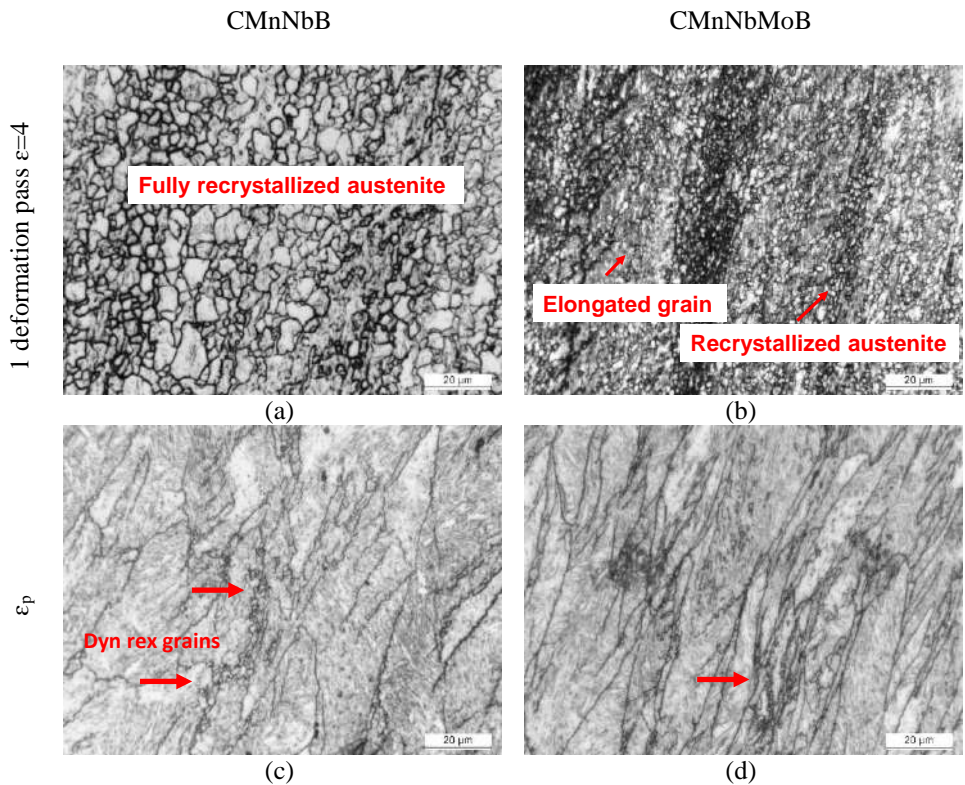


Figure 5.5. Optical images corresponding to the austenitic structure obtained after (a,b) a roughing simulation +1 deformation pass of 4 at 850 °C. (c,d) Austenitic structure related to ϵ_p for (a,c) Nb and (b,d) NbMo microalloyed steels.

For analysing the critical strain activating dynamic recrystallization, single pass deformation cycles have been interrupted at lower strain values. At the strain of peak stress, ϵ_p , being 1.26 and 1.30 for Nb and NbMo steel grades, respectively, dynamic recrystallization is activated, as clearly observed in Figure 5.5c and d.

Based on the current study, it can be concluded that the addition of Mo is shown to be an effective means of suppressing dynamic recrystallization. This effect of molybdenum in addition to its established hardenability effects hence safeguards the formation of fully martensitic microstructures particularly in direct quenching processes. The presence of fine-grained austenite generated by DRX is shown to produce soft phases upon quenching under an industrial cooling rate of 30 °C/s. It has been argued that the sudden and late increase of austenite grain boundary area caused by DRX can weaken the hardenability effect related to boron. Therefore, molybdenum alloying acts twofold, by its high inherent hardenability effect as well as by avoiding DRX.

5.2. Phase transformation analysis

When heavy gauge plates are produced, the complexity involved in achieving high cooling rates in the plate core is increased and the formation of undesirable soft phases within martensite is common. Therefore, in order to avoid the formation of softer phases, further knowledge regarding the impact of adding Mo and NbMo as well as the impact of processing route (CQ or DQ) on phase transformation is required. In the following lines, the effect of cooling rate, chemical composition and processing strategy are discussed in depth, in terms of CCT diagrams, hardness and formed microstructure.

Concerning the influence of chemical composition on transformation temperatures, the results suggest that the addition of Mo and NbMo considerably affects the phase transformation kinetics. The CCT illustrated in Figure 5.6a clearly shows that after DQ, the addition of Mo delays the CCT diagram to lower temperatures, suppresses the formation of ferritic phases and promotes the formation of bainitic/martensitic microstructures at lower cooling rates. In the case of the Mo steel, the martensitic phase becomes dominant at cooling rates above 20 °C/s. Therefore, at 50 °C/s, a significantly harder microstructure is formed in the case of Mo-alloyed steel compared with CMnB base steel (467 HV versus 338 HV), this being associated with the formation of martensite instead of bainite.

The effect of cooling rate and chemistry is also evident, when the hardness evolution is compared for each steel grade, as shown in Figure 5.6b. At low cooling rates, the hardness is on a low level and only slightly increasing with the cooling rate, whereas

hardness saturates on an upper plateau at higher cooling rates (see Figure 5.6b), achieving a value of 420 HV and remaining below the calculated maximum, due to self-tempering. For CMnB and CMnNbB steels, a gradual change from ferrite-pearlite microstructures to more bainitic ones causes a slight hardness increment for cooling rates up to 20 °C/s, although in this Mo-free steels rates above 100 °C/s are needed to obtain fully martensitic microstructures. With the addition of 0.5% Mo, noticeably harder microstructures are obtained for all cooling rates (see Figure 5.6b).

When Nb is added to a Mo microalloyed steel, lower hardness values are measured than for Mo steel (see Figure 5.6b). In NbMo steel higher strain accumulation is achieved in the austenite, leading to an increase in the ferrite nucleation sites, which encourages a faster nucleation of the bainitic laths and increases the critical cooling rate required to obtain pure martensite. Furthermore, the co-addition of Mo successfully suppresses dynamic recrystallization and thus prevents early ferrite formation.

Regarding the effect of processing route, a different behaviour is noticed depending on the alloy concept. As shown in Figure 5.6c, in the case of CMnB grade, a completely martensitic microstructure is only obtained by the CQ process. In CMnNbB steel, niobium microalloying remains solute in austenite after hot rolling and lowers the transformation temperature, encouraging the formation of ferrite, despite equiaxed austenite morphology and an absence of accumulated strain in CQ process. This ferrite formation is potentially caused by co-precipitation of boron with niobium. These temperature-stable particles efficiently control the austenite grain size before quenching by boundary pinning [143]. Moreover, the addition of Nb retards recrystallization ensuring the accumulation of energy and thus, promoting ferrite formation. In addition, dynamic recrystallization results in austenite grain boundaries insufficiently protected by segregated boron. Adding Mo, the effect of the considered strategy is lower, as illustrated in Figure 5.6d. Similar transformation start temperatures are observed comparing CQ and DQ routes, in the entire range of cooling rates. The critical cooling rate required for full martensite formation is reduced to much lower values of between 20 and 30 °C/s for both DQ and CQ processes.

Therefore, the phase transformation analysis indicated that boron alloying by itself cannot fully prevent ferrite formation. However, the combined addition of B and Mo promotes the suppression of ferrite nucleation. The excellent hardenability observed in Mo alloyed steel is related to two main effects. Firstly, molybdenum reduces the nucleation rate of ferrite independently of temperature in the range of diffusional transformations, as demonstrated by Kinsman and Aaronson [144]. Secondly, a

major solute drag effect acts on the carbon-rich interphase boundaries that attract molybdenum, due to its high binding energy with carbon. The segregation of solute B atoms at the austenite grain boundaries also efficiently suppresses the nucleation of ferrite, although this effect is lost when boron forms $Fe_{23}(C, B)_6$ or Fe_2B precipitates. Particularly in the DQ process, molybdenum alloying suppresses dynamic recrystallization, thus enhancing the probability of boron-depleted new austenite grain boundaries. Identical steel alloys are less hardenable under DQ conditions than under CQ conditions, and this is due to accumulated strain and a larger total grain boundary surface of pancaked austenite offering more nucleation sites for ferrite in the DQ process. Therefore, it can be concluded that considering DQ strategy, Mo addition becomes essential to ensure hardenability and to achieve fully martensitic microstructures. Mo steel grade seems to be the optimum alloy concept when DQ strategy is applied.

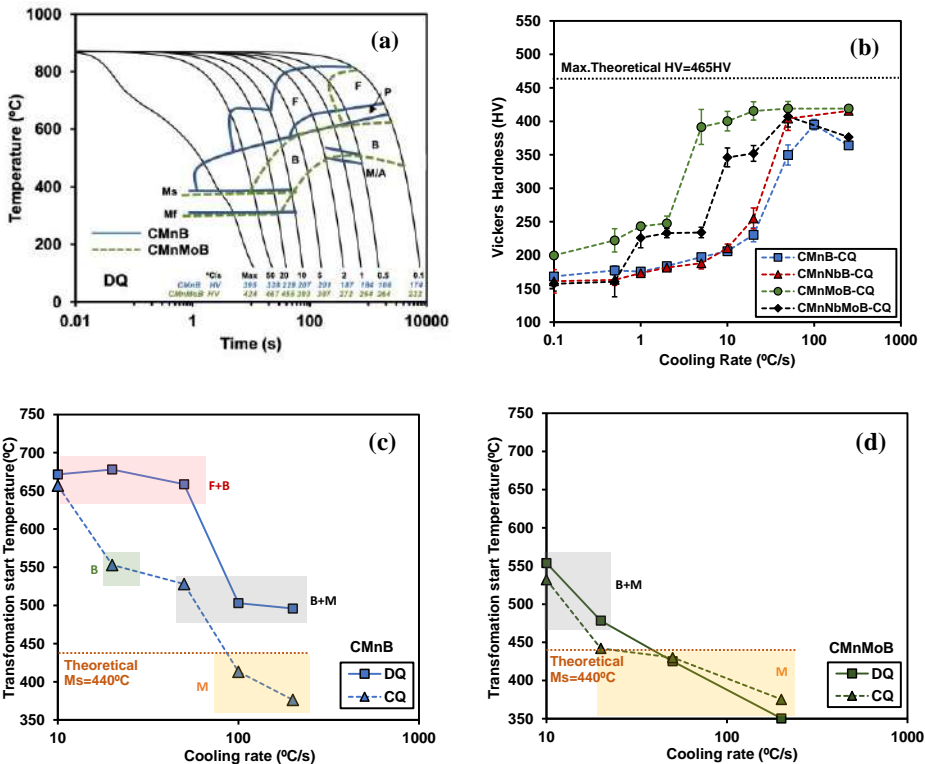


Figure 5.6. (a) Comparison between CCT diagrams corresponding to CMnB and CMnMoB steels and the direct quenching (DQ) cycle. (b) Vickers Hardness as a function of cooling rate for conventional quenching (CQ) cycles. Effect of cooling rate on transformation start temperature when direct quenching and conventional quenching cycles are applied for (c) CMnB and (d) CMnMoB steels.

5.3. Relationship between microstructure and mechanical properties

In the current work, the relationship between the microstructure and the resulting mechanical properties (tensile and toughness properties) is analysed.

5.3.1. Tensile properties

In order to evaluate the effect of adding microalloying elements on direct quenched martensitic microstructures, a detailed EBSD analysis was carried out. For the quenched state, even though fully martensitic microstructures are observed for all chemical compositions, slight differences are detected depending on the chemistry. The coarsest martensitic microstructure is observed in CMnB grade, before tempering and the formation of very fine martensitic microstructure is observed in the Mo containing steels.

The influence of adding Mo is evidently reflected in the grain boundary maps (see Figure 5.7). Significantly finer microstructures are achieved when Mo is added, considering both, low angle (2° - 15°) and high angle ($>15^{\circ}$) misorientation criteria, as shown in Figure 5.7c and d. Additionally, Mo alloying increases the low angle boundary density in the quenched steel. The microstructural refinement identified in the microalloyed steels could be explained by the differences in the austenitic microstructure morphology.

In the CMnB steel, an equiaxed and homogeneous austenite grain structure is observed. For the CMnNbB steel, a mixed structure consisting of pancaked and dynamically recrystallized fine grains is found, in agreement with previous experimental observations. Nevertheless, the Mo containing grades comprise a fully pancaked austenite microstructure showing a high degree of strain accumulation, resulting in grain size refinement of the final microstructure and thus, improving mechanical properties.

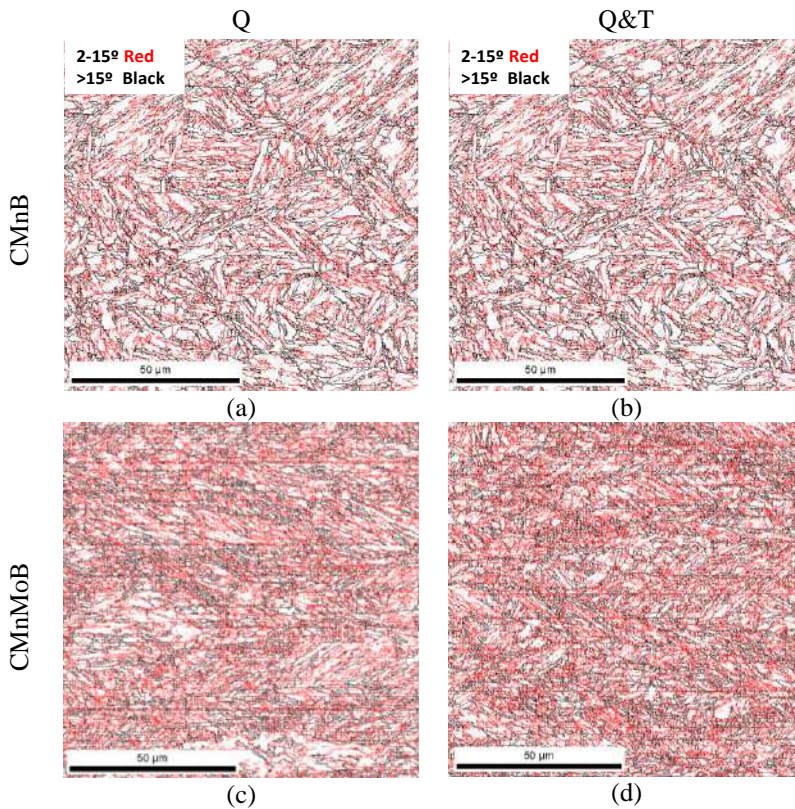


Figure 5.7. Influence of tempering on the grain boundary maps related to (a,c) CMnB and (b,d) CMnMoB steels.

In addition, in this work, the dislocation density is evaluated by means of KAM maps. Regarding the effect of chemistry, the addition of microalloying elements leads to the increment of KAM values and therefore, increases dislocation density. For the Q condition, KAM values increase from 1.2° to 1.35° , when Nb and Mo are added (see Figure 5.8).

Concerning the influence of tempering treatment, different behaviour is noticed depending on the alloy-concept. For microalloyed grades, no effect of tempering is noticed in terms of unit size and dislocation density (see Figure 5.7c and d). On the contrary, tempering of the CMnB steel evidently results in a slight reduction of the low angle boundary density and a slight unit size coarsening (see Figure 5.7 a and b). Additionally, a slight coarsening of the microstructure for the CMnB steel is observed during the heat treatment and the tempering treatment slightly shifts the KAM distribution to lower values. The tempering treatment is well known to soften

the martensitic microstructure thereby promoting an improvement of toughness and ductility.

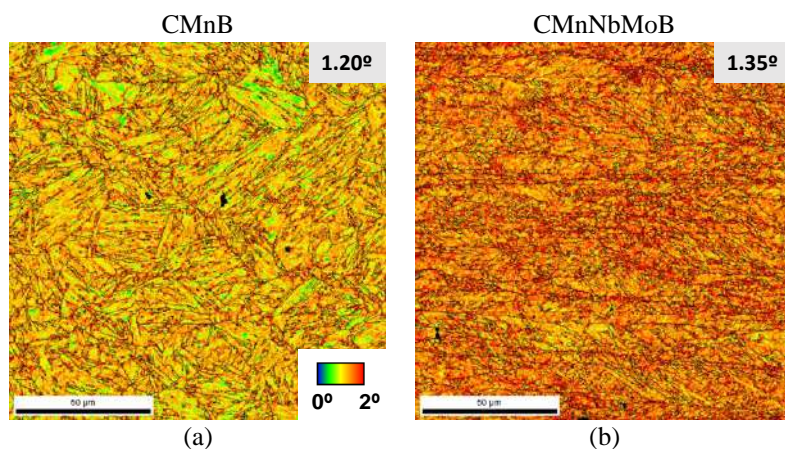


Figure 5.8. Kernel average misorientation maps corresponding to (a) CMnB and (b) CMnNbMoB steels and quenched condition.

The tensile behaviour of the quenched steels show “round-house” curves with high and continuous work hardening immediately after yielding as typically observed for martensitic steels (Figure 5.9a). The CMnB steel has the lowest strength and largest total elongation. The steels with Mo addition reach the highest strength level of over 1400 MPa tensile strength. The Nb and Mo combined alloyed steel not only shows the highest strength but also presents the best total elongation, confirming the synergy effect between Nb and Mo. Tempering drastically changes the tensile behaviour, with a significant drop to values in the range of 700 to 1034 MPa, depending on the alloy concept. The losses in yield and tensile strength after tempering are compared in Figure 5.9b. The smaller strength loss in the Mo containing steels, suggest that Mo not only provides high tempering resistance but also recovers the strength by secondary hardening. The lowest softening after tempering was observed for the combined addition of Nb and Mo. The Nb alloyed steel shows indications of secondary hardening as well yet it has clearly lower tempering resistance as compared to the Mo-added steels. This phenomenon could be related to the finer-sized carbide particles as well as high particle density observed in the steels alloyed with Mo after tempering.

Based on the information obtained by the EBSD characterization, the estimation of the contribution of strengthening mechanisms to yield strength is estimated. The yield strength is calculated considering a linear sum of individual strengthening

mechanisms based on different approaches reported in the literature [48, 115–117]. Figure 5.9c and d show the contribution of different strengthening mechanisms for the different strengthening mechanisms for Q and Q&T cycles respectively.

Regarding the quenched state (Figure 5.9c), similar contribution due to solid solution are estimated for all steels. The results suggest that the most relevant strengthening mechanism is associated with grain size refinement. Contributions ranging from 472 to 528 MPa are quantified for CMnB and CMnMoB steels, respectively. No significant effect on the hardening related to dislocation density is apparent from adding microalloying elements as this contribution only increases from 114 to 121 MPa at the most. The hardening due to carbon in solid solution is computed in the unaccounted strength. This contribution is calculated as the difference between experimental yield strength and the sum of all other contributions. Values higher than 300 MPa are quantified in all cases for the unaccounted strength.

Concerning tempering treatment (Figure 5.9d), no considerable impact of tempering is noticed on the contributions related to solid solution, grain size and dislocation density. In CMnB steel, the grain size contribution is estimated to be slightly lower after tempering, due to the observed coarsening of the microstructure after heat treatment. The experimentally observed yield strength drop after tempering is dominantly controlled by the unaccounted strength term. For the CMnB and Nb-only alloyed steel the unaccounted strength drops to a marginal level after tempering. This can be associated with thermally activated diffusion of carbon during tempering and the lack of carbon in interstitial solution remaining after tempering in the CMnB and CMnNbB steels. In addition, the CMnB steel does not contain free microalloying elements before the tempering stage and thus the unaccounted strength is zero. Nb in CMnNbB steel can be in solid solution to a small amount before tempering, preventing precipitation hardening. Conversely, in the Mo-bearing steels, a high contribution of the unaccounted strength is calculated after tempering. This could be related to a lack of complete diffusion of carbon out of the martensite lattice and/or by the formation of very fine precipitates during the tempering treatment.

Based on the precipitation analysis performed by TEM, it can be concluded that intense fine precipitation takes place (smaller than 10 nm) during tempering treatment on both Mo containing grades, resulting in a particularly strong effect on yield strength of 185 and 229 MPa for Mo and NbMo steel grades, respectively.

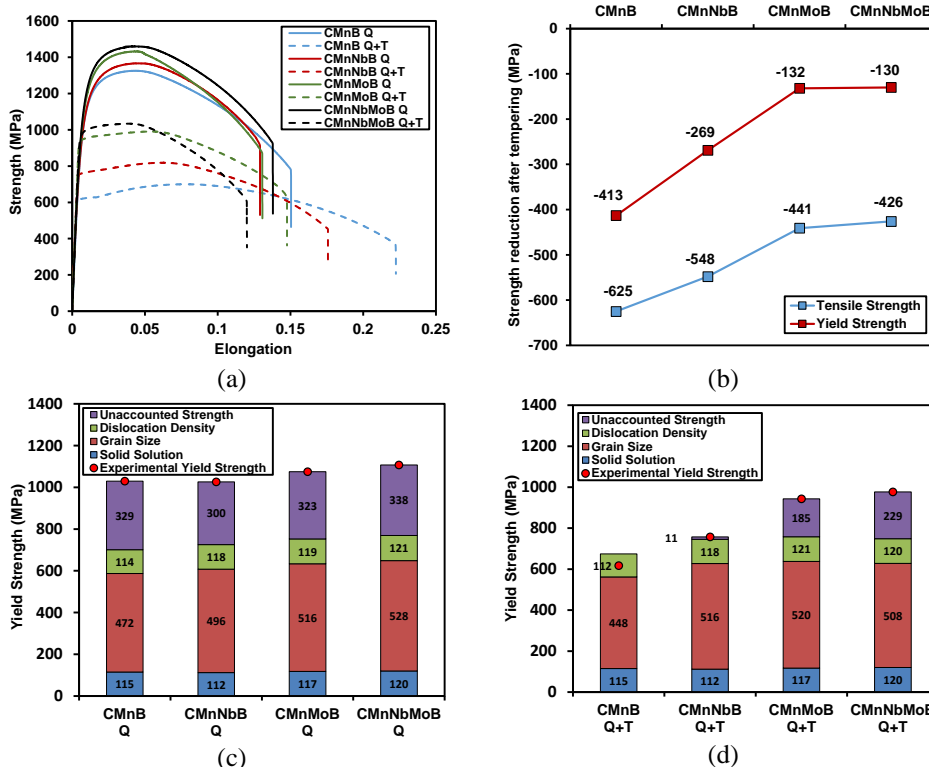


Figure 5.9. (a) Tensile curves in Q and Q&T cycles, (b) reduction of yield strength after tempering treatment and (c, d) contribution of different strengthening mechanisms to yield strength: (c) Q and (d) Q&T states.

5.3.2. Toughness properties

In relation to toughness properties, Figure 5.10a shows the impact transition curves measured in each chemical composition. Slightly better toughness properties are observed in CMnNbB and CMnMoB steels compared to the CMnB grade one. ITT50% values of -66 , -75 and -84 °C are quantified for the CMnB, CMnNbB and CMnMoB grades, respectively. Conversely, when Nb and Mo are added simultaneously, the impact transition curve shifts to higher temperatures, showing worse toughness properties with an ITT50% value of -10 °C. Considering the fracture surfaces analysis, coarser facets are noticed in Nb grade steel, whereas Mo microalloyes steel shows the finest facets. In both steels some inclusions, such as coarse Ti nitride particles, were identified in the crack-initiation regions.

Based on the equation proposed in the literature by Larzabal et al. [133] (see Equation 2.15) which was developed for ferritic-pearlitic and bainitic microstructures, a modified relationship was worked out for predicting the impact transition temperature (ITT50%) in ultrahigh-strength steels with tempered martensitic microstructures, see Equation 5.1. In this equation, in addition to the effect of chemical composition, the positive effect of refining cleavage unit size, the detrimental effect of heterogeneity, MA size and fraction are taken into account. For considering the negative effect of heterogeneity, the ratio between $D_{c20\%}$ and $D15^\circ$ mean unit size is added in the equation. The modified approach includes contributions by dislocation hardening, σ_p , and unaccounted strength, σ_{us} . Moreover, the harmful effect of carbide size, t , is also considered.

$$ITT50\% = -11(\%Mn) + 42(\%Si) + 700(\%N_{free})^{0.5} + 15(\%MA)^{1/3} + 18(D_{MA})^{0.5} - 14(D_{15^\circ})^{-0.5} + 0.26(\sigma_p + \sigma_{us}) + 63\left(\frac{D_{c20\%}}{D_{15^\circ}}\right)^{0.5} + 112(t)^{0.5} \quad 5.1$$

The ratio of $D_{c20\%}/D15^\circ$ shown in Figure 5.10b increases considerably for the CMnNbMoB, indicating the presence of a more heterogeneous microstructure. The $D_{c20\%}/D15^\circ$ ratios for the other alloys are nearly identical and approximately half of that found in the CMnNbMoB steel. From the data, it can be concluded that the inhomogeneity must have been generated during the first deformation stage.

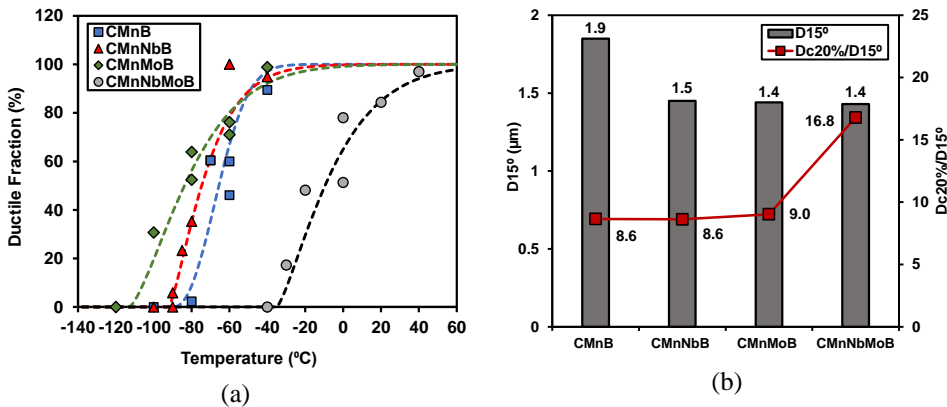


Figure 5.10. (a) Effect of the addition of microalloying elements on toughness properties for Q&T condition (ductile fraction as a function of test temperature) and (b) $D15^\circ$ and $D_{c20\%}/D15^\circ$ values.

It is demonstrated that the addition of boron to a Nb-microalloyed steel accelerates the precipitation of Nb (C,N) and induces it to occur at higher temperatures. Additionally, boron and molybdenum segregating to grain boundaries and dislocations can retard recrystallization after deformation. It is thus possible that

particularly the combined alloying of niobium, molybdenum and boron already impedes recrystallization at rather high deformation temperatures, resulting in individual unrecrystallized austenite grains growing in size.

The contribution to yield strength regarding dislocation density (σ_p) and unaccounted strength (σ_{us}) is plotted in Figure 5.11a. Dislocation strengthening slightly increases when microalloying elements are added, increasing from 112 to 121 MPa for CMnB and Mo-microalloyed steel, respectively. The contribution related to unaccounted strength is nearly negligible for CMn and Nb steels, whilst for Mo containing grades, the impact of this contribution is considerably higher (185 and 229 MPa, for CMnMoB and CMnNbMoB, respectively). This larger yield strength could be attributed to the formation of ultra-fine Mo-based precipitates during the tempering treatment. The synergy between Mo and Nb further enhances this precipitation strengthening effect.

The relative contribution of different strengthening mechanisms on both tensile and toughness properties is illustrated in Figure 5.11b. The contribution to strength of MA phase, only present in Nb grade, is marginal and does not increase the ITT50%. The clearly biggest contribution to strength is related to the microstructural refinement. The generally extremely fine-grained structure of martensite accounts for a yield strength increase of 450-520 MPa correlating in that range with the severity of austenite conditioning. Simultaneously, the transition temperature is significantly decreasing with the strength increase, manifesting this well-established and unique benefit of microstructural refinement. Other mechanisms such as dislocation strengthening and unaccounted strength cause an increase in transition temperature, which however is largely overcompensated by the microstructural refinement. Thus, the strategy for strengthening of first maximizing grain refinement before employing other mechanisms typically result in an improved ductile-to-brittle transition behaviour. The main deleterious effect on the ductile-to-brittle behaviour is related to heterogeneity in the grain size distribution. Especially the 20% fraction of largest grains is harmful to ITT50% whereas its impact on strength is neutral. Large grains are sensitive to cleavage at higher temperature than smaller ones. Simultaneously the starting cracks caused by cleaving of larger individual grains are more likely to propagate. The fraction of very small prior austenite grains in the CMnNbB steel resulting from dynamic recrystallization is thus not expected to negatively affect ITT50%. However, the co-existence of very fine and larger grains can cause a serious level of residual stress in quenched steels, leading to macroscopic distortion. The occurrence of the very fine grains by dynamic recrystallization was found to be suppressed in the current steels by sufficient alloying of molybdenum.

NbMo steel show more heterogeneities compared to CMnNbB and CMnMoB grades, as well as higher contribution of hardening due to fine precipitation, negatively affecting ITT50%.

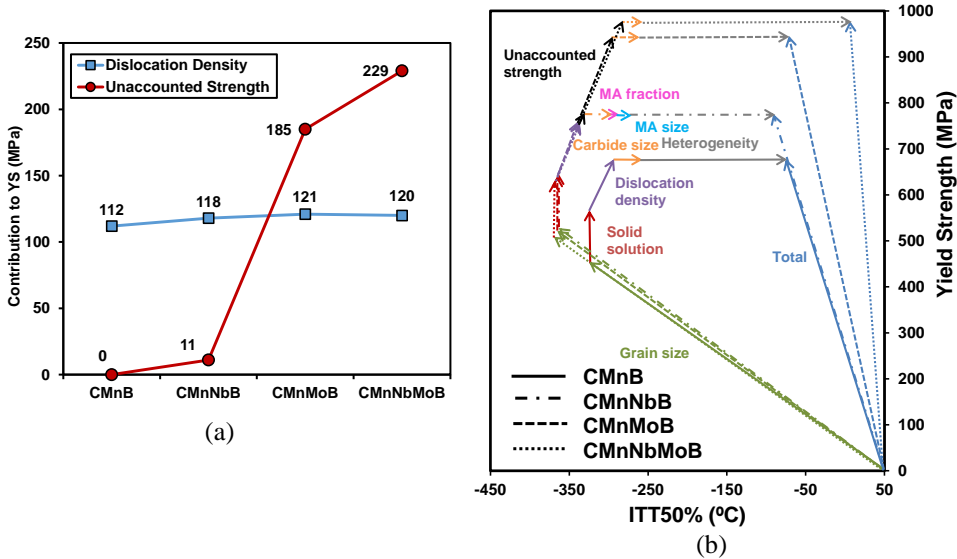


Figure 5.11. (a) Contribution of dislocation density and unaccounted strength to yield strength and (b) relative contribution of different strengthening mechanisms on both strength and toughness properties.

5.4. Industrial trials

Recently, several industrial trials have been carried out at Dillinger. In this industrial trials, the market requirement regarding martensitic microstructure and tensile/toughness properties have been successfully achieved. After industrial trials, a detailed characterization has also been performed at Ceit following the same characterization procedure as in the current PhD.

The obtained microstructures have been characterized by optical microscopy and FEGSEM. Furthermore, the carbide sizes and the mean unit sizes have been quantified before and after tempering. The microstructural analysis has been completed by hardness measurements. Based on the information obtained from EBSD characterization, the contribution of different strengthening mechanisms to yield strength has been estimated.

Due to confidentiality, the results obtained at the industrial tests could not be shown in this work.

6. Conclusions and future work

This part summarizes the obtained conclusions for each topic and explains the future work to be done.

Hot working behaviour

- The addition of Nb, Mo and Nb-Mo promotes a delay in softening kinetics, in the deformation temperature range between 1100-850 °C, being the effect of microalloying more significant at the lowest deformation temperature of 850 °C.
- The combined addition of Nb and Mo results in a synergetic behaviour on recrystallization kinetics. At higher deformation temperatures, both niobium and molybdenum exert a strong solute drag effect. At lower deformation temperatures, Nb partially precipitates and in combination with solute drag exerted by Mo completely suppresses fractional softening.
- The accuracy of a microstructural evolution model predicting the time for 50% recrystallization was validated for the current steels with higher Mo content (0.5%).
- The highest T_{nr} values were obtained for the combined addition of Nb and Mo, followed by CMnMoB, CMnNbB and CMnB. A slight effect of strain per pass and interpass time on T_{nr} was noticed in the studied steels. The increase of strain per pass leads to higher T_{nr} values. Furthermore, when larger interpass time was applied, a reduction in T_{nr} value is noticed. Both effects are more pronounced for Mo alloyed steels.
- MicroSim-PM® software was used for predicting the recrystallized fraction of austenite from pass to pass and estimating the evolution of fractional softening during plate hot rolling simulation. The obtained results showed reasonably good agreement with the experimental behaviour.

- During hot rolling simulation, at the finishing deformation passes, dynamic recrystallization is activated in the Nb microalloyed steel. Conversely, the addition of Mo completely suppresses DRX under the same conditions.
- When a large single-pass strain ($\varepsilon = 4$) is applied instead, Mo alloying does not completely prevent the initiation of dynamic recrystallization, showing a mixed microstructure consisting of elongated and recrystallized grains.
- The addition of Mo becomes crucial in order to suppress the activation of DRX, to ensure hardenability and to avoid the formation of softer bainitic phases in the final martensitic microstructure.

Phase transformation analysis

- The addition of Mo (0.5%) reduces the critical cooling rate and becomes essential to ensure hardenability and to obtain fully martensitic microstructures.
- The excellent hardenability in the Mo-alloyed steel is related to intrinsic effects of molybdenum reducing the ferrite nucleation rate and exerting strong solute drag on the carbon-enriched interphase area. Furthermore, Mo enhances the efficiency of B by preventing partial precipitation into $\text{Fe}_{23}(\text{B,C})_6$.
- Identical steel alloys are less hardenable under Direct Quenching (DQ) condition as compared to Conventional Quenching (CQ) condition. This can be explained by accumulated strain and a larger total grain boundary surface of pancaked austenite offering more nucleation sites for ferrite in the DQ process. Both effects are further promoted by Nb microalloying.
- Applying DQ strategy, Mo addition becomes necessary to fulfil completely martensitic microstructures and to decrease the critical cooling rate to achieve martensite. Therefore, Mo alloy concept seems to be the best option when DQ strategy is considered.

Relationship between microstructure and mechanical properties

Tensile properties

- In as-quenched condition, the steels with Mo addition reach the highest strength level. Yield strength values of 1030 and 1107 MPa were obtained for CMnB and NbMo grades, respectively.

- Upon tempering (600°C/900s), the CMnB steel experiences a large drop of yield and tensile strength in the order of 400 MPa and 600 MPa, respectively. The NbMo steel, however, shows the best tempering resistance, with a drop of yield strength of 130 MPa.
- Detailed EBSD analysis revealed that the small Nb addition is highly efficient in retaining the extremely fine large-angle and small-angle unit sizes present in the quenched condition during tempering, while the CMnB steel shows measurable coarsening of these. Mo alloying achieves a particularly fine-sized low-angle grain boundary structure in the quenched steel that is being retained even after tempering.
- The most relevant strengthening mechanism is associated with grain size refinement. Regarding the quenched state, the effect of carbon in solid solution has been confirmed in all steel grades (involved in “unaccounted strength” term).
- No considerable impact of the tempering treatment is noticed for the contributions by solid solution, unit size and dislocation density. The most relevant yield strength drop is related to the unaccounted strength term. For CMn and Nb alloys, marginal levels of carbon in solid solution have been noticed, due to the formation of carbides during tempering and the lack of C in solid solution. Conversely, in the Mo alloyed steels, a high contribution of “unaccounted strength” of 185 and 229 MPa, for Mo and NbMo grades, respectively is measured. This could be associated with the remaining C in solid solution or with the formation of fine precipitates during the tempering treatment. In both Mo and NbMo steel grades, ultra-fine Mo-rich precipitates have been identified by TEM.

Toughness properties

- Slightly better toughness properties are observed in CMnNbB and CMnMoB steel grades when compared to CMnB. Conversely, the NbMo combination results in worst toughness properties. This worsening is related to microstructural heterogeneity, the presence of fine precipitates and high dislocation density.
- An equation able to predict ITT50% in tempered martensitic microstructures was worked out. The excellent agreement between predicted and experimental data suggest that the modified relationship not only is appropriate for predicting transition temperatures of tempered martensitic microstructures but also allows for the identification of major influencing effects.

Future work

- To improve the constitutive equations implemented in MicroSim-PM®, in order to better account for the austenite grain boundary segregation behaviour of molybdenum and boron. In addition, to implement dynamic recrystallization in MicroSim-PM®.
- To analyse the crystal structure of the achieved martensitic microstructures via X Ray diffraction and analyse the evidence of tetragonality. Further study is needed in order to confirm if carbon is in solid solution after tempering in Mo-grades.
- To study the feasibility of boron free Mo and Nb-Mo alloy concepts and to evaluate the effect of DQ in terms of microstructure, tensile and toughness properties in this boron free steels. To analyse if Mo and Nb-Mo addition is sufficient to ensure hardenability.
- To study the impact of adding Ni besides Mo to enhance hardenability and ensure the formation of fully martensitic microstructures especially for heavy gauge plates.

References

- [1] J. Hannula, D. Porter, A. Kajjalainen, M. Somani, and J. Kömi, “Optimization of niobium content in direct quenched high-strength steels,” *Metals (Basel)*, vol. 10, no. 6, pp. 1–16, 2020.
- [2] I. Zurutuza, N. Isasti, E. Detemple, V. Schwinn, H. Mohrbacher, and P. Uranga, “Effect of Thermomechanical Strategy and Mo-Nb-B Alloying Additions on High Strength Medium Carbon Q/Q&T Steels,” in *Materials Science and Technology (MS&T19)*, 2019, pp. 1401–1408.
- [3] H. Mohrbacher, “Synergies of niobium and boron microalloying in molybdenum based bainitic and martensitic steel, Fundamentals and Applications of Mo and Nb alloying in High Performance Steels,” *CBMM, IMO A TMS*, vol. 1, pp. 83–108, 2014.
- [4] S. Vervynckt, K. Verbeken, B. Lopez, and J. J. Jonas, “Modern HSLA steels and role of non-recrystallisation temperature,” *Int. Mater. Rev.*, vol. 57, no. 4, pp. 187–207, 2012.
- [5] “<https://www.imoa.info/molybdenum-uses/molybdenum-grade-alloy-steels-irons/heat-treatable-plate-steel.php>.”
- [6] P. Cizek, B. P. Wynne, C. H. J. Davies, B. C. Muddle, and P. D. Hodgson, “Effect of composition and austenite deformation on the transformation characteristics of low-carbon and ultralow-carbon microalloyed steels,” *Metall. Mater. Trans. A Phys. Metall. Mater. Sci.*, vol. 33, no. 5, pp. 1331–1349, 2002.
- [7] T. Hara, H. Asahi, R. Uemori, and H. Tamehiro, “Role of combined addition of niobium and boron and of molybdenum and boron on hardenability in low carbon steels,” *ISIJ Int.*, vol. 44, no. 8, pp. 1431–1440, 2004.
- [8] S. K. Dhua and S. K. Sen, “Effect of direct quenching on the microstructure and mechanical properties of the lean-chemistry HSLA-100 steel plates,” *Mater. Sci. Eng. A*, vol. 528, no. 21, pp. 6356–6365, 2011.
- [9] A. Kajjalainen, S. Pallaspuro, and D. A. Porter, “Tempering of direct quenched low-alloy ultra-high-strength steel, part I - Microstructure,” *Adv. Mater. Res.*, vol. 922, pp. 316–321, 2014.
- [10] I. Zurutuza, N. Isasti, E. Detemple, V. Schwinn, H. Mohrbacher, and P. Uranga, “Effect of Nb and Mo additions in the microstructure/tensile property relationship in high strength quenched and quenched and tempered boron steels,” *Metals (Basel)*, vol. 11, no. 1, pp. 1–21, 2021.
- [11] I. Zurutuza, N. Isasti, E. Detemple, V. Schwinn, H. Mohrbacher, and P. Uranga, “Toughness property control by Nb and Mo additions in high-strength quenched and tempered boron steels,” *Metals (Basel)*, vol. 11, no. 1, pp. 1–20, 2021.
- [12] C. Revilla, B. López, and J. M. Rodriguez-Ibabe, “Carbide size refinement by controlling the heating rate during induction tempering in a low alloy steel,” *Mater. Des.*, vol. 62, pp. 296–304, 2014.
- [13] G. Krauss, “Martensite in steel: Strength and structure,” *Mater. Sci. Eng. A*, vol. 273–275, pp. 40–57, 1999.
- [14] J.W. and Sons, “HSLA Steels, Microalloying and Offshore Engineering Steels,” *Chinese Soc. Met.*, 2015.
- [15] Y. H. Bae, J. S. Lee, J. K. Choi, W. Y. Choo, and S. H. Hong, “Effects of austenite conditioning on austenite/ferrite phase transformation of HSLA steel,” *Mater. Trans.*, vol. 45, no. 1, pp. 137–142, 2004.

References

- [16] D. A. Skobir, “High-Strength Low Alloy (HSLA) Steels,” *Mater. Sci. Technol.*, vol. 45, no.4, pp. 295–301, 2011.
- [17] J. W. Cahn, “The impurity-drag effect in grain boundary motion,” *Acta Metall.*, vol. 10, no. 9, pp. 789–798, 1962.
- [18] M. Suehiro, “An Analysis of the Solute Drag Effect of Nb on Recrystallization of Ultra Low Carbon Steel,” *ISIJ Int.*, vol. 38, no. 6, pp. 547–552, 1998.
- [19] J. J. Jonas, “Mechanical testing for the study of austenite recrystallization and carbonitride precipitation,” in *D. P. Dunne y T. Chandra, eds. Conference on High Strength Low Alloy Steels*, 1984, pp. 80–91.
- [20] R. D. Doherty *et al.*, “Current issues in recrystallization: A review,” *Mater. Sci. Eng. A*, vol. 238, no. 2, pp. 219–274, 1997.
- [21] M. D. C. Sobral, P. R. Mei, and H. J. Kestenbach, “Effect of carbonitride particles formed in austenite on the strength of microalloyed steels,” *Mater. Sci. Eng. A*, vol. 367, no. 1–2, pp. 317–321, 2004.
- [22] A. Iza-Mendia, M. A. Altuna, B. Pereda, and I. Gutiérrez, “Precipitation of Nb in ferrite after austenite conditioning. Part I: Microstructural characterization,” *Metall. Mater. Trans. A Phys. Metall. Mater. Sci.*, vol. 43, no. 12, pp. 4553–4570, 2012.
- [23] C. Y. Chen *et al.*, “Precipitation hardening of high-strength low-alloy steels by nanometer-sized carbides,” *Mater. Sci. Eng. A*, vol. 499, no. 1–2, pp. 162–166, 2009.
- [24] A. J. Deardo, “Niobium in modern steels,” *Int. Mater. Rev.*, vol. 48, pp. 371–402, 2003.
- [25] K. Hulka, A. Kern, and U. Schriefer, “Application of Niobium in Quenched and Tempered High-Strength Steels,” *Mater. Sci. Forum*, vol. 500–501, pp. 519–526, 2005.
- [26] B. Pereda, B. López, and J.M Rodríguez- Ibabe, “Increasing the non-recrystallization temperature of Nb microalloyed steels by Mo addition,” 2007.
- [27] G. Larzabal, N. Isasti, J. M. Rodríguez-Ibabe, and P. Uranga, “Precipitation Strengthening by Induction Treatment in High Strength Low Carbon Microalloyed Hot-Rolled Plates,” *Metall. Mater. Trans. A Phys. Metall. Mater. Sci.*, vol. 49, no. 3, pp. 946–961, 2018.
- [28] B. Pereda, A. I. Fernández, B. López, and J. M. Rodríguez-Ibabe, “Effect of Mo on dynamic recrystallization behavior of Nb-Mo microalloyed steels,” *ISIJ Int.*, vol. 47, no. 6, pp. 860–868, 2007.
- [29] J. Hannula, D. A. Porter, A. Kaijalainen, and J. Kömi, “Evaluation of Mechanical Properties and Microstructures of Molybdenum and Niobium Microalloyed Thermomechanically Rolled High-Strength Press Hardening Steel,” *JOM*, vol. 71, no. 7, pp. 2405–2412, 2019.
- [30] I. Zurutuza, N. Isasti, E. Detemple, V. Schwinn, H. Mohrbacher, and P. Uranga, “Effect of Quenching Strategy and Nb-Mo Additions on Phase Transformations and Quenchability of High-Strength Boron Steels,” *JOM*, 2021.
- [31] J. Hannula *et al.*, “Effect of Boron on the Strength and Toughness of Direct-Quenched Low-Carbon Niobium Bearing Ultra-High-Strength Martensitic Steel,” *Metall. Mater. Trans. A Phys. Metall. Mater. Sci.*, vol. 48, no. 11, pp. 5344–5356, 2017.
- [32] N. Isasti, D. Jorge-Badiola, M. L. Taheri, and P. Uranga, “Phase transformation study in Nb-Mo microalloyed steels using dilatometry and EBSD quantification,” *Metall. Mater. Trans. A Phys. Metall. Mater. Sci.*, vol. 44, no. 8, pp. 3552–3563, 2013.
- [33] P. Cizek, B. P. Wynne, C. H. J. Davies, and P. D. Hodgson, “The Effect of Simulated Thermomechanical Processing on the Transformation Behavior and Microstructure of a Low-Carbon Mo-Nb Linepipe Steel,” *Metall. Mater. Trans. A Phys. Metall. Mater. Sci.*, vol. 46, no. 1, pp. 407–425, 2015.

- [34] W. B. Lee, S. G. Hong, C. G. Park, K. H. Kim, and S. H. Park, "Influence of Mo on precipitation hardening in hot rolled HSLA steels containing Nb," *Scr. Mater.*, vol. 43, no. 4, pp. 319–324, 2000.
- [35] N. Isasti, D. Jorge-Badiola, M. L. Taheri, and P. Uranga, "Microstructural and precipitation characterization in Nb-Mo microalloyed steels: Estimation of the contributions to the strength," *Met. Mater. Int.*, vol. 20, no. 5, pp. 807–817, 2014.
- [36] B. Pereda, B. López, and J. M. Rodríguez-Ibabe, "Role of Mo on Static Recrystallization Kinetics in Coarse Grained Nb Microalloyed Steels," *Mater. Sci. Forum*, vol. 753, pp. 453–458, 2013.
- [37] K. Ishikawa, H. Nakamura, R. Homma, M. Fujioka, and M. Hoshino, "Effect of molybdenum content on the combined effect of boron and molybdenum on hardenability of low-carbon boron-added steels," *ISIJ Int.*, vol. 58, no. 3, pp. 551–560, 2018.
- [38] A. Larrañaga-Otegui, B. Pereda, D. Jorge-Badiola, and I. Gutiérrez, "Austenite Static Recrystallization Kinetics in Microalloyed B Steels," *Metall. Mater. Trans. A Phys. Metall. Mater. Sci.*, vol. 47, no. 6, pp. 3150–3164, 2016.
- [39] M. Sharma, I. Ortlepp, and W. Bleck, "Boron in Heat-Treatable Steels: A Review," *Steel Res. Int.*, vol. 90, no. 11, 2019.
- [40] H. Kejian and T. N. Baker, "The effects of small titanium additions on the mechanical properties and the microstructures of controlled rolled niobium-bearing HSLA plate steels," *Mater. Sci. Eng. A*, vol. 169, no. 1–2, pp. 53–65, 1993.
- [41] H. Mohrbacher, "Property optimization in as-quenched martensitic steel by molybdenum and niobium alloying," *Metals (Basel)*, vol. 8, no. 4, pp. 1–22, 2018.
- [42] H. Mohrbacher, "Principal Effects of Mo in HSLA Steels and Cross Effects with Microalloying elements," in *International seminar on applications of Mo in steels*, 2010, pp. 74–96.
- [43] J.M Rodríguez- Ibabe, "Online course : Optimizing the application of microalloying in value-added steel grades Principles of hot working : controlled rolling," no. August, 2020.
- [44] J.M Rodríguez- Ibabe, "Metallurgical Aspects of Rolling Process," in *The Making, Shaping and Treating of Steels*, Flat Products, Ed. 2014, pp. 113–170.
- [45] B. M. Kim, K. H. Lee, and J. B. Jeon, "Short Stroke Control Model for Improving Width Precision at Head and Tail of Slab in Hot Vertical–Horizontal Rolling Process," *Int. J. Precis. Eng. Manuf.*, vol. 21, no. 4, pp. 699–710, 2020.
- [46] J.M Rodríguez- Ibabe, "Online course : Optimizing the application of microalloying in value-added steel grades Principles of hot working : austenite evolution," no. June, 2020.
- [47] J. M. Rodríguez-Ibabe and J. J. Urkola, *Metalurgia Física de los Aceros*. San Sebastián: Universidad de Navarra, 2005.
- [48] F. B. Pickering and T. Gladman, "Metallurgical Developments in Carbon Steels," *Iron Steel Inst.*, p. Special Report No.81, 1963.
- [49] T. Siwecki, "Modelling of Microstructure Evolution during Recrystallization Controlled Rolling," *ISIJ Int.*, vol. 32, no. 3, pp. 368–376, 1992.
- [50] J. Hannula, D. Porter, A. Kaijalainen, M. Somani, and J. Kõmi, "Mechanical properties of direct-quenched ultra-high-strength steel alloyed with molybdenum and niobium," *Metals (Basel)*, vol. 9, no. 3, 2019.
- [51] A. Saastamoinen, A. Kaijalainen, D. Porter, P. Suikkanen, J. R. Yang, and Y. T. Tsai, "The effect of finish rolling temperature and tempering on the microstructure, mechanical properties and dislocation density of direct-quenched steel," *Mater. Charact.*, vol. 139, no. June 2017, pp. 1–10, 2018.

References

- [52] Z. J. Xie, C. J. Shang, X. L. Wang, X. P. Ma, S. V. Subramanian, and R. D. K. Misra, "Microstructure-property relationship in a low carbon Nb-B bearing ultra-high strength steel by direct-quenching and tempering," *Mater. Sci. Eng. A*, vol. 727, no. March, pp. 200–207, 2018.
- [53] M. S. Baek, Y. K. Kim, T. W. Park, J. Ham, and K. A. Lee, "Hot-rolling and a subsequent direct-quenching process enable superior high-cycle fatigue resistance in ultra-high strength low alloy steels," *Materials (Basel)*, vol. 13, no. 20, pp. 1–17, 2020.
- [54] C. S. Roberts, B. L. Averbach, and M. Cohen, "The Mechanism and Kinetics of the First Stage of Tempering," *Trans. ASM*, vol. 45, pp. 576–604, 1953.
- [55] B. S. Lement, B.L.Averbach, and M. Cohen, "Microstructural Changes on Tempering Iron-Carbon Alloys," *Trans. ASM*, vol. 46, pp. 851–881, 1954.
- [56] F. E. Werner, B. L. Averbach, and M. Cohen, "The Tempering of Iron-Carbon Martensitic Crystals," *Trans. ASM*, vol. 49, pp. 823–841, 1957.
- [57] B. S. Lement, B. L. Averbach, and M. Cohen, "Further Study of Microstructural Changes on Tempering Iron-Carbon Alloys," *Trans. ASM*, vol. 47, pp. 291–319, 1955.
- [58] S. Yusa, T. Hara, K. Tsuzaki, and T. Takahashi, "Refinement of grain boundary cementite in medium-carbon tempered martensite by thermomechanical processing," *Mater. Sci. Eng. A*, vol. 273–275, pp. 462–465, 1999.
- [59] T. Furuhashi, K. Kobayashi, and T. Maki, "Control of cementite precipitation in lath martensite by rapid heating and tempering," *ISIJ Int.*, vol. 44, no. 11, pp. 1937–1944, 2004.
- [60] M. Hayakawa, S. Matsuoka, K. Tsuzaki, H. Hanada, and M. Sugisaki, "Atomic force microscopy of induction- and furnace-heating-tempered prestressed steels with different delayed fracture properties," *Scr. Mater.*, vol. 47, no. 10, pp. 655–661, 2002.
- [61] J. Lin, D. Balint, and M. Pietrzyk, *Microstructure Evolution in Metal-Forming Processes*, Woodhead P. 2012.
- [62] A. I. Fernández, B. López, and J. M. Rodríguez-Ibabe, "Study of nucleation mechanisms during dynamic recrystallization of a coarse Nb microalloyed austenite," *Mater. Sci. Forum*, vol. 467–470, no. II, pp. 1169–1174, 2004.
- [63] A. I. Fernández, P. Uranga, B. López, and J. M. Rodríguez-Ibabe, "Dynamic recrystallization behavior covering a wide austenite grain size range in Nb and Nb-Ti microalloyed steels," *Mater. Sci. Eng. A*, vol. 361, no. 1–2, pp. 367–376, 2003.
- [64] J. A. Stendal, M. Bambach, M. Eisentraut, I. Sizova, and S. Weiß, "Applying machine learning to the phenomenological flow stress modeling of TNM-B1," *Metals (Basel)*, vol. 9, no. 2, pp. 1–18, 2019.
- [65] J.P. Sah, G.L. Richardson, and C.M. Sellars, "Grain-Size Effects during Dynamic Recrystallization of Nickel," *Met.Sci.*, vol. 8, pp. 325–331, 1974.
- [66] C.M Sellars, "The Physical Metallurgy of Hot Working," *Hot Work. Form. Process. Met. Soc.*, pp. 3–15, 1980.
- [67] M. Avrami, "Kinetics of phase change. I: General theory," *J. Chem. Phys.*, vol. 7, no. 12, pp. 1103–1112, 1939.
- [68] J. H. Beynon and C. M. Sellars, "Modelling Microstructure and Its Effects during Multipass Hot Rolling," *ISIJ Int.*, vol. 32, no. 3, pp. 359–367, 1992.
- [69] M. Džubinský, Z. Husain, and W. M. Van Haaften, "Comparison of recrystallisation kinetics determined by stress relaxation, double hit, optical metallography and EBSD approaches," *Mater. Charact.*, vol. 52, no. 2, pp. 93–102, 2004.

- [70] S. F. Medina and J. E. Mancilla, "Elements in Solution on Static Recrystallization of Hot Deformed Steels," *ISIJ Int.*, vol. 36, no. 8, pp. 1063–1069, 1996.
- [71] B. Dutta and C.M Sellars, "Effect of Composition and Process Variables on Nb(C,N) Precipitation in Niobium Microalloyed Austenite," *Mater. Sci. Technol.*, vol. 3, pp. 197–206, 1987.
- [72] P.D Hodgson, "Models of Recrystallization behaviour of CMn and Nb Microalloyed Steels during Hot Working Processes," *Mater. Forum*, vol. 17, p. 403, 1993.
- [73] O. Kwon, "A Technology for the Prediction and Control of Microstructural Changes and Mechanical Properties in Steel," *ISJ Int.*, vol. 32, p. 350, 1992.
- [74] S. F. Medina and A. Quispe, "Improved model for static recrystallization kinetics of hot deformed austenite in low alloy and Nb/V microalloyed steels," *ISIJ Int.*, vol. 41, no. 7, pp. 774–781, 2001.
- [75] R. Abad, A. I. Fernández, B. López, and J. M. Rodríguez-Ibabe, "Interaction between recrystallization and precipitation during multipass rolling in a low carbon niobium microalloyed steel," *ISIJ Int.*, vol. 41, no. 11, pp. 1373–1382, 2001.
- [76] A. I. Fernández, P. Uranga, B. López, and J. M. Rodríguez-Ibabe, "Static recrystallization behaviour of a wide range of austenite grain sizes in microalloyed steels," *ISIJ Int.*, vol. 40, no. 9, pp. 893–901, 2000.
- [77] B. Pereda, "Study of the Effect of Mo Addition on the austenite Microstructure Evolution during Hot rolling of Nb Microalloyed steels. Application to Thin Slab Direct Rolling Technologies," Universidad de Navarra, San Sebastián, 2009.
- [78] C. M. Sellars, "Hot Working and Forming Processes," in *An International Conference*, 1979, pp. 3–15.
- [79] K. Lücke and K. Detert, "A quantitative theory of grain-boundary motion and recrystallization in metals in the presence of impurities," *Acta Metall.*, vol. 5, no. 11, pp. 628–637, 1957.
- [80] K. Lücke and H. P. Stüwe, "On the theory of impurity controlled grain boundary motion," *Acta Metall.*, vol. 19, no. 10, pp. 1087–1099, 1971.
- [81] C.S. Smith, "Introduction to grains, phases, and interfaces - An interpretation of microstructure," *Trans. AIME*, 1948, vol. 175, pp. 15-51, by C.S. Smith," *Metall. Mater. Trans. B Process Metall. Mater. Process. Sci.*, vol. 41, no. 3, p. 457, 2010.
- [82] M. Arribas, B. López, and J. M. Rodríguez-Ibabe, "Influence of Ti on static recrystallization in near net shape steels," *Mater. Sci. Forum*, vol. 500–501, pp. 131–138, 2005.
- [83] M. Gómez and S. F. Medina, "Recrystallisation Driving and Pinning Forces during Hot Rolling of a Low Nb-Microalloyed Steel," *Mater. Sci. Forum*, vol. 500–501, pp. 147–154, 2005.
- [84] S. S. Hansen, J. B. V. Sande, and M. Cohen, "Niobium carbonitride precipitation and austenite recrystallization in hot-rolled microalloyed steels," *Metall. Trans. A*, vol. 11, no. 3, pp. 387–402, 1980.
- [85] J. M. Rodríguez-Ibabe, "Thin Slab Direct Rolling of Microalloyed Steels," *Mater. Sci. Forum*, vol. 500–501, pp. 49–62, 2005.
- [86] J. Cao, Q. Yong, Q. Liu, and X. Sun, "Precipitation of MC phase and precipitation strengthening in hot rolled Nb-Mo and Nb-Ti steels," *J. Mater. Sci.*, vol. 42, no. 24, pp. 10080–10084, 2007.
- [87] G. Larzabal, "Efecto de los parámetros de laminación y post-tratamiento térmico por inducción en la mejora de propiedades mecánicas de aceros microaleados," Universidad de Navarra, 2017.

References

- [88] L. García Sesma, "Control de la secuencia de precipitación para reducir la dispersión en propiedades mecánicas de aceros microaleados con altos contenidos de Ti," Universidad de Navarra, 2019.
- [89] B. López and J. M. Rodríguez-Ibabe, *Recrystallisation and grain growth in hot working of steels*. Woodhead Publishing Limited, 2012.
- [90] B. Dutta, E. J. Palmiere, and C. M. Sellars, "Modelling the kinetics of strain induced precipitation in Nb microalloyed steels," *Acta Mater.*, vol. 49, no. 5, pp. 785–794, 2001.
- [91] Y. Funakawa, T. Shiozaki, K. Tomita, T. Yamamoto, and E. Maeda, "Development of high strength hot-rolled sheet steel consisting of ferrite and nanometer-sized carbides," *ISIJ Int.*, vol. 44, no. 11, pp. 1945–1951, 2004.
- [92] H. W. Yen, P. Y. Chen, C. Y. Huang, and J. R. Yang, "Interphase precipitation of nanometer-sized carbides in a titanium-molybdenum-bearing low-carbon steel," *Acta Mater.*, vol. 59, no. 16, pp. 6264–6274, 2011.
- [93] N. Isasti, "Estudio de las transformaciones de fase en aceros microaleados con Nb y Nb-Mo. Relación entre microestructura y propiedades mecánicas," Universidad de Navarra, 2013.
- [94] N. Isasti, D. Jorge-Badiola, M. L. Taheri, B. López, and P. Uranga, "Effect of composition and deformation on coarse-grained austenite transformation in Nb-Mo microalloyed steels," *Metall. Mater. Trans. A Phys. Metall. Mater. Sci.*, vol. 42, no. 12, pp. 3729–3742, 2011.
- [95] E.C. Bain, "The Nature of Martensite," *Trans. AIME*, vol. 70, pp. 25–35, 1924.
- [96] J.W. Christians, "Martensite Fundamentals and Technology".
- [97] K. W. Andrews, "Empirical formulae for the calculation of some transformation temperatures," *jisi*, vol. 203, pp. 721–727, 1965.
- [98] G. Krauss, *Quench and Tempered Martensitic Steels: Microstructures and Performance*, vol. 12. Elsevier, 2014.
- [99] "The tempering of martensite, 9.," *Carbon N. Y.*, pp. 183–208.
- [100] G. Krauss and S. W. Thompson, "Ferritic Microstructures in Continuously Cooled Low- and Ultralow-carbon Steels," *ISIJ Int.*, vol. 35, no. 8, pp. 937–945, 1995.
- [101] H. I. Aaronson, "The decomposition of austenite by diffusional processes," *Interscience*, 1962.
- [102] H. K. D. H. Bhadeshia and J. W. Christian, "Bainite in steels," *Metall. Trans. A*, vol. 21, no. 3, pp. 767–797, 1990.
- [103] R. G. Thiessen, J. Sietsma, T. A. Palmer, J. W. Elmer, and I. M. Richardson, "Phase-field modelling and synchrotron validation of phase transformations in martensitic dual-phase steel," *Acta Mater.*, vol. 55, no. 2, pp. 601–614, 2007.
- [104] G. Reisner, E. A. Werner, and F. D. Fischer, "Micromechanical modelling of martensitic transformation in random microstructures," *Int. J. Solids Struct.*, vol. 35, no. 19, pp. 2457–2473, 1998.
- [105] S. W. Thompson, D. J. Colvin, and G. Krauss, "Austenite decomposition during continuous cooling of an HSLA-80 plate steel," *Metall. Mater. Trans. A Phys. Metall. Mater. Sci.*, vol. 27, no. 6, pp. 1557–1571, 1996.
- [106] H. J. Jun, J. S. Kang, D. H. Seo, K. B. Kang, and C. G. Park, "Effects of deformation and boron on microstructure and continuous cooling transformation in low carbon HSLA steels," *Mater. Sci. Eng. A*, vol. 422, no. 1–2, pp. 157–162, 2006.
- [107] C. Fossaert, G. Rees, T. Mauricx, and H. K. D. H. Bhadeshia, "The effect of niobium on the hardenability of microalloyed austenite," *Metall. Mater. Trans. A*, vol. 26, no. 1, pp. 21–30, 1995.

- [108] F. Han, B. Hwang, D.-W. Suh, Z. Wang, D. L. Lee, and S.-J. Kim, "Effect of molybdenum and chromium on hardenability of low-carbon boron-added steels," *Met. Mater. Int.*, vol. 14, no. 6, pp. 667–672, 2008.
- [109] A. Terzic, M. Calcagnotto, S. Guk, T. Schulz, and R. Kawalla, "Influence of Boron on transformation behavior during continuous cooling of low alloyed steels," *Mater. Sci. Eng. A*, vol. 584, pp. 32–40, 2013.
- [110] J. D. Baird, "The effects of strain-ageing due to interstitial solutes on the mechanical properties of metals," *Metall. Rev.*, vol. 16, no. 1, pp. 1–18, 1971.
- [111] U. Mayo, "Impact of intercritical deformation on microstructural evolution and mechanical properties in low carbon steels," Universidad de Navarra, 2019.
- [112] G. T. Hahn, "Microalloyed Vanadium Steels," 1990.
- [113] D. J. Abson and J. J. Jonas, "The Hall-Petch Relation and High-Temperature Subgrains," *Met. Sci. J.*, vol. 4, no.1, pp. 24–28, 1970.
- [114] D. Kuhlmann-Wilsdorf, "Theory of plastic deformation: - properties of low energy dislocation structures," *Mater. Sci. Eng. A*, vol. 113, no. C, pp. 1–41, 1989.
- [115] A. Iza-Mendia and I. Gutiérrez, "Generalization of the existing relations between microstructure and yield stress from ferrite-pearlite to high strength steels," *Mater. Sci. Eng. A*, vol. 561, pp. 40–51, 2013.
- [116] L. P. Kubin and A. Mortensen, "Geometrically necessary dislocations and strain-gradient plasticity: A few critical issues," *Scr. Mater.*, vol. 48, no. 2, pp. 119–125, 2003.
- [117] M. Calcagnotto, D. Ponge, E. Demir, and D. Raabe, "Orientation gradients and geometrically necessary dislocations in ultrafine grained dual-phase steels studied by 2D and 3D EBSD," *Mater. Sci. Eng. A*, vol. 527, no. 10–11, pp. 2738–2746, 2010.
- [118] C. Garcia-Mateo, F. G. Caballero, C. Capdevila, and C. G. de Andres, "Estimation of dislocation density in bainitic microstructures using high-resolution dilatometry," *Scr. Mater.*, vol. 61, no. 9, pp. 855–858, 2009.
- [119] M. J. Roberts, "Effect of transformation substructure on the strength and toughness of Fe-Mn alloys," *Metall. Trans.*, vol. 1, no. 12, pp. 3287–3294, 1970.
- [120] M. K. Graf, H. G. Hillrbrand, and P. A. Peters, "Accelerated cooling of plate for high-strength large-diameter pipe," in *Accelerated cooling of steel*, 1985, pp. 165–180.
- [121] G.M Smith, "PhD Thesis," University of Cambridge, 1984.
- [122] E. Orowan, "Internal stresses in metals and alloys," *Inst. Met.*, 1948.
- [123] Y. Xu, W. Zhang, M. Sun, H. Yi, and Z. Liu, "The blocking effects of interphase precipitation on dislocations' movement in Ti-bearing micro-alloyed steels," *Mater. Lett.*, vol. 139, pp. 177–181, 2015.
- [124] M. F. Ashby, "Oxide Dispersion Strengthening," 1958.
- [125] B. Mintz, "The influence of martensite on the strength and impact behavior of steel," *Metall. Mater. Trans. A Phys. Metall. Mater. Sci.*, vol. 28, no. 10, pp. 2073–2084, 1997.
- [126] M. E. Bush and P. M. Kelly, "Strengthening mechanisms in bainitic steels," *Acta Metall.*, vol. 19, no. 12, pp. 1363–1371, 1971.
- [127] J. M. Rodriguez-Ibabe, "Online course: Optimized application of microalloying in added value steel grades Microstructure-mechanical properties relationships: toughness," no. May, 2020.
- [128] B. Mintz, G. Peterson, and A. Nassar, "Structure-property relationships in ferrite-pearlite steels," *Ironmak. Steelmak.*, vol. 21, pp. 215–222, 1994.

References

- [129] B. Mintz, W. B. Morrison, and A. Jones, "Influence of carbide thickness on impact transition temperature of ferritic steels," *Met. Technol.*, vol. 6, no. 1, pp. 252–260, 1979.
- [130] I. Gutiérrez, "Effect of microstructure on the impact toughness of Nb-microalloyed steel: Generalisation of existing relations from ferrite-pearlite to high strength microstructures," *Mater. Sci. Eng. A*, vol. 571, pp. 57–67, 2013.
- [131] A. From and R. Sandström, "Influence of mixed grain size distributions on the toughness in high and extra high strength steels," *Mater. Charact.*, vol. 42, no. 2, pp. 111–122, 1999.
- [132] T. Hanamura, F. Yin, and K. Nagai, "Ductile-brittle transition temperature of ultrafine ferrite/cementite microstructure in a low carbon steel controlled by effective grain size," *ISIJ Int.*, vol. 44, no. 3, pp. 610–617, 2004.
- [133] G. Larzabal, N. Isasti, J. M. Rodriguez-Ibabe, and P. Uranga, "Evaluating strengthening and impact toughness mechanisms for ferritic and bainitic microstructures in Nb, Nb-Mo and Ti-Mo microalloyed steels," *Metals (Basel)*, vol. 7, no. 2, 2017.
- [134] P. Uranga, C. J. Shang, T. Senuma, J. R. Yang, A. M. Guo, and H. Mohrbacher, "Molybdenum alloying in high-performance flat-rolled steel grades," *Adv. Manuf.*, vol. 8, no. 1, pp. 15–34, 2020.
- [135] J. Hannula, A. Kaijalainen, D. A. Porter, M. C. Somani, and J. Kömi, "Evaluation of Mechanical Properties and Microstructures of Direct-Quenched and Direct-Quenched and Tempered Microalloyed Ultrahigh-Strength Steels," *Steel Res. Int.*, vol. 92, no. 3, 2021.
- [136] S. Pallaspuro, A. Kaijalainen, T. Linnell, and D. A. Porter, "Tempering of direct quenched low-alloy ultra-high-strength steel, Part II - Mechanical properties," *Adv. Mater. Res.*, vol. 922, pp. 580–585, 2014.
- [137] L. Sanz, B. Pereda, and B. López, "Validation and Analysis of the Parameters for Reconstructing the Austenite Phase from Martensite Electron Backscatter Diffraction Data," *Metall. Mater. Trans. A Phys. Metall. Mater. Sci.*, vol. 48, no. 11, pp. 5258–5272, 2017.
- [138] M. Bellavoine, M. Dumont, J. Drilllet, V. Hébert, and P. Maugis, "Combined Effect of Heating Rate and Microalloying Elements on Recrystallization During Annealing of Dual-Phase Steels," *Metall. Mater. Trans. A Phys. Metall. Mater. Sci.*, vol. 49, no. 7, pp. 2865–2875, 2018.
- [139] M. Hoerner, J. Speer, and M. Eberhart, "Comparison of Ab-initio solute-boundary binding energies and experimental recrystallization data in austenite for solute Nb and other elements," *ISIJ Int.*, vol. 57, no. 10, pp. 1847–1850, 2017.
- [140] L. J. Cuddy and J. C. Raley, "Austenite grain coarsening in microalloyed steels," *Metall. Trans. A*, vol. 14, no. 10, pp. 1989–1995, 1983.
- [141] X. Azpeitia, N. Isasti, P. Uranga, J. M. Rodriguez-Ibabe, D. Stalheim, and M. Rebellato, "Through-Thickness Microstructural Optimization in Plate Rolling of Nb Microalloyed Steels 1," no. c, pp. 83–92, 2018.
- [142] L. Sanz, B. López, and B. Pereda, "Characterization of austenite microstructure from quenched martensite using conventional metallographic techniques and a crystallographic reconstruction procedure," *Metals (Basel)*, vol. 8, no. 5, 2018.
- [143] Y. J. Li, D. Ponge, P. Choi, and D. Raabe, "Segregation of boron at prior austenite grain boundaries in a quenched martensitic steel studied by atom probe tomography," *Scr. Mater.*, vol. 96, no. C, pp. 13–16, 2015.
- [144] K. . Kinsman and H. I. Aaronson, "Transformation and Hardenability in Steels," in *Climax Molybdenum*, 1967, p. 39.